Stochastic Power Quality Assessment and Harmonic Mitigation in Distribution Systems with Renewable Energy Sources

PhD Thesis

Jiajun Ma

A thesis submitted for the degree of

Doctor of Philosophy

Department of Electronic and Electrical Engineering

University of Strathclyde, Glasgow

February 2026

Declaration of Author's Right

Additional Statement on Research Progress

The author wishes to note that between February 2020 and May 2022, the progress of this research was affected by the COVID-19 pandemic. During this period, access to research resources and normal working conditions was limited, which led to delays in various stages of the study. The pandemic also had an impact on the author's physical and mental well-being. Despite these challenges, the author made every effort to complete the research to the required academic standard.

Acknowledgments

"In this year, during the golden era of my life..."

This long-contemplated acknowledgment was drafted countless times in my mind from matriculation to graduation. Each attempt to commit it to paper felt daunting. How could mere words encapsulate these years? As I slowly unfolded the tapestry of memories, those fleeting fragments of youth seemed destined for preservation once the curtain fell. Thus arrived my farewell, and with it, the closing act of my student days.

Looking back on two decades of scholarship, it felt like a murmuring stream finally breaking through mountain after mountain. Those years saw me emerge from a sheltered upbringing: those countless walks under streetlights amid bouts of self-doubt now converged in that moment, as I watched the vibrant pulse of life stream endlessly beyond the campus gates, much like the unending flow of traffic. It echoed that summer day when I stood at the podium for my master's graduation, sunlight streaming through the windows as I looked toward the horizon.

To those who illuminated my path:

My deepest gratitude went to my supervisor, Professor Kwok Lun Lo. The privilege of being guided by such an extraordinary scholar has been a beacon throughout my academic journey. He saw potential in a rough stone and sculpted it with discerning vision. His profound scholarship, tireless mentorship, rigorous academic standards, and relentless pursuit of excellence have profoundly shaped me. His guidance at every crossroads — professional counsel during uncertainties, bold encouragement for ambitious plans — granted me wings to soar to greater heights.

A tree may grow a thousand feet tall, but its roots lie deep in fertile soil. My family of origin remained my greatest fortune - their unconditional love created both spiritual and material abundance. To my parents: their silent support through twenty years of education, their teachings that nurtured independence and free-spirited growth, and their unwavering faith in every choice I made — these became my anchor through storms of doubt. May this achievement justify their boundless trust.

To kindred spirits across seasons:

Those impulsive dawn hikes to mountain peaks, sunlit barbecues and rainy-day hot

pots, and cross-city journeys just to share laughter — how precious it was to find resonant souls at each life stage. In that era of relentless motion, true companionship became a rare treasure. I'll forever cherish our sun-dappled pathways echoing with mirth, and the mutual solace we offered during trials.

This doctoral pilgrimage carried its weight:

The paralysis of writer's block, collisions between scholarship and life's chaos, and repeated shattering of ideals against reality's rocks — each struggle left indelible marks. Countless sleepless nights questioning my suitability for a Ph.D now culminated in this nearing finish line. To my persevering self: thank you. Thank you for embracing imperfections, for slow but steady progress, and for learning to love our ordinary yet extraordinary world. May I continue accepting every iteration of myself, finding joy in authenticity.

As I conclude, raindrops began tracing patterns on my windowpane.

This thesis is dedicated to my once-in-a-lifetime youth. Until we meet again at 99 George Street.

Abstract

This thesis investigates probabilistic power flow analysis, stochastic harmonic analysis, power quality assessment, and optimal configuration of Active Power Filters (APFs) in distribution networks with high penetration of renewable energy sources. The study addresses the combined effects of uncertainty, three-phase unbalance, and harmonic distortion on distribution network operation.

Firstly, a probabilistic power flow model considering uncertainties in distributed generation and load is developed. Wind power, photovoltaic generation, and load demand are modelled using appropriate probabilistic distributions, and correlations among random input variables are handled using the Nataf transformation. A probabilistic power flow method based on the Three-Point Estimation Method is implemented and validated on a benchmark distribution system. The results show that the proposed method provides accurate statistical characteristics of system states with improved computational efficiency compared to conventional sampling-based approaches.

Secondly, a three-phase stochastic harmonic power flow analysis and operational risk assessment are conducted using Monte Carlo simulation, explicitly accounting for the three-phase unbalance characteristics of distribution networks. System operational risk indices, including voltage limit violations and branch power overloads, are formulated to quantify operational risks under uncertainty. In addition, a comprehensive power quality evaluation index system is established to identify weak points associated with harmonic distortion and unbalanced operation. Simulation results demonstrate that the proposed framework can effectively identify critical nodes and operating conditions with elevated power quality risks.

Thirdly, an optimal configuration strategy for Active Power Filters is proposed based on an improved Particle Swarm Optimization algorithm. A double-layer economic optimization model is developed to determine optimal APF placement and capacity. The improved optimization strategy enhances global search capability and solution stability. Case studies show that the optimized APF configuration effectively suppresses harmonic distortion and reduces overall harmonic mitigation costs while satisfying power quality requirements.

The proposed methodologies provide a systematic framework for uncertainty analysis, power quality assessment, and harmonic mitigation in renewable-rich distribution networks.

Keywords: Distributed Generation; Probabilistic Power Flow; Three-Point Estimation Method; Stochastic Harmonic Analysis; Power Quality Assessment; Risk Assessment; Active Power Filter; Improved Particle Swarm Optimization

List of Abbreviations and Definitions

3PEM	Three-Point Estimation Method
AC/DC	Alternating Current/ Direct Current
ADRC	Active Disturbance Rejection Control
AHP	Analytic Hierarchy Process
AI	Artificial Intelligence
APF	Active Power Filter
ARIMA	Auto Regressive Integrated Moving Average
BCBV	Branch Current to Bus Voltage
BIBC	Bus Injection to Branch Current
BPSO	Binary Particle Swarm Optimization
CCPS	Compensated Carrier PWM Synchronization
CDF	Cumulative Distribution Function
CRITIC	Criteria Importance Through Intercriteria Correlation
DER	Distributed Energy Resources
DG	Distributed Generation
DSP	Digital Signal Processor
EENS	Expected Energy Not Served
EMC	Electromagnetic Compatibility
EMI	Electromagnetic Interference
EV	Electric Vehicle
FAHP	Fuzzy Analytic Hierarchy Process
GA	Genetic Algorithm
GRA	Grey Relational Analysis
HAPF	Hybrid Active Power Filter
HGCN	Harmonic Gated Compensation Network
IEC	International Electrotechnical Commission
IGBT	Insulated Gate Bipolar Transistor
IIR	Infinite Impulse Response
LOLP	Loss-Of-Load Probability
MCS	Monte Carlo Simulation

ML	Machine Learning
MPC	Model Predictive Control
mRMR	Minimum Redundancy Maximum Relevance
NIS	Negative Ideal Solution
PDF	Probability Density Function
PEM	Point Estimation Methods
PFC	Power Factor Correction
PHEV	Plug-In Hybrid Electric Vehicle
PIC	Proportional–Integral Controller
PIS	Positive Ideal Solution
PCC	Point Common Coupling
PLF	Probabilistic Load Flow
PMU	Phasor Measurement Unit
PPF	Probabilistic Power Flow
PSO	Particle Swarm Optimization
PV	Photovoltaic
PWM	Pulse-Width Modulation
RES	Renewable Energy Sources
RMS	Root Mean Square
SAPF	Shunt Active Power Filter
SCADA	Supervisory Control and Data Acquisition
SI	Swarm Intelligence
SLF	Stochastic Load Flow
TCLC	Thyristor-Controlled LC
THD	Total Harmonic Distortion
THDU	Total Harmonic Distortion of Voltage
TOPSIS	Technique For Order Preference by Similarity to Ideal Solution
TVIW	Time Varying Inertia Weight
UPQC	Unified Power Quality Conditioners
VPP	Virtual Power Plant
VRE	Variable Renewable Energy

List of Symbols

A_k	Linear Function
a_P	Availability Rate of the Active Power
a_Q	Availability Rate of the Reactive Power
$C(X_i, X_j)$	Cumulative Distribution Function
C_k	Gram-Charlier
C_i	Closeness Coefficient of Alternative i-th
C_{ins}	Installation Cost of the APF
C_{inv}	Equivalent Cost of Investment, Operation, and Maintenance of the APF
CR	Consistency Ratio
$C(s)$	Indicator Function of Failure State s
d_s	Mean Duration of State s
$E[C]$	Expected Value of the Failure Indicator
f_s	Frequency of Occurrence of State s
F	Set of All System Failure States
$f_i(x_i)$	Probability Density Function
H	Jacobian Matrix of the Fundamental Power Flow Equations (Newton–Raphson Method)
$H_k(x)$	Hermite Polynomials
I_{rk}, I_{ik}	Real and Imaginary Components of the k-th Harmonic Current
$\Delta I_{R,t}^{(k)}$, $\Delta I_{I,t}^{(k)}$	Real and Imaginary Parts of k-th Harmonic Injection Current at Nonlinear Node t-th
$\Delta \mathbf{I}_R^{(k)}$, $\Delta \mathbf{I}_I^{(k)}$	Vector of Mismatches in Real and Imaginary Parts of k-th Harmonic Injection Currents at Nonlinear Nodes
$\mathbf{J}^{(k)}$	Jacobian Matrix of the k-th Harmonic Power Flow Equations (Nonlinear Nodes Only)
J	Jacobian Matrix

κ_k	Semi-Invariants of X
m	Number of Sampling Points
N_f, N_w	Number of Failed and Operational Components in State s
N_{APF}	Total Number of APF Units Installed
σ	Standard Deviation
σ_{x_i}	Standard Deviation of X_i
$\Phi^{-1}(\cdot)$	Inverse Cumulative Distribution Function of the Standard Normal Distribution
σ_j	Standard Deviation of Column j
σ_P, σ_Q	Standard Deviation of the Active and Reactive Power
$\phi_X(t)$	Characteristic Function
$\Delta\mathbf{P}$, $\Delta\mathbf{Q}$	Vector of Active and Reactive Power Mismatches at System Nodes
P_i, Q_i	Measured Active and Reactive Power at Node i-th
p_i, q_i	Probability that Component i-th is Operational and Failed
$\overline{p}_j$	Mean of Column j
$P_{P_{ij}}(p)$	PDF of the Branch Power Flow
p_s	Probability of System State s
P_i, S_i	Probability and Severity of the i-th Risk Event
$P_{i,\mathrm{calc}}$, $Q_{i,\mathrm{calc}}$	Calculated Active and Reactive Power at Node i-th
$P_{V_i}(v)$, $P_{V_j}(v)$	PDFs of Nodal Voltages at Nodes i-th and j-th
P1	Three-Phase Voltage Imbalance
P2	Node Voltage Deviation Rate
P3	Average Harmonic Voltage Distortion Rate
P4	Harmonic Voltage Three-Phase Imbalance Degree
P5	Maximum Over-Limit Risk Value of Node Voltage
P6	Active Power Over-Limit Risk Value of Node Injection Branch
RI	Random Index

$S_{V_i}(v)$, $S_{V_j}(v)$	Severity Functions for Voltage Violations at Nodes i-th and j-th
S_i^+, S_i^-	Euclidean Distance of Alternative i from the Positive and Negative Ideal Solution
$S_{P_{ij}}(p)$	Severity Function for Overload
$S_{\mathrm{APF},i}$	Capacity of the APF at Node i-oh
$S_{\mathrm{DG},i}^{\mathrm{rated}}$	Rated Capacity of the DG at Node i-th
U_{rk}, U_{ik}	Real and Imaginary Components of the k-th Harmonic Voltage
μ_3	Third Central Moment
μ_{x_i}	Expected Value (Mean) of X_i
μ_P	Expected Values (Means) of the Active Power
μ_Q	Expected Values (Means) of the Reactive Power
V_{upper}, V_{lower}	Upper and Lower Voltage Thresholds
V^+, V^-	Positive and Negative Ideal Solution
v_j^+, v_j^-	Positive and Negative Ideal Value of Criterion j
$\Delta\boldsymbol{\theta}$	Correction Vector of Fundamental Voltage Angles
$\Delta\mathbf{V}$	Correction Vector of Fundamental Voltage Magnitudes
$\Delta\boldsymbol{\theta}^{(k)}$	Correction Vector of k-th Harmonic Voltage Angles
$\Delta\mathbf{V}^{(k)}$	Correction Vector of k-th Harmonic Voltage Magnitudes
v	Wind Speed
v_{in}, v_{out}	Cut-In and Cut-Out Wind Speed
$w_{\mathrm{AHP},j,e}$	Weight from Expert e
X	Random Variable
x_α	α-Quantile of X,
X_i, X_j	Original Data Samples of the i-th and j-th Random Variables
x_i, x_j	Transformed Data of the i-th and j-th Random Variables Mapped to the Interval $[0,1]$
z_α	α-Quantile of the Standard Normal Distribution

$\xi_{x_i,k}$	Location Coefficient for the k -th Sampling Point
$\lambda_{i,3}$	Third Standardized Central Moments of X_i,
Γ	Gamma Function
η	Energy Conversion Efficiency
$\Delta\delta_i$	Phase Angle Deviation of the Node Voltages
*	Complex Conjugation
λ_k	Transition Rate of Component k
ξ	Distinguishing Coefficient
$\lambda_{\max}$	Maximum Allowable DG Penetration Rate

List of Figures

List of Tables

Content

Chapter 1 Introduction

1.1 Motivation and Research Justification

The rapid integration of renewable energy sources (RES), such as wind turbines and photovoltaic (PV) systems, into modern power distribution networks represents a transformative shift toward sustainable energy systems. Driven by global commitments like the Paris Agreement and the imperative to decarbonize, RES penetration has escalated. According to the International Energy Agency's (IEA) Net Zero by 2050 scenario, renewables could constitute nearly 90% of global electricity generation by 2050 [1].

However, this paradigm shift introduces significant challenges to distribution networks historically designed for unidirectional power flows. The intermittent nature of wind and solar outputs, coupled with stochastic load demands, leads to uncertainties that manifest as voltage fluctuations, power reversals, and increased operational risks [2]. Compounding these issues are nonlinear loads and power electronic interfaces—ubiquitous in electric vehicles and RES inverters—which inject harmonic distortions, compromising power quality and causing equipment degradation [3].

Harmonic distortions arise from the non-sinusoidal currents drawn by nonlinear devices, propagating through the network and interacting with system impedances to produce voltage harmonics. In unbalanced three-phase systems, common in distribution networks due to asymmetric loads and single-phase connections, these harmonics exacerbate phase unbalances, leading to elevated total harmonic distortion (THD) and violations of standards such as IEEE Standard 519 [4]. Recent large-scale disturbance events, including the 2019 UK blackout [5] highlight the importance of system-level analysis under high renewable penetration. Similarly, recent discussions following the April 2025 Spanish grid blackout indicate that renewable energy sources were not the sole cause of the event but likely acted as one of several contributing factors interacting within a complex system [6].

These developments underline the need for analytical tools capable of modelling uncertainty, correlation, and three-phase harmonic propagation simultaneously. In this context, uncertainty primarily arises from the stochastic nature of load demand, PV generation, and wind power output. Correlations exist both among loads (due to shared behavioural and environmental drivers), between load and PV generation (e.g., daytime demand patterns coinciding with solar availability), and between load and wind generation (often exhibiting negative or weak correlation depending on temporal and seasonal characteristics).

Traditional deterministic power flow analyses, such as the Newton-Raphson or Forward-Backward Sweep methods, fail to capture these stochastic elements, often resulting in overly conservative or planning decisions without full information [7]. While effective for conventional systems, they cannot represent stochastic variability, input correlations, or harmonic interactions in unbalanced networks. The stochastic variability mainly arises from uncertain load demand and renewable generation outputs, PV and wind power. Input correlations exist among loads (due to shared consumption patterns), between load and PV generation (driven by daytime demand and solar availability), and between load and wind generation (which may exhibit negative or weak correlation depending on temporal characteristics). As a result, planning decisions may be either overly conservative or insufficiently informed.

Extensive research has advanced probabilistic power flow (PPF) and harmonic analysis [8], [9]. For fundamental-frequency PPF, Monte Carlo Simulation (MCS) has been widely applied to incorporate uncertainties from loads, wind, and PV [10], [11]. Whilst MCS provides high statistical accuracy and can represent arbitrary distributions, particularly when it is applied to three-phase unbalanced systems with harmonic-inclusive scenarios, nevertheless it demands long computational time. But this method is still one of the most popular and efficient approaches to analyse large-scale systems.

Point estimation methods (PEM), including the Three-Point Estimation Method (3PEM), offer computational efficiency by approximating statistical moments with few deterministic runs [12], [13]. However, PEM-based approaches typically assume independence among input variables and are often developed under balanced system assumptions. When applied to unbalanced three-phase networks, phase asymmetry may amplify uncertainty propagation, reducing the accuracy of moment estimation. This may be overcome by better selected of initial points as demonstrated in this thesis.

To address dependency among uncertain inputs, correlation handling has progressed through Nataf transformation, enabling non-normal dependent variables in PPF [14], [15], [16]. The interaction between correlation structure and phase coupling is rarely analyzed in detail in published literature, resulting in potential underestimation of voltage and loss variability [12], [13], [15], [16], [17].

In harmonic domain, deterministic methods like Newton-Raphson-based harmonic load flow [18] and frequency-domain approaches [19] solve for individual harmonics. These approaches assume fixed harmonic injections and ignore uncertainty in Distributed Energy Resources (DER) outputs and nonlinear loads. Consequently, they cannot quantify probabilistic THD risk.

Probabilistic extensions based on MCS have been proposed to incorporate DER variability in harmonic studies [20], [21], [22]. However, many of these studies still assume balanced systems or aggregate three-phase quantities, neglecting phase-specific harmonic propagation. This simplification often results in optimistic THD estimates and insufficient identification of downstream violation risks in radial feeders. Although recent work [23] considers time-varying uncertainty, the combination of correlated stochastic inputs with three-phase harmonic modeling remains limited, leading to incomplete risk characterization.

For power quality assessment, multi-criteria index systems are commonly employed. The Analytic Hierarchy Process (AHP) provides a structured way to assign weights based on expert judgment [24]. Nevertheless, AHP heavily depends on subjective pairwise comparisons, which may introduce bias and inconsistency in the evaluation process.

Entropy-based weighting methods capture objective data variability but they primarily rely on dispersion measures and overlook interdependencies among indicators, such as the coupling between voltage unbalance and harmonic distortion[25]. Existing hybrid weighting schemes attempt to combine subjective and objective information, yet few are rigorously integrated with probabilistic outputs for identifying weak nodes under correlated renewable uncertainty [26], [27].

Active Power Filter (APF) placement and sizing are commonly solved using genetic optimization algorithms, particularly Particle Swarm Optimization (PSO) and its variants. Standard PSO performs well in multi-objective trade-offs between harmonic reduction and cost. However, it is prone to premature convergence to local optima, especially in high-dimensional, non-convex problems involving both discrete placement and continuous sizing variables. Such problems typically contain multiple local optima, making it difficult for algorithms to identify the global optimum. [28], [29], [30].

Multi-objective and improved PSO variants enhance diversity but still face scalability challenges when objective functions depend on probabilistic THD distributions rather than deterministic values [31]. Most existing studies also rely on deterministic worst-case scenarios, rather than explicitly minimizing stochastic harmonic risk under correlated uncertainty [32].

The above limitations in existing approaches offer incomplete information gaps for system and operational planning. The gaps are listed below and the research in this thesis will try to bridge them.

(1) insufficient integration of correlation-aware, efficient PPF (e.g., 3PEM-Nataf) with three-phase stochastic harmonic propagation;

(2) lack of granular, phase-specific probabilistic risk metrics that quantify violation probabilities and severities under correlated uncertainties;

(3) absence of economically optimized APF configuration that explicitly accounts for stochastic harmonic risks in unbalanced networks, rather than deterministic worst-case assumptions.

Existing approaches tend to be fragmented: efficient but simplified estimation methods without unbalance representation, accurate but computationally expensive Monte Carlo frameworks without efficiency enhancement, or optimization strategies that do not directly incorporate probabilistic risk measures. Consequently, a unified and computationally tractable analytical framework for renewable-dominated unbalanced distribution systems remains necessary.

A detailed critical literature review is contained in Chapter 2.

1.2 Objectives of research

The overarching goal of this research is to develop and validate a comprehensive probabilistic framework for analyzing and mitigating power quality issues in distribution networks with high penetration of Distributed Generation (DG) and nonlinear loads. This framework aims to accurately quantify operational risks under uncertainty and optimize mitigation strategies to enhance system reliability.

To achieve this goal, the specific objectives of the thesis are defined as follows:

- **To synthesize the theoretical foundation and identify research gaps through a comprehensive literature review.** A detailed review of power flow algorithms, stochastic modeling techniques, and harmonic propagation mechanisms is conducted. This establishes the necessity of moving from deterministic to probabilistic approaches and identifies the limitations of existing studies in handling correlations and three-phase unbalances.
- **To develop an efficient probabilistic power flow model based on the 3PEM and Nataf transformation.** This objective focuses on addressing the correlation among input random variables (e.g., wind, PV, and load). The proposed method is designed to improve computational efficiency for fundamental frequency power flow analysis while using Monte Carlo Simulation as a benchmark for comparison. The proposed 3PEM–Nataf framework is solver-agnostic: it can be applied to both balanced and unbalanced networks, provided that a three-phase power-flow formulation is used.
- **To establish a three-phase stochastic harmonic power flow framework using MCS.** Different from the fundamental frequency analysis, this objective employs MCS to capture the complex stochastic characteristics of **harmonic propagation** in **unbalanced** networks. It aims to quantify phase-specific risks, including voltage deviations and Total Harmonic Distortion (THD) exceedances, under 10,000 stochastic scenarios.
- **To construct a multi-criteria power quality assessment and risk evaluation model.** A hybrid weighting scheme combining the Analytic Hierarchy Process

(AHP) and the Criteria Importance Through Intercriteria Correlation (CRITIC) method is proposed to evaluate system performance. This objective allows for the objective identification of "weak nodes" by integrating indices such as harmonic distortion, voltage deviation, and power losses into a unified risk metric.

- **To design and implement an Improved Particle Swarm Optimization (IPSO) algorithm for Active Power Filter (APF) configuration.** The algorithm aims to determine the optimal placement and sizing of APFs. Enhancements such as niche-based subpopulation evolution are introduced to avoid premature convergence, ensuring a balance between minimizing network-wide harmonic distortion and reduction of economic costs.
- **To validate the proposed models and algorithms via the IEEE 33-bus distribution system.** The final objective is to verify the effectiveness and robustness of the integrated framework through rigorous case studies, ensuring the proposed methods are applicable to IEEE 33-bus scenarios involving renewable integration.

1.3 Original contribution

This thesis makes several original and interlinked contributions to the field of probabilistic power systems analysis and power quality management in distribution networks with renewable penetration. These contributions collectively address gaps in the integrated treatment of correlated uncertainties, three-phase harmonic propagation, risk quantification, and economically optimal mitigation. The major contributions to knowledge are listed below:

1. Dependence-Aware Probabilistic Power Flow Framework

The thesis proposes and validates an integrated Three-Point Estimation Method (3PEM) enhanced by Nataf transformations to explicitly model rank correlations among uncertain inputs (loads, wind, and PV generation). This dependence-aware approach significantly improves the fidelity of estimated moments for node voltages, branch powers, and network losses compared with independent-variable assumptions. The framework is further extended to probabilistic harmonic power flow, enabling fast yet accurate screening of Total Harmonic Distortion (THD) distributions under correlated uncertainties, representing a novel combination that fills a methodological gap in existing literature.

2. Comprehensive Three-Phase Stochastic Harmonic Risk Assessment with Hybrid Weighting

A three-phase Monte Carlo-based stochastic harmonic power flow model (10,000 scenarios) is developed, incorporating realistic harmonic injection spectra and unbalanced loading conditions. This framework enables a detailed and data-driven characterisation of how uncertainty and harmonic distortions propagate across phases in radial distribution networks. In addition, a hybrid weighting scheme combining the Analytic Hierarchy Process (AHP) with an improved CRITIC method (incorporating redundancy entropy) is proposed to balance expert judgment with objective data information, leading to a robust prioritisation of power quality weak points, with particular emphasis on three-phase harmonic voltage imbalance under renewable penetration. The results reveal a clear downstream amplification of uncertainty and systematically higher violation risks in the most heavily loaded phase, highlighting behaviours that cannot be captured by deterministic or single-phase analyses.

3. Enhanced Optimization Strategy for Active Power Filter Placement and Sizing

An improved Particle Swarm Optimization (PSO) algorithm incorporating niche division and periodic subpopulation elimination is introduced to solve the multi-objective APF configuration problem. By strategically allowing controlled over-compensation at selected buses, the method exploits network topology to achieve global harmonic suppression more efficiently than conventional local-matching approaches. Case studies on the IEEE 33-bus system demonstrate that the proposed approach significantly reduces voltage harmonic distortion while meeting IEEE Standard 519 requirements, achieving an effective balance between harmonic mitigation performance and overall investment cost.

These contributions form an end-to-end methodological chain – from fast dependence-aware probabilistic screening (3PEM), through detailed three-phase risk profiling (MCS + risk metrics), to structured weak-point identification based on a hybrid AHP–

CRITIC weighting method, and finally to economically optimized mitigation (enhanced PSO based on voltage THD). Together, they advance both the theoretical understanding of uncertainty-harmonic interactions and the practical toolkit available to distribution network planners and operators.

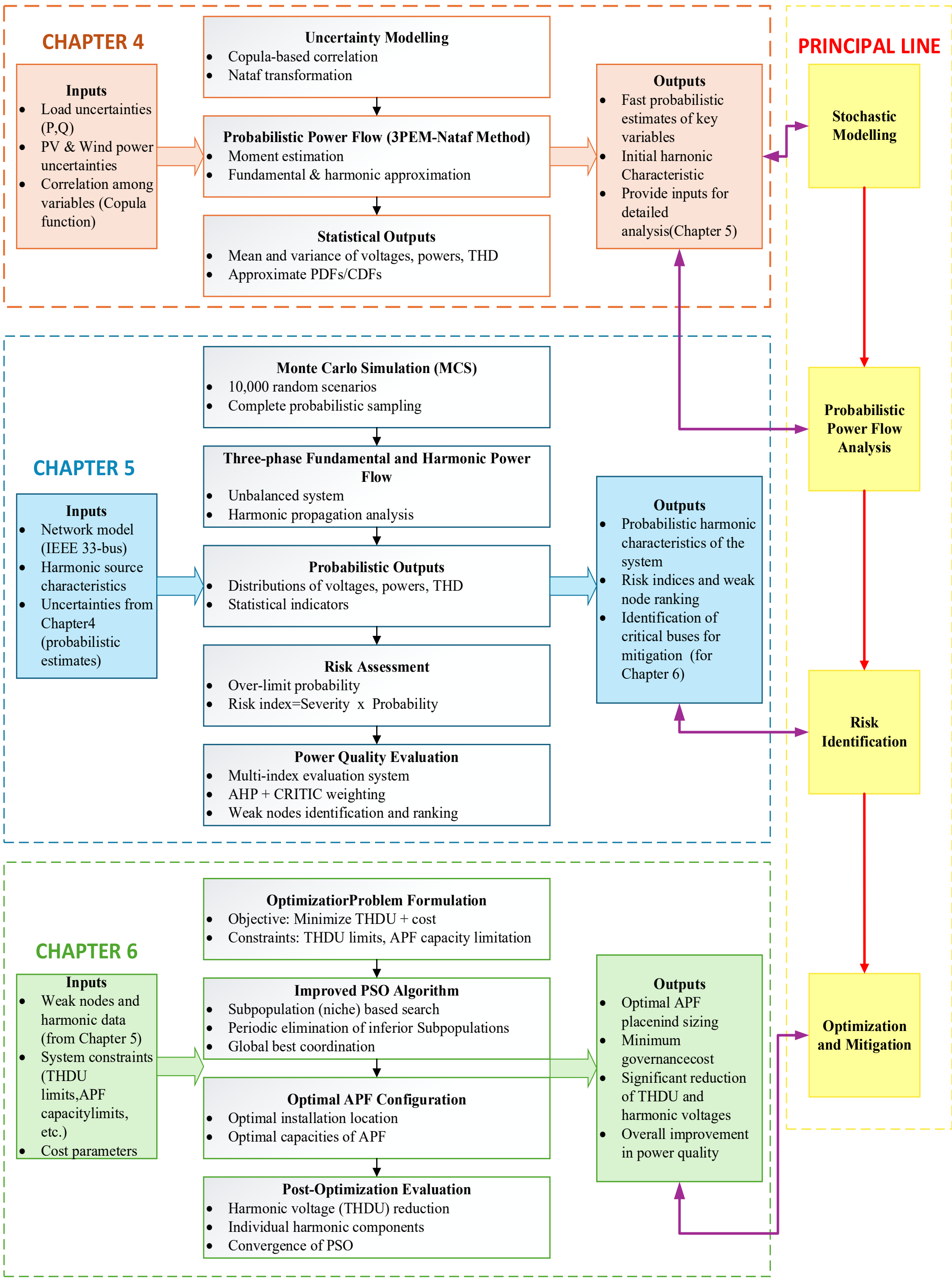

Figure 1-1 Principal Research Line of the Thesis

As shown in Figure 1-1 presents an integrated workflow linking Chapters 4 to Chapter 6 in this thesis. The proposed research follows a structured progression from stochastic modelling to optimization-based mitigation. The framework begins with dependence-aware probabilistic modelling using the 3PEM–Nataf approach, which provides efficient initial estimates of system uncertainty characteristics. Building upon this, a detailed three-phase Monte Carlo-based harmonic power flow analysis is conducted to capture the full probabilistic behaviour of voltages, power flows, and harmonic distortion under realistic operating conditions.

These probabilistic results are then used to quantify system risk through over-limit probabilities and severity-based risk indices, followed by a hybrid AHP–CRITIC evaluation to identify and prioritise power quality weak points. Finally, the identified weak buses and harmonic characteristics serve as key inputs to the optimization stage, where an enhanced PSO algorithm determines the optimal placement and sizing of APFs to achieve cost-effective harmonic mitigation.

This end-to-end workflow highlights the interdependency between modelling, analysis, risk assessment, and optimization, demonstrating how each contribution builds upon the previous stage to form a complete and practically applicable solution for power quality management in distribution networks with high renewable penetration.

1.4 Thesis structure

The thesis is organized into seven chapters, systematically progressing from theoretical modeling to probabilistic analysis, risk assessment, and mitigation optimization. The structure is outlined as follows:

- **Chapter 1 – Introduction:** Presents the research motivation, background, and the specific challenges posed by renewable integration and harmonic pollution. It defines the research objectives, summarizes the original contributions, and outlines the overall organization of the thesis.
- **Chapter 2 – Literature Review:** Provides a comprehensive review of existing methodologies in power flow calculation, harmonic modeling, stochastic analysis techniques (MCS, PEM), and power quality mitigation. It critically analyzes the limitations of current deterministic and single-phase approaches,

identifying the specific research gaps this thesis aims to address.

- **Chapter 3 – Theoretical Modelling and Methodology:** Establishes the mathematical foundations for the study. It details the probabilistic modeling of uncertain variables (wind, PV, and load), the handling of input correlations using Nataf transformation, and the fundamental principles of the 3PEM and MCS. Additionally, it introduces the harmonic source models and network equations that are later applied in the probabilistic and three-phase analyses.
- **Chapter 4 – Dependence-Aware Probabilistic Power Flow Analysis:** Proposes and validates a probabilistic power flow framework based on 3PEM and Nataf transformation. This chapter focuses on quantifying the impact of input variable correlations on system states (voltages and losses). It compares the proposed method with Monte Carlo Simulation to demonstrate its computational efficiency and accuracy in fundamental frequency analysis and preliminary harmonic screening.
- **Chapter 5 – Three-Phase Stochastic Harmonic Analysis and Risk Assessment:** Extends the investigation to a three-phase unbalanced framework using Monte Carlo Simulation. This chapter analyzes the propagation of harmonics under stochastic conditions and introduces a probabilistic risk assessment framework based on over-limit indicators. A hybrid weighting method combining Analytic Hierarchy Process (AHP) and Criteria Importance Through Intercriteria Correlation (CRITIC) is applied to evaluate power quality performance and identify weak nodes in the distribution network.
- **Chapter 6 – Optimization of Active Power Filter Configuration:** Focuses on the mitigation of harmonic distortion and develops an optimization framework for the placement and sizing of Active Power Filters (APFs), combining discrete location selection and continuous capacity optimization. An Improved Particle Swarm Optimization (IPSO) algorithm, incorporating niche techniques, is proposed and implemented to minimize total investment costs and harmonic distortion, ensuring compliance with power quality standards.
- **Chapter 7 – Conclusion and Future Work:** Summarizes the key findings and

methodological contributions of the research, and outlines directions for future work in power system analysis.

1.5 Publication

J. Ma and K. Lo, "*Stochastic Power Flow Calculation in Distribution Networks Based on the Point Estimation Method and a Comparison with the Monte Carlo Algorithm*," in Recent Advances in Circuits and Systems, Lecture Notes in Networks and Systems, Springer, 2026. [Online]. Available: https://link.springer.com/book/10.1007/978-3-032-20362-5

Chapter 2 Literature Review on Power Flow and Harmonic Analysis in Modern Power Systems

This chapter presents a comprehensive overview and in-depth analysis of three critical aspects associated with power flow studies in modern power systems: power flow and harmonic analysis, stochastic power flow with probabilistic methods, and power quality enhancement strategies.

- Section 2.1 reviews the latest developments in power flow calculation models and methods, focusing on their evolution and the inherent complexities involved. It further explores various harmonic source models, delineating the mechanisms through which harmonics propagate within electrical networks. In addition, this section critically compares several harmonic power flow calculation methods, highlighting their relative advantages and limitations in practical applications.
- Section 2.2 investigates the current state of stochastic power flow and probabilistic analysis. It emphasizes the significance of incorporating uncertainty within power system studies by examining different stochastic modelling approaches for loads, wind power generation, and photovoltaic systems. The section provides detailed insights into methodologies such as the Monte Carlo Simulation (MCS) and Three-Point Estimation method, assessing their practical implications and effectiveness in addressing uncertainty. Moreover, the influence of correlation modelling among random variables on stochastic power flow results is discussed, underscoring its relevance for accurate power system planning and operation.
- Section 2.3 addresses methodologies for power quality assessment, specifically discussing evaluation index systems and various weight selection techniques. This enables an objective quantification and prioritization of power quality parameters critical for maintaining system reliability and operational efficiency.
- Section 2.4 covers principles and mathematical modelling associated with Active Power Filters (APFs). It explains the fundamental operation of APFs and their role

in mitigating harmonic distortions. The section also reviews applications of optimization algorithms in configuring these filters, highlighting their capability to enhance overall power system quality and performance effectively.

Overall, this chapter lays a foundation by synthesizing theoretical advancements and practical methodologies necessary for addressing complex issues in power flow analysis, harmonic mitigation, and quality enhancement within contemporary electrical power systems.

2.1 Research Progress on Power Flow and Harmonic Flow

2.1.1 Evolution of Power Flow Calculation Models

Power flow calculations are essential for analyzing distribution networks and ensuring reliable operation. Various methods have been developed to address the inherent non-linearity of distribution systems while improving computational efficiency and accuracy. One of the foundational approaches is the Newton-Raphson method, widely adopted due to its accuracy and robust convergence properties [33]. While the method can handle both balanced and unbalanced systems, its computational intensity increases significantly with network size, limiting its applicability in large-scale real-time simulations and dynamic scenarios [34], [35] .

To address the specific requirements of distribution networks, the Forward-Backward Substitution Method was introduced, particularly for handling voltage drop computations in radial systems [36]. This iterative approach, which involves a forward sweep for voltage updates and a backward sweep for current calculations, has proven effective for unbalanced and heavily loaded feeders. Expanding on this methodology, the Forward-Backward Sweep Algorithm improves numerical stability in three-phase unbalanced network analyses, offering advantages in convergence speed and computational efficiency [37].

Beyond iterative approaches, matrix-based techniques have gained attention for their ability to organize and streamline power flow calculations in three-phase networks. Bus impedance and admittance matrix formulations enable efficient handling of meshed and interconnected systems, forming the basis for advanced methodologies such as the Implicit Z-Bus, Forward-Backward Sweep, and current injection techniques, particularly in the presence of transformers and distributed loads [12], [15],

[38]. Additionally, linear modelling approaches have been explored for multi-energy systems, integrating electricity-heat interactions and expanding power flow studies to broader energy domains [39].

Despite these advancements, challenges remain in optimizing power flow models for emerging power system requirements. The increasing penetration of distributed energy resources, bidirectional power flows, and the need for real-time operation demand novel algorithmic formulations that balance accuracy, scalability, and computational efficiency. Future research directions should explore hybrid methodologies that combine iterative and direct methods, leverage artificial intelligence for adaptive convergence strategies, and integrate physics-informed machine learning techniques to enhance power flow solvers. These innovations could contribute to more efficient power system analysis, enabling real-time optimization and decision-making in distribution network [40], [41].

The main characteristics of various power flow calculation methods are summarized as follows. Various power flow calculation methods used in distribution networks exhibit distinct characteristics in terms of accuracy, computational efficiency, and applicability. The Newton–Raphson method offers high accuracy and robust convergence and is applicable to both balanced and unbalanced systems, although it is computationally intensive. Forward–backward substitution methods provide moderate accuracy and efficiency and are particularly suitable for radial systems due to their simple implementation, but their applicability is limited to such topologies. Similarly, forward–backward sweep methods achieve medium to high accuracy with high computational efficiency and are well suited for radial or weakly meshed networks, especially in unbalanced conditions, although their performance may decline in more complex network structures. Matrix-based techniques deliver high accuracy and are flexible enough to handle meshed systems, but they involve relatively high implementation complexity. Linear modelling approaches, particularly those used in multi-energy systems, enable fast computation and facilitate coupling between different energy domains, albeit with reduced accuracy due to linearisation. In addition, sparse matrix solvers are highly effective for large-scale systems, providing both high accuracy and efficiency through computational acceleration, although they require careful structural design. Overall, these methods involve clear trade-offs between accuracy, efficiency, and applicability, and no single method is universally optimal. Therefore, the selection of an appropriate approach should be determined by the specific network structure and analysis requirements.

2.1.2 Harmonic Sources and Characteristics

The harmonic behaviour in distribution networks arises from both traditional non-linear loads and emerging inverter-based DG, resulting in increasingly complex and dynamic spectral characteristics.

Historically, harmonic distortion was primarily attributed to non-linear loads on the demand side. As established in the seminal work in Ref. [42], these loads draw non-sinusoidal currents even under sinusoidal voltage supply, thereby introducing harmonic components into the system. These harmonic currents propagate through the network and interact with system impedances, leading to voltage distortion. With the widespread adoption of domestic and commercial power electronic devices, such as Compact Fluorescent Lamps, the impact of harmonic distortion has extended beyond industrial environments to general distribution systems. Although individual low-power devices contribute limited distortion, their aggregated effect—characterised by diverse phase angles and partial harmonic cancellation or reinforcement—can pose significant risks to transformer thermal limits and neutral conductor loading [43].

In addition to traditional sources, distribution networks have experienced a significant transition toward active systems with high penetration of inverter-based distributed generation. PV systems, while designed to deliver clean energy, introduce harmonic components due to high-frequency switching operations and control loop dynamics. These harmonics often exhibit broadband characteristics and may include both low-order and high-order components, depending on inverter topology and operating conditions [44], [45]. Moreover, the harmonic emission from PV systems is not constant but varies with irradiance levels and operating states, leading to time-varying spectral behaviour.

Wind turbine generators introduce further complexity. In addition to injecting harmonic currents, they modify the network impedance characteristics, particularly when multiple units are connected within the same feeder. This interaction can shift the natural resonant frequencies of the system, giving rise to harmonic amplification phenomena, where specific frequency components are significantly magnified [46]. Such resonance-related effects highlight that harmonic distortion is not solely determined by source magnitude but also by the interaction between sources and network properties.

The harmonic content observed in distribution networks is therefore inherently complex and non-stationary. Beyond steady-state harmonic distortion, transient events—such as switching operations, converter commutations, and load variations—can generate short-duration but high-magnitude spectral components that exceed steady-state limits [47]. These transient harmonics are particularly important as they may contribute to insulation stress and protection malfunctions, even if their duration is limited.

Furthermore, the spectral characteristics of harmonics are strongly influenced by converter topology and design. For instance, the transition from conventional two-level converters to multilevel inverter structures significantly alters the harmonic profile. Multilevel converters can effectively reduce low-order harmonic distortion by producing stepped voltage waveforms, thereby shifting harmonic energy toward higher frequency ranges that are easier to filter [48], [49]. This indicates that harmonic characteristics are not only dependent on source type but are also intrinsically linked to the physical and operational structure of power electronic interfaces.

Overall, the harmonic profile of distribution networks is shaped by the combined influence of diverse sources, time-varying operating conditions, and evolving converter technologies. This results in a multi-frequency, dynamic distortion environment, which presents significant challenges for accurate modelling, analysis, and subsequent mitigation.

Building on the above observations, a key research gap lies in the lack of unified analytical frameworks that can simultaneously capture the stochastic nature of harmonic sources, their interactions within unbalanced distribution networks, and the resulting impact on system-level power quality. Existing studies often treat harmonic sources, propagation mechanisms, and mitigation strategies in isolation, without fully accounting for their coupled effects under uncertainty.

2.1.3 Mechanisms of Harmonic Propagation

Harmonic distortion has become a serious concern in power systems, largely due to the rise of nonlinear loads and power electronic devices. These devices introduce current and voltage harmonics that can move through networks and affect equipment operation, power quality, and system reliability.

Several studies have investigated how harmonics spread in distribution networks with different types of loads and generation units. For example, in Ref. [20] used the Electromagnetic Transient Program (EMTP) to model devices that produce harmonics and to identify parameters affecting harmonic propagation. Their study investigated how these signals move within a system and identified the main parameters (such as circuit topology and component ratings) that affect the spread of harmonic content. The authors provided a systematic approach to gauge the sensitivity of the network to different load profiles and switching events. In Ref. [13] discussed traction Pulse-Width Modulation (PWM) converters, highlighting how their operating points can be seen as single-phase PQ loads for load flow and harmonic penetration studies. Their results helped illustrate how traction converters, when operating under various speed and load conditions, can introduce harmonic components that must be managed to meet power quality requirements. When focusing on renewable energy sources, in Ref. [50] examined resonance damping in a 400MW wind power plant, aiming to reduce high-frequency oscillations and maintain stable voltage profiles.

In Ref. [51] studied the effects of multiple distributed energy resources on harmonic interactions in power distribution systems. Their findings underlined that renewable generators and power electronics-based units can significantly alter harmonic flow paths. Research has also targeted harmonic state estimation methods to pinpoint specific sources of distortion. In marine applications, in Ref. [52] proposed an inductive filtering method that combines a transformer-integrated reactor with a voltage-source inverter, aiming to improve power quality in shipboard environments. By analyzing the impedance seen by the inverter and applying coordinated control methods, they showed how this combined setup improves power quality and reduces stress on onboard equipment. In Ref. [53] introduced a non-parametric confidence interval estimation approach to forecast harmonics produced by high-speed electric trains, enabling better planning of railway power supplies.

Beyond power distribution, harmonic source modelling and wave propagation are studied in diverse areas. In electromagnetic compatibility, in Ref. [54] developed a near-field analytical model to reduce interference in wireless power transfer systems using an nth harmonic shielding coil.

Harmonic wave propagation in mechanical structures has been investigated by several researchers. In Ref. [55] derived an analytical solution for layered asphalt pavement under a moving harmonic load, offering insights into stress and strain profiles in complex materials. In Ref. [56] examined how a lubricant film changes the dynamic response of rotating elements under harmonic excitation, with implications for bearing design and vibration control. In Ref. [57] studied distinctive resonance features at zero group velocity frequencies, working to explain special trembling patterns that occur in certain waveguide modes.

In summary, research on harmonic propagation mechanisms reveals a complex interplay between network topology and physical media. In electrical systems, the focus has transitioned toward understanding how circuit parameters and multi-source interactions define the flow paths and penetration of harmonic currents. Simultaneously, the integration of insights from mechanical wave analysis and electromagnetic field theory provides a more holistic view of wave attenuation, resonance, and energy transfer. This multi-disciplinary understanding of propagation pathways is essential for developing predictive models that can accurately track the spatiotemporal evolution of harmonics across diverse and interconnected systems.

2.1.4 Harmonic Mitigation Strategies

Harmonic mitigation in distribution networks has evolved from traditional passive filtering techniques to advanced, adaptive, and converter-based control strategies. This subsection reviews the main mitigation approaches, including passive and active filtering, inverter-based compensation, and emerging intelligent control methods.

The evolution of harmonic mitigation reflects a transition from static hardware solutions to dynamic, software-defined compensation. While traditional passive filters were once the mainstay, their limitations—specifically fixed frequency response and susceptibility to resonance—have led to the dominance of active topologies.

Active Filtering via Distributed Generation (DG): A landmark paradigm shift, as proposed in Ref. [58], involves repurposing DGs as distributed active filters. By utilizing the existing power electronic interfaces of DGs, the system can damp background harmonic propagation without requiring dedicated compensation hardware. In Ref. [59] and [60] further elaborate that these active strategies are essential for radial networks where source impedance fluctuations render passive filters ineffective.

Hybrid and Multi-Level Control: The literature increasingly favors hybrid solutions that combine the cost-efficiency of passive filters with the precision of active control. This is particularly vital in industrial settings where, in Ref. [61] note, high-magnitude harmonic currents from heavy machinery necessitate a robust, state-of-the-art system design to prevent equipment derating and failure.

Modern distribution networks are no longer just passive recipients of energy; they are active ecosystems where converter-interfaced renewables serve a dual role.

Ancillary Services and Microgeneration: In Ref. [62] and [63] explore the prosumer potential of PV systems. Beyond energy injections, these inverters provide harmonic compensation as an ancillary service. In Ref. [63] utilize sensitivity analysis to demonstrate that with optimized control loops, renewable sources can autonomously mitigate voltage harmonics, effectively transforming a pollution source into a stabilizing asset.

Industrial vs. Residential Tailoring: The mitigation requirements differ significantly in Ref. [64] contrast the high-power, low-order harmonic issues of industrial zones with the high-frequency, stochastic distortion found in urban/residential feeders. They argue that residential mitigation requires high-resolution monitoring and adaptive filtering due to the diverse and unpredictable nature of consumer electronics.

The most significant frontier in doctoral research is the application of Artificial Intelligence (AI) to handle the non-linearities of modern grid harmonics.

AI and Hybrid Control Models: Traditional linear controllers often fail under the highly dynamic conditions of urban networks. In Ref. [65] propose hybrid AI-based models—integrating neural networks or fuzzy logic—to predict harmonic trends and optimize filter response in real-time. This "intelligent mitigation" allows the system to preemptively adjust to load changes, a capability far beyond the reach of conventional PI controllers.

Component-Level Diagnostics: In Ref. [66] introduces a unique correlation between harmonic pollution and physical asset health, specifically citing transformer oil degradation as a consequence (and source) of harmonic stress. This suggests that future mitigation strategies must be integrated into Asset Management System, where harmonic suppression is linked to extending the operational lifespan of grid infrastructure.

Despite the significant progress in harmonic mitigation techniques, existing approaches often face limitations in handling the increasing complexity, uncertainty, and multi-source interactions in modern distribution networks. In particular, conventional methods lack coordinated optimisation capabilities for the placement and sizing of compensation devices under stochastic operating conditions. To address these challenges, the following chapter investigates an optimisation-based framework for harmonic mitigation, focusing on the optimal configuration of APF in distribution networks.

2.1.5 Comparison of Various Harmonic Power Flow Calculation Methods

Harmonic flow calculations are important in several engineering applications, including electrical power systems, fluid dynamics, and thermal processes. Such calculations help identify how distortions, oscillations, or oscillatory energy propagate through systems, allowing researchers and practitioners to improve design, enhance efficiency, and maintain reliable operation. This review examines different methods proposed in the literature, focusing on their underlying principles, areas of application, and potential benefits for both industry and academia.

Several methods have been developed for harmonic load flow calculations, each with distinct principles and applications:

1. Newton-Raphson Method [18]:

The Newton–Raphson method is an iterative numerical technique used to solve nonlinear equations by linearising them around an initial estimate and updating the solution until convergence is achieved. In the context of harmonic load flow analysis, it is applied to solve the nonlinear equations arising from harmonic injections and their impact on system voltages and currents. This method is well suited for complex power systems with strong harmonic interactions, as it provides high accuracy in calculating bus voltages and branch currents across multiple harmonic orders. However, its main drawback lies in its relatively high computational cost, particularly for large-scale systems or when a wide range of harmonic frequencies is considered. In addition, convergence performance can be sensitive to the choice of initial conditions and may deteriorate in systems with severe distortion or strong nonlinearities.

2. Fast Decoupled Load Flow Method [67]:

The fast decoupled method is an approximation of the Newton–Raphson approach that reduces computational complexity by separating active and reactive power calculations. This is achieved through simplifying assumptions, such as neglecting line conductance and assuming voltage magnitudes remain close to unity, which allows the Jacobian matrix to be decoupled into independent submatrices. As a result, the method is computationally efficient and is particularly suitable for large-scale systems where speed is a key concern, such as transmission networks, while still providing acceptable accuracy for harmonic-related studies [67]. However, this simplification comes at the cost of reduced accuracy compared to the full Newton–Raphson method, especially in systems with significant harmonic distortion or strong nonlinear behaviour. In such cases, the underlying assumptions may not be held, which can lead to convergence difficulties or less reliable results.

3. Backward/Forward Sweep Method:

The backward/forward sweep method is a two-step iterative technique commonly used for radial distribution networks. It operates by first performing a backward sweep, in which branch currents are calculated from downstream nodes toward the upstream nodes, followed by a forward sweep that updates node voltages from the root node toward the terminal nodes. This approach avoids matrix inversion and therefore has low computational cost, making it highly efficient for radial systems such as those typically found in suburban and rural distribution networks. However, its applicability is limited to radial topologies, and it is not suitable for meshed networks. In addition, convergence performance may degrade under conditions with high harmonic distortion or strong nonlinearities.

4. Frequency Domain Methods[19]:

Decoupled harmonic analysis methods treat each harmonic frequency independently by assuming the network behaves linearly at each frequency. Under this assumption, standard AC load flow techniques can be applied separately for each harmonic order, which simplifies the overall solution process. This approach is computationally efficient and is well suited for systems where interactions between different harmonic components are weak, making it useful for preliminary studies or situations where quick estimates are required. However, because each harmonic is solved in isolation, these methods do not capture coupling effects between different harmonic orders. As a result, they may produce less accurate results in systems with strong nonlinear loads, where harmonic interactions are significant and can lead to higher levels of distortion than predicted.

5. Probabilistic Harmonic Load Flow Methods [21]:

Probabilistic harmonic analysis methods extend conventional approaches by incorporating uncertainties in harmonic sources and loads. They use techniques such as Monte Carlo Simulation (MCS) or data clustering to evaluate a range of possible operating conditions and estimate the resulting variation in harmonic distortion. This allows the analysis to produce statistical descriptions, such as probability distributions of voltage distortion levels, rather than single deterministic values. Such methods are particularly useful in planning and design of modern distribution systems, where renewable generation and load behaviour are inherently variable, as they provide a more realistic representation of system performance under uncertainty. However, these approaches are generally more complex and computationally demanding than deterministic methods, and they require detailed information on the probability distributions of inputs, which may not always be readily available in practice.

Table 2-1 presents a comparative summary of the main harmonic power flow methods in terms of accuracy, computational efficiency, applicability, and key limitations, highlighting the trade-offs between precision and computational cost.

Table 2-1 Comparison of Each Method

Method	**Accuracy**	**Computational Efficiency**	**Applicability**	**Limitations**
Newton-Raphson	High	Low	Complex systems, significant interactions	Intensive computation, convergence issues
Fast Decoupled Load Flow	Moderate	Moderate	Large systems, acceptable approximation	Less accurate, convergence in distorted systems
Backward/Forward Sweep	Moderate	High	Radial distribution networks	Limited to radial systems, convergence issues
Frequency Domain Methods	Moderate to Low	High	Minimal interactions, quick analysis	Misses harmonic interactions, potential inaccuracies
Probabilistic Harmonic Load Flow	Variable (statistical)	Low	Uncertain systems, planning	Complex, data-intensive, computationally heavy

A variety of studies have explored methods to model and manage harmonic flow in electrical networks. For example, one approach involves using abstract data types with complex parameters combined with a backward/forward sweep algorithm to assess load flow in networks experiencing harmonic pollution [68]. By capturing nonlinear characteristics introduced by distributed generation units and loads, the algorithm handles both fundamental and harmonic frequencies in the same framework. This unified approach allows more accurate predictions of harmonic voltage and current levels at various nodes and branches in the network.

In a different context, in Ref. [69] investigated the impact of harmonic distortion on induction motor performance using a slotted semi-analytical harmonic model. The study demonstrated that harmonic voltages can lead to additional rotor losses, thermal stress, and mechanical vibrations due to slotting effects. These findings highlight the practical consequences of harmonic distortion on electrical equipment, reinforcing the importance of accurate harmonic analysis and effective mitigation strategies in distribution networks. One study [70] presented a method called compensated carrier PWM synchronization (CCPS) for power converters exposed to AC unbalances. This synchronization strategy helps converters operate smoothly when connected to industrial grids with fluctuating power quality. The proposed method adjusts the phase and frequency of the carrier signals so that the converter's switching actions remain synchronized, even when the grid supply deviates from ideal conditions. By doing so, the converter can maintain stable operation, mitigate additional harmonic content, and support industrial grids where supply quality often fluctuates.

In a more recent contribution [22] and [71], the authors presented a harmonic power-flow algorithm designed for three-phase networks that include converter-interfaced distributed energy resources. Their formulation adds frequency-dependent terms to conventional load-flow equations, capturing the dynamic interactions between converters and the rest of the system. With high penetration of renewable resources, these converters become significant sources of harmonic injections, making accurate modelling critical for evaluating system performance and designing harmonic mitigation measures.

In summary this section compares several harmonic power flow calculation methods, including the Newton-Raphson approach, fast decoupled approach, backward/forward sweep approach, frequency domain methods, and probabilistic harmonic load flow methods. Each method has different strengths, computational demands, and ranges of application. For instance, the Newton-Raphson approach offers high accuracy but can be slow, while the fast decoupled approach is faster but less precise in highly distorted systems. The backward/forward sweep approach works well for radial networks but is not suitable for meshed ones, and frequency domain methods handle each harmonic order separately but ignore possible interactions among them. The probabilistic approach considers uncertainties in harmonic sources and loads, though it requires extensive data and can be more time-consuming.

These studies demonstrate the evolving nature of harmonic power flow analysis. Some focus on improved computational frameworks for distribution systems, while others address specific components like induction motors and power converters. The inclusion of frequency-dependent terms in recent research highlights the increasing role of renewable energy integration, emphasizing the need for more advanced harmonic mitigation strategies.

2.2 Current Research Status of Stochastic Power Flow and Probabilistic Analysis

2.2.1 Stochastic Load Models

Stochastic load models provide mathematical methods to capture the variability of loads in different systems. These loads can vary because of changes in weather, traffic, or operational conditions, and their fluctuations can significantly affect the performance and reliability of infrastructures, power grids, and mechanical components. Stochastic load models incorporate random variations to better estimate system behaviour, improving reliability in fields like power systems and structural engineering.

One of the uses of stochastic modelling in power systems was in short-term load forecasting, where external factors like weather conditions are central to predicting hourly demands. In Ref. [72] showed how adaptive methods that factor in temperature or precipitation can improve the accuracy of load forecasts. Accurate forecasts are important for utilities that need to balance generation and demand, especially under changing conditions.

Alongside forecasting, models for dynamic state estimation have been proposed to assess power system security. In Ref. [73] introduced dynamic state estimators that integrate uncertain load inputs to improve real-time assessment of system stability and voltage deviations. This approach allows system operators to anticipate possible threats to system stability and apply corrective measures ahead of time. Including stochastic load behaviour helps identify conditions under which a system might experience voltage collapses, frequency deviations, or other stressors that could disrupt normal operations.

Researchers also investigated how stochastic load modelling can benefit unit commitment tasks in power systems. In these tasks, operators decide which generating units to turn on or off at different time intervals to meet the expected demand. However, load predictions are never exact, making uncertainty a key factor in planning reserves and preventing shortages or overloads. One study [74] examined how load uncertainty influences unit commitment risk and suggested that stochastic approaches improve rescheduling policies and grid stability. Following this line of work, in Ref. [75] examined the economic trade-offs in reliability planning by introducing a stochastic unit commitment framework. This framework weighs the financial cost of meeting uncertain loads against the need to maintain security margins. The study provided numerical results showing how probabilistic modelling helps operators balance the cost of additional generation against the risk of power interruptions.

With the rise of electric vehicles and distribution generation, interest in load modelling became broader. In Ref. [76] highlighted how plug-in hybrid electric vehicles (PHEVs) introduce unpredictable load variations due to random charging behaviours, requiring probabilistic models to capture arrival and departure times. In Ref. [77] proposed a medium-term feeder model based on actual measurements, thereby capturing real-world fluctuations in distribution networks. This research emphasized the importance of reliable stochastic load models for designing transformers and other distribution assets that can handle sudden demand changes without compromising performance.

Beyond power grids, stochastic modelling has also been applied in transportation networks. One study in Ref. [78] described a stochastic load model for traction power in electrified railways. The intent was to capture random fluctuations related to train schedules, speeds, and passenger loads, making power demand less predictable. In Ref. [79] then proposed a two-sided stochastic source-load approach, highlighting interactive randomness in both generation and consumption within power networks.

In Ref. [80] looked at carbon emission constraints tied to load uncertainty. By embedding stochastic elements into the optimization of power system dispatch, they showed that decision-making can account for both environmental goals and load variability. In Ref. [81] moved this conversation to a longer time scale, employing Monte Carlo Tree Search to plan for geographically shiftable resources while aiming for lower carbon footprints.

In Ref. [82] proposed a hybrid approach that combines data-driven and model-based methods to predict loads and manage the lifespan of wind turbines. By linking operational data with damage accumulation calculations, their model offers more robust control strategies for turbine performance. In Ref. [83] employed scenario reduction and distributed methods for stochastic AC optimal power flow, aiming to handle load uncertainty in a scalable manner.

These contributions point to a trend where stochastic load modelling is broadening to include energy markets, carbon accounting, and advanced optimization. By capturing random variations in all parts of a system—loads, sources, and constraints—researchers are working toward more agile and resilient infrastructures.

Recent research trends suggest that stochastic load models will continue to evolve, incorporating advanced algorithms for uncertainty quantification and cost-effective planning to improve system reliability.

2.2.2 Wind Power Stochastic Models

Stochastic modelling of wind power has become increasingly important due to the intermittent and unpredictable nature of wind resources. Accurate models help system operators schedule generators, design reliable energy markets, and maintain system stability. In this context, accuracy refers to the ability of a stochastic model to reproduce key statistical characteristics of system variables, including expected values, variances, and probability distributions, typically validated against benchmark methods such as MCS. The following review highlights significant developments in wind power stochastic models, focusing on optimization methods, scenario generation, and the integration of multiple energy sources.

Initial studies in wind power integration concentrated on the optimal scheduling of conventional thermal units alongside wind generation. In Ref. [84] introduced a stochastic cost model that combines wind power forecasts with generator constraints to determine the best commitment schedule. This approach recognizes that wind availability can depart from forecasted values and allows for scheduling adjustments in the thermal units to manage potential shortfalls or oversupply. The same emphasis on balancing conventional and renewable sources appears in [85], who used a chance-constrained two-stage approach to handle uncertainties in wind output. These efforts demonstrated that stochastic optimization can reduce the risk of unmet demand or wasted wind energy by accounting for fluctuating wind profiles. By modelling the probability of different wind output scenarios, these frameworks offer a systematic way to account for changing wind patterns. As a result, system operators are better positioned to balance generation and demand without missing opportunities to harness available wind energy.

Beyond generation scheduling, researchers have explored how wind variability affects other energy systems. In Ref. [86] explored combined heat and power dispatch strategies with uncertain wind power input, emphasizing that the inherent variability in wind can disturb the balance of electricity and heat production. Adjusting dispatch schedules to handle probabilistic wind availability can improve overall system efficiency and reduce the cost of standby thermal generation.

ARIMA-based models (Auto Regressive Integrated Moving Average), as proposed in Ref. [87], offered early examples of data-driven approaches that capture temporal patterns in wind speeds and outputs. These predictive methods were paired with stochastic optimization to adjust wind turbine power factors. Such models demonstrated how statistical techniques can enhance both short-term forecast accuracy and real-time control.

In Ref. [88] investigated the effect of charging patterns for plug-in hybrid electric vehicles on wind-thermal scheduling. By treating vehicle demand as another source of uncertainty, the researchers showed that coordinated charging (and vehicle-to-grid strategies) could help absorb surplus wind energy. This highlights how uncertainties from different sectors—renewable generation and electric vehicles—can overlap, requiring integrated stochastic models.

Several works highlight the role of energy storage in mitigating wind variability. [89] used stochastic predictive control for battery systems linked to wind farms, relying on probabilistic wind forecasts. In Ref. [89] explored scheduling approaches for battery-based energy storage transportation systems, treating forecast errors and random disturbances as central factors. Both studies underscore that improved modelling of wind uncertainty expands the set of viable control methods for energy storage.

In Ref. [90] turned attention to voltage stability by focusing on optimal reactive power dispatch in the presence of uncertain wind generation. Their approach accommodates multiple objectives—such as loss minimization and system stability—while managing unpredictable changes in wind farm outputs. This aligns with the industry's growing recognition that voltage regulation is essential for grids with high renewable penetration.

In Ref. [91] introduced a fuzzy stochastic unit commitment model that handles uncertainties in both wind power generation and demand response. They incorporated conditional value-at-risk to gauge the potential worst-case scenarios. This type of combined risk measure is increasingly popular, reflecting a trend toward robust planning methods that hedge against multiple uncertainties simultaneously.

In Ref. [92] showed how wind power can be matched with pumped-hydro storage for day-ahead coordination. By targeting multi-objective outcomes—like cost, emissions, and reliability—these models can produce balanced schedules that leverage hydropower's storage ability to buffer wind variations.

In Ref. [93] focused on offshore wind, introducing a spatiotemporal kriging model for long-term predictions. Because offshore conditions can differ significantly from land-based wind, refined modelling techniques are needed to capture complex wind flow patterns. Such advanced geospatial tools help developers decide where to site offshore turbines and how to schedule maintenance.

For systems with a high share of variable renewable energy (VRE), in Ref. [94] considered frequency support from wind power in a stochastic planning framework. This highlights how wind farms can contribute not only active power but also crucial frequency regulation. Separately, [95] explored transformer ratings in large wind farms, using probabilistic methods to decide on appropriate equipment sizes to handle wind variability.

Studies such as in Ref. [96] present a data-driven approach for sizing energy storage in nuclear-renewable hybrid systems, showing that wind can be paired with other energy sources while meeting specific performance or environmental targets. These examples point to a future where multi-energy systems and advanced computational models combine to handle the randomness of wind in synergy with other resources.

In Ref. [97] explored distributed load frequency control, indicating how wind uncertainty can be balanced in a decentralized manner. Distributed methods can improve scalability and resilience, essential for large-scale adoption of renewables. By placing control algorithms closer to the source, grids become more adaptive, ensuring stable operation despite sudden wind power changes.

Stochastic modelling of wind power has evolved from early applications focused on the scheduling of wind–thermal systems to more advanced frameworks involving multi-objective and multi-energy optimization. In this context, unit commitment and economic dispatch problems aim to balance operational cost, system reliability, and renewable penetration under probabilistic wind forecasts. At the same time, the integration of energy storage systems—such as batteries, pumped-hydro storage, and electric vehicles—has become an effective approach to managing wind variability by absorbing excess energy or supplying power during deficits. In addition, maintaining voltage and frequency stability is increasingly important in systems with high wind penetration, which often require advanced reactive power control strategies and distributed frequency regulation mechanisms. Furthermore, expansion planning must consider long-term uncertainties in wind availability, weather conditions, and load growth, often in combination with other uncertain resources such as solar generation and demand response, to ensure robust and resilient power system development.

Beyond these operational and planning aspects, increasing attention has been given to probabilistic modelling of wind generation within distribution networks, particularly in the context of uncertainty propagation, correlation modelling, and power quality assessment. The stochastic nature of wind power introduces significant variability in node voltages and power flows, especially in networks with high renewable penetration and three-phase unbalance. Moreover, the interaction between wind generation and nonlinear loads contributes to harmonic distortion, which further complicates system behaviour. These challenges highlight the need for integrated probabilistic power flow frameworks that can capture both fundamental and harmonic characteristics, as well as their associated risks. In this regard, the present research contributes by combining dependence-aware probabilistic modelling with harmonic power flow analysis and risk-based evaluation, providing a more comprehensive understanding of wind-induced uncertainties in modern distribution systems.

Stochastic wind power models have evolved to address a range of operational and planning challenges, from generation scheduling to system stability and energy storage integration. Advances in probabilistic forecasting, multi-energy coordination, and decentralized control are shaping future research. As wind penetration increases, improving scenario generation techniques, uncertainty quantification, and real-time optimization will be critical for ensuring reliable and cost-effective wind integration.

2.2.3 Photovoltaic Stochastic Models

The increasing PV systems in electrical networks has prompted extensive research on stochastic modelling approaches that can account for uncertainty in solar irradiation, panel performance, and system conditions. Such models are essential for planning, scheduling, and operational strategies in micro-grids, virtual power plants, and broader power systems. Early work in the field highlighted the need to consider randomness in PV power output and battery performance, while more recent research has expanded to include advanced forecasting methods, sophisticated optimization frameworks, and integrated energy systems.

One of the references in this domain comes from [98], who developed a stochastic model for a PV power supply equipped with rechargeable batteries. They examined how battery life uncertainty affects the reliability of power delivery under different grid configurations. This research laid the groundwork for subsequent studies that target not only the reliability of PV-battery systems but also their economic and operational aspects.

In residential settings, in Ref. [99] quantified the degree of self-consumption for PV-powered households with electric vehicle (EV) home charging. Their work suggests that the variability in both solar output and EV usage patterns benefits from a probabilistic framework to optimize self-consumption. In Ref. [100] used probabilistic load flow methods to determine optimal PV placement in distribution networks, minimizing voltage deviations and power losses. Meanwhile, in Ref. [101] proposed a method for sizing and scheduling batteries in home energy management systems, explicitly modelling uncertain solar generation to improve household-level planning.

In Ref. [102] developed a stochastic scheduling model for virtual power plants (VPPs), incorporating uncertainties in load, PV generation, and demand response. The study highlights the role of VPPs in enhancing grid flexibility and optimizing energy trading under uncertain renewable conditions. In Ref. [103] expanded this perspective to micro-grids with multiple renewable technologies, highlighting how thermal and electrical systems in PV modules can be managed under probabilistic conditions.

In Ref. [104] introduced novel stochastic techniques for predicting short-term solar radiation, aiming to refine the accuracy of PV power forecasts. In Ref. [105] compared a very short-term forecasting model incorporating stochastic factors to a simple persistence method, finding superior performance under rapid irradiation changes. These advancements confirm that incorporating detailed probability distributions yields improved forecasting and dispatch strategies.

Stochastic modelling of PV systems has broadened to encompass large-scale integration scenarios. In Ref. [106] combined concentrating solar power with other renewables in a chance-constrained unit commitment framework, targeting reliable system operation at higher penetration levels. In Ref. [107] proposed a scheduling approach that leverages the flexible ramping and storage capabilities of hydropower to mitigate variability in wind and PV generation.

Several studies emphasize multi-objective optimization to handle economic, reliability, and environmental criteria simultaneously. For example, the work of [101] shows that battery storage strategies must factor in uncertain solar output to avoid overinvestment or underutilization. Scheduling for micro-grids with multiple power sources often requires advanced algorithms that can balance cost, energy losses, and system stability under random PV production patterns.

In Ref. [108] investigated internal PV panel faults by combining unsupervised deep-learning segmentation with real-time monitoring, enabling the identification of malfunctioning modules. Additional efforts, such as the study reported in Ref. [109], focused on modelling solar irradiance during extreme weather events (e.g., hurricanes). By using mixed-effect regression, they were able to capture irradiance decay, which is crucial for maintaining grid stability in regions prone to severe storms.

Recent work has explored stochastic model predictive control (MPC) for systems with PV generation. For instance, an alternative control strategy in Ref. [110] evaluated probabilistic and multivariate forecasts to coordinate battery, load, and PV output. Economic control strategies, such as those presented in [111], introduced uncertainty in electricity demand and PV supply to refine scheduling in residential PV-battery setups. The role of dust accumulation in dynamic PV output power profiles has been captured via Markov chain approaches [112], providing a clearer perspective on real-world performance over time.

Studies have also looked at the expansion of charging stations integrated with PV and battery systems and the use of stochastic techno-economic optimization for hybrid energy systems [113]. These frameworks typically weigh capital and operational costs against uncertain solar resources, electricity prices, and policy incentives. Meanwhile, innovative work in electromagnetic interference (EMI) modelling highlights the unpredictability of electronic system behaviours in PV installations, indicating a growing interest in hardware reliability as well as energy management. Research in combined voltage/frequency control with solar PV inputs [114] shows that robust stochastic models help maintain stable operation even in grids with high renewable shares.

Research on stochastic models for PV systems has evolved from early reliability analyses of simple PV–battery configurations to more advanced and multidimensional frameworks that integrate forecasting, optimization, and system-level coordination. Initial studies mainly focused on reliability and system sizing, particularly examining how uncertainty in battery performance affects power delivery. More recent approaches incorporate dynamic factors such as dust accumulation and panel degradation, enabling more accurate life-cycle-based sizing decisions. In parallel, forecasting techniques have progressed significantly, with hybrid methods combining statistical models, machine learning algorithms, and physical modelling to improve prediction accuracy and robustness.

With the increasing penetration of renewables, PV systems are now commonly integrated with other energy sources such as wind, hydropower, and energy storage, which require advanced scheduling and dispatch strategies that explicitly consider correlated uncertainties among multiple sources. In addition, stochastic modelling plays an important role in market and policy design, supporting the development of tariffs, incentives, and operational strategies that balance cost, risk, and system reliability. Emerging research topics further extend the scope of PV studies to include the interaction with electric vehicles, the impact of extreme weather conditions, and the application of advanced control methods such as stochastic model predictive control. Moreover, considerations related to electromagnetic compatibility and electromagnetic interference (EMC/EMI) indicate that hardware-level uncertainties are increasingly relevant in the design of robust and reliable PV-integrated systems.

In the context of distribution networks, the stochastic nature of PV generation introduces significant variability and uncertainty in power flow behaviour, particularly when combined with load fluctuations and other renewable sources. These uncertainties not only affect voltage profiles and power flows but also interact with nonlinear loads and power electronic interfaces, contributing to harmonic distortion and time-varying power quality issues. This highlights the need for probabilistic modelling approaches that can capture both the fundamental and harmonic characteristics of PV-integrated systems, as well as their correlation with other uncertain variables. The present research addresses these challenges by incorporating dependence-aware probabilistic modelling and harmonic power flow analysis to provide a more comprehensive assessment of PV-related uncertainties in modern distribution networks.

Future research may need to refine stochastic PV models by leveraging improved sensor technology, big data analytics, and computational advances. The integration of weather forecasting, power electronics, and machine learning will further enhance the reliability and economic viability of PV systems.

Future developments in stochastic PV modelling will require advances across several key areas. High-resolution forecasting is expected to improve significantly with the use of enhanced sensor data and AI-driven prediction methods, enabling more accurate short-term estimation of solar generation. In addition, co-optimization with energy storage systems and electric vehicles will become increasingly important, as integrated models coordinate PV output with flexible resources to enhance system adaptability and operational efficiency. Another critical direction involves improving resilience under extreme weather conditions, where stochastic models can be used to assess and mitigate the impacts of events such as hurricanes and other climate-related disruptions. Furthermore, economic and market design will play a growing role, with stochastic modelling supporting the development of tariff structures, investment strategies, and policy frameworks required for large-scale PV integration.

2.2.4 Monte Carlo Method and its Applications in Power Systems

The MCS method is widely recognized for its capability to analyze complex systems with inherent randomness. In power systems, this technique enables researchers and operators to simulate a range of operational conditions by sampling random variables that represent uncertainties such as load variations, wind speeds, and equipment failures. MCS methods enable power system operators to simulate a wide range of uncertainties, including load variations, renewable energy fluctuations, and component failures. While early studies focused on economic analysis, modern applications extend to security, reliability, and component aging.

One of the first notable references is [10], who applied a MCS approach to evaluate the hour-by-hour operation of a power system incorporating wind energy. By simulating numerous possible wind generation scenarios, the study provided insights into how different levels of wind penetration may affect system costs and operational feasibility. This approach allowed for an estimation of the economic benefits of wind integration under varying levels of uncertainty and system constraints. The findings highlighted the importance of probabilistic methods in capturing the fluctuating nature of wind resources, which deterministic models fail to capture adequately.

Building on this foundation, in Ref. [11] expanded the scope of wind integration studies by estimating the energy credit of wind energy conversion systems. Their work focused on quantifying the reliability contributions of wind generation to the power grid, a key factor in determining how much firm capacity wind power can provide. They employed time series forecasting methods to predict hourly wind speeds and incorporated these predictions into MCS. This combined approach enabled a more accurate assessment of wind power's ability to contribute to system adequacy and reduce dependence on conventional generation sources. By generating reliability indices such as loss-of-load probability (LOLP) and expected energy not served (EENS), the study offered a comprehensive framework for evaluating the capacity value of wind energy.

Beyond wind energy applications, MCS methods play a crucial role in power system security assessments. Recent studies apply probabilistic simulations to evaluate contingency risks, voltage stability, and infrastructure resilience.

In Ref. [115] developed two synthetic wind speed generation methods to analyze steady-state security in wind-integrated power systems. Their techniques captured spatial correlations between multiple wind farms, improving risk assessment under fluctuating wind conditions. The first relies on statistical correlation matrices, whereas the second considers conditional probabilities of wind speeds in multiple wind farms. Such modelling approaches allow system planners to explore how simultaneous wind variations in different locations might affect power flow and system stability.

In Ref. [116] applied importance sampling—an enhancement to MCS—to compute expected power loss under protection system failures. Their work extended to contingency analysis, incorporating probabilistic measures into risk-based security assessments. These studies highlight that MCS methods are not limited to evaluating specific components; they are also suitable for broader system-level security simulations.

In Ref. [117] used MCS to model planning and repair process in power distribution systems. They combined queueing theory with stochastic processes to assess how maintenance activities and system failures interplay over time. On the transmission side, [118] explored chance-constrained approaches for network expansion planning under uncertain load growth and wind power forecasts. MCS techniques underpinned the scenario generation, illustrating that these methods are crucial for planning under significant data variability.

In Ref. [119] tested a measurement-based mode shape identification method using MCS simulation data. By subjecting the system to random disturbances, they validated the approach's robustness in identifying electromechanical modes. In Ref. [120] extended such work by investigating small-signal stability under high wind penetration levels. They employed MCS to capture the range of possible operating points driven by wind fluctuations, quantifying the likelihood of stability issues in large-scale systems.

In Ref. [121] introduced an affine arithmetic-based method for voltage stability assessments, comparing it to MCS in terms of computational efficiency and accuracy. In affine arithmetic, uncertain variables are expressed as affine combinations of central values and noise terms, enabling the tracking of dependencies between variables and reducing overestimation compared to traditional interval methods. While MCS remains a standard tool, their approach showed that approximate methods can reduce simulation time while providing reliable results. This demonstrates ongoing research into complementing or replacing brute-force MCS with less computationally intensive techniques.

Recent work by [122] applied MCS to assess metallized film capacitor aging under dynamic stress conditions, which is critical for ensuring long-term reliability in power converters used in renewable energy systems. Incorporating time-varying mission profiles into Monte Carlo-based simulations provided more accurate estimates of component aging. This type of modelling is becoming essential as power systems evolve to include more fast-switching converters and other sensitive devices.

MCS methods also appear in renewable technology design. In Ref. [123] used MCS optical modelling and inverse adding-doubling to optimize building-integrated photovoltaic smart windows. Their approach offered insights into the light transmittance and heat flow characteristics that affect both energy generation and occupant comfort.

In Ref. [124] integrated Gaussian Process learning with probabilistic optimal power flow, leveraging MC-style uncertainty sampling to enhance computational efficiency in high-dimensional optimization problems. In Ref. [125] examined how climate change affects PV systems at multiple hierarchical levels, again leaning on MCS to capture extreme weather variations. This underlines the relevance of MCS for addressing future uncertainties linked to climate patterns and extreme events.

MCS methods have evolved considerably in power system applications, demonstrating strong flexibility in addressing a wide range of challenges. Early studies focused on economic and reliability assessments, where MCS was used to evaluate the integration of wind power under uncertain wind speeds and demand patterns by simulating diverse operating conditions. Subsequently, its application expanded to security and contingency analysis, with techniques such as importance sampling improving computational efficiency and enabling more effective evaluation of system risk and vulnerability. In addition, MCS has been widely applied to small-signal stability and voltage constraint studies, allowing detailed investigation of how stochastic variations in renewable generation and load demand may affect system stability. More recently, research has extended to component-level reliability, where time-varying stress conditions and device ageing are incorporated to better understand lifecycle performance in distribution networks. Furthermore, the integration of machine learning techniques, such as Gaussian Processes, has been explored to complement or partially replace traditional MCS, particularly in handling high-dimensional uncertainty and reducing computational burden.

In this thesis, MCS is employed as a benchmark and high-fidelity analysis tool for probabilistic power flow and harmonic studies in distribution networks. Specifically, it is used to generate large numbers of stochastic scenarios that capture the combined uncertainty of loads, photovoltaic systems, and wind generation, including their correlation structures. This enables the derivation of full probabilistic distributions of key system variables, such as three-phase node voltages, branch power flows, and total harmonic distortion (THD). Moreover, the MCS results provide the basis for calculating risk indices, including over-limit probabilities and associated risk values, which are essential for subsequent power quality assessment and multi-criteria evaluation. By offering a detailed and unbiased representation of system behaviour under uncertainty, MCS serves both as a validation reference for approximate methods and as a core tool for risk-based analysis in this research.

Going forward, hybrid approaches that merge MCS sampling with machine learning or surrogate models are likely to increase in popularity, enabling faster simulations of large systems. Additionally, as the share of intermittent generation grows and climate volatility intensifies, accurate representation of uncertain resources, weather events, and component aging will be even more essential. These developments ensure that MCS methods will remain a core tool in power system research and operations for the foreseeable future.

Future advancements in MCS applications are expected to focus on improving computational efficiency, expanding the modelling of extreme events, and enhancing component-level reliability analysis. In terms of efficiency, the integration of surrogate models and machine learning techniques is anticipated to significantly accelerate large-scale simulations, making MCS more practical for complex power system studies. At the same time, greater attention will be given to extreme event modelling, where refined MCS-based approaches can better capture the impacts of climate-related disturbances on system performance and resilience. In addition, component degradation analysis will play an increasingly important role, with MCS incorporating real-world operating conditions and stress factors to support more accurate predictive maintenance and lifecycle reliability assessments.

2.2.5 Three-Point Estimation Method and Their Applications in Power Systems

The Three-Point Estimation Method (3PEM) is traditionally known from project management, where it refines estimates of duration or cost by considering best-case, most-likely, and worst-case scenarios. This approach can also be adapted to power systems to manage the high levels of uncertainty found in load forecasts, renewable energy outputs, and component failures. Modern power grids increasingly rely on data-driven and probabilistic methods to estimate system variables, highlighting parallels between Three-Point Estimation and other advanced estimation frameworks.

In power systems, effective estimation methods play a key role in supporting both operation and planning tasks. They are widely used in short-term load forecasting, where accurate demand prediction helps ensure reliable and economical system operation. In renewable energy applications, estimation techniques are essential for maximum power point tracking, enabling photovoltaic and wind systems to operate at optimal efficiency under varying environmental conditions. They are also fundamental to system state estimation, which provides real-time information on voltages, currents, and other system variables, including dynamic states under both normal and faulted conditions. In addition, estimation methods support uncertainty quantification in wind and solar forecasts, helping operators understand and manage variability in renewable generation. They are further applied in topology identification and fault location, improving system observability and enabling faster detection and isolation of faults. Finally, these methods contribute to efficient energy management across distributed resources by providing accurate system information that supports coordinated control and decision-making.

Traditional forecasting models rely on statistical methods like covariance matrix estimation [126] , while Three-Point Estimation provides an alternative by explicitly modelling best-case, most-likely, and worst-case scenarios. This enables a structured assessment of forecast uncertainty, which is crucial for operational planning and cost control. While they did not specifically rely on the 3PEM, their work set a precedent for treating uncertainty in system parameters as a critical factor in forecasting performance.

In Ref. [127] applied neural networks to PV power forecasting by learning from historical weather patterns. While neural networks predict point estimates, 3PEM can complement such models by bounding the uncertainty range, ensuring robust decision-making under fluctuating solar conditions. Neural networks depend on data-driven training processes, while 3PEM takes a more explicit approach by setting best-case, most-likely, and worst-case scenarios. Taken together, these studies illustrate how forecasting and estimation methods must account for inherent variability in power systems to enhance decision-making and improve reliability.

Dynamic estimation approaches have played a major role in stabilizing power systems under fluctuating conditions. Kalman filtering [128] , commonly used for real-time dynamic state estimation, provides continuous updates to power system variables.

While it differs from 3PEM, which explicitly models scenario-based uncertainties, combining Kalman filters with 3PEM could improve reliability assessment by incorporating both real-time updates and predefined uncertainty bounds. Building on similar principles, in Ref. [129] focused on wind power forecasting through refined statistical methods. Their methods enabled short-to-medium term predictions that recognize the stochastic nature of wind speed and generation output.

These foundational studies helped establish the value of robust estimation techniques. Though they may not apply 3PEM outright, they share the same primary objective: capturing the uncertainty in system variables and adjusting control strategies to maintain stability and reliability. This alignment with the key concepts behind 3PEM—namely bounding errors and identifying a range of possible outcomes—demonstrates how multiple estimation methods can address the same underlying challenge of unpredictability in power systems.

In Ref. [130] introduced a real-time detection method for voltage disturbances by merging discrete wavelet transforms with an extended Kalman filter. They showed that accurate, immediate assessment of power quality events can help system operators intervene before minor issues grow into large-scale disruptions. Concurrently, in Ref. [131] refined electromechanical mode shape estimation through transfer function identification. These algorithms are oriented toward real-time analysis, which is especially relevant in complex grids subject to rapid load or generation swings.

Although these frameworks do not use 3PEM directly, they benefit from a similar principle: bounding uncertainty in measurements and parameters to inform quick, data-driven decisions. In practice, operators may integrate scenario-based analyses, like 3PEM, to account for best-case and worst-case operating conditions. This approach can serve as a safeguard when deciding on corrective measures or reconfiguring system operation to prevent instability.

In Ref. [132] further advanced dynamic state estimation by applying the unscented Kalman filter, which is capable of handling stronger nonlinearities than the standard Kalman filter. This focus on accommodating nonlinear system behaviours is important in power systems that feature distributed generation, power electronics, and other complex components. While it diverges from 3PEM in method, it addresses a similar need: acknowledging and representing random variations in ways that are manageable for real-time operations.

Growing penetration of renewable sources introduces additional uncertainty into power systems, making advanced estimation strategies even more vital. In Ref. [133] developed a mean-variance approach to estimate wind power forecast errors. Their results underline the value of mapping out a distribution of potential outcomes, similar to the three-scenario mindset behind 3PEM. Reducing forecast error is critical in grids where wind generation can fluctuate over short intervals.

Machine learning-based estimation [134], [135] introduces techniques for extracting structured uncertainty from high-dimensional data. While originally developed for wireless networks, similar hybrid data-driven approaches are increasingly applied in power system forecasting and state estimation. Combining such models with 3PEM could provide structured uncertainty bounds to improve decision reliability. Although these studies are drawn from wireless communications, the overarching principle of merging data-based insights with structured uncertainty handling parallels the logic of 3PEM: use multiple scenarios or distributions to represent system unpredictability and guide decisions.

In integrated energy management, in Ref. [135] proposed an energy-circuit framework requiring synchronized real-time estimates. By incorporating best-case, most-likely, and worst-case scenarios, scenario-based methods like 3PEM can enhance dispatch and scheduling decisions in smart grid environments. Such estimates inform dispatch decisions and resource scheduling. By comparing real-time measurements with model predictions, this approach reflects a scenario-driven mindset like that of 3PEM, where one identifies the best-case, most-likely, and worst-case conditions to plan resource usage effectively. This approach is especially relevant in smart grids that involve energy storage, demand response, and other distributed resources.

Many power system studies implicitly adopt scenario-based approaches, such as the 3PEM, particularly in forecasting and contingency planning. While advanced data-driven models can improve estimation accuracy, the incorporation of structured uncertainty bounds remains essential to ensure system reliability and resilience. In this context, different representative scenarios are typically considered. The best-case scenario reflects conditions of minimum demand or maximum generation, which is useful for identifying potential oversupply situations or stress on system components. The most-likely scenario represents typical operating conditions and is commonly used to guide routine dispatch and scheduling decisions. In contrast, the worst-case scenario captures extreme conditions, such as peak demand, component outages, or low renewable generation, and is critical for reliability assessment and contingency planning.

By integrating advanced data-driven models (machine learning, neural networks, Bayesian filters) with scenario-based frameworks, researchers can make robust decisions despite large uncertainties.

These studies indicate a clear trend that robust and flexible estimation methods are essential for power systems operating under diverse sources of uncertainty, ranging from renewable energy variability to fault events and dynamic system conditions. In this context, the 3PEM, originally developed in project management, provides a simple yet effective way to bound uncertainty and complements more advanced data-driven and probabilistic approaches. Scenario-based methods, including 3PEM, play an important role in uncertainty management for short-term forecasting, system planning, and real-time operation. At the same time, the integration of data-driven techniques—such as neural networks, support vector machines, Kalman filtering, and hybrid models—can further refine these estimates and provide deeper insight into system behaviour. These estimation strategies are widely applied across power system applications, including dynamic state estimation, renewable generation forecasting, topology identification, and resource management in embedded systems, highlighting their broad relevance in modern grid operation under uncertainty.

Moving forward, the continued integration of classical scenario-based methods with advanced computational techniques is expected to further improve the reliability, resilience, and efficiency of modern power systems, particularly as grids incorporate higher shares of variable renewable energy and evolve into more intelligent and interconnected networks. In this context, future research should focus on hybrid uncertainty modelling approaches that combine the 3PEM with machine learning and probabilistic techniques to enhance forecasting accuracy and support real-time decision-making. In addition, scenario-driven energy management strategies based on 3PEM can be developed to optimize demand response, storage utilization, and renewable integration. Another important direction involves fault and anomaly detection, where structured scenario estimation can improve the identification of abnormal operating conditions and support faster system recovery. As power systems continue to integrate renewable resources and digital control technologies, the combination of 3PEM with AI-driven estimation methods will play an important role in maintaining system stability and operational efficiency.

A key gap in existing approaches lies in the lack of computationally efficient methods that can provide accurate probabilistic analysis without relying on large numbers of MCS. This is particularly challenging in distribution networks with high uncertainty and complex interactions. In this work, the focus is placed on addressing this gap through the proposed 3PEM-based probabilistic framework, which improves computational efficiency while maintaining acceptable accuracy compared to conventional MCS. The integration of machine learning or surrogate modelling techniques is considered as a potential direction for future research building upon this framework.

2.2.6 Influence of Correlation Modelling on Stochastic Power Flow Results

With the increasing penetration of renewable resources and the inherent variability of load demand, probabilistic load flow (PLF) studies have taken center stage in power system research. Traditional deterministic analyses cannot adequately capture uncertainties arising from fluctuating wind and solar generation, time-varying loads, and spatial correlations among system components. A robust treatment of these uncertainties often requires considering the correlation between multiple random variables.

Various studies highlight the importance of modelling correlation to avoid inaccurate or overly simplified results. Within this context, the Nataf transformation and other correlation modelling techniques have demonstrated effectiveness in representing the joint distributions of uncertain variables, such as load, solar PV, and wind power [17]. By applying these methods, researchers have shown that accurate correlation modelling can improve both the reliability and the accuracy of power flow simulations.

Even in the works of probabilistic load flow [136], the distribution of result variables—such as bus voltages, line flows, and system losses—was recognized as highly sensitive to how uncertainties are characterized. Ignoring or mishandling correlation can lead to skewed or unrealistic probability distributions. For instance, two adjacent wind farms might produce correlated power outputs if subject to similar wind conditions, while load demand in different regions may show partial synchronicity based on common economic activities or weather patterns. Ignoring these relationships can skew probability distributions, making results unrealistic. PLF studies confirm that poor correlation modelling can misrepresent voltage stability margins, leading to incorrect estimations of reserve requirements and hosting capacities for renewables.

Authors in Ref. [137] showed that voltage stability assessments depend on accurate correlation modelling between wind power and load demand. Misrepresenting these dependencies can lead to incorrect stability margins, affecting grid reliability under high renewable penetration. Without properly accounting for correlation (e.g., between local loads and PV generation), the computed stability margins may be misleading. Similarly, efforts to assess or enhance hosting capacity for renewables, like those in Ref. [138],[139],[140] confirm that correlated uncertainties require more refined tools than purely independent or perfect correlation assumptions.

The Nataf transformation maps correlated random variables into a Gaussian space, where established probability techniques (e.g., convolution) simplify computations in Ref. [141]. Unlike Copula-based approaches in Ref. [142], which flexibly model nonlinear dependencies, the Nataf transformation is computationally efficient for moderate to strong correlations. This allows for the use of well-established techniques from probability theory, such as convolution in the Gaussian domain, before transforming the results back to the original space. The method excels in handling moderate to strong correlations and has been applied to power flow studies with uncertain wind power and load in Ref. [16]. Its ability to preserve marginal distributions and correlation structures makes it especially relevant for multi-variable scenarios.

In Ref. [16], researchers propose combining point estimation methods with the inverse Nataf transformation to handle correlated uncertainties in distribution networks. Point estimation provides an efficient route for approximating the mean and variance of the output variables. When merged with an inverse Nataf framework, it becomes possible to propagate correlated input variables consistently, enabling faster analyses than full-scale MCS methods but retaining an acceptable level of accuracy for operational planning and risk assessment.

Beyond single-site correlations, some investigators extend correlation modelling to spatial correlations among geographically connected components. For instance, in Ref. [143] integrates spatial dependency into new risk analysis methods, acknowledging that not only are local variables correlated (e.g., wind speeds at neighbouring turbines), but also that system components can fail in correlated manners based on location and environment. This deeper level of modelling complexity marks a transition toward more holistic, system-wide stochastic assessments.

Correlation is equally crucial for stochastic multi-stage joint expansion planning in Ref. [144]. In this context, correlation between wind power and load demand over time influences decisions about where and when to invest in new transmission lines or generation capacity. Failing to capture correlated variations can result in suboptimal or risk-prone expansion strategies.

Beyond standard onshore networks, in Ref. [145] analyzed space-time correlations in offshore wind farms using high-resolution Supervisory Control and Data Acquisition (SCADA) data. Due to stronger wake effects and highly variable marine weather, offshore wind power fluctuations exhibit more complex correlations than onshore wind, requiring refined modelling techniques for accurate reserve and balancing needs. Their approach addresses variable flow conditions in turbine wakes, showing that modelling correlations is vital to accurately representing the power output distribution and planning the system's reserve and balancing needs.

A significant hurdle in correlation modelling is balancing accuracy with computational tractability. MCS with correlated variables can become computationally expensive as the number of uncertain factors grows. Techniques like point estimation or advanced sampling (Latin hypercube, quasi-Monte Carlo) can mitigate computational burden but may introduce approximation errors. Researchers continue to refine these methods, seeking a balance between accuracy and efficiency.

As distribution networks incorporate more diverse energy resources—energy storage, electric vehicles, demand response—modelling correlation among numerous random variables becomes even more demanding. Nataf transformation or similar correlation approaches may need modifications to handle highly nonlinear dependencies or high-dimensional spaces, pushing research toward new transformations or hybrid data-driven strategies.

Another emerging trend is the assimilation of real-time measurements (from Phasor Measurement Unit (PMUs) or SCADA) into correlation-based stochastic models. Real-time data can help identify shifts in correlation structures, especially for rapidly changing conditions in renewable-dense systems or offshore wind farms. Adapting correlation modelling on-the-fly could significantly improve situational awareness and operational decision-making.

Future research is likely to focus on improving computational efficiency, better handling nonlinear dependencies, and integrating real-time, data-driven correlation models to enhance situational awareness in renewable-dominated power systems. In particular, accurately representing joint uncertainties is essential, as correlated wind, load, and solar PV profiles can significantly influence bus voltage behaviour, line power flows, and hosting capacity assessments. Ignoring such correlations may lead to inaccurate reliability and risk evaluations, including overestimation or underestimation of system stability margins and reserve requirements. To address these challenges, increasing attention is being given to the integration of advanced methods, where point estimation techniques, Monte Carlo simulation, and scenario-based approaches are combined with correlation modelling frameworks. This enables researchers to capture complex system interactions while maintaining a reasonable computational cost, thereby supporting more reliable and realistic power system analysis.

As the power sector continues to evolve with higher renewable penetration, storage integration, and real-time data streams, correlation modelling will remain indispensable for thorough risk assessment, planning, and operation. Advanced transformation methods, ongoing research into spatial dependencies, and computational optimizations all contribute to a more robust, data-driven understanding of power systems under uncertainty.

Future research should focus on advancing correlation modelling techniques, improving real-time adaptability, enhancing computational efficiency, and extending modelling frameworks to multi-sector energy systems. In particular, further development of advanced correlation transformations—such as improved Nataf and Copula-based methods—is needed to better capture nonlinear and high-dimensional dependencies in renewable-dominated power systems. At the same time, real-time correlation adaptation will become increasingly important, where data from PMUs and SCADA systems can be used to dynamically update correlation structures and improve situational awareness under rapidly changing grid conditions. In terms of computational performance, hybrid approaches that combine techniques such as quasi-Monte Carlo sampling and deep learning-based surrogate models offer promising pathways to reduce computational burden in large-scale stochastic simulations. Additionally, future work should extend correlation modelling beyond the power sector to include coupled energy systems, such as heating and transportation, enabling a more comprehensive representation of interdependent uncertainties in integrated energy networks.

These directions extend beyond the scope of this thesis. This work focuses on addressing a gap, namely the lack of computationally efficient methods for representing correlated uncertainties in probabilistic power flow analysis. By combining the 3PEM with the Nataf transformation, the proposed framework captures input correlations while significantly reducing computational effort compared to conventional MCS. Future research may extend this framework toward more advanced correlation modelling, real-time adaptation using measurement data, and multi-energy system integration.

2.3 Power Quality Assessment Methods

2.3.1 Evaluation Index System and Weight Selection Methods

Power quality assessment is fundamental to ensuring the reliability, stability, and performance of contemporary power systems. The increasing integration of renewable energy sources and the advent of advanced digital monitoring technologies have heightened the need for assessment methods that are both comprehensive and encompassing multiple dimensions such as technical, economic, and environmental indicators—and precise, grounded in robust weighting and data-driven analysis. This literature review critically examines existing research on evaluation index systems and weight selection methods, with a focus on their application to power quality and broader energy system evaluations. By synthesizing these approaches, this study aims to highlight its theoretical and methodological contributions to the field.

2.3.2 Evaluation Index Systems

The importance of multi-criteria evaluation is underscored by [146], who developed a General Sustainability Index to assess biomass-fired power plants, incorporating environmental and economic metrics. This multi-criteria framework aligns with power quality assessment by demonstrating how diverse indicators can be systematically weighted to reflect system performance. Multi-criteria approach naturally align with power quality assessment, where voltage deviations, frequency stability, and harmonic distortion, among others, must be captured.

In contrast, in Ref. [147] employed extension evaluation theory to assess wind power project quality, tailoring the index system to region-specific conditions like wind variability and infrastructure readiness. While this improves the accuracy and relevance of the assessment within a specific region, the resulting model is closely tied to local conditions and assumptions, making it less applicable to other regions with different wind patterns, grid characteristics, or infrastructure levels.

As the digital transformation accelerates in the power sector, building index systems that capture both operational and cyber dimensions is gaining traction. In Ref. [148] emphasize data quality evaluation in power systems by constructing an index system through a Fuzzy Analytic Hierarchy Process (FAHP). This shift toward data-driven index systems appears in [149], who addressed power communication network operation quality by carefully selecting and optimizing relevant indicators.

Meanwhile, in Ref. [24] proposed a digital transformation index system for power grids, integrating conventional power quality indicators (e.g., reliability and outage frequency) with digital metrics (e.g., cybersecurity and data analytics capability). This approach reflects the evolving role of digital infrastructure in power system assessment. By merging standard power quality indicators (like reliability, losses, and outage frequency) with digital readiness (data analytics capacity, cybersecurity posture), they reflect the evolving nature of power system assessment.

2.3.3 Weight Selection Methods

Selecting proper weights for power quality indicators is important for objective evaluations in power system studies. Among the well-known techniques, the Analytic Hierarchy Process (AHP) and the entropy weight method are frequently adopted due to their distinct approaches to balancing expert input and data-based assessments.

AHP is a decision-making tool that uses pairwise comparisons of different factors to compute weights. By relying on expert judgments, it can capture complex interrelationships among power quality indicators. In this study, the expert group consists of individuals with relevant academic and practical experience in power systems, particularly in power quality assessment and distribution network operation. For example, in Ref. [24] employed neural network modules to compute a security index for power systems, yet the weighting of factors such as line overload or reactive power margins still relied on AHP-based expertise.

In contrast, the entropy weight method limits subjectivity by focusing on the variability of data. This approach computes weights based on the degree of dispersion in a dataset [25]. Although applied in groundwater quality assessments, the entropy weight method has demonstrated robustness in capturing the relative importance of different indicators, suggesting its applicability to power system studies. The same approach can be transferred to power systems, where changes in operating conditions affect the significance of specific indicators. Further, in Ref. [150] introduced an ambiguity entropy concept to gauge index weights in evaluating economic benefits of power grid projects. By considering uncertain or incomplete data, their approach showed how entropy-based methods can adapt to real-world complexities in power networks.

In summary, AHP and the entropy weight method offer complementary strategies. AHP incorporates expert judgment, making it useful for interpreting complex interrelationships among power quality indicators, while entropy-based weighting objectively captures variability but lacks domain interpretability. Combining both techniques enhances robustness by balancing expert insight with data-driven precision. Both techniques have gained recognition in power system research and combining them can further improve weight allocation by bridging subjective and objective perspectives.

In Ref. [151] introduced machine learning (random forest) to refine weighting methods for power system evaluation. By learning from historical data, machine learning reduces expert bias, adapts to emerging conditions, and enhances weight selection efficiency, particularly in cybersecurity and intrusion detection applications. This advanced approach highlights that weighting may not always be a purely mathematical or expert-driven process; predictive analytics can also guide which indicators matter most under real-world threat scenarios.

In the context of distribution network reliability with renewable energy access [26], weighting must consider both conventional factors (line capacity and voltage level). Similar synergy emerges in the minimum redundancy maximum relevance (mRMR) - based feature selection used in Ref. [27], which effectively assigns importance to features (i.e., indicators) by balancing relevance and redundancy—akin to weighting indicators in a multi-criteria environment.

Many methods focus on integrating renewables, which often exacerbate power quality issues (harmonics, voltage fluctuations, intermittency). In Ref. [152] introduced a comprehensive evaluation method for low voltage distribution districts specifically addressing the current level of business digitization. This method underscores the interplay of operational reliability, policy/regulatory constraints, and digital monitoring.

In Ref. [153] extended power system evaluation beyond technical parameters by incorporating social equity metrics, using entropy-based weighting to measure local grid development. This broader approach acknowledges that power quality assessments must balance technical performance with accessibility and fairness in energy distribution. This approach implies a broader societal perspective in weighting, acknowledging that power quality includes not only technical metrics but also equity and access dimensions.

The reviewed literature highlights three main challenges in power quality assessment, each associated with different methodological approaches. The first challenge lies in managing multiple indicators, where multi-criteria frameworks are effective in integrating diverse metrics but often face difficulties in maintaining weighting consistency and addressing interdependence among indicators. Hybrid methods provide a potential solution by enabling more adaptive and balanced weighting strategies. The second challenge involves handling data uncertainty. Entropy-based methods use data variability to improve objectivity and generally outperform approaches such as AHP in this regard, although they lack the interpretability offered by subjective methods. More advanced techniques, such as mRMR, can further enhance robustness, but this often comes with increased computational complexity. The third challenge relates to adapting to technological change. Digital-oriented index systems are designed to address emerging requirements in modern power systems, but they may suffer from overgeneralization. Machine learning-based weighting methods offer scalability and flexibility; however, their lack of transparency can reduce confidence in applications where reliability and interpretability are critical.

A robust evaluation index system, together with an appropriate weight selection method, is essential for achieving comprehensive and accurate power quality assessment. In this context, hybrid weighting techniques that combine expert-driven approaches (such as AHP and Delphi) with data-driven methods (such as entropy and machine learning) can help balance interpretability and objectivity. At the same time, the development of dynamic index systems is important to reflect real-time changes in grid conditions, particularly under increasing renewable penetration and digital transformation. In addition, uncertainty-aware evaluation frameworks that incorporate probabilistic weighting strategies can improve robustness under variable operating conditions. Finally, enhancing computational efficiency is also a key direction, where AI-based feature selection and high-dimensional optimization techniques can be used to improve scalability and performance in complex assessment problems.

Contemporary studies continue to advance power quality assessment by integrating complementary methods—such as Weighted Principal Component Analysis for reducing indicator redundancy, Fuzzy Analytic Hierarchy Process (FAHP) for handling uncertain expert inputs, entropy weighting for objectively deriving weights from data variability, and machine learning-based feature selection for dynamically prioritizing key metrics. Together, these techniques empower stakeholders to more precisely evaluate and uphold the reliability of power systems, particularly under the strains of renewable integration and digital transformation.

2.4 Active Power Filters for Harmonic Mitigation in Distribution Networks

2.4.1 Operating Principles of Active Power Filters

Active power line conditioners, commonly known as active power filters (APFs), are advanced solutions designed to address harmonic distortions and power quality challenges in electrical networks. Introduced conceptually in the 1970s [154], APFs utilize inverter circuits with semiconductor switches to generate controlled harmonic currents or voltages. However, limited circuit technology at the time restricted their development to experimental stages. The development of bipolar junction transistors and static induction thyristors have revitalized interest in APFs enabling their use in reactive power and harmonic compensation. A key milestone occurred in 1982 with the deployment of an 800 kVA shunt active conditioner employing gate turn-off (GTO) thyristors, marking the first practical application of this technology.

Modern active power line conditioners leverage power electronics and digital signal processing (DSP) to effectively mitigate nonlinear load effects, including harmonics, reactive power, and load unbalances [155]. This section provides an overview of widely adopted APF configurations which are selected based on their prominence in academic literature and industrial applications.

2.4.1.1 Shunt Active Power Filters

Shunt APFs operate by injecting currents into the network that counteract harmonic currents produced by nonlinear loads, ensuring a sinusoidal source current [156]. Unlike passive filters, they are less affected by system impedance, reducing resonance risks. However, their implementation faces several challenges. The design and construction of high-power pulse-width modulation (PWM) converters with fast dynamic response and low losses are technically demanding. In addition, the overall cost of active power filters can be higher than that of traditional passive filtering solutions. Furthermore, the injected compensating currents may interact with other network components, such as capacitors or existing passive filters, which can introduce additional operational complexity and potential stability issues.

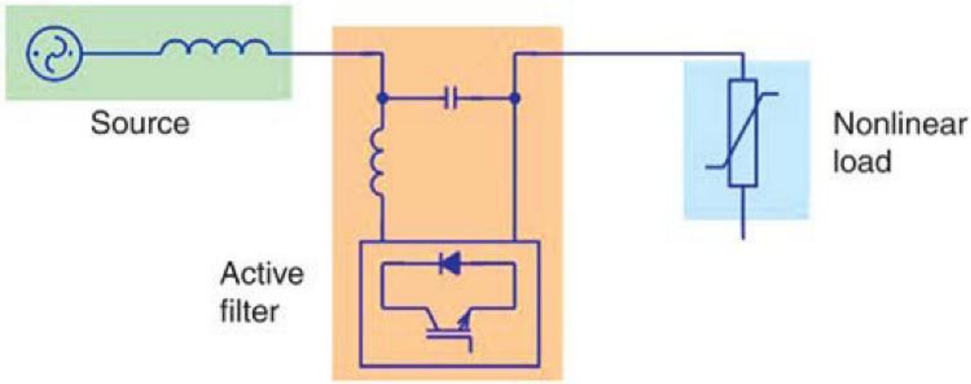

Figure 2-1 Basic Scheme of Active Filter with Series Connection [157]

These limitations have driven the development of alternative topologies to enhance efficiency and practicality.

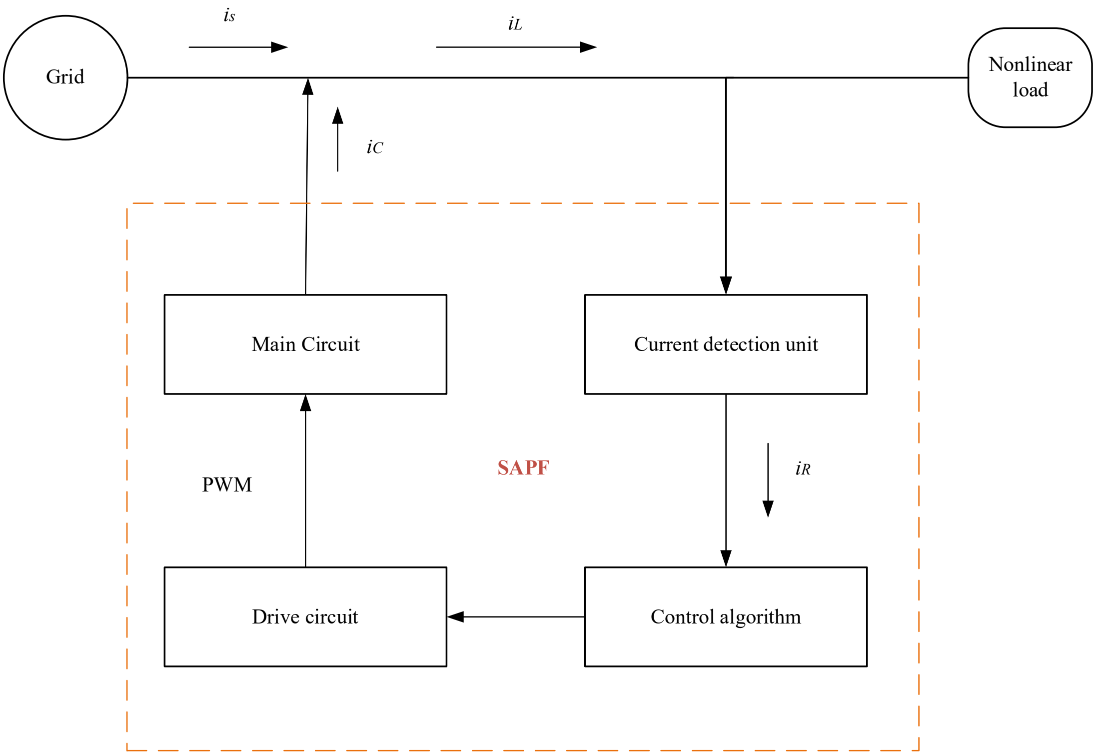

Figure 2-2 Schematic Diagram of a Shunt Active Power Filter (SAPF) Control System

The shunt active power filter (SAPF) as shown in Figure 2-2 is connected in parallel with the distribution feeder to suppress harmonic currents generated by nonlinear loads and to improve power quality at the point of common coupling. In this configuration, the nonlinear load draws a distorted current from the grid, which contains both harmonic and reactive components. The SAPF continuously measures the load current and determines the reference compensating current, representing the harmonic and reactive parts to be cancelled. A current-tracking control algorithm forces the actual compensating current produced by the inverter to follow this reference, ensuring that the grid current remains nearly sinusoidal and in phase with the supply voltage. The inverter is controlled by a pulse-width modulation (PWM) scheme, which generates the appropriate switching signals to synthesize the required compensating current. The drive circuit amplifies and isolates these control signals to operate the power switches safely and reliably. The current detection unit and control algorithm operate in real time to minimize the error between the reference and the actual compensating current, while the DC-link voltage is maintained by a slow outer control loop that balances converter losses. As a result, the SAPF injects a current equal in magnitude and opposite in phase to the undesired components of the load current, making the source current predominantly fundamental and sinusoidal. This closed-loop operation effectively mitigates current harmonics, compensates reactive power, and enhances the overall power quality and efficiency of the distribution system.

2.4.1.2 Hybrid Active Filters

Hybrid active filters combine passive and active filtering techniques to optimize performance and cost-effectiveness [158]. Several configurations have been explored, with the following being the most notable:

- **Parallel Hybrid Configuration:** A passive filter and an active filter are connected in parallel with the load [159]. The passive filter targets major harmonics, lowering the power demand on the active filter. However, it retains the resonance vulnerabilities of passive filters.

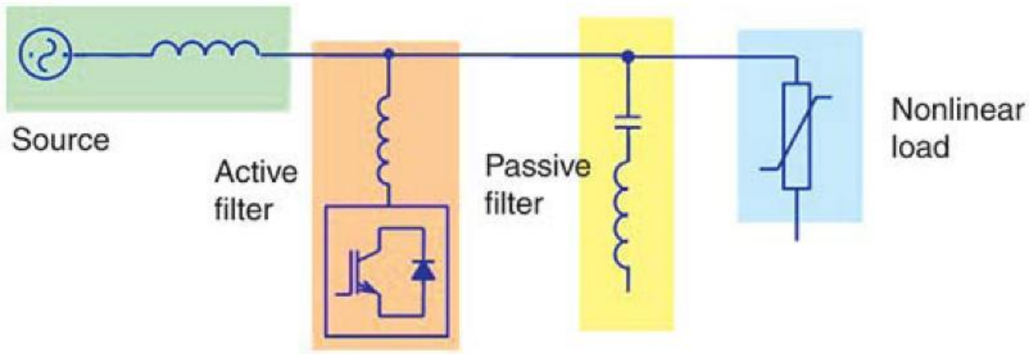

Figure 2-3 Parallel Combination of an Active and a Passive Filter [157]

- **Series-Parallel Hybrid Configuration:** An active filter is placed in series with the source, paired with a passive filter in parallel with the load [160]. Control techniques enhance the passive filter's performance by using the active filter as a harmonic barrier, minimizing resonance and dependency on source impedance [161]. This reduces the active filter's required power rating.

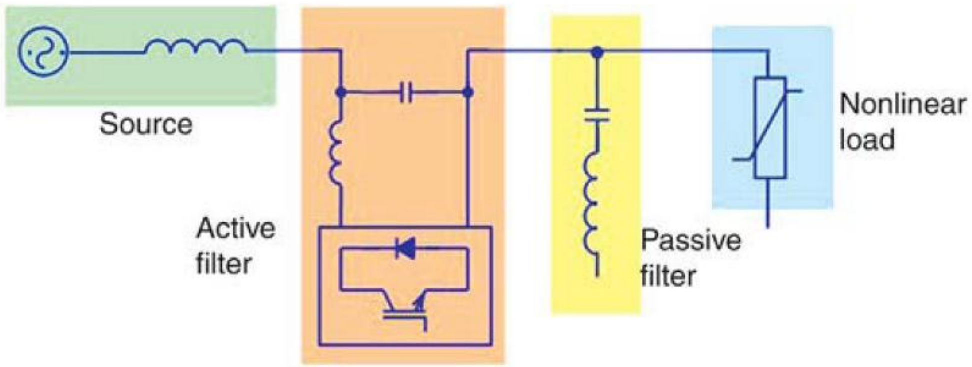

Figure 2-4 Hybrid Topology with Series Active Filter and Passive Filter in Parallel with the Load [157]

- **Series-Connected Hybrid Configuration:** An active and a passive filter are connected in series, with the pair paralleled to the load [162]. The active filter produces a voltage proportional to source current harmonics, boosting the passive filter's effectiveness with a smaller power capacity compared to standalone shunt APFs.

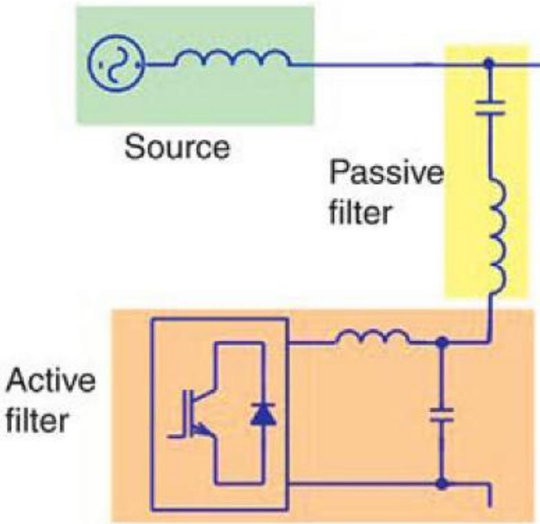

Figure 2-5 Combined Topology of Series Active and Passive Filters, in Parallel with the Load [157]

These hybrid designs balance cost and performance, making them a focal point in power quality research.

2.4.1.3 Unified Power Quality Conditioners

Unified Power Quality Conditioners (UPQCs) integrate a series active filter and a shunt active filter to address both voltage and current disturbances. The series filter corrects voltage issues (e.g., sags or harmonics), while the shunt filter compensates for current harmonics and reactive power. Known as universal active filters, UPQCs provide comprehensive power quality improvement [163]. However, their high cost limits widespread use

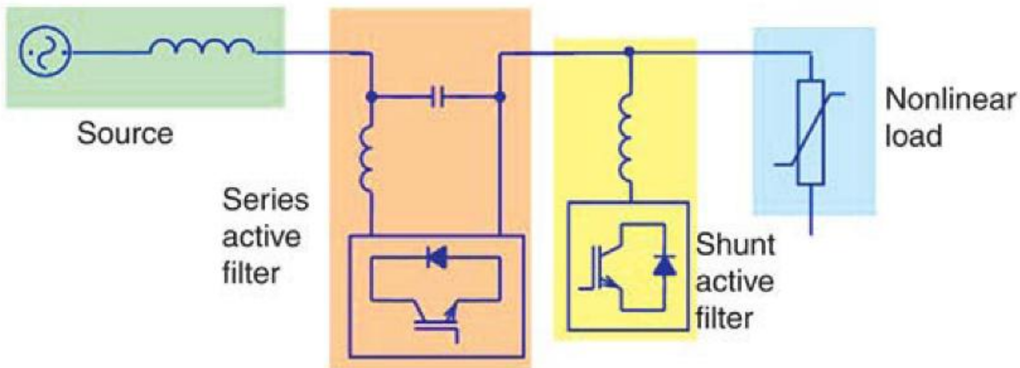

Figure 2-6 Combined Topology of a Series Active Filter and a Parallel Active Filter

In Ref. [164] demonstrated the efficacy of shunt APFs in three-phase systems for harmonic reduction and reactive power compensation. Their reliance on coordinated control algorithms underscores a strength: adaptability to dynamic loads. However, a limitation emerges—shunt APFs are less effective against voltage harmonics, while series APFs struggle with high-current harmonics, necessitating hybrid designs for comprehensive power quality solutions. The choice of configuration thus drives modelling complexity and control design.

Modern APFs leverage digital control platforms, typically implemented via digital signal processor (DSPs) or microcontrollers. MATLAB/Simulink-based framework as in [165] enable rapid prototyping by modelling switching dynamics, sensor delays, and reference generation. This approach excels in flexibility and simulation speed, yet oversimplifications (e.g., neglecting thermal effects or hardware-specific latencies) limit its real-world applicability, highlighting the need for hardware-in-the-loop validation to bridge simulation and implementation.

A robust mathematical model often begins with describing the grid-load-inverter interactions. In a shunt APF, the filter is typically modelled by an inverter bridge, a DC-link capacitor, and various sensors. Equations are written in the *abc* or *dq* reference frame, enabling the design of controllers that regulate harmonic currents and DC-link voltage.

Hybrid APFs integrate passive filtering with active compensation, requiring mathematical models that account for both resonance effects and real-time current/voltage control. In Ref. [166] developed an average model for a three-phase series hybrid power filter, combining a series active filter with a tuned passive filter to enhance harmonic mitigation. Their formulation enables transient and steady-state performance analysis, crucial for optimizing filter resonance interactions.

In Ref. [167] introduced a novel shunt hybrid APF based on magnetic flux compensation. By creating a mathematical model that captures flux variations, they analyzed system stability under different load conditions.

High-Power-Factor Rectifiers: In Ref. [167] proposed a single-phase rectifier with a two-quadrant shunt APF. Their mathematical model helped verify how the filter stabilizes input current waveforms to achieve near-unity power factor.

Aircraft Electric Power Systems: In Ref. [168] examined a cascaded shunt APF with feedforward load current compensation. They identified how accurate load current modelling is critical for dynamic performance, especially in harsh aircraft environments.

DC-Side Ripple Management: In Ref. [169] addressed low-frequency power ripple in a single-phase quasi-Z-source inverter. Their active filtering approach maintained constant inductor currents and capacitor voltages, demonstrating how modelling must capture the DC side's dynamics to prevent large voltage fluctuations.

These application-specific models highlight a key limitation: tailored solutions often lack transferability, necessitating broader frameworks.

2.4.2 Active Power Filters Control Strategies

Classical Proportional–Integral (PI) controllers are widely adopted for their simplicity but falter under nonlinear or variable loads due to fixed parameters, because their fixed control parameters are tuned for a specific operating point and cannot adapt to changing system dynamics, resulting in reduced control performance when load conditions vary.

In Ref. [170] introduced a type-2 fuzzy logic controller for a three-level shunt APF, leveraging adaptive membership functions to handle nonlinear system uncertainties. Unlike conventional fuzzy controllers, which rely on fixed fuzzy sets, type-2 fuzzy logic dynamically adjusts parameters, improving harmonic compensation under varying load conditions. This method enhances robustness but requires high computational resources for real-time implementation. Fuzzy logic outperforms PI in robustness, yet its computational intensity and tuning requirements pose challenges for real-time deployment, illustrating a trade-off between adaptability and practicality.

Active Disturbance Rejection Control (ADRC), as in Ref. [171], estimates disturbances (e.g., harmonics) in real-time, enhancing compensation accuracy. Decoupling control [172], isolates real and reactive power dynamics, improving response speed. ADRC's strength is its resilience, but it relies on precise disturbance estimation, which falters in noisy conditions. Decoupling assumes linearity, limiting its efficacy under severe nonlinearities. Both methods advance control precision but expose methodological gaps in handling complex disturbances.

Hybrid APFs combine active and passive elements, requiring sophisticated resonance management. Intelligent controllers, such as the probabilistic feature-based approach in Ref. [173], employ machine learning to adapt to uncertainties. Hybrid designs reduce costs but complicate stability analysis, while intelligent methods promise adaptability yet lack transparency and require extensive training data, underscoring a shift toward data-driven innovation with unresolved implementation hurdles.

Designing an APF involves selecting parameters (e.g., DC-link capacitance, switching frequency, filter inductance) that align with harmonic mitigation goals and operational constraints. In Ref. [174] tackled the parameter design of a thyristor-controlled LC-coupled hybrid APF (TCLC-HAPF), addressing how unbalanced three-phase power flow complicates compensation. Detailed modelling ensures that the chosen parameters suppress relevant harmonics without causing overcompensation or resonance.

Beyond harmonic mitigation, APFs also influence electromagnetic interference (EMI) due to high-frequency switching. Effective APF designs must consider EMI filter integration to suppress conducted noise and maintain power system compliance. In Ref. [175] demonstrated a comprehensive design of an EMI filter for a three-phase boost power factor correction (PFC) rectifier used in avionics, focusing on conducted EMI analysis. While EMI filtering is often treated separately from harmonic filtering, both require thorough modelling of switching noise sources and filter transfer functions. This interplay highlights that effective APF design also includes electromagnetic compatibility aspects.

Recent works point toward multi-functional devices that combine active filtering with other power electronics functions—like DC ripple elimination, high-power-factor rectification, and unbalanced load compensation. Such integration requires robust system-level models that unify different control objectives in a single platform.

As power grids increasingly incorporate variable renewable energy sources and flexible loads, active power filters (APFs) are required to adapt rapidly to changing operating conditions. In this context, adaptive and predictive control strategies—often supported by machine learning techniques—have shown significant potential. These approaches enable the rapid detection of emerging harmonic components, facilitate online parameter tuning to maintain dynamic performance, and support seamless integration of APFs within microgrids and distributed generation systems.

Digital twins, or high-fidelity simulation models that mirror physical APFs in real time, could accelerate development cycles and reduce testing costs. This approach requires consistent, validated mathematical models that accurately reflect both the steady-state and transient behaviour of APFs under diverse load conditions.

The principles and mathematical modelling of active power filters form the foundation for enhancing power quality in complex power systems. The reviewed literature highlights several important insights. First, comprehensive modelling—ranging from system-level representations to detailed component-level descriptions—plays a critical role in ensuring that control and design strategies meet stringent harmonic standards. In addition, advanced control strategies, including fuzzy logic, active disturbance rejection, and other intelligent control methods, enable APFs to effectively handle nonlinearities, wide load variations, and uncertain operating conditions.

Furthermore, appropriate parameter design and optimisation are essential for achieving stable and cost-effective harmonic mitigation, with careful selection of inductors, capacitors, and DC-link components being particularly important. Finally, the evolution of APFs toward multi-functional power quality devices has opened new opportunities for integration with related technologies, such as electromagnetic interference filters, DC ripple suppression, and adaptive microgrid control, thereby offering further improvements in overall system performance.

Taking together, these studies highlight how mathematical modelling remains pivotal, guiding the design and implementation of APFs to deliver reliable, efficient power quality solutions across diverse sectors—from aircraft electric systems to hybrid renewable setups.

2.4.3 Application of Optimization Algorithms in Filter Configuration

Optimization algorithms, notably Particle Swarm Optimization (PSO), have emerged as critical tools for solving complex, multi-dimensional engineering problems, including filter configuration. Inspired by the social dynamics of bird flocks and fish schools, PSO leverages swarm intelligence to navigate non-linear, constrained optimization landscapes effectively. This section critically evaluates the application of PSO and its variants across filter configuration, and distributed generation (DG) in power systems. By systematically comparing research methods, system constraints, and application contexts, this review elucidates the strengths, limitations, and innovations of these approaches, identifying gaps that future study seeks to bridge.

In Ref. [28] provided an early demonstration of PSO's utility in designing passive power filters and hybrid active power filters (HAPFs) to address harmonic distortion and reactive power compensation in high-voltage systems. Their approach formulated a multi-objective optimization problem, integrating harmonic attenuation and cost minimization, and was validated through an industrial case study. The method's strength lies in its rapid convergence and ability to manage large-scale, constrained optimization tasks, making it suitable for industrial applications. However, its reliance on static system assumptions limits its effectiveness in dynamic environments with fluctuating harmonic profiles. This highlights a methodological gap: the need for adaptive PSO variants capable of real-time adjustments, a challenge rooted in the static nature of the data sources and system models employed.

PSO's adaptability extends across diverse filter design challenges in power electronics, including reducing THD, minimizing filter size, and ensuring compliance with grid standards. Its success derives from its capacity to explore complex, multi-constraint design spaces efficiently. Nonetheless, limitations emerge in high-dimensional problems, where premature convergence reduces solution diversity. Research methods relying on standard PSO implementations often lack mechanisms to maintain exploration, underscoring the need for enhanced variants or hybrid approaches to overcome this theoretical weakness.

In Ref. [176] advanced PSO through the Advanced Pareto-front Non-Dominated Sorting Multi-Objective PSO for optimizing DG placement in radial distribution networks, tested on the IEEE 33-bus system. This method excels in balancing conflicting objectives—loss reduction, voltage stability, and cost—producing a set of Pareto-optimal solutions. Its strength lies in its comprehensive multi-objective framework, grounded in rigorous simulation-based validation. However, its computational burden, driven by large population sizes and complex sorting mechanisms, limits scalability in larger systems, a constraint linked to the method's data-intensive nature and system scale.

With the rise of distributed generation and adjustable loads, multi-objective PSO variants address integrated challenges in filter sizing, placement, and scheduling. These Pareto-based approaches effectively optimize cost, voltage profiles, power losses, and harmonic levels concurrently. Yet, their efficacy depends heavily on accurate system modelling and parameter tuning, often impractical in data-scarce real-world settings. This methodological limitation emphasizes the need for robust, data-driven frameworks to enhance practical applicability.

PSO is a population-based optimisation algorithm in which particles iteratively update their positions and velocities based on their own best-known solution and the global best solution found by the swarm. Tailored PSO variants—such as Binary Particle Swarm Optimization (BPSO), multi-objective PSO, and chaotic PSO—extend the basic framework to address specific problem characteristics. Compared to standard PSO, BPSO adapts the position update mechanism to handle discrete or binary decision variables, multi-objective PSO incorporates mechanisms to balance and explore trade-offs between multiple objectives, and chaotic PSO introduces chaotic sequences to enhance exploration and avoid premature convergence. While these adaptations enhance flexibility, they introduce challenges such as increased parameter sensitivity and slower convergence, reflecting trade-offs in their design and implementation complexity.

Hybrid PSO-GA models combine PSO's fast convergence with Genetic Algorithm (GA)'s mutation-based diversity, preventing premature convergence and improving solution robustness. This synergy is particularly useful in filter design problems, where PSO efficiently identifies near-optimal configurations, while GA ensures a broader search space exploration. However, increased algorithmic complexity complicates tuning and deployment, a practical limitation that future research must address through simplified hybrid models.

As power systems evolve into dynamic, data-rich environments, real-time optimization gains prominence. PSO's iterative nature holds promise for adaptive filter configuration, but its computational demands in high-dimensional spaces remain a barrier. Integrating machine learning, such as neural networks for predictive heuristics, could reduce this burden, marking a theoretical frontier for future innovation.

The existing literature consistently demonstrates that PSO and its variants—including binary, multi-objective, and hybrid formulations—are effective tools for solving complex engineering optimisation problems. In the context of harmonic mitigation, PSO has been widely applied to filter configuration, where its multi-objective capability enables efficient handling of trade-offs among harmonic suppression performance, cost, and system size in both passive and hybrid active power filter designs. Furthermore, in distribution network planning and operation, multi-objective PSO approaches have been successfully employed to optimise the placement of distributed generation, balancing reliability, economic performance, and environmental considerations.

Despite these advances, several challenges remain that motivate further research. In particular, there is a need to develop adaptive PSO variants that incorporate self-learning mechanisms and online parameter tuning to support real-time optimisation. In addition, hybrid optimisation frameworks that combine PSO with machine learning techniques, such as reinforcement learning, may provide improved predictive search capabilities. Addressing scalability and computational efficiency is also critical, especially for high-dimensional and large-scale optimisation problems such as coordinated APF deployment. Finally, the application of PSO can be extended beyond traditional power system problems to broader domains, including electromagnetic compatibility filtering, renewable energy integration, and microgrid optimisation.

2.5 Summary

This chapter has provided a thorough literature review on key elements of power flow studies in power systems, critically examining their theoretical underpinnings, methodological advancements, and practical challenges. In Section 2.1, the evolution of power flow models was analyzed, highlighting complexities such as unbalanced loads and nonlinearities, alongside a comparative evaluation of harmonic source models and calculation methods (e.g., unified vs. decoupled approaches). The critique emphasized mathematical limitations, such as convergence issues in iterative solvers and assumptions in harmonic propagation equations, which may lead to inaccuracies in high-distortion scenarios—defended through comparisons of computational efficiency and error bounds from referenced studies.

Section 2.2 delved into stochastic power flow and probabilistic analysis, underscoring the necessity of uncertainty modelling for renewable integrations like wind and photovoltaic systems. Approaches including MCS and the Three-Point Estimation method were scrutinized for their statistical robustness, with discussions on variance reduction techniques and the impact of correlation matrices on result accuracy (e.g., via covariance modelling). Critically, while MCS offers high fidelity, its computational demands were contrasted against approximation methods, revealing trade-offs in bias-variance errors that must be justified in large-scale applications.

In Section 2.3, power quality assessment methodologies were explored, focusing on index systems and weighting techniques (e.g., analytic hierarchy process vs. entropy methods). The analysis critically assessed their objectivity in quantifying parameters like voltage sag and harmonics, noting potential biases in subjective weighting and the need for empirical validation to ensure reliability in diverse grid conditions.

Finally, Section 2.4 reviewed the principles and optimization of APFs, including mathematical models for shunt and hybrid configurations. The role of algorithms like particle swarm optimization was evaluated for harmonic mitigation, with critiques on convergence rates and local optima traps, supported by published simulation-based evidence of performance gains in distortion reduction.

Building on this review, Chapter 3 extends these concepts by presenting detailed theoretical fundamentals and modelling frameworks. It begins with essentials of probability and statistics (e.g., moments, distributions, and point estimation methods), progresses to probabilistic modelling of distributed generation and correlations via Nataf transformations, and covers advanced harmonic power flow calculations, risk assessment, power quality evaluation models, and optimization techniques for APFs using bio-inspired algorithms. This chapter thus transits from literature synthesis to the core analytical tools and proposed models that underpin the thesis's contributions to power system analysis under uncertainty.

Chapter 3 Theoretical Foundations and Probabilistic Methods for Harmonic Analysis, Risk Assessment, and Optimal Active Power Filter Placement in Power Systems

Following the literature review in Chapter 2, which surveyed developments in power flow models, stochastic analysis, power quality assessment, and active power filter optimization, this chapter outlines the theoretical principles that underpin the simulation and modeling of power systems. Chapter 2 identified issues such as uncertainties in renewable energy sources, harmonic distortions from nonlinear loads, and computational considerations in methods like Monte Carlo Simulation (MCS) and point estimation. This chapter builds on those observations by presenting analytical frameworks for managing uncertainties, nonlinear effects, and the incorporation of distributed generation and mitigation technologies. These frameworks serve as the basis for the empirical studies in later chapters.

The chapter is divided into six sections, each focusing on a particular component of power system analysis:

- Section 3.1 presents probabilistic and statistical concepts, including mathematical expectation, moments, Gram-Charlier and Cornish-Fisher expansions, Beta and Weibull distributions, and probabilistic power flow methods such as three-point estimation and MCS.
- Section 3.2 describes modelling approaches for distributed generation, utilizing the Newton-Raphson method in polar coordinates, probabilistic descriptions of input variables (e.g., loads, conventional generators, photovoltaic, and wind generation), and the Nataf inverse transformation for handling correlations.
- Section 3.3 examines harmonic power flow calculations, covering harmonic source models for power electronics and nonlinear loads, simplified models

(constant current source, Norton equivalent, cross-frequency admittance matrix, least squares approximation), network equations, and solution methods including unified, alternating iteration, decoupled, and direct approaches.

- Section 3.4 discusses risk assessment in power systems, including principles of risk theory, state enumeration and MCS methods, their comparative analysis, and models for calculating risk indicators related to voltage and branch overloads.
- Section 3.5 addresses power quality evaluation, reviewing associated challenges and standards, fundamental requirements and characteristics, proposed evaluation index systems, and models for identifying weak points.
- Section 3.6 reviews optimization methods for active power filters, encompassing harmonic mitigation strategies (active and passive), configurations such as shunt, hybrid, and unified power quality conditioners, grid configuration models, a double-layer economic optimization framework (outer layer for placement, inner layer for parameters), and the particle swarm optimization algorithm with its parameters and modifications.

3.1 Related Fundamentals of Probability and Statistics

3.1.1 Mathematical Expectation and Variance

In probability theory, numerical characteristics are specific values associated with the distribution of a random variable. These include measures such as central moments, probability density, mathematical expectation, and variance, which collectively provide insight into the behaviour and properties of the random variable.

The mathematical expectation, often referred to simply as the expectation or mean, is a fundamental numerical characteristic that represents the average value of a random variable over many trials. It is denoted by $E(X)$, where X is the random variable in question.

1. For a continuous random variable x:

Suppose x has a probability density function $f(x)$. The mathematical expectation

$E(X)$ is defined as the integral $E(X)=\int_{-\infty}^{+\infty}|x|f(x)dx$, provided that the absolute moment $\int_{-\infty}^{+\infty}|x|f(x)dx$ converges (i.e., is finite). This integral quantifies the central tendency of X by weighing each possible value x by its likelihood $f(x)$.

2. For a discrete random variable X:

Let x take on values x_i (where $i=1,2,3,\dots$) with corresponding probabilities $P(X=x_i)=p_i$. The mathematical expectation is given by $E(X)=\sum_{i=1}^{\infty}x_i p_i$, provided that the infinite series $\sum_{i=1}^{\infty}|x_i|\, p_i$ converges. This sum represents the weighted average of all possible outcomes, where each value x_i is weighted by its probability p_i. If the series diverges, the expectation does not exist.

The expectation is a crucial measure because it provides a single summary statistic that captures the "center" of the distribution of X, serving as a baseline for understanding its typical behaviour.

While the mathematical expectation describes the average value of a random variable, it alone is insufficient to fully characterize the distribution. To gain a deeper understanding, which must also consider the extent to which the values of the random variable fluctuate around this average. This variability, or the degree of deviation from the expectation, is quantified by the variance. The variance measures how spread out the values of X are relative to $E(X)$, offering insight into the consistency or randomness of the variable's behaviour.

1. For a continuous random variable X:

The variance of X, denoted $\mathrm{Var}(X)$, is defined as

$$\mathrm{Var}(X)=E[(X-E(X))^2] \tag{3.1}$$

provided this expectation exists. Expanding this, it can express the variance as

$$\mathrm{Var}(X)=\int_{-\infty}^{+\infty}(x-E(X))^2 f(x)dx \tag{3.2}$$

This integral calculates the expected value of the squared deviations of X from its mean, effectively measuring the average "spread" of the distribution. A larger variance indicates greater dispersion of the random variable's values.

2. For a discrete random variable X:

Given a probability distribution $(P(X = x_i) = p_i)$,(where $i = 1, 2, 3, \dots$), the variance is defined as:

$$\mathrm{Var}(X) = E[(X - E(X))^2] = \sum_{i=1}^{\infty} (x_i - E(X))^2 p_i \tag{3.3}$$

Assuming this sum is finite. This expression computes the weighted average of the squared differences between each possible value x_i and the mean $E(X)$, with weights given by the probabilities p_i. Like its continuous counterpart, the variance reflects the extent to which X deviates from its expected value.

The mathematical expectation and variance together provide a more comprehensive picture of a random variable's distribution. The expectation serves as a measure of location, pinpointing the central value around which the random variable oscillates, while the variance quantifies the degree of dispersion or uncertainty inherent in the variable's outcomes. For instance, two random variables might share the same expectation but differ significantly in variance, indicating different levels of predictability or stability. These characteristics are foundational in statistical analysis and are widely applied in fields such as economics, engineering, and the natural sciences to model and interpret random phenomena.

3.1.2 Origin Moments and Central Moments

In probability theory, moments are numerical characteristics that provide detailed insights into the shape and properties of a random variable's distribution. They are classified into two main types: origin moments and central moments, each serving distinct purposes in statistical analysis [29].

The origin moment of a random variable refers to the weighted sum of the k -th powers of the data points relative to the origin (i.e., zero), where the weights are determined by the probabilities or probability density of the random variable. Here, k

is a positive integer, typically starting from 1 and increasing sequentially. Origin moments are essential for computing various statistical measures, such as the mean, variance, skewness, and kurtosis, which collectively describe the distribution's characteristics.

The k -th origin moment of a random variable X is defined as the mathematical expectation of X^k, denoted by $v_k(X)$. Mathematically, it is expressed as follows:

1. For a discrete random variable X :

If X takes on values x_i with probabilities $P(X = x_i) = p_i$ $(where$ $(i = 1,2,3,\dots)$, the k -th origin moment is given by:

$$v_k(X) = E(X^k) = \sum_i x_i^k p_i, \tag{3.4}$$

provided the sum converges.

2. For a continuous random variable X :

If X has a probability density function $f(x)$, the k -th origin moment is defined as:

$$v_k(X) = E(X^k) = \int_{-\infty}^{+\infty} x^k f(x)dx \tag{3.5}$$

assuming the integral is finite.

A special case of particular importance is the first origin moment ($k = 1$), which corresponds to the mathematical expectation of X :

$$v_1(X) = E(X).$$

This is simply the mean of the random variable, providing a measure of its central tendency. Higher-order origin moments $(k \geq 2)$ offer additional information about the distribution, such as its spread or shape, though they are less commonly interpreted directly compared to central moments.

Central moments, in contrast, measure the weighted sum of the k -th powers of the deviations of the data points from the mean (i.e. $E(X)$), with weights again determined by the probabilities or density function. Here, k is a positive integer, typically starting from 2, as the first central moment ($k=1$) is always zero by definition. Central moments are particularly useful for describing the shape and dispersion of a distribution, including properties like variance, skewness, and kurtosis [177].

The k -th central moment of a random variable X is defined as the expectation of $[X-E(X)]^k$, denoted by $\mu_k(X)$, and is given by:

$$\mu_k(X)=E\left\{[X-E(X)]^k\right\} \tag{3.6}$$

1. For a discrete random variable X :

With a probability distribution $P(X=x_i)=p_i$ (where $i=1,2,3,\dots$), the k -th central moment is:

$$\mu_k(X)=\sum_i[x_i-E(X)]^k p_i \tag{3.7}$$

provided the sum exists.

2. For a continuous random variable X :

Given a probability density function $f(x)$, the k -th central moment is:

$$\mu_k(X)=\int_{-\infty}^{+\infty}[x-E(X)]^k f(x)dx \tag{3.8}$$

assuming the integral converges.

Notably, the first central moment ($\mu_1(X)=E[X-E(X)]$) is always zero, as the deviations from the mean cancel out in expectation. The second central moment ($\mu_2(X)$) is the variance:

$$\mu_2(X)=E[(X-E(X))^2] \tag{3.9}$$

which measures the spread of the distribution. Higher-order central moments, such as the third ($\mu_3(X)$) and fourth ($\mu_4(X)$), are used to compute skewness (which indicates asymmetry) and kurtosis (which describes the "tailedness" of the distribution), respectively.

Origin moments and central moments are closely related, as central moments can be expressed in terms of origin moments via the binomial expansion of $[X - E(X)]^k$. For example, the variance $\mu_2(X)$ can be rewritten as $E(X^2) - [E(X)]^2$, linking the second origin moment $\nu_2(X)$ to the expectation. These moments collectively provide a systematic framework for analyzing the properties of a random variable's distribution, making them indispensable tools in statistical modelling, hypothesis testing, and data interpretation across various disciplines.

Characteristic Functions and Independence

Consider two independent random variables X and Y, with characteristic functions $\phi_X(t)$ and $\phi_Y(t)$, respectively. The characteristic function of a random variable is defined as the Fourier transform of its probability distribution and provides a powerful tool for studying sums of independent variables. According to the theorem on the expectation of the product of independent factors, the characteristic function of the sum $Z = X + Y$ is given by:

$$\phi_Z(t) = E[e^{it(X+Y)}] = E[e^{itX}] \cdot E[e^{itY}] = \phi_X(t) \cdot \phi_Y(t) \tag{3.10}$$

This result stems from the independence of X and Y, which allows the expectation of the product to be expressed as the product of the expectations. This property can be generalized to the sum of n independent random variables, leading to the conclusion that the characteristic function of the sum is the product of the individual characteristic functions.

Cumulative Distribution Functions and Convolution

Let the cumulative distribution functions (CDFs) of X and Y be $F_X(x)$ and $F_Y(y)$, respectively. The CDF of the sum $Z = X + Y$, denoted $F_Z(z)$, is then [178]:

$$F_Z(z) = P(Z \le z) = P(X + Y \le z) \tag{3.11}$$

From Equation (3.10), it follows that the CDF of the sum of two independent random variables is the convolution of their individual CDFs. Mathematically, this is expressed as:

$$F_Z(z) = (F_X * F_Y)(z) = \int_{-\infty}^{+\infty} F_X(z-y)dF_Y(y) \tag{3.12}$$

This convolution operation reflects the combined effect of the two distributions and is a direct consequence of the multiplicative property of characteristic functions under independence.

Semi-Invariants and Their Additivity

From the previous section, it is shown that once the origin moments or central moments of a random variable are obtained, they can be transformed using specific relationships to derive the corresponding v-th order semi-invariants. With these semi-invariants in hand, it can leverage their properties to simplify the complexity of convolution computations, a process that is particularly valuable in probability theory and statistical analysis [179].

The semi-invariants (or cumulants) of a random variable are derived from the logarithm of its characteristic function. Specifically, if $\phi_X(t)$ is the characteristic function of X, the k-th semi-invariant $\kappa_k(X)$ is defined via the expansion [30]:

$$\ln \phi_X(t) = \sum_{k=1}^{\infty} \kappa_k(X) \frac{(it)^k}{k!} \tag{3.13}$$

For the sum $Z = X + Y$, the characteristic function is

$$\phi_Z(t) = \phi_X(t) \cdot \phi_Y(t) \tag{3.14}$$

So:

$$\ln \phi_Z(t) = \ln \phi_X(t) + \ln \phi_Y(t) \tag{3.15}$$

By comparing the coefficients of the power series expansions on both sides, it can obtain a key property of semi-invariants: for two independent random variables X and Y, the k-th semi-invariant of their sum is the sum of their individual k-th semi-invariants:

$$\kappa_k(Z) = \kappa_k(X) + \kappa_k(Y) \tag{3.16}$$

This additivity property generalizes to n independent random variables $X_1, X_2, \ldots, X_n$, where the k -th semi-invariant of the sum $S = X_1 + X_2 + \cdots + X_n$ is:

$$\kappa_k(S) = \kappa_k(X_1) + \kappa_k(X_2) + \cdots + \kappa_k(X_n) \tag{3.17}$$

The additivity of semi-invariants offers a significant computational advantage. While the convolution of n CDFs (as required to compute the distribution of the sum) can be computationally intensive, especially as n increases, Equation (3.17) allows us to replace this complex operation with a simple summation of semi-invariants. This transformation not only simplifies the mathematical representation of the random variable's characteristics but also reduces the computational burden, markedly improving efficiency.

For example, the first semi-invariant κ_1 is the mean, the second κ_2 is the variance, and higher-order semi-invariants relate to skewness and kurtosis. By expressing the distribution of the sum in terms of these additive quantities, it can efficiently analyze the properties of composite systems without directly handling convoluted integrals or sums. This property makes semi-invariants a powerful tool in statistical modelling, particularly in applications involving sums of independent random processes, such as signal processing, financial mathematics, and queueing theory.

3.1.3 Gram-Charlier Series and Cornish-Fisher Series

The Gram-Charlier series expansion is frequently utilized in stochastic simulation of power systems. It enables the approximation of a random variable's probability density function and cumulative distribution function using its known moments or cumulants, combined with the derivatives of a normal random variable [180].

Given a function $f(x)$, where $x \in (-\infty, +\infty)$, and I is an interval within $(-\infty, +\infty)$, it can approximate $f(x)$ using the following method. Let $\omega(x)$ be a continuous function such that $\omega(x) > 0$ for $x \in I$. If I is an infinite interval, it is required that the integral $\int_I x^k \omega(x)dx$ exists for any polynomial π. In this thesis, all integrals are evaluated over I. Let $\pi_0(x), \pi_1(x), \ldots$ be orthogonal polynomials with respect to the weight function ω:

$$\int_I \pi_i(x)\pi_k(x)\omega(x)dx = \begin{cases} 0 & \text{if } i \neq k \\ C_k & \text{if } i = k \end{cases} \tag{3.18}$$

where $\pi_k(x)$ is a polynomial of degree k, which can be determined recursively starting from $\pi_0(x)=1$, followed by $\pi_1(x), \pi_2(x), \ldots$. Furthermore, define:

$$C_k = \int_I [\pi_k(x)]^2 \omega(x)dx, k = 0,1,\ldots \tag{3.19}$$

For a sufficiently well-behaved function $f(x)$, it can be expanded into a series:

$$f(x) = A_0\pi_0(x)\omega(x) + A_1\pi_1(x)\omega(x) + \ldots \tag{3.20}$$

The coefficients $A_0, A_1, \ldots$ can be determined by:

$$\int_I \pi_k(x) f(x)dx = A_k C_k \tag{3.21}$$

Thus,

$$A_k = \frac{\int_I \pi_k(x) f(x)dx}{C_k} \tag{3.22}$$

Therefore, A_k is a linear function of the first k moments of the function $f(x)$. If $f(x)$ is the density function of a random variable S, then:

$$A_k = \frac{E[\pi_k(S)]}{C_k} \tag{3.23}$$

By truncating the series, to obtain an approximation:

$$f(x) \approx A_0\pi_0(x)\omega(x) + \ldots + A_n\pi_n(x)\omega(x) \tag{3.24}$$

From the above process, it is evident that the probability density function $f(x)$ of a random variable can be approximately described by its n-th moments.

For any random variable ξ, assuming its mean and standard deviation are μ and σ respectively, the standardized random variable is:

$$x = \frac{\xi - \mu}{\sigma} \tag{3.25}$$

Take $I = (-\infty, +\infty)$ and $\omega(x) = \phi(x)$, where $\phi(x)$ is the standard normal probability density function, and $\Phi(x)$ is the standard normal cumulative distribution function. Let $F(x)$ be the cumulative distribution function of the standardized random variable x, and $f(x) = F'(x)$ its probability density function. Then, $F(x)$ and $f(x)$ can be expressed as:

$$F(x) = \sum_{i=0}^{n} \frac{C_i}{i!} H_i(x)\Phi(x) + \ldots \tag{3.26}$$

$$f(x) = \sum_{i=0}^{n} \frac{C_i}{i!} H_i(x)\phi(x) + \ldots \tag{3.27}$$

This is known as the Gram-Charlier series expansion, where:

$$C_k = (-1)^k \int_{-\infty}^{+\infty} H_k(x) f(x) dx, \quad k = 1, 2, 3, \ldots \tag{3.28}$$

and $H_k(x)$ are the Hermite polynomials, defined as:

$$H_k(x) = (-1)^k \frac{\phi^{(k)}(x)}{\phi(x)}, \quad k = 0, 1, \ldots \tag{3.29}$$

The first four Hermite polynomials are:

$$\begin{aligned} H_0(x) &= 1 \\ H_1(x) &= x \\ H_2(x) &= x^2 - 1 \\ H_3(x) &= x^3 - 3x \\ H_4(x) &= x^4 - 6x^2 + 3 \end{aligned} \tag{3.30}$$

The expressions for the first six C_k are given as follows:

$$\begin{aligned} C_0 &= 1 \\ C_1 &= C_2 = 0 \\ C_3 &= -\mu_3 \\ C_4 &= \mu_4 - 3 \\ C_5 &= -\mu_5 + 10\mu_3 \\ C_6 &= \mu_6 - 15\mu_4 + 30 \end{aligned} \tag{3.31}$$

Where $\mu_3 = E[x^3]$ is the third central moment; $\mu_4 = E[x^4]$ is the fourth central moment; $\mu_5 = E[x^5]$ and $\mu_6 = E[x^6]$.

Since x is standardized $(E[x]=0, (E[x^2]=1)$, $C_0 = 1$ (total probability), $C_1 = -E[x] = 0$, $C_2 = E[x^2-1] = 1-1 = 0$, and higher C_k terms depend on the central moments $\mu_k = E[x^k]$. The text appears incomplete after listing the first few terms, but these are derived based on standard Gram-Charlier conventions and the definition $C_k = (-1)^k E[H_k(x)]$.

The Cornish-Fisher series is closely related to the Gram-Charlier series, as both are expansions that use the standard normal distribution to approximate the distribution of a random variable. However, unlike the Gram-Charlier series, which directly approximates the PDF and CDF, the Cornish-Fisher series focuses on approximating the quantiles (or percentiles) of the distribution. This makes it particularly suited for estimating the inverse CDF (i.e., the quantile function) based on the α-level percentile [181].

The Cornish-Fisher series often provides better fitting accuracy for non-normal distributions compared to the Gram-Charlier series. This advantage is especially pronounced for distributions like the Beta distribution, which is commonly used to model photovoltaic power generation due to its flexibility in capturing skewed and bounded data. By incorporating semi-invariants up to the fifth order, the Cornish-Fisher series offers a robust approximation for such cases [182].

For a standardized random variable $z = \dfrac{X-\mu}{\sigma}$, the Cornish-Fisher expansion expresses the α-quantile of X in terms of the standard normal quantile $z_\alpha = \Phi^{-1}(\alpha)$. The expansion, truncated at the fifth order:

$$x_\alpha = \mu + \sigma \begin{bmatrix} z_\alpha + \dfrac{\kappa_3}{6\sigma^3}(z_\alpha^2 - 1) + \dfrac{\kappa_4}{24\sigma^4}(z_\alpha^3 - 3z_\alpha) \\ -\dfrac{\kappa_3^2}{36\sigma^6}(2z_\alpha^3 - 5z_\alpha) + \dfrac{\kappa_5}{120\sigma^5}(z_\alpha^4 - 6z_\alpha^2 + 3) + \cdots \end{bmatrix} \tag{3.32}$$

Where:

x_α is the α-quantile of X,

z_α is the α-quantile of the standard normal distribution (i.e., $\Phi(z_\alpha)=\alpha$),

κ_k are the semi-invariants of X, and

σ is the standard deviation.

Each term in the Cornish-Fisher expansion adjusts the standard normal quantile z_α based on the higher-order semi-invariants, accounting for skewness (κ_3), kurtosis (κ_4), and beyond. For instance, the term involving κ_3 corrects for asymmetry, while κ_4 adjusts for the thickness of the tails. This quantile-based approach is particularly valuable in applications requiring precise estimation of extreme values, such as risk analysis or renewable energy forecasting.

Compared to the Gram-Charlier series, the Cornish-Fisher series excels in practical scenarios where direct quantile estimation is preferred over full distribution approximation. Its effectiveness for Beta-distributed photovoltaic generation highlights its utility in modelling real-world systems with non-normal characteristics, offering a balance of accuracy and computational feasibility.

3.1.4 The Beta Distribution and Weibull Distribution [183]

The Beta distribution is a continuous probability distribution defined on the interval [0,1], widely recognized in Bayesian statistics as a conjugate prior for the Bernoulli and binomial distributions. Its probability density function is expressed as:

$$f(x;\alpha,\beta)=\frac{x^{\alpha-1}(1-x)^{\beta-1}}{B(\alpha,\beta)} \quad (0\le x\le 1) \tag{3.33}$$

where $\alpha>0$ and $\beta>0$ are shape parameters, and

$$B(\alpha,\beta)=\int_0^1 t^{\alpha-1}(1-t)^{\beta-1}dt \tag{3.34}$$

is the Beta function, which can also be expressed in terms of the Gamma function as

$$B(\alpha,\beta)=\frac{\Gamma(\alpha)\Gamma(\beta)}{\Gamma(\alpha+\beta)} \tag{3.35}$$

A key characteristic of the Beta distribution is its capacity to incorporate prior information, making it particularly suitable for modelling random variables—such as light intensity—that are associated with existing statistical data. This prior information facilitates the establishment of an initial probability distribution for the random variable X . When new data becomes available or conditions change, the distribution can be updated by incorporating additional information, leveraging the conjugate prior property for efficient computation. The flexibility of the Beta distribution is further enhanced by its ability to model various shapes of probability densities, such as uniform, unimodal, or U-shaped, depending on the values of α and β . This adaptability allows it to capture different patterns of variability in the data.

In the context of this thesis, the probability distribution of photovoltaic power output is modeled using the Beta distribution. This choice is appropriate because the parameters α and β can be estimated from historical statistical data on light intensity in a specific region, typically employing methods such as maximum likelihood estimation or the method of moments. By fitting the Beta distribution to these data, the model effectively captures the variability and patterns inherent in solar power generation, providing a data-driven representation of photovoltaic power output.

The Weibull distribution is a unimodal, two-parameter family of distribution functions, originally proposed by Swedish physicist Waloddi Weibull for analyzing component lifetimes and fatigue. Its probability density function is given by [184]:

$$f(x;\lambda,k)=\frac{k}{\lambda}\left(\frac{x}{\lambda}\right)^{k-1} e^{-(x/\lambda)^k} \quad (x\geq 0) \tag{3.36}$$

where x is the random variable, $\lambda>0$ is the scale parameter, and $k>0$ is the shape parameter.

The Weibull distribution's versatility in modelling various types of failure rates and degradation processes has made it a valuable tool in reliability engineering and statistical modelling. In the field of renewable energy, its application has been notably successful in wind speed modelling. For instance, in 1976, Justus et al. demonstrated that the Weibull distribution effectively fits wind speed data [185], establishing its utility in capturing the probabilistic behaviour of wind speed variations. Consequently, in this dissertation, the probability distribution of wind power output is modeled using the Weibull distribution. The parameters λ and k are determined from statistical data on wind speeds in a specific region, enabling a realistic and data-driven representation of wind power generation variability.

Table 3-1 compares parameter estimation methods for Beta and Weibull distributions, highlighting their applicability:

Table 3-1 Comparison of Parameter Estimation Methods for Beta and Weibull Distributions

Method	**Beta Distribution (α,β)**	**Weibull Distribution (k,λ)**
Method of Moments	Solve equations using sample mean and variance, involving gamma function for Beta.	Use sample mean and variance, involving gamma function.
Maximum Likelihood Estimation (MLE)	Maximize the likelihood function, often requiring numerical optimization.	Maximize the likelihood function, typically numerical.

3.1.5 Point Estimation Methods for Probabilistic Power Flow

3.1.5.1 Theoretical Foundation of the Point Estimation Method

The point estimation method is a widely adopted approximate computational technique in probabilistic power flow (PPF) analysis [186]. This method excels in accounting for correlations among input random perturbations, thereby mitigating their influence on computational outcomes. By doing so, it reduces errors in the results while maintaining a relatively short computation time. Among the various methodologies available for PPF, the point estimation method stands out as one of the most representative and effective approaches. In this section, this method will be used to explore approximation techniques in power flow studies, with a focus on its application to flexible interconnected distribution networks [187].

The point estimation method is rooted in probability and statistics, offering a systematic approach to handling uncertainty [188]. When the probability distributions of input random variables are known, the method enables the calculation of the statistical moments of these variables up to any desired order. The accuracy of the estimated output random variables improves as the number of estimation points increases. However, this enhancement in precision comes at the cost of significantly increased computational complexity. To strike a balance between accuracy and computational efficiency, the three-point estimation method emerges as an optimal choice. It delivers sufficiently precise estimates without excessively complicating the computation process. This section elaborates on the mechanics and advantages of the three-point estimation method [189].

In practical power system applications, the probabilistic characteristics of input variables can be modeled according to their underlying physical behaviour [190]. The active power demand of conventional loads is typically represented by a normal distribution, reflecting its relatively stable and predictable variability under aggregated consumption patterns. In contrast, the active power output of PV systems is commonly modeled using a Beta distribution, which effectively captures the bounded and asymmetric nature of solar generation due to irradiance fluctuations.

For wind power generation, wind speed—being the primary driving factor—is generally described by a two-parameter Weibull distribution, allowing for an accurate representation of its stochastic and non-uniform characteristics. Based on these active power models, reactive power is further determined by assuming a constant power factor, thereby establishing a direct and simplified relationship between active and reactive components.

To account for the dependencies among these input variables, this study adopts the Nataf transformation. This method enables the mapping of correlated random variables into an equivalent uncorrelated standard normal space, thereby facilitating efficient and accurate probabilistic analysis while preserving the original correlation structure.

Traditional methods such as MCS and alternating iteration techniques are widely recognised for their robustness; however, they often incur significant computational costs when applied to AC/DC probabilistic power flow calculations. In this thesis, both

MCS and the PEM are employed in a complementary manner. Specifically, PEM is adopted for efficient probabilistic analysis due to its low computational burden and suitability for repeated evaluations, while MCS is utilised as a benchmark method to validate the accuracy of the proposed approach and to provide detailed probabilistic characteristics where computational cost is acceptable. This combined strategy ensures a balance between computational efficiency and result reliability.

The semi-invariant method struggles to handle systems with multiple random variables during alternating iterations, limiting its applicability. In contrast, the point estimation method, when combined with the Newton-Raphson algorithm, offers a more efficient and suitable solution for probabilistic power flow analysis in flexible interconnected distribution networks. This hybrid approach leverages the iterative convergence properties of the Newton-Raphson method alongside the statistical efficiency of point estimation [191].

3.1.5.2 Mathematical Formulation of the Three-Point Estimation Method [192]

For a given random variable X_i, the three-point estimation method utilizes three sampling points, defined as:

$$x_{i,k} = \mu_{x_i} + \xi_{x_i,k}\sigma_{x_i} \quad (k = 1,2,3) \tag{3.37}$$

Where:

μ_{x_i} is the expected value (mean) of X_i,

σ_{x_i} is the standard deviation of X_i,

$\xi_{x_i,k}$ is the location coefficient for the k-th sampling point.

The location and weight coefficients for the three-point estimation are calculated as follows:

$$\begin{cases} \xi_{xi,k} = -\dfrac{\lambda_{i,3}}{2} + (-1)^{3-k}\sqrt{\lambda_{i,4} + \dfrac{3}{4}\lambda_{i,3}^2} \quad (\mathrm{k} = 1,2) \\ \xi_{xi,3} = 0 \\ p_{xi,k} = \dfrac{(-1)^{3-k}}{\xi_{xi,k}\left(\xi_{xi,1} - \xi_{xi,2}\right)} \quad (k = 1,2) \\ p_{xi,3} = \dfrac{1}{m} - \dfrac{1}{\lambda_{i,4} - \lambda_{i,3}^2} \end{cases} \tag{3.38}$$

Where:

$\lambda_{i,3}$ and $\lambda_{i,4}$ are the third and fourth standardized central moments of X_i, respectively,

m is the number of sampling points (here, $m = 3$).

For many practical distributions (e.g., normal or near-normal), $\lambda_{i,3}$ (skewness) is typically set to 0, and $\lambda_{i,4}$ (kurtosis) is set to 3, aligning with the characteristics of a Gaussian distribution.

Once the sampling points $x_{i,k}$ and their corresponding weights $p_{x_i,k}$ are determined, the ν-th order raw moment of the output variable $\mathbf{Z}$ is approximated through deterministic power flow calculations [193]:

$$E(\mathbf{Z}^\nu) \approx \sum_{i=1}^{n}\sum_{k=1}^{m} p_{x_i,k} \times (\mathbf{Z}(i,k))^\nu \quad (\nu = 1,2,3,\ldots) \tag{3.39}$$

Where:

n is the total number of input random variables,

m is the number of sampling points per variable (i.e., 3),

$\mathbf{Z}(i,k)$ represents the output of the deterministic power flow calculation at the k-th sampling point of the i-th variable.

This formulation enables the efficient estimation of statistical properties (e.g., mean, variance) of the output variables, such as bus voltages or line flows, in the probabilistic power flow context.

The three-point estimation method provides a computationally efficient and accurate framework for probabilistic power flow analysis. By integrating it with the Newton-Raphson algorithm and employing Nataf transformation for correlation handling, this approach is well-suited for analyzing distribution networks with flexible interconnections and diverse renewable energy sources. The subsequent sections will further explore its implementation and validation in practical case studies.

3.1.6 Monte Carlo Simulation in Probabilistic Power Flow Analysis

3.1.6.1 Theoretical Foundation of Monte Carlo Simulation

MCS is a computational method that uses repeated random sampling to estimate the behaviour of complex systems under uncertainty. In essence, the MCS constructs a model of possible outcomes by drawing random samples for uncertain input variables from their probability distributions and computing the corresponding outputs. By performing this experiment, a large number of times (often thousands or more), MCS builds up an approximate probability distribution of the outcomes. This repeated-trial approach provides numerical solutions to problems that may be analytically intractable. The underlying principle is rooted in the Law of Large Numbers: as the number of independent random trials increases, the empirical distribution of the simulation results converges to the true probability distribution of the system's outcomes [194].

In practice, MCS methods yield estimates of statistical measures (means, variances, quantiles, etc.) with increasing accuracy as more samples are simulated. Each sample or scenario is typically generated by randomizing inputs according to their uncertainty distributions, and the collection of many such samples produces a statistical ensemble from which outcome probabilities can be inferred.

A key strength of MCS is its generality and flexibility. It makes minimal assumptions about the form of the underlying probability distributions or the linearity of the model. Any input variable that can be described by a probability distribution can be incorporated into the simulation, and complex interactions or nonlinear relations are naturally captured by the repeated evaluation of the actual system model. This means that MCS can handle highly nonlinear systems and non-Gaussian or correlated random inputs without requiring simplifying approximations. The trade-off for this generality is that MCS is a brute-force numerical approach: it relies on the law of averages rather than an explicit analytical solution. Consequently, its accuracy is statistical – controlled by the number of samples – rather than deterministic. There is an inherent sampling error that decreases only as $1/\sqrt{N}$ with the number of simulations N (i.e. to reduce the error by half, one needs roughly four times as many samples) [195]. This slow convergence rate means that achieving very high precision or estimating extremely rare event probabilities can demand an extremely large number of trials. Nonetheless, with sufficient samples, MCS provides an unbiased and asymptotically exact estimate of the true outcome distribution and has become a standard technique for probabilistic analysis in many fields.

3.1.6.2 Application of MCS in Probabilistic Power Flow

In power systems analysis, MCS is extensively used for PPF studies. Probabilistic power flow generalizes the conventional deterministic power flow by treating generation, load, and other inputs as random variables rather than fixed values. Uncertainties arise from many sources: fluctuations in consumer demand, random outages of generators or equipment, and the inherent variability of renewable energy sources like wind and solar. Modern grids with high penetration of renewables and distributed generation experience significant variability in both generation and load, making purely deterministic analysis inadequate. PPF analysis aims to compute not just one power flow solution, but the entire distribution of possible power flow outcomes (bus voltage magnitudes, line power flows, generator outputs, etc.) given probabilistic models of the inputs.This enables engineers and researchers to assess risks and reliability – for example, to determine the probability that a line might be overloaded or a bus voltage might exceed acceptable limits under uncertain conditions [196] [197].

MCS provides a straightforward and rigorous way to perform PPF. The MCS-based PPF process proceeds as follows: first, probability distributions (or statistical models) are assigned to all uncertain input parameters – for instance, load demands might be modeled as normal or log-normal random variables with a certain mean and variance, and wind farm outputs might be modeled by a Weibull or Beta distribution derived from wind speed data. Then, the simulation runs a large number of power flow trials (scenarios). In each trial, a random sample is drawn for every uncertain input (independently or according to a prescribed correlation structure among inputs), and a deterministic power flow calculation (e.g. using the Newton–Raphson method) is solved for that set of inputs. This yields one possible realization of the system state (voltage profile, power flows, losses, etc.). By repeating this process N times – each time with a new random draw of generation and load values – which can obtain N different outcomes for the power flow. Collectively, these outcomes form an empirical distribution for each quantity of interest. For example, after many simulations one can construct a histogram or probability density function for the voltage at a particular bus or the flow on a particular transmission line.

Through this MCS approach, uncertainties in generation, load, and renewables are directly translated into uncertainties in system outputs. The method does not linearize or simplify the power flow equations; it evaluates them in full for each random draw. Thus, any nonlinear effects (such as the impact of voltage-dependent loads or generator reactive power limits) are inherently captured. MCS can easily accommodate correlated inputs as well – for instance, spatially correlated wind speeds at different wind farms, or correlations between load levels in different regions. These correlations are handled by sampling from a joint distribution of inputs, preserving statistical relationships. This capability is particularly important for renewable energy modelling: e.g., the power outputs of two nearby solar PV plants might rise and fall together under moving cloud cover, and MCS can account for such correlated behaviour in a straightforward manner.

The output of an MCS-based probabilistic load flow is rich in information. From the ensemble of simulation results, one can estimate mean values (expected voltages, power flows, losses, etc.) as well as higher moments like variance (which indicates the level of uncertainty or volatility in those quantities). More importantly, one can directly compute probabilities of specific events or limits being violated. For instance, by counting the fraction of MCS trials in which a line's flow exceeds its thermal rating, one obtains an estimate of the overload probability for that line. Likewise, the fraction of simulations where a bus voltage falls outside acceptable bounds gives the risk of voltage violation. These risk metrics are a key output of probabilistic power flow analysis and are crucial for system planning and reliability assessment. MCS naturally produces these metrics since it effectively samples the full range of system behaviour under uncertainty. In fact, researchers have used MCS PPF results to evaluate rare event probabilities such as line overloads or bus under-voltage occurrences.

MCS considers all possible combinations of input fluctuations, to the extent covered by the sampling, and therefore does not miss failure scenarios that deterministic studies might overlook. This is why MCS is often regarded as a benchmark or reference method for probabilistic power flow, and any other approximate method is typically validated against the "ground truth" estimated by a sufficiently large MCS study..

3.1.7 Comparison of Probabilistic Power Flow Methods and Method Selection

MCS is one of several methodologies available for probabilistic power flow analysis. Alternative approaches include analytical methods (based on direct probability calculations) and approximate numerical methods such as point estimation techniques. Each approach has its own strengths and limitations, and the choice often depends on the specific needs (accuracy vs. efficiency) of the study. A brief comparison is given below, highlighting how MCS differs from these other methods [198]:

Analytical methods attempt to derive the output distributions of power flow variables through analytical computations rather than sampling. Early work on probabilistic load flow, dating back to Borkowska (1974) [199], adopted analytical techniques.

A common analytical approach is to assume a functional form (probability density function, PDF) for each random input and then use the power flow equations (often linearized) to derive the PDF of the outputs. This can involve convolution integrals (for combining independent random variables' distributions) or moment-based expansions (such as the cumulant method with Cornish–Fisher expansion to approximate the output distribution). Analytical methods are attractive because they can be computationally fast – instead of many iterative simulations, they solve the problem with a few mathematical operations or manipulations of distributions. However, they usually require strong assumptions or approximations. For example, one analytical technique called Stochastic Load Flow (SLF) assumes that the distribution of the output variables (e.g. bus voltages or line flows) is normal (Gaussian), to simplify calculations.

In practice, power flow outputs are not guaranteed to be normal, especially under large uncertainties or nonlinear operating conditions, and indeed this normality assumption has been shown to be unreliable in subsequent research.

More generally, analytical PLF methods often rely on linearizing the power flow equations (e.g. using a first-order Taylor series around an operating point) so that input uncertainties can be propagated through a linear mapping. This linearization can introduce errors if the system operates in a nonlinear region (for instance, if generator reactive power limits are hit, or voltage control devices switch states, etc.). Analytical methods also struggle with handling dependent (correlated) inputs and non-standard distributions; each new complexity requires a custom extension to the mathematical formulation. As a result, while analytical probabilistic load flow techniques can be very efficient for simplified or moderately uncertain systems, their accuracy may degrade when dealing with highly stochastic, nonlinear, or strongly correlated scenarios. The need for complicated mathematics to account for various grid realities is another drawback. In summary, analytical methods offer speed but at the possible cost of modelling fidelity, whereas MCS offers very high modelling fidelity but at the cost of computational effort.

PEM provides a compromise between full MCS and fully analytical solutions. In a point estimation method, one does not sample thousands of random scenarios; instead, one carefully selects a small number of representative scenarios, or points, and uses them to calculate approximate statistics of the output. In a 2PEM, for each random input variable, two deterministic values are chosen, often symmetrically around the mean, such as mean ± one standard deviation, appropriately weighted, so that these two points reproduce the input's mean and variance. By evaluating the power flow at these carefully chosen input levels and combining results in a weighted sum, one can estimate the mean and variance of the outputs without doing many simulations.

In general, a 2m-point estimation method requires exactly $2m$deterministic power flow evaluations for m uncertain input variables, while a 3PEM requires $3m$ evaluations. Therefore, the computational effort of PEM is explicitly determined by the number of input variables and remains relatively low even for moderately sized systems.

In contrast, the number of simulations required in MCS is not fixed and depends on the desired statistical accuracy and confidence level. According to statistical theory, the estimation error decreases proportionally to $1/\sqrt{N}$, where N is the number of samples. As a result, achieving higher accuracy requires a substantial increase in the number of simulations. In practical power system applications, this often leads to the use of thousands or even tens of thousands of power flow evaluations.

For example, for a system with 10 uncertain inputs, a 2PEM requires only 20 deterministic power flow solutions, whereas MCS may require 5,000–10,000 simulations to obtain statistically reliable results, depending on the required accuracy. This illustrates the fundamental trade-off between computational efficiency and statistical precision.

The strength of PEM lies in its computational efficiency and simplicity. It is much faster than MCS while often yielding accurate estimates of the output mean and variance that closely align with MCS results in many applications, particularly when the underlying relationships are not highly nonlinear. For many planning studies, getting the approximate mean and standard deviation of line flows and voltages may be sufficient, and point estimate methods can deliver that quickly.

However, the limitations of PEM should also be recognized. Because only a few points are used, PEM inherently cannot capture complex distribution shapes (e.g. multi-modal distributions or heavy tails) as well as a full distribution obtained from MCS. It typically provides good estimates for lower-order moments (mean, variance, perhaps skewness with 3PEM) but might miss nuances in the tails of the distribution. If one needs the full probability distribution or the exact probability of rare events, MCS is more reliable. Moreover, point estimate methods may need to be re-derived or adjusted for each new type of distribution or if input variables are correlated (some extensions exist for correlated variables, but they add complexity). In summary, point estimation methods are a valuable tool for fast probabilistic assessment, often used when MCS is too slow, but they serve as an approximation and may be used in conjunction with MCS for validation.

MCS's primary advantage is its accuracy and robustness when a large number of samplings is used. It will converge with the correct solution for any well-defined probabilistic power flow problem, regardless of complexity. It does not linearize equations or assume normality, so it captures the full nonlinear effects and any distribution shape of outputs. It is a universal approach – essentially, one can view it as numerically solving the multidimensional integral that defines the probabilistic power flow problem. Additionally, MCS is easy to implement using existing deterministic power flow tools: one can treat it as a black-box that repeatedly calls a power flow solver, making it straightforward to apply even on very complex system models (there is no need to derive new equations).

The main drawback of MCS is its computational inefficiency: it requires a very large number of power flow solutions to obtain results with high confidence. As noted earlier, the error decreases slowly with more sampling, which means getting even moderately tight confidence intervals on output statistics, one might need thousands of simulations. This can be "very time-consuming" and can challenge its practicality to use on large systems.

Each individual AC power flow solve might take only a fraction of a second, but thousands of them can add up to significant computation time, especially if the system is large (e.g., hundreds or thousands of buses) or if the power flow has difficulty converging for some of the random cases. In contrast, analytical methods (when applicable) can produce results almost instantaneously (since they involve direct calculations) but might sacrifice accuracy or require unrealistic assumptions.

Point estimation methods sit in between: they are much faster than MCS and typically more flexible than purely analytical formulas, but they are approximations whose accuracy must be verified case by case.

In practice, researchers often use a combination of methods. For example, a point estimate or analytical method might be used to get quick insights or for online applications, while MCS is run offline or as a benchmarking tool to validate the approximate method's results. MCS is also used when no reliable analytical solution exists (for instance, with many complicated uncertainty sources and constraints) or when one needs to evaluate a new control/protection scheme under uncertainty and it is easier to just simulate it many times. With improvements in computation speed and parallel processing, larger MCS-based PPF studies have become more tractable, but the method's high computational cost remains a consideration and has motivated a lot of research into accelerating techniques.

3.2 Distributed Generation Analysis and Modelling

3.2.1 Newton-Raphson Method in Polar Coordinates

The Newton-Raphson method in polar coordinates is an iterative technique that relies on successive linearization to solve power flow equations in electrical networks. This approach involves repeatedly formulating and solving correction equations, expressed in the following iterative format [200]:

$$\Delta X^{(k)} = -J^{-1}F(X^{(k)}) \tag{3.40}$$

$$X^{(k+1)} = X^{(k)} + \Delta X^{(k)} \tag{3.41}$$

Here, $F(X^{(k)})$ represents an n-dimensional vector of power mismatch functions at the k-th iteration, $X^{(k)}$ is the state vector comprising the system variables, $\Delta X^{(k)}$ is the correction vector, and J denotes the Jacobian matrix[201] .

When employing polar coordinates, the voltage at node i is expressed as:

$$V_i = |V_i| e^{j\theta_i} \tag{3.42}$$

Where $|V_i|$ is the voltage magnitude and θ_i is the voltage angle. The active and reactive power injections at node i are given by:

$$P_i = \sum_{j=1}^{n} |V_i||V_j|(G_{ij}\cos\theta_{ij} + B_{ij}\sin\theta_{ij}) \tag{3.43}$$

$$Q_i = \sum_{j=1}^{n} |V_i||V_j|(G_{ij}\sin\theta_{ij} - B_{ij}\cos\theta_{ij}) \tag{3.44}$$

Where $\theta_{ij} = \theta_i - \theta_j$ is the voltage angle difference between nodes i and j, $G_{ij} + jB_{ij} = Y_{ij}$ is the (i, j)-th element of the bus admittance matrix, and the summation extends over all n nodes in the system. Note that for j not directly connected to i, $Y_{ij} = 0$, effectively limiting the summation to nodes connected to i, including the self-term ($i = j$) [202].

For clarity, PQ nodes refer to load buses where both active power (P) and reactive power (Q) are specified. PV nodes denote generator buses where active power (P) and voltage magnitude (V) are specified, while reactive power (Q) is determined during the solution process. The slack bus (or reference bus) is a special node where both the voltage magnitude and phase angle are specified, and its active and reactive power outputs are adjusted to balance the overall system power mismatch.

where P and Q are the specified active and reactive power injections at node i, respectively. For PQ nodes, both P and Q are computed; for PV nodes, only P is considered since V is fixed and Q is unspecified; and for the slack bus, neither of its power injections is specified, as its output adjusts to balance the system.

The power mismatch equations are defined as:

$$\Delta P_i = P_i^{\text{spec}} - P_i \tag{3.45}$$

$$\Delta Q_i = Q_i^{\text{spec}} - Q_i \tag{3.46}$$

Where P_i^{spec} and Q_i^{spec} are the specified active and reactive power injections at node$i$, respectively. For PQ nodes, both ΔP_i and ΔQ_i are computed; for PV nodes, only ΔP_i is considered since $|V_i|$ is fixed and Q_i^{spec} is unspecified; and for the slack bus, neither its active nor reactive power injections are specified, no power mismatch can be calculated.

The correction equations are formulated as:

$$J\Delta X = -\Delta S \tag{3.47}$$

Where $\Delta S = [\Delta P^{\top}, \Delta Q^{\top}]^{\top}$ is the vector of power mismatches, and $\Delta X = [\Delta\theta^{\top}, \Delta|V|^{\top}]^{\top}$ contains the corrections to the voltage angles and magnitudes. Specifically:

For PQ nodes, ΔX includes both $\Delta\theta_i$ and $\Delta|V_i|$,

For PV nodes, ΔX includes only $\Delta\theta_i$,

For the slack bus, no corrections are applied as θ_i and $|V_i|$ are fixed.

The Jacobian matrix J comprises partial derivatives of the mismatch equations with respect to the state variables, defined as [203]:

$$\begin{cases} H_{ij} = \dfrac{\partial \Delta P_i}{\partial \theta_j} = -\dfrac{\partial P_i}{\partial \theta_j} \\ N_{ij} = \dfrac{\partial \Delta P_i}{\partial |V_j|} = -\dfrac{\partial P_i}{\partial |V_j|} \\ J_{ij} = \dfrac{\partial \Delta Q_i}{\partial \theta_j} = -\dfrac{\partial Q_i}{\partial \theta_j} \\ L_{ij} = \dfrac{\partial \Delta Q_i}{\partial |V_j|} = -\dfrac{\partial Q_i}{\partial |V_j|} \end{cases} \tag{3.48}$$

For $i \neq j$, these elements are non-zero only when node j is directly connected to node i through a line (i.e., $j \in \mathcal{N}_i$, where $\mathcal{N}_i$ denotes the set of nodes adjacent to i). The diagonal elements ($i = j$) incorporate contributions from all terms in the power equations involving θ_i or $|V_i|$.

Alternatively, aligning with standard power flow literature, the Jacobian can be defined without the negative signs:

$$J = \begin{bmatrix} \dfrac{\partial P}{\partial \theta} & \dfrac{\partial P}{\partial |V|} \\ \dfrac{\partial Q}{\partial \theta} & \dfrac{\partial Q}{\partial |V|} \end{bmatrix} \tag{3.49}$$

with the correction equation expressed as:

$$J \begin{bmatrix} \Delta \theta \\ \Delta |V| \end{bmatrix} = \begin{bmatrix} \Delta P \\ \Delta Q \end{bmatrix} \tag{3.50}$$

Both formulations are mathematically equivalent, as $\dfrac{\partial \Delta P_i}{\partial \theta_j} = -\dfrac{\partial P_i}{\partial \theta_j}$ and the sign adjustment is absorbed in the equation structure. The latter is adopted here for consistency with common practice.

- Computational Procedure

The computational steps for the Newton-Raphson power flow in polar coordinates are outlined as follows [204]:

1. Initialization: Set the iteration counter $k=0$ and assign initial values $|V_i^{(0)}|$ and $\theta_i^{(0)}$ for all nodes based on typical assumptions (e.g., flat start: $|V_i|=1.0\text{p.u.}$, $\theta_i=0^{\circ}$).

2. Calculate Power Mismatches: Using the current estimates $|V_i^{(k)}|$ and $\theta_i^{(k)}$, compute $P_i^{(k)}$ and $Q_i^{(k)}$ via the power equations, then determine the mismatches $\Delta P_i^{(k)}=P_i^{\text{spec}}-P_i^{(k)}$ and $\Delta Q_i^{(k)}=Q_i^{\text{spec}}-Q_i^{(k)}$ for PQ nodes, and $\Delta P_i^{(k)}$ for PV nodes.

3. Convergence Check: Evaluate the maximum absolute mismatches. If $\max|\Delta P_i^{(k)}|\le\epsilon$ and $\max|\Delta Q_i^{(k)}|\le\epsilon$ (where ϵ is a predefined tolerance, e.g., 10^{-4}p.u.), the iteration converges. Proceed to calculate line power flows and slack bus power, then output results. Otherwise, continue.

4. Compute Jacobian Elements: Calculate $H_{ij}^{(k)}$, $N_{ij}^{(k)}$, $J_{ij}^{(k)}$, and $L_{ij}^{(k)}$ (or equivalently, $\frac{\partial P_i}{\partial\theta_j}$, etc.) using the current voltage estimates.

5. Solve Correction Equations: Solve the linear system $J^{(k)}\Delta X^{(k)}=-\Delta S^{(k)}$ (or $J\Delta X=\Delta S$ in the standard form) to obtain $\Delta\theta_i^{(k)}$ and $\Delta|V_i|^{(k)}$.

6. Update Voltages: Adjust the state variables: $\theta_i^{(k+1)}=\theta_i^{(k)}+\Delta\theta_i^{(k)}$, $|V_i|^{(k+1)}=|V_i|^{(k)}+\Delta|V_i|^{(k)}$, for PQ nodes (both) and PV nodes ($\Delta\theta_i$ only).

7. Increment Counter: Set $k=k+1$ and return to step 2.

Upon convergence, compute the slack bus power to balance the system and determine the power flows across all lines using the final voltage solution.

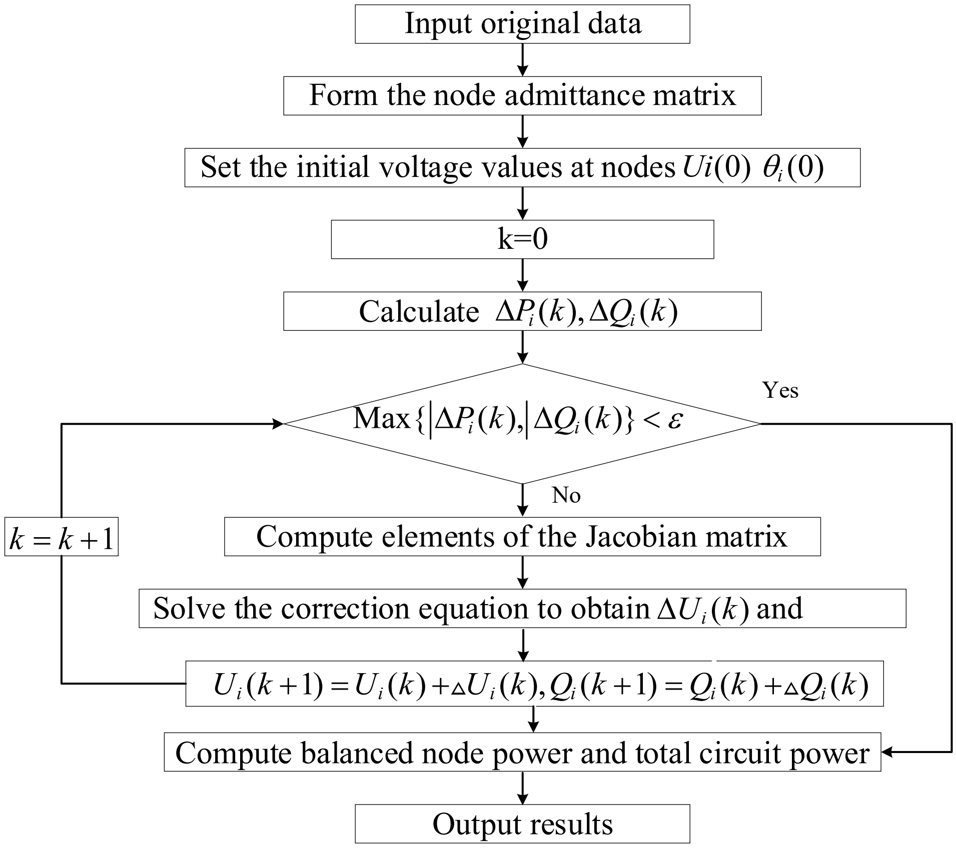

Figure 3-1 Flow Chart of Newton-Raphson Power Flow Calculation

3.2.2 Probabilistic Models of Uncertain Input Variables

3.2.2.1 Load Probability Model

Load fluctuations are influenced by a multitude of factors, none of which exert a singularly decisive impact. These fluctuations exhibit periodic and regular patterns, aligning with the characteristics of a normal distribution. The load is usually modelled as a random variable following a normal distribution. The probability density functions (PDFs) for the active power (P) and reactive power (Q) of the load are expressed as follows:

$$f(P) = \frac{1}{\sqrt{2\pi}\sigma_P} \exp\left(-\frac{(P-\mu_P)^2}{2\sigma_P^2} \right) \tag{3.51}$$

$$f(Q) = \frac{1}{\sqrt{2\pi}\sigma_Q} \exp\left(-\frac{(Q-\mu_Q)^2}{2\sigma_Q^2} \right) \tag{3.52}$$

Where μ_P and μ_Q represent the expected values (means) of the active power and reactive power, respectively, and σ_P and σ_Q denote their corresponding standard deviations. These parameters are derived from empirical data or system-specific characteristics, ensuring the model's applicability to the studied context [205].

3.2.2.2 Probability Model of Conventional Generators

To streamline computations and reduce model complexity, this study simplifies the operational states of conventional generators to two mutually exclusive conditions: normal operation and failure outage. Consequently, the probability model adheres to binomial distribution. The probabilities for the active power (P_G) and reactive power (Q_G) are defined as:

$$P(P_G = P_{G,\text{rated}}) = a_P, \quad P(P_G = 0) = 1 - a_P \tag{3.53}$$

$$P(Q_G = Q_{G,\text{rated}}) = a_Q, \quad P(Q_G = 0) = 1 - a_Q \tag{3.54}$$

Here, a_P and a_Q represent the availability rates (i.e., the probabilities of normal operation) for active power and reactive power, respectively, while $P_{G,\text{rated}}$ and $Q_{G,\text{rated}}$ denote the rated capacities under normal operating conditions. This binary simplification enhances computational efficiency while maintaining sufficient fidelity for the purposes of this analysis [206].

3.2.2.3 Probability Model of Photovoltaic Generation

By determining the probability distribution of solar radiation intensity, the PDFs for the power outputs of PV generation can be derived. Empirical evidence suggests that solar radiation intensity (r) follows a Beta distribution over a specified time interval, characterized by the following PDF:

$$f(r) = \frac{\Gamma(\alpha+\beta)}{\Gamma(\alpha)\Gamma(\beta)} \left(\frac{r}{r_{\max}} \right)^{\alpha-1} \left(1 - \frac{r}{r_{\max}} \right)^{\beta-1} \quad (0 \le r \le r_{\max}) \tag{3.55}$$

Where r is the solar radiation intensity ($\mathrm{W/m^2}$), $r_{\max}$ is the maximum solar radiation intensity, and α and β are the shape parameters of the Beta distribution, estimated from historical solar data. The Gamma function (Γ) ensures proper normalization of the distribution.

Given the linear relationship between PV output and solar radiation, the active power output (P_{PV}) for each PV generation unit is modeled as:

$$P_{\mathrm{PV}} = \mathrm{r}\eta Ar \tag{3.56}$$

Where η is the energy conversion efficiency, A is the effective area of each PV component, and r is the solar radiation intensity. This formulation assumes negligible reactive power output, consistent with typical PV system characteristics, unless otherwise specified by system design [207].

3.2.2.4 Probability Model of Wind Generation

The uncertainty of wind speed itself leads to a certain degree of randomness in the power output of the wind turbine. Therefore, in order to establish the wind turbine power output model, the first step is to obtain the probability distribution model of the wind speed, and the Weibull distribution function is the most widely recognized and used density function to describe the distribution of wind speed in a certain area.

$$f(v) = \frac{k}{\lambda}\left(\frac{v}{\lambda}\right)^{k-1} \exp\left(-\left(\frac{v}{\lambda}\right)^{k}\right) \quad (v \geq 0) \tag{3.57}$$

Where v is the wind speed (in $\mathrm{m/s}$), k is the dimensionless shape parameter, and λ is the scale parameter. These parameters can be related to the mean wind speed (μ_v) and standard deviation (σ_v) as follows:

$$\begin{cases} \mu_v = c\Gamma\left(1+\dfrac{1}{k}\right) \\ \sigma_v = c\sqrt{\Gamma\left(1+\dfrac{2}{k}\right)-\left[\Gamma\left(1+\dfrac{1}{k}\right)\right]^2} \end{cases} \tag{3.58}$$

Where Γ denotes the Gamma function, c is the scale parameter of the Weibull distribution, representing the characteristic wind speed level of the site, and k is the shape parameter that defines the spread and skewness of the distribution. These expressions facilitate parameter estimation from empirical wind speed statistics.

The active power output of a wind turbine (P_W) is predominantly governed by wind speed, with their relationship depicted in Figure 3-2. Under stable wind speed conditions, the power output is modeled as a piecewise function:

$$P_W = \begin{cases} 0 & \text{if } v < v_{\text{in}} \text{ or } v > v_{\text{out}} \\ P_{\text{rated}} \dfrac{v - v_{\text{in}}}{v_{\text{rated}} - v_{\text{in}}} & \text{if } v_{\text{in}} \le v < v_{\text{rated}} \\ P_{\text{rated}} & \text{if } v_{\text{rated}} \le v \le v_{\text{out}} \end{cases} \tag{3.59}$$

Where v_{in} and v_{out} are the cut-in and cut-out wind speeds, respectively, beyond which the turbine cannot operate effectively; v_{rated} is the rated wind speed; and P_{rated} is the rated power output. Figure 3-2 illustrates this relationship, highlighting the operational constraints of wind turbines [208].

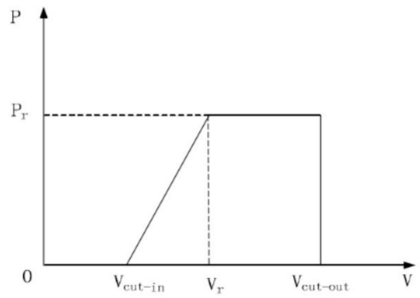

Figure 3-2 Wind Turbine Active Output Versus Wind Speed

3.2.3 Nataf Transformation and Its Inverse

3.2.3.1 Correlation Modelling

In power generation systems, light intensity, load demand, and wind speed exhibit inherent correlations due to shared environmental and operational factors. Compared to the Spearman rank correlation coefficient, the Kendall rank correlation coefficient more effectively captures the dependence structure between continuous random variables.

To model these dependencies, Copula functions are employed due to their flexibility in representing nonlinear and non-Gaussian correlations. In this study, a multi-dimensional Copula is used to describe the correlation between PV generation and load demand as a representative case. It should be noted that this formulation can be naturally extended to a multivariate Copula framework to capture multi-dimensional dependencies among multiple uncertain variables.

In addition to the PV–load correlation, correlations among loads at different nodes, between load and wind generation, and between PV and wind generation are also considered through a predefined correlation coefficient matrix. This matrix provides a unified representation of spatial and cross-source dependencies across the network.

The correlation coefficient matrix τ is defined as follows [209]:

$$\tau_{ij} = 4\left(\iint_{x_i,x_j\in(0,1)} C(X_i,X_j)d(x_i,x_j)\right)-1 \tag{3.60}$$

Where:

$\tau_{ij} > 0$ indicates a positive correlation between the two random variables,

$\tau_{ij} < 0$ indicates a negative correlation between the two random variables,

$\tau_{ij} = 0$ suggests that the two random variables are relatively independent,

X_i and X_j represent the original data samples of the i-th and j-th random variables, respectively,

x_i and x_j denote the transformed data of the i-th and j-th random variables mapped to the interval $[0,1]$,

$C(X_i,X_j)$ is the cumulative distribution function, specifically the t-Copula function, selected in this study for its ability to effectively capture tail dependence characteristics.

3.2.3.2 Nataf Inverse Transformation Process

The Nataf inverse transformation begins with the standardization of marginal distributions. Consider n random variables denoted as $\mathbf{X} = (X_1, X_2, \ldots, X_n)$, where each random variable X_i has a probability density function $f_i(x_i)$ and a cumulative distribution function $F_i(x_i)$. Using the marginal distribution functions, each random variable is transformed into a standard normal random vector $\mathbf{Y} = [Y_1, Y_2, \ldots, Y_n]$ via the following expression:

$$Y_i = \Phi^{-1}(F_i(X_i)) \tag{3.61}$$

Where $\Phi^{-1}(\cdot)$ is the inverse cumulative distribution function of the standard normal distribution.

Let ρ_0 and ρ represent the linear correlation coefficient matrices of $\mathbf{Y}$ and $\mathbf{X}$, respectively. The Kendall rank correlation coefficient matrix ρ between multiple PV systems and loads is computed using the multi-dimensional Copula distribution function. Due to the nonlinear nature of the transformation $\Phi^{-1}(\cdot)$, the elements ρ_{0ij} and ρ_{ij} (for $i \neq j$) in the corresponding positions of ρ_0 and ρ are generally unequal. According to the Nataf transformation, the relationship between ρ_{0ij} and ρ_{ij} is given by [210]:

$$\begin{aligned}\rho_{ij} &= \int_{-\infty}^{+\infty}\int_{-\infty}^{+\infty} \frac{x_i-\mu_i}{\sigma_i}\cdot\frac{x_j-\mu_j}{\sigma_j} F_{ij}(x_i,x_j)dx_i dx_j \\ &= \int_{-\infty}^{+\infty}\int_{-\infty}^{+\infty} \frac{F_i^{-1}(\Phi(y_i))-\mu_i}{\sigma_i}\cdot\frac{F_j^{-1}(\Phi(y_j))-\mu_j}{\sigma_j}\cdot\phi_2(y_i,y_j,\rho_{0ij})dy_i dy_j\end{aligned} \tag{3.62}$$

Where:

μ_i and μ_j are the means of the random variables X_i and X_j, respectively,

σ_i and σ_j are the standard deviations of X_i and X_j, respectively,

$\phi_2(y_i,y_j,\rho_{0ij})$ is the joint probability density function of the multi-dimensional standard normal random variables Y_i and Y_j, with correlation coefficient ρ_{0ij}.

The value of ρ_{0ij} can be determined through numerical integration combined with root-finding algorithms.

Typically, ρ_0 is a symmetric positive definite matrix, which permits Cholesky decomposition to yield a lower triangular matrix $\mathbf{B}$:

$$\rho_0 = \mathbf{B}\mathbf{B}^T \tag{3.63}$$

Where the superscript ^{T} denotes the matrix transpose.

Having obtained the lower triangular matrix $\mathbf{B}$, independent standard normal random variables $\mathbf{Z}$ can be generated as:

$$\mathbf{Y} = \mathbf{B}\mathbf{Z}$$

This process transforms the correlated random variables $\mathbf{X}$ into independent standard normal variables $\mathbf{Z}$, constituting the Nataf transformation. Conversely, the inverse of this process enables the generation of correlated random variables from independent standard normal variables, facilitating correlation modelling.

3.3 Harmonic Power Flow Calculation Modelling and Analysis

Harmonic power flow calculation is a cornerstone of harmonic analysis and control within power systems. This methodology enables the determination of harmonic voltages at each node and harmonic currents in each branch, providing critical insights into the presence of harmonic amplification or resonance. Such information is indispensable for devising effective harmonic mitigation strategies, ensuring system stability, and maintaining power quality.

Compared to fundamental power flow calculations, which focus on the sinusoidal steady-state operation at the fundamental frequency, harmonic power flow calculations are inherently more intricate. A primary source of this complexity lies in the modelling of harmonic sources—nonlinear devices such as power converters that inject harmonic currents into the system. The harmonic current produced by a source is a function not only of the fundamental voltage but also of every harmonic voltage present at its terminals. This interdependence introduces coupling between the fundamental power flow and harmonic power flows, as well as among harmonic flows of different orders.

In practical systems, harmonic sources vary widely in type, capacity, and operating conditions, rendering the construction of precise, individualized models impractical. Consequently, the development of accurate yet simplified harmonic source models is essential for effective harmonic analysis and control. To address this challenge, researchers have proposed various simplified models that balance fidelity with computational feasibility. Mathematically, harmonic power flow calculation entails solving a set of harmonic network equations—one for each harmonic order under consideration—alongside the characteristic equations governing all harmonic sources. This process demands a robust framework to capture the multifaceted interactions within the system [211].

3.3.1 Harmonic Power Flow Calculation Model

In power systems containing harmonic sources, the total power flow comprises both fundamental and harmonic components. Fundamental power flow originates from generators and is consumed by loads, following a well-defined path through the network. In contrast, harmonic power flow is generated by nonlinear devices, such as power conversion equipment, which produce non-sinusoidal currents. These harmonic sources effectively transform a portion of the fundamental power into harmonic power, which then propagates throughout the network, impacting generators, impedances, and loads alike.

To elucidate the propagation and directionality of harmonic power flow, consider the simplified circuit depicted in the Figure 3-3. Here, a generator G supplies a fundamental sinusoidal voltage to a resistive load R_{L1}, controlled by a converter, through a system impedance Z_{S1}. The equivalent circuits for fundamental and harmonic power flows are illustrated in Figure 3-3 (a) and Figure 3-3 (b), respectively.

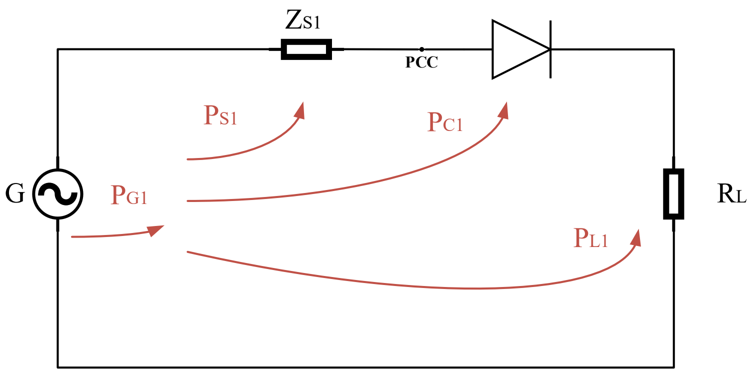

(a) Fundamental Power Flow

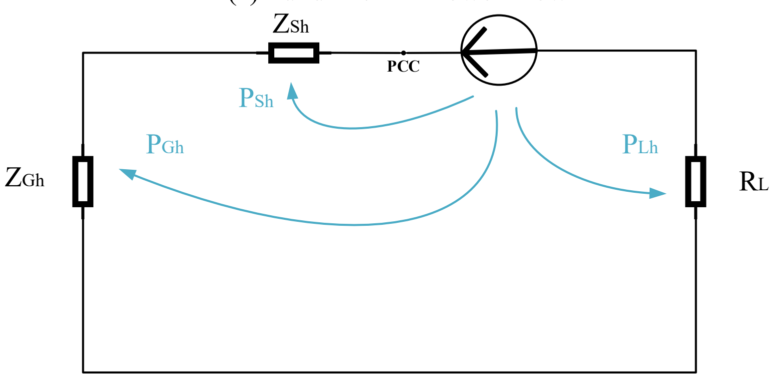

(b) Harmonic Power Flow

Figure 3-3 Fundamental and Harmonic Power Flow in the System

The fundamental and harmonic networks exhibit distinct characteristics, as highlighted in Figure 3-3. In the fundamental power flow (Figure 3-3 a), the generator G delivers power P_{G1}. A small fraction, P_{S1}, is dissipated across the system impedance Z_{S1}, while the remaining power reaches the point of common coupling (PCC). At the PCC, the majority of the power, P_{L1}, is consumed by the load, with a smaller portion, P_{C1}, absorbed by the converter. The power balance at the fundamental frequency is thus expressed as:

$$P_{G1} = P_{S1} + P_{L1} + P_{C1} \tag{3.64}$$

Due to the nonlinearity of the converter, the absorbed fundamental power P_{C1} is converted into harmonic power (assuming the power dissipated through conduction losses in the convertor power P_{C1} can be ignored). This harmonic power is injected into the network as a harmonic current source, flowing toward the system's impedance, the generator, and the load. These flows contribute to harmonic power components P_{Sh}, P_{Gh}, and P_{Lh}, respectively, satisfying the harmonic power balance:

$$P_{C1} = P_{Sh} + P_{Gh} + P_{Lh} \tag{3.65}$$

The total system power loss encompasses both the fundamental loss P_{S1} and the harmonic losses $(P_{Sh} + P_{Gh})$. This analysis underscores that harmonic power flow originates from the fundamental power flow through the action of nonlinear components. Harmonic sources do not generate power independently; rather, they redistribute a portion of the fundamental power into harmonic frequencies, integrating it into the overall system power flow. Consequently, harmonic power must be accounted for in the comprehensive power balance of the network to ensure an accurate representation of system behaviour.

In the fundamental network (Figure 3-3 a), the generator acts as a voltage source, and the converter behaves as a nonlinear load. Conversely, in the harmonic network (Figure 3-3 b), the generator functions as a harmonic impedance, while the converter operates as a harmonic current source. This role reversal results in differing flow directions for fundamental and harmonic power. Furthermore, the parameters of these networks—such as impedances are frequency-dependent, varying significantly between the fundamental frequency and higher harmonic orders. These differences amplify the analytical complexity, necessitating tailored approaches for each frequency component.

3.3.2 Review of Harmonic Source Models

To effectively characterize the harmonic currents produced by harmonic sources within power systems, it is imperative to develop suitable models that reflect their behaviour. Harmonic sources in power systems are broadly categorized into two distinct groups:

3.3.2.1 Power Electronic Devices

This category encompasses devices incorporating semiconductor-based nonlinear components, such as inverters and rectifiers. These devices function by switching circuits on and off in accordance with specific patterns, resulting in the injection of harmonic currents into the system. The harmonic currents generated can be precisely determined by considering factors such as the supply voltage waveform, the circuit structure, the device parameters, and the employed control methods.

3.3.2.2 Nonlinear Loads with Electric Arcs or Ferromagnetic Components

This category includes devices like transformers, electric arc furnaces, and fluorescent lamps, which exhibit nonlinear voltage-current characteristics due to the presence of electric arcs or ferromagnetic materials. During steady-state operation, the harmonic currents produced by these devices can be calculated based on the supply voltage waveform and the specific voltage-current properties of the load.

For both types of harmonic sources, the harmonic current generated can be mathematically expressed as a function of the node voltage (comprising both fundamental and harmonic components) and the load control parameters. This relationship is given by:

$$I_k = f_k(U_1, U_3, \ldots, U_n; C_1, C_2, \ldots, C_m) \qquad (k = 1, 3, 5, \ldots, n) \tag{3.66}$$

Where:

k denotes the harmonic order,

I_k represents the k-th harmonic current produced by the nonlinear load,

$U_1, U_3, \ldots, U_n$ are the fundamental and harmonic voltage components at the node of the nonlinear load,

$C_1, C_2, \ldots, C_m$ are the load control parameters, which vary by source type.

For power electronic devices, these parameters pertain to the circuit structure and control settings, such as the firing angle and overlap angle of a converter. For nonlinear loads with electric arcs or ferromagnetic components, they describe the voltage-current characteristics, such as the re-ignition voltage and extinction voltage of an electric arc.

In a more explicit form, the function $f_k(\cdot)$ may be interpreted as the Fourier coefficient of the nonlinear current waveform over one fundamental period, i.e.,

$$I_k = \frac{1}{T}\int_0^T i\left(t; U_1, U_3, \ldots, U_n, C_1, C_2, \ldots, C_m\right) e^{-jk\omega_0 t}\, dt \tag{3.67}$$

Where:

T is the fundamental period;

ω_0 is the fundamental angular frequency;

$i(t;\cdot)$ is the instantaneous nonlinear current response of the load, determined by the applied voltage waveform and the internal control or physical parameters of the device.

Thus, the k-th harmonic current is obtained by extracting the k-th Fourier component of the current waveform generated under the combined action of the fundamental and harmonic voltages and the device parameters.

Theoretically, this functional expression provides a precise model for harmonic sources. If all voltage waveforms and control parameters at the load node are fully known, the harmonic currents can be accurately computed using numerical methods. However, in practical power systems, several challenges arise. First, the wide diversity of harmonic source types makes it difficult to establish a universal analytical form of $f_k(\cdot)$. Second, comprehensive information on device operating conditions and internal parameters is often unavailable in real systems. Third, the nonlinear and device-specific nature of the current-generation mechanism makes the exact function difficult to derive explicitly, which limits its direct use in routine harmonic analysis.

As a result, obtaining a closed-form analytical expression is generally infeasible in practical applications. In steady-state analysis, it is therefore commonly assumed that the control parameters of harmonic source loads remain constant over the period of interest. Under this assumption, the harmonic current depends only on the nodal voltage waveform, and the model can be simplified to:

$$I_k = f_k(U_1, U_3, \ldots, U_n) \qquad (k = 1, 3, 5, \ldots, n) \tag{3.68}$$

Correspondingly, the simplified form may also be written as:

$$I_k = \frac{1}{T}\int_0^T i(t; U_1, U_3, \ldots, U_n)\, e^{-jk\omega_0 t}\, dt \tag{3.69}$$

Where the current waveform $i(t; U_1, U_3, \ldots, U_n)$is now determined only by the nodal voltage components, while the control parameters are treated as constants embedded in the function itself.

It indicates that, under steady-state conditions, the k-th harmonic current can be regarded as a voltage-dependent harmonic source. In other words, the injected harmonic current is no longer expressed as a function of time-varying control actions, but as a nonlinear function of the local voltage spectrum. This assumption significantly reduces modelling complexity and is widely adopted in harmonic power flow analysis.

Nevertheless, even in the simplified form, the exact functional relationship remains difficult to define explicitly for general nonlinear loads. Therefore, further simplifications are usually introduced in practice, leading to commonly used equivalent harmonic source models, such as constant current source models, voltage-controlled current source models, Norton equivalent models, and other linearized representations. These simplified models retain the essential dependence of harmonic current on the nodal voltage while providing more practical tools for harmonic analysis and numerical computation.

3.3.3 Simplified Harmonic Source Models

Harmonic power flow analysis necessitates the effective modelling of harmonic sources to predict harmonic currents and voltages in power systems. Due to the complexity involved in modeling diverse harmonic sources, simplified models are often employed to balance computational efficiency with the level of detail provided [212]. The following review examines four key simplified harmonic source models, detailing their mathematical formulations, underlying assumptions, respective strengths, and limitations. A comparative analysis is subsequently provided to evaluate their applicability and performance in practical scenarios.

3.3.3.1 Constant Current Source Model

The Constant Current Source Model is the simplest and most widely used approach in harmonic analysis. It assumes that the harmonic current I_k at order k depends solely on the fundamental voltage U_1 at the node, ignoring the influence of harmonic voltages. This simplifies the general harmonic source relationship to:

$$I_k = g_k(U_1) \tag{3.70}$$

If U_1 remains constant over the study period, I_k is treated as a fixed value, modelling the source as an ideal current source with infinite internal impedance. This assumption holds in systems with low harmonic distortion—common where passive or active filters reduce total harmonic distortion (THD) below regulatory limits. Here, harmonic voltages are significantly smaller than U_1, and their effect on I_k is negligible.

Strengths: Its simplicity and ease of implementation make it ideal for practical engineering applications where high accuracy is not critical.

Limitations: It overlooks harmonic voltage influences, reducing accuracy in systems with significant distortion.

3.3.3.2 Norton Model

The Norton Model enhances the Constant Current Source Model by accounting for the harmonic voltage U_k at the same order [213]. It represents the harmonic source as a parallel combination of a constant current source I_{k0} and a fixed impedance Z_k:

$$I_k = I_{k0} + \frac{U_k}{Z_k} \tag{3.71}$$

Here, I_{k0} is determined by U_1, making the harmonic current a function of both fundamental and same-order harmonic voltages:

$$I_k = g_k(U_1, U_k) \tag{3.72}$$

This model captures the interaction between I_k and U_k, offering a more refined representation than the Constant Current Source Model. However, it neglects the influence of harmonic voltages on other orders, despite evidence that such cross-order effects exist.

Strengths: It balances simplicity and improved accuracy, suitable when same-order voltage effects dominate.

Limitations: Its partial consideration of harmonic interactions limits its completeness.

3.3.3.3 Simplified Model Based on Cross-Frequency Admittance Matrix

This model assumes that the nonlinear characteristics of a harmonic source can be linearized around an operating point, expressing I_k as a linear combination of fundamental and harmonic voltages:

$$I_k = Y_{k1}U_1 + Y_{k3}U_3 + \ldots + Y_{kk}U_k + \ldots + Y_{kn}U_n \tag{3.73}$$

The cross-frequency admittance matrix Y captures couplings between harmonic orders. Its elements are derived experimentally [214]:

1. Apply a pure fundamental voltage U_1, measure I_k, and compute Y_{k1}.

2. Superimpose a harmonic voltage U_k with U_1 constant, measure the new I_k, and calculate:

$$Y_{kk} = \frac{I_k - Y_{k1}U_1}{U_k} \tag{3.74}$$

Strengths: It models the influence of multiple harmonic voltages, enhancing accuracy.

Limitations: Linearization lacks theoretical justification, and applying isolated harmonic voltages in practice is challenging, complicating implementation.

3.3.3.4 Simplified Model Based on Least Squares Approximation

This model expresses I_k 's real (I_{rk}) and imaginary (I_{ik}) components as functions of fundamental and harmonic voltages, plus a constant term [215]:

$$I_k = \begin{bmatrix} I_{rk} \\ I_{ik} \end{bmatrix} = \begin{bmatrix} a_{k0} + a_{k1}U_1 + \sum_{k=3}^{n}\left(a_{rkk}U_{rk} + a_{ikk}U_{ik}\right) \\ b_{k0} + b_{k1}U_1 + \sum_{k=3}^{n}\left(b_{rkk}U_{rk} + b_{ikk}U_{ik}\right) \end{bmatrix} \tag{3.75}$$

Where:

I_{rk} and I_{ik} are the real and imaginary components of the k -th harmonic current.

U_{rk} and U_{ik} are the real and imaginary components of the k -th harmonic voltage.

a_{k0}, b_{k0}, a_{k1}, b_{k1}, a_{rkk}, a_{ikk}, a_{ikk}, b_{rkk}, b_{ikk} are parameters that need to be determined based on multiple measurements in actual operation using the least squares method.

Strengths: It accounts for multiple voltage interactions and a constant component, offering high accuracy.

Limitations: Extensive measurements for parameter estimation make it complex and resource intensive.

Table 3-2 Comparative Evaluation of Harmonic Power Flow Models

Model	**Complexity**	**Accuracy**	**Practical Use**
Constant Current	Low	Low	High
Norton	Moderate	Medium	Medium
Cross-Frequency Matrix	High	High	Low
Least Squares	Very High	Very High	Low

These four simplified harmonic source models offer distinct approaches to balancing accuracy and practicality in harmonic analysis. The Constant Current Source Model excels in simplicity, the Norton Model adds moderate refinement, while the Cross-Frequency Admittance Matrix and Least Squares Approximation models provide greater detail at the cost of complexity. Understanding their assumptions and trade-offs enables informed model selection tailored to specific power system analysis needs.

3.3.4 Harmonic Network Equations

To perform harmonic power flow calculations in a power system, two essential steps must be completed:

(1) establishing accurate harmonic source models, as addressed in prior sections,

(2) determining the mathematical model of the harmonic network.

The harmonic network is typically represented by the harmonic node admittance matrix, denoted as $\mathbf{Y}_k$, which describes the interconnections of the k-th harmonic network and the harmonic admittance values of its branches. Mathematically, harmonic power flow calculations involve solving the harmonic network equation alongside the harmonic source characteristic equations. The harmonic network equation is expressed as:

$$\mathbf{I}_k = \mathbf{Y}_k \mathbf{U}_k \tag{3.76}$$

Where:

$\mathbf{I}_k$: Column vector of injected harmonic currents at each node for the k-th harmonic.

$\mathbf{Y}_k$: Harmonic admittance matrix of the system for the k-th harmonic.

$\mathbf{U}_k$: Column vector of harmonic voltages at each node for the k-th harmonic.

To formulate $\mathbf{Y}_k$, it is necessary to develop harmonic mathematical models for the relevant power system components, determine their parameters, and understand their interconnections.

Key Characteristics of Component Harmonic Models

The harmonic models of power system components exhibit several critical characteristics, summarized as follows [216]:

1. Frequency Dependence

Harmonic parameters vary with the harmonic order k, reflecting their dependence on frequency. This affects components such as lines, transformers, and loads.

2. Generator Representation

In harmonic studies, generators are no longer treated as voltage sources. Instead, they are typically modeled as harmonic impedances, which may be resistive, inductive, or capacitive depending on their construction and control schemes.

3. Skin Effect

The harmonic models for overhead lines, cable lines, transformers, and loads must incorporate the skin effect, which increases resistance at higher frequencies due to uneven current distribution.

4. Distributed Parameter Effects

For overhead and cable lines, long-line effects due to distributed parameters must be considered. These are accurately modeled using hyperbolic functions to derive the harmonic parameters of equivalent π-type circuits.

5. Shunt Capacitors and Resonance

Shunt capacitors can amplify harmonics or cause resonance phenomena. Thus, they must be explicitly included in the harmonic network model to capture their impact on harmonic behaviour.

These characteristics highlight the complexity of harmonic modelling. Proper consideration of frequency dependence, component-specific behaviours, and network interactions ensures that the harmonic admittance matrix $\mathbf{Y}_k$ accurately represents the system's response to harmonic currents. This precision is critical for reliable harmonic power flow calculations, enabling engineers to assess and mitigate harmonic distortions effectively.

3.3.5 Harmonic Power Flow Calculation Methods

Harmonic power flow analysis is a critical process for understanding how harmonics are distributed within a power system. This analysis helps assess harmonic distortion and develop strategies to mitigate its effects. Depending on how the fundamental power flow (at the system's base frequency) interacts with the harmonic power flow (at higher frequencies), four main calculation methods are widely recognized:

1. Unified Method

2. Alternating Iteration Method

3. Decoupled Method

4. Direct Solution Method

Below, each method is explained in detail, including its approach, steps, advantages, and limitations.

For clarity, the formulations presented here assume a single-phase equivalent model, which is standard for balanced systems or positive-sequence analysis in power flow studies. This simplification focuses on per-phase quantities (e.g., scalar voltage magnitudes $V_i$and angles θ_i) and is widely used when the system is approximately balanced or when computational efficiency is prioritized. However, these methods can be extended to full three-phase (e.g., ABC-phase) modeling, where each node voltage $\mathbf{V}_i$comprises three components (V_{iA}, V_{iB}, V_{iC}) with corresponding phase angles, to account for unbalances introduced by nonlinear loads or asymmetrical network elements. In such extensions, admittance matrices and injection vectors become 3x3 blocks per node, increasing dimensionality but capturing phase-specific interactions. The single-phase formulations below are adopted for expository purposes, with three-phase considerations noted where relevant (e.g., in the Alternating Iteration Method, where explicit three-phase steps are outlined).

3.3.5.1 Unified Method

The Unified Method, proposed by D. Xia and G. Heydt [217], adapts the Newton-Raphson (N-R) iterative technique—commonly used for fundamental power flow—to solve both fundamental and harmonic power flows simultaneously. It combines the fundamental power flow equations (power balance equations) and harmonic network equations (current balance equations) into a single system, solved iteratively using the N-R algorithm.

In the Unified Solution Method, the fundamental power flow equations are formulated as power balance equations, whereas the harmonic power flow equations for each harmonic order are expressed as current balance equations. The computational approach for this method is illustrated in Figure 3-4.

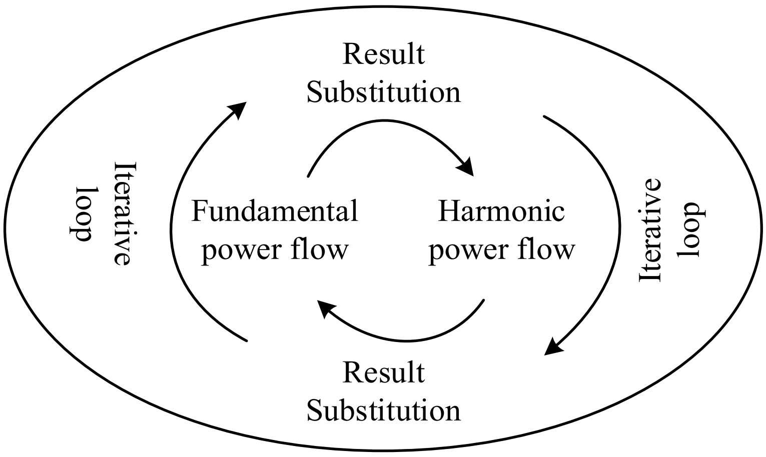

Figure 3-4 Schematic of the Unified Solution Method

For a power system comprising n nodes, where N denotes the number of linear nodes, the number of nonlinear nodes is given by $n-N$. To minimize algorithmic complexity, the nodes are numbered as follows: Node 1 is designated as the slack node, linear nodes are assigned numbers from 2 to N, and nonlinear nodes are numbered from $N+1$ to n. The unknowns in the harmonic power flow calculation consist of the magnitudes and phases of both the fundamental voltage and each harmonic voltage at all nodes.

Drawing from the node power balance equations for the fundamental power flow and the current balance equations for the harmonic power flow, the harmonic power flow equations can be represented as follows:

$$\begin{bmatrix} \Delta\mathbf{P} \\ \Delta\mathbf{Q} \\ \Delta\mathbf{I}_R^{(k)} \\ \Delta\mathbf{I}_I^{(k)} \end{bmatrix}^{(s)} = \begin{bmatrix} \mathbf{H} & \mathbf{0} \\ \mathbf{0} & \mathbf{J}^{(k)} \end{bmatrix} \begin{bmatrix} \Delta\boldsymbol{\theta} \\ \Delta\mathbf{V} \\ \Delta\boldsymbol{\theta}^{(k)} \\ \Delta\mathbf{V}^{(k)} \end{bmatrix}^{(s)} \tag{3.77}$$

Where:

$\Delta\mathbf{P}$ and $\Delta\mathbf{Q}$ are vectors representing the deviations in active and reactive power at the nodes, encompassing the total power contributions from both the fundamental and harmonic components. Specifically, $\Delta P_i = P_i - P_{i,\text{calc}}$ and $\Delta Q_i = Q_i - Q_{i,\text{calc}}$, where P_i and Q_i are the measured active and reactive power at node i, and $P_{i,\text{calc}}$ and $Q_{i,\text{calc}}$ are the corresponding calculated values derived from the node power equations.

$\Delta\mathbf{I}_R^{(k)}$ and $\Delta\mathbf{I}_I^{(k)}$ are vectors representing the deviations in the real and imaginary parts of the k-th harmonic injection currents at the nonlinear nodes. Specifically, $\Delta I_{R,t}^{(k)} = I_{R,t}^{(k)} - I_{R,t,\text{calc}}^{(k)}$ and $\Delta I_{I,t}^{(k)} = I_{I,t}^{(k)} - I_{I,t,\text{calc}}^{(k)}$, where $I_{R,t}^{(k)}$ and $I_{I,t}^{(k)}$ denote the real and imaginary parts of the k-th harmonic injection current at nonlinear node t.

$\Delta\boldsymbol{\theta}$ and $\Delta\mathbf{V}$ are vectors of corrections for the fundamental voltage angles and magnitudes, respectively.

$\Delta\boldsymbol{\theta}^{(k)}$ and $\Delta\mathbf{V}^{(k)}$ are vectors of corrections for the k-th harmonic voltage angles and magnitudes, respectively.

$\mathbf{H}$ is the Jacobian matrix associated with the fundamental power flow equations in the Newton-Raphson method.

$\mathbf{J}^{(k)}$ is the Jacobian matrix for the k-th harmonic power flow equations, applicable only to the nonlinear nodes, comprising partial derivatives of the harmonic injection currents with respect to the harmonic voltage angles and magnitudes.

In all equations, $k = 1, 2, \ldots, K$, where K represents the highest harmonic order under consideration.

This mathematical formulation facilitates the simultaneous solution of the fundamental and harmonic power flows through an iterative process, typically employing the Newton-Raphson method. Iterations proceed until the power and current mismatches are reduced to within acceptable tolerance levels.

The Unified Solution Method is characterised by its ability to solve the fundamental and harmonic power flow equations simultaneously within each iteration. In this approach, all equations are integrated into a single system, allowing both fundamental and harmonic variables to be updated concurrently until convergence is achieved. This unified framework enables a consistent treatment of interactions between fundamental and harmonic components, which can improve modelling accuracy in systems with strong coupling effects.

However, this method also presents several challenges. The integration of both fundamental and harmonic equations significantly increases the size of the system matrix, leading to higher computational demand in terms of memory and processing time. As a result, the method may experience slower convergence or even divergence, particularly in large-scale systems. In addition, numerical instability can arise due to the substantial difference in magnitude between fundamental and harmonic quantities. Since harmonic components are typically much smaller than their fundamental counterparts, even minor variations in fundamental voltages can lead to disproportionately large changes in harmonic currents, thereby affecting convergence behaviour.

Due to these limitations, the Unified Solution Method is generally more suitable for small-scale systems or research-oriented studies, where computational resources and convergence issues are less restrictive. Its application in large practical power systems is often limited by its computational intensity and potential instability.

3.3.5.2 Alternating Iteration Method

The Alternating Iteration Method tackles the coupling between fundamental and harmonic power flows by solving them alternately in an iterative loop, reducing complexity compared to the Unified Method.

The basic concept of the alternating solution method is based on a sequential and iterative procedure that decouples the fundamental and harmonic power flow calculations. Initially, the fundamental power flow is solved under the assumption that no harmonic voltages are present, providing an initial estimate of the system’s fundamental voltage profile.

Based on this solution, the harmonic power flow is then calculated using the obtained fundamental voltages, allowing the corresponding harmonic voltages to be determined. These harmonic results are subsequently fed back into the fundamental power flow calculation, where the influence of harmonic distortion on the fundamental operating point is considered.

This process is repeated iteratively, with fundamental and harmonic solutions being updated in an alternating manner, until convergence is achieved for both components.

This process is repeated iteratively, with fundamental and harmonic solutions being updated in an alternating manner, until convergence is achieved for both components, as illustrated in Figure 3-5.

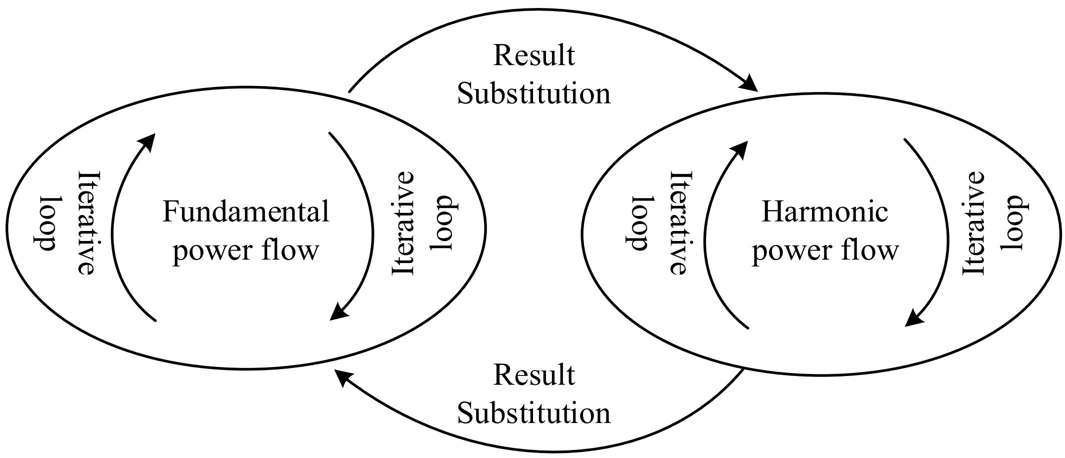

Figure 3-5 Schematic of the Alternating Iteration Method

Three-Phase Fundamental Power Flow Calculation

The three-phase fundamental power flow is calculated using the PQ decomposition method, an iterative technique. The computational steps are as follows:

Step 1: Construct the three-phase fundamental admittance matrix and generate the factor table for efficient matrix operations.

Step 2: Assign initial values to the node voltages.

Step 3: Compute the active power mismatch ΔP and the normalized active power mismatch ΔP/ V for each node, where V represents the voltage magnitude.

Step 4: Evaluate whether the active power iteration has converged. If not, proceed to the next iteration; if converged, advance to **Step 7**.

Step 5: Solve the correction equation to determine the voltage angle corrections for each node and update the voltage angles accordingly. The correction equation is expressed as:

$$\begin{bmatrix} \dfrac{\Delta P_1}{V_1} \\ \dfrac{\Delta P_2}{V_2} \\ \vdots \\ \dfrac{\Delta P_{n-1}}{V_{n-1}} \end{bmatrix} = -\begin{bmatrix} B_{11} & B_{12} & \cdots & B_{1,n-1} \\ B_{21} & B_{22} & \cdots & B_{2,n-1} \\ \vdots & \vdots & \ddots & \vdots \\ B_{n-1,1} & B_{n-1,2} & \cdots & B_{n-1,n-1} \end{bmatrix} \begin{bmatrix} V_1 \Delta\delta_1 \\ V_2 \Delta\delta_2 \\ \vdots \\ V_{n-1}\Delta\delta_{n-1} \end{bmatrix} \tag{3.78}$$

Where

n is the number of system nodes;

B represent the corresponding element of the Jacobian matrix, simplified as the element of the admittance matrix;

V_i denote the voltage magnitude at each node;

$\Delta\delta_i$ denote the phase angle deviation of the node voltages.

Step 6: Adjust the voltage angles of each node based on the computed corrections $\delta_i^{(k+1)} = \delta_i^{(k)} + \Delta\delta_i^{(k)}$.

Step 7: Calculate the reactive power mismatch ΔQ and the normalized reactive power mismatch ΔQ/V for each node.

Step 8: Assess whether the reactive power iteration has converged. If not, continue to the next iteration; if converged, proceed to **Step 10**.

Step 9: Solve the reactive power correction equation to obtain the voltage magnitude corrections for each node and update the voltage magnitudes. The correction equation is given by:

$$\begin{bmatrix} \frac{\Delta Q_1}{V_1} \\ \frac{\Delta Q_2}{V_2} \\ \vdots \\ \frac{\Delta Q_m}{V_m} \end{bmatrix} = -\begin{bmatrix} B_{11} & B_{12} & \cdots & B_{1,m} \\ B_{21} & B_{22} & \cdots & B_{2,m} \\ \vdots & \vdots & \ddots & \vdots \\ B_{m,1} & B_{m,2} & \cdots & B_{m,m} \end{bmatrix} \begin{bmatrix} \Delta V_1 \\ \Delta V_2 \\ \vdots \\ \Delta V_m \end{bmatrix} \tag{3.79}$$

Where:

m be the number of PQ buses;

$\Delta \mathbf{V}$ denote the voltage deviation vector to be solved.

Step 10: Determine the updated voltage magnitudes for each node.

Step 11: Compute the branch power flows and the power at the slack node.

The iterative steps for calculating the three-phase harmonic power flow are outlined below:

Step 1: Form the admittance matrices for each harmonic order and create the corresponding factor tables.

Step 2: Calculate the harmonic injection currents for each load node using the following expression:

$$I_L^{(k)} = f\left(V^{(k)}\right) \tag{3.80}$$

Where $I_L^{(k)}$ denotes the k-th harmonic current injected into the system by the load, and $V^{(k)}$ is the k-th harmonic voltage at the load node.

Step 3: Solve the node voltage equation to determine the k -th harmonic voltages at each node:

$$\mathbf{V}^{(k)} = \left[\mathbf{Y}^{(k)}\right]^{-1} \mathbf{I}^{(k)} \tag{3.81}$$

Where $\mathbf{V}^{(k)}$ is the vector of k -th harmonic node voltages, $\mathbf{Y}^{(k)}$ is the k -th harmonic admittance matrix, and $\mathbf{I}^{(k)}$ is the vector of k -th harmonic injection currents.

Step 4: Check if the accuracy requirements are satisfied. If met, terminate the iteration; otherwise, return to **Step 2**.

Step 5: Calculate the harmonic currents in each branch.

The alternating iteration method offers several advantages in terms of accuracy, efficiency, and numerical stability. In terms of accuracy, it is capable of capturing the coupling effects between fundamental and harmonic components through the use of precise harmonic source models. From a computational perspective, the method improves efficiency by separating the fundamental and harmonic calculations within each iteration, thereby reducing memory requirements and overall computational burden.

In addition, the method exhibits strong numerical stability. Since the fundamental voltages, which dominate the behaviour of harmonic currents, are solved first, the iterative process typically converges rapidly, often within one to three iterations.

Due to these characteristics, the alternating iteration method is particularly suitable for unbalanced three-phase systems with strong coupling effects, such as distribution networks with nonlinear loads. The extension to three-phase modelling further ensures accurate representation of phase unbalance in practical applications.

3.3.5.3 Decoupled Method

The Decoupled Method simplifies the Alternating Iteration Method by fully separating fundamental and harmonic power flow calculations. It assumes that while fundamental power flow strongly affects harmonics, the reverse effect is negligible, thus ignoring harmonic impacts on the fundamental solution [218]. Unlike the Alternating Iteration Method, which includes a feedback loop to update the fundamental with harmonic effects, the Decoupled Method solves the fundamental power flow only once (ignoring harmonics), then iteratively solves the harmonic power flow using the fixed fundamental voltages. This eliminates alternation, making it truly "decoupled" without bidirectional iteration, as illustrated in Figure 3-6.

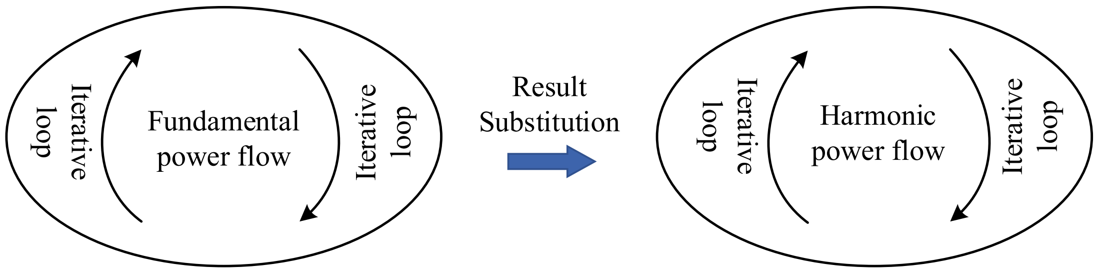

Figure 3-6 Schematic of the Decoupled Method

Step 1: Initialize Fundamental Voltage: Set $U_1 = 1.0\angle 0^{\circ}$.

Step 2: Fundamental Power Flow:

Use given injected power for linear load nodes.

For harmonic source nodes, compute fundamental power: $I_1 = g_1(U_1)$, $S = U_1 I_1^*$, updating injected power as U_1 changes in N-R iterations.

Step 3: Initialize Harmonic Voltages: Set $U_3 = U_5 = \ldots = U_n = 0.0\angle 0^{\circ}$.

Step 4: Harmonic Currents: Compute I_k using the harmonic source model.

Step 5: Harmonic Voltages: Solve $I_k = Y_k U_k$.

Step 6: Convergence: Check harmonic solution; repeat from Step 4 if needed.

The Decoupled Method exhibits moderate performance in terms of accuracy, convergence, efficiency, and applicability. Its accuracy is generally lower than that of the Alternating Iteration Method, as it neglects the feedback effect of harmonic components on the fundamental power flow. However, the method demonstrates strong convergence characteristics, owing to its simplified structure and the absence of bidirectional coupling between fundamental and harmonic calculations.

From a computational perspective, the Decoupled Method is relatively efficient and is well suited for medium-sized systems with moderate computational requirements. Nevertheless, its effectiveness depends on the availability and accuracy of harmonic source models, which may limit its applicability in cases where such data are incomplete or uncertain. Overall, the method is most appropriate for systems in which the influence of harmonic components on the fundamental power flow is minimal.

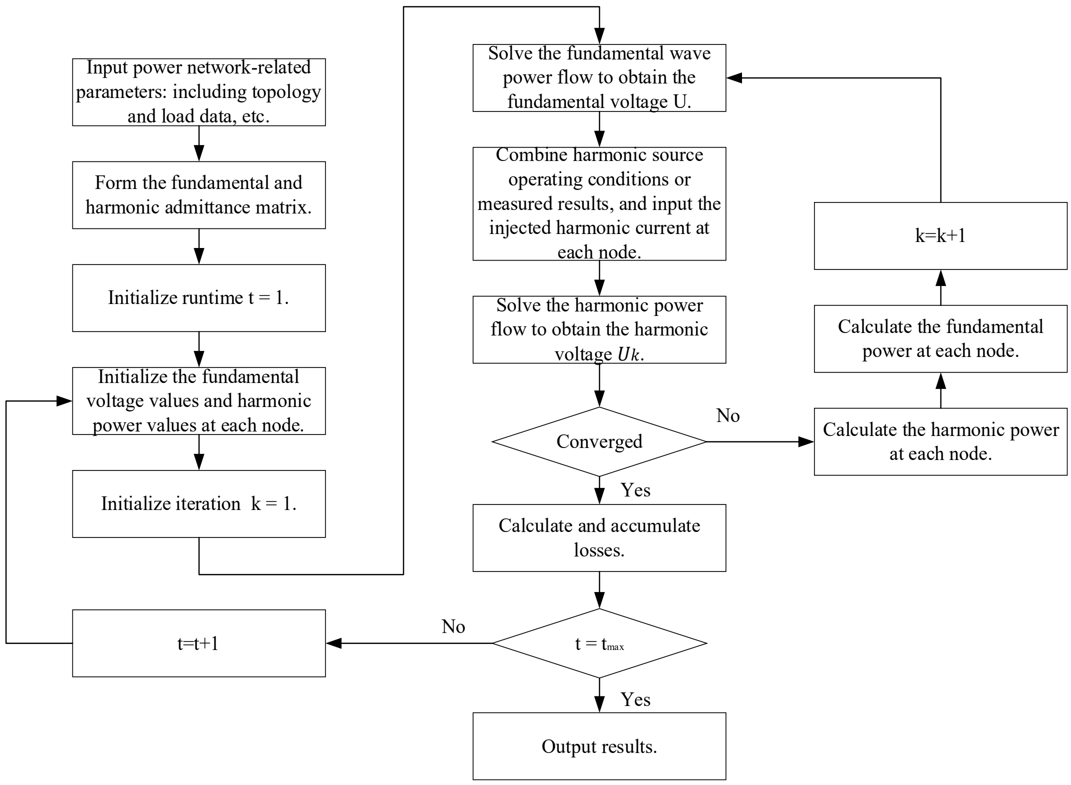

Figure 3-7 Flowchart of the Decoupled Method for Harmonic Power Flow Calculation

The Figure 3-7 illustrates the Decoupled Method, where the fundamental power flow is solved once without harmonic feedback, followed by iterative harmonic calculations. The outer loop (t) represents multiple operating scenarios, not bidirectional coupling (distinguishing it from the Alternating Iteration Method). Formulations are shown in single-phase equivalent for simplicity; extendable to three-phase (ABC) with vectorized voltages.

While both separate fundamental and harmonic computations, the alternating method iterates bidirectionally (updating fundamental with harmonics), capturing stronger couplings at the cost of more iterations. The decoupled method avoids this feedback, assuming negligible harmonic influence on fundamental, leading to faster but potentially less accurate results in highly coupled systems.

3.3.5.4 Direct Solution Method

The Direct Solution Method is a further simplification of the iterative harmonic power flow component within the Decoupling Method.

It relies on two key matrices:

- **BIBC** (Bus Injection to Branch Current)
- **BCBV** (Branch Current to Bus Voltage)

The primary concept involves utilizing the topology and line impedances of the distribution network to construct the BIBC and BCBV matrices. Specifically, the BIBC matrix, combined with the harmonic currents injected at load nodes, is used to compute the harmonic currents in the network branches. These branch harmonic currents, along with the BCBV matrix, are then used to determine the voltage differences between the harmonic voltages at the nodes and the source node, ultimately yielding the node harmonic voltages with ensured precision. This algorithm offers fast computation speed, reduced time consumption, and low memory usage. Moreover, the BIBC and BCBV matrices can be modified to accommodate distribution systems with unbalanced three-phase loads and looped configurations [219].

1) Solution of Incidence Matrices

In the calculation process, it is first necessary to convert the equivalent injected power at the nodes into equivalent injected currents, as expressed by the following formula:

$$I_i^{k+1} = \left(\frac{S_i}{V_i^k}\right)^* = \left(\frac{P_i + jQ_i}{V_i^k}\right)^* \tag{3.82}$$

Where:

$I_i^{(k+1)}$ is the injected current at node i required for the $(k+1)$-th iteration,

S_i is the injected power at node i,

$V_i^{(k)}$ is the voltage at node i obtained from the k-th iteration,

$*$ denotes the complex conjugation.

(a) Formation of the BIBC Matrix

For a distribution network with m branches and n nodes, the BIBC matrix has dimensions $m \times (n-1)$. The formation procedure is as follows:

1. If branch k connects nodes i and j:

- Copy the column in the BIBC matrix corresponding to node i to the column corresponding to node j.
- Set the element in row k and the column corresponding to node j to 1.

2. Repeat the above steps for all branches until the BIBC matrix encompasses the entire network.

The relationship between branch currents and node injected currents can be expressed in matrix form as:

$$\begin{bmatrix} B_1 \\ B_2 \\ \vdots \\ B_{n-1} \end{bmatrix} = \left[BIBC\right] \begin{bmatrix} I_2 \\ I_3 \\ \vdots \\ I_n \end{bmatrix} \tag{3.83}$$

Where:

B is the branch current vector,

I is the node injected current vector,

BIBC is the node injection to branch current incidence matrix, an upper triangular matrix containing only 0 and 1.

(b) Formation of the BCBV Matrix

For the same distribution network, the BCBV matrix has dimensions $(n-1) \times m$. The formation procedure is as follows:

1. If branch k connects nodes i and j:

- Copy the row in the BCBV matrix corresponding to node i to the row corresponding to node j.
- Set the element in the row corresponding to node j and column k to the branch impedance Z_k.

2. Repeat the above steps for all branches until the BCBV matrix encompasses the

entire network.

The relationship between node voltages and branch currents can be expressed in matrix form as:

$$\Delta V=\begin{bmatrix} V_1 \\ V_1 \\ \vdots \\ V_1 \end{bmatrix}-\begin{bmatrix} V_2 \\ V_3 \\ \vdots \\ V_n \end{bmatrix}=\left[BCBV\right]\begin{bmatrix} B_1 \\ B_2 \\ \vdots \\ B_{n-1} \end{bmatrix} \tag{3.84}$$

Where:

ΔV is the vector of voltage differences between the nodes and the source node,

2) Power Flow Calculation Algorithm Procedure

The steps of the power flow calculation algorithm are as follows:

a) Input Data: Enter the relevant data for the distribution network, including line topology and parameters, load powers, and parameters of harmonic sources required for harmonic power flow calculation.

b) Matrix Formation: Construct the incidence matrices BIBC and BCBV, as well as the sensitivity matrix M . Initialize the node voltages $V^{(0)}$ under fundamental frequency and the injected powers S_i^0 for PQ nodes. Set the slack bus voltage $V_1^{SP}=1.0\angle 0^{\circ}$ for the fundamental power flow.

In this study, the sensitivity matrix M represents the linear relationship between nodal current injections and voltage variations in the distribution network. It is derived based on the network topology and line impedance parameters, and can be expressed as: $\Delta V = M\,\Delta I$, where ΔV is the vector of nodal voltage variations and $\Delta I$is the vector of nodal current injections.

For radial distribution networks, the matrix M is typically constructed using the Bus Injection to Branch Current (BIBC) matrix and the Branch Current to Bus Voltage (BCBV) matrix, such that: $M = BCBV \times BIBC$. The sensitivity matrix M is used to efficiently update nodal voltages during the iterative power flow calculation, avoiding repeated solution of nonlinear equations and thereby improving computational efficiency.

c) Parameter Setting: Define the injected active power, reactive power, or injected currents for PV nodes and PQ nodes. Set the iteration precision ϵ and initialize the iteration counter $k=1$.

d) Iterative Calculation: Compute the I^k, ΔV^{k+1} and V^{k+1} for each node.

e) Convergence Check: Verify if the iteration has converged by checking if the maximum voltage deviation satisfies $\max\{V^{k+1}-V^k\}<\varepsilon$. If convergence is achieved, terminate the iteration; otherwise, update the node voltages $V^{k+1}=V^{SP}-\Delta V^{k+1}$, adjust the Q^{k+1} and I^{k+1} based on the node type models, increment the iteration counter $k=k+1$, and return to step d) to continue the iteration.

f) Output Results: Upon completion of the calculation, output the voltages at each node.

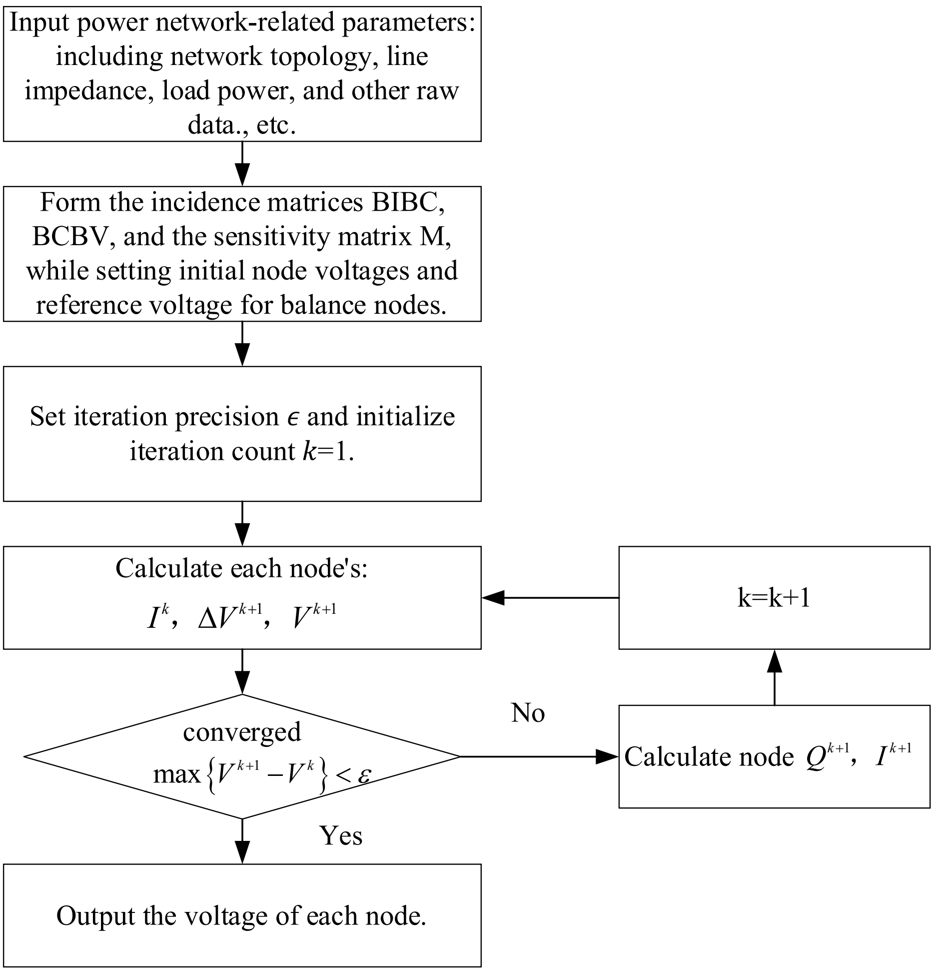

Figure 3-8 Flowchart of Direct Solution Method Based on BIBC and BCBV

As illustrated in Figure 3-8, the direct solution method based on the BIBC and BCBV matrices follows a systematic iterative process for power flow computation.

The method offers several advantages. It is simple to implement and computationally efficient, as the use of linear equations eliminates the need for iterative procedures and avoids convergence issues. In addition, it is widely applied in practice due to its ability to provide sufficiently accurate results for many engineering cases.

However, certain limitations should also be noted. The accuracy of the method may be reduced because it neglects the influence of harmonic voltages on harmonic currents.

In terms of applicability, this approach is particularly suitable for large-scale systems or situations where detailed harmonic source data is limited.

Table 3-3 Comparative Evaluation of Methods

Method	Pros	Cons	Best For
Unified Method	Precise, theoretically sound	High computational load, unstable in large systems	Small-scale or academic studies
Alternating Iteration Method	Accurate, stable, efficient	Needs detailed harmonic source models	Systems with significant coupling
Decoupled Method	Stable, moderately efficient	Less accurate, model-dependent	Medium-sized systems
Direct Solution Method	Fast, simple, no convergence issues	Slightly less accurate	Large systems and practical engineering

Common Challenge: All methods use the harmonic admittance matrix Y_k, which grows large in extensive networks, straining memory and computation. Even the Direct Solution Method faces efficiency issues in very large systems, highlighting the need for advanced optimization techniques.

Selecting a harmonic power flow method depends on system size, data availability, and accuracy needs. The Unified Method excels in precision but falters in large systems. The Alternating Iteration Method offers a strong balance of accuracy and efficiency. The Decoupled Method simplifies calculations with good stability, while the Direct Solution Method prioritizes speed and practicality, making it the most common choice in engineering. As power systems evolve, improving computational efficiency will remain key to managing harmonics effectively.

The choice of harmonic power flow method depends on several key factors, including the size of the system under study, the required level of accuracy, and the availability of harmonic source models. Larger systems typically require more computationally efficient methods, while higher accuracy requirements may necessitate more detailed or computationally intensive approaches. In addition, the selection of an appropriate method is influenced by whether accurate and sufficient harmonic source models are available, as these directly affect the reliability of the analysis.

3.4 Power System Risk Assessment

3.4.1 Basic Principles of Risk Theory

The concept of "risk" has evolved alongside societal progress and found application across a wide range of scientific disciplines. From the perspective of uncertainty, while the loss resulting from a risk event is certain should the event occur, the occurrence of that event remains uncertain. From the perspective of loss, risk constitutes an evaluation of the magnitude of potential damage to an entity. Within the domain of power systems, risk is defined as a comprehensive measure that integrates two key dimensions: the uncertainty of loss and the consequences of that loss. This dual nature implies that for events with identical probabilities of occurrence, the resulting impacts may differ, leading to varying risk levels. Conversely, for events producing equivalent impacts, differences in their probabilities of occurrence similarly yield distinct risk profiles.

Risk is formally defined as the possibility of disasters capable of causing harm, coupled with the severity of that harm. Risk assessment entails a systematic process that employs a series of logical steps, enabling designers and safety engineers to methodically evaluate potential disasters arising from equipment use. This structured approach supports the identification and implementation of appropriate safety measures. To facilitate this evaluation, risk indicators are employed to quantitatively capture the factors that determine risk levels—namely, the likelihood of an accident and the severity of its consequences. These indicators provide a holistic representation of an accident's impact on the entire power system. Commonly, risk is quantified as the product of the probability of an accident and the magnitude of its consequences, offering a standardized metric for risk analysis.

A key advantage of risk theory lies in its applicability to individual safety concerns, accidents, or system components. Models constructed based on risk theory exhibit a clear parallel structure, allowing for flexibility in analysis. This structure permits the aggregation of risk assessments for individual components or accidents into a comprehensive evaluation of the system as a whole. Alternatively, it enables the decomposition of an overall system risk assessment into constituent analyses of specific components or incidents. Such a framework is particularly conducive to parallel computation, significantly enhancing the efficiency and speed of the risk assessment process [220].

3.4.2 Risk Calculation Methods

3.4.2.1 State Enumeration Method [221]

The state enumeration method involves systematically analyzing and calculating risk indicators by evaluating each possible failure state of the components within a selected set. As the number of components in the system increases, the number of potential system states grows exponentially. For systems with a large number of electrical components, exhaustively enumerating all operational states using current computational technology is challenging to achieve. Consequently, a common practice is to truncate the enumeration process at a specified level, typically defined by the order of failures, such as second- or third-order failures.

Based on the two-state component failure model, each component can exist in one of two states: operational or failed. Let p_i and q_i represent the probabilities of the i -th component being operational and failed, respectively. The following expansion holds:

$$(p_1+q_1)(p_2+q_2)\cdots(p_n+q_n)=1 \tag{3.85}$$

The probability of a specific system state s is determined by:

$$p_s=\prod_{i=1}^{N_f} q_i \prod_{j=1}^{N_w} p_j \tag{3.86}$$

Where N_f and N_w denote the number of failed and operational components in state s, respectively, and s may represent either an operational or failed system state.

The frequency of occurrence f_s and duration d_s of system state s are expressed as:

$$f_s=p_s\sum_{k=1}^{n}\lambda_k \tag{3.87}$$

$$d_s=\frac{p_s}{f_s} \tag{3.88}$$

Where λ_k is the transition rate of component k from the current state s. If the component is operational, λ_k denotes the failure rate; if it is failed, λ_k denotes the repair rate. Here, n is the total number of components.

The expected value of the indicator function for all system failure states is calculated as:

$$E[C]=\sum_{s\in F} C(s)p_s \tag{3.89}$$

Where $C(s)$ is the indicator function for failure state s, and F is the set of all failure states.

3.4.2.2 Monte Carlo Simulation Method

1. Non-Sequential Monte Carlo Simulation

The non-sequential MCS method, also known as the state sampling method, determines the state of each component by sampling from its respective probability distribution. For each component, a random number u_i, uniformly distributed between 0 and 1, is generated. Assuming each component has two states—failed and operational—the state s_i of component i is assigned as follows [222]:

$$s_i = \begin{cases} 0 & \text{if } 0 \le u_i < q_i \\ 1 & \text{if } q_i \le u_i \le 1 \end{cases} \tag{3.90}$$

Where 0 represents the failed state, 1 represents the operational state, and q_i is the failure probability of component i.

When the number of samples is sufficiently large, the frequency of a particular state s in the samples serves as an unbiased estimate of its probability:

$$p_s \approx \frac{N_s}{N} \tag{3.91}$$

Where N is the total number of samples, and N_s is the number of occurrences of state s in the samples.

Ensuring the precision of the MCS method depends on appropriate convergence criteria. The coefficient of variation is commonly employed as a stopping criterion, although an alternative approach is to predefine a maximum number of samples to terminate the sampling process.

2. Sequential Monte Carlo Simulation

The sequential MCS simulation method involves randomly simulating the system's operational states over a specified time period. Among various approaches, the state duration sampling method is the most commonly used. This method samples the duration a component remains in a particular state based on its probability distribution, typically assumed to follow an exponential distribution. The duration d_i that component i remains in a state is determined by:

$$d_i = -\frac{1}{\lambda_i}\ln(u_i) \tag{3.92}$$

Where u_i is a random number uniformly distributed between 0 and 1, and λ_i is the transition rate of component i from its current state. If the component is operational, λ_i is the failure rate; if it is failed, λ_i is the repair rate.

3.4.2.3 Comparison of the Two Calculation Methods

The state enumeration method and the MCS method represent two distinct approaches to risk analysis, each with its own advantages and limitations. The choice between them depends on the specific characteristics of the problem under consideration. Table 3-4 provides a comparison of the strengths and weaknesses of both methods.

Table 3-4 Comparison of State Enumeration and Monte Carlo Simulation Methods

Aspect	State Enumeration Method	Monte Carlo Simulation Method
Applicability	Suitable for systems with fewer components and low failure probabilities.	Suitable for large-scale systems with higher failure rates.
Computational Results	Cannot effectively compute frequency and duration indicators.	Can flexibly model any probability distribution and provide probabilistic characteristics.
Computational Burden	Requires less computation time and memory space.	Requires more computation time and memory space.
Study Period	Capable of risk calculation for any time period.	Non-sequential Monte Carlo applies to any period; sequential Monte Carlo is typically limited to annual simulations.

In summary, the state enumeration method is computationally efficient but limited in its applicability to smaller systems with simpler failure characteristics. Conversely, the MCS method offers greater flexibility and is better suited for large, complex systems, albeit at the cost of increased computational resources.

3.4.3 Risk Indicator Calculation Models

The increasing penetration of renewable energy sources, such as PV systems, into modern distribution networks introduces significant operational challenges due to their inherent variability and intermittency. These challenges manifest as uncertainties in nodal power injections and the potential for stochastic component failures, which can precipitate operational risks such as voltage limit violations and branch flow overloads. To address these issues, this thesis employs Probabilistic Load Flow (PLF) as a cornerstone methodology for evaluating the behaviour of power systems under uncertainty. This section presents a PLF model based on the Newton-Raphson method, followed by the formulation of risk indicators to quantitatively assess the safety and reliability of distribution networks integrated with power electronic devices and renewable generation.

Traditional deterministic load flow analysis, which assumes fixed operating conditions, is not well suited for systems with significant renewable energy integration, particularly under conditions of large fluctuations caused by intermittent generation. In contrast, probabilistic load flow (PLF) provides a more appropriate framework by representing system variables as random quantities, thereby capturing inherent uncertainties in system operation. In this study, the Newton–Raphson method is adopted due to its computational efficiency and reliable convergence when solving nonlinear power flow equations.

The PLF model in this work considers two primary sources of uncertainty. First, stochastic nodal power injections are considered, where the outputs of PV systems, influenced by meteorological factors such as solar irradiance, are treated as random variables. These are typically described using probability distributions, such as normal or Beta distributions, based on historical data or predictive models. Second, component failure probabilities are incorporated, recognising that the operational reliability of network elements, including transmission lines and transformers, is subject to random failures, with probabilities estimated from historical reliability statistics.

The PLF computation leverages MCS to generate a large set of operational scenarios. For each scenario, the Newton-Raphson method iteratively solves the power flow equations, producing probabilistic distributions—characterized by statistical measures such as mean, variance, and probability density functions (PDFs) for nodal voltages and branch power flows. These distributions serve as the foundation for the risk assessment framework detailed below.

3.4.4 Voltage and Branch Overload Risk Assessment

In the context of power systems, risk is defined as the potential for undesirable outcomes resulting from uncertainties in operating conditions, such as renewable output variability or equipment failures, and their consequent impact on system safety over a specified time horizon. Risk is quantified through two key dimensions [223]:

Probability of Occurrence (P): The likelihood of a risk event, determined from probabilistic models or empirical data.

Severity of Consequences (S): The magnitude of the impact on system performance should the event occur.

The risk value R for a given event is expressed as:

$$R = P \times S \tag{3.93}$$

For a specific risk source k within the distribution network, the cumulative risk R_k across multiple events is calculated as:

$$R_k = \sum_{i=1}^{N} P_i \cdot S_i \tag{3.94}$$

Where P_i and S_i represent the probability and severity of the i -th risk event, respectively, and N is the total number of events associated with the k -th risk source. This formulation underpins the development of specific risk indicators for voltage and branch flow constraints.

1. Voltage Limit Violation Risk Indicator

The integration of PV systems can induce significant voltage fluctuations across network nodes, potentially exceeding predefined operational limits (1.05 p.u. for the upper bound and 0.95 p.u. for the lower bound). Such violations threaten system stability and equipment integrity. The voltage limit violation risk indicator R_{voltage} quantifies this risk by integrating the probability and severity of voltage deviations beyond acceptable thresholds. For the entire network, it is defined as:

$$R_{\text{voltage}} = \sum_{i=1}^{n} \int_{V_{\text{upper}}}^{\infty} P_{V_i}(v) \cdot S_{V_i}(v) dv + \sum_{j=1}^{m} \int_{-\infty}^{V_{\text{lower}}} P_{V_j}(v) \cdot S_{V_j}(v) dv \tag{3.95}$$

Where:

n and m denote the number of nodes exceeding the upper limit and falling below the lower limit, respectively,

V_{upper} and V_{lower} are the upper and lower voltage thresholds,

$P_{V_i}(v)$ and $P_{V_j}(v)$ are the PDFs of nodal voltages at nodes i and j, derived from PLF,

$S_{V_i}(v)$ and $S_{V_j}(v)$ are severity functions for voltage violations.

The severity functions, rooted in utility theory, measure the impact of voltage deviations and are defined as:

$$S_{V_i}(v) = \begin{cases} 0, & v \le V_{\text{upper}} \\ \dfrac{v - V_{\text{upper}}}{V_{\max} - V_{\text{upper}}}, & v > V_{\text{upper}} \end{cases} \tag{3.96}$$

$$S_{V_j}(v) = \begin{cases} 0, & v \ge V_{\text{lower}} \\ \dfrac{V_{\text{lower}} - v}{V_{\text{lower}} - V_{\min}}, & v < V_{\text{lower}} \end{cases} \tag{3.97}$$

Here, $V_{\max}$ and $V_{\min}$ represent the absolute maximum and minimum allowable voltages. The severity ranges from 0 (no violation) to 1 (maximum deviation), providing a normalized measure of impact.

2.Branch Flow Overload Risk Indicator

PV integration transforms traditional unidirectional power flows into bidirectional patterns, increasing the likelihood of branch overloads when flows exceed rated capacities. The branch flow overload risk indicator $R_{\text{flow}_{ij}}$ for branch ij is formulated as:

$$R_{\text{flow}_{ij}} = \int_{P_{\text{ij}}^{\text{rated}}}^{\infty} P_{P_{\text{ij}}}(p) \cdot S_{P_{\text{ij}}}(p) dp \tag{3.98}$$

Where:

P_{ij}^{rated} is the rated branch flow limit adopted in this study, defined as the maximum allowable apparent power (or active power, depending on the modelling assumption) that the branch can safely carry under normal operating conditions.

In this thesis, P_{ij}^{rated} is determined based on the thermal limit of the line, which is derived from the maximum permissible current magnitude and the nominal bus voltage, i.e., $P_{ij}^{rated} = \sqrt{3} V_{ij}^{nom} I_{ij}^{max}$ for three-phase systems (or its single-phase equivalent where applicable).

This limit represents the steady-state thermal capacity of the conductor and is used as the threshold beyond which branch overloading is considered to occur.

$P_{P_{\mathrm{ij}}}(p)$ is the PDF of the branch power flow, obtained from PLF,

$S_{P_{\mathrm{ij}}}(p)$ is the severity function for overloads.

The severity function is defined as:

$$S_{P_{\mathrm{ij}}}(p) = \begin{cases} 0, & p \le P_{\mathrm{ij}}^{\mathrm{rated}} \\ \dfrac{p - P_{\mathrm{ij}}^{\mathrm{rated}}}{P_{\mathrm{ij}}^{\mathrm{max}} - P_{\mathrm{ij}}^{\mathrm{rated}}}, & p > P_{\mathrm{ij}}^{\mathrm{rated}} \end{cases} \tag{3.99}$$

Where $P_{\mathrm{ij}}^{\mathrm{max}}$ is the maximum allowable flow, typically set by thermal or safety constraints. This function similarly ranges from 0 to 1, reflecting the degree of overload severity.

In this study, the rated branch flow P_{ij}^{rated} represents the normal operating limit of the branch under steady-state conditions, while the maximum allowable flow P_{ij}^{max} denotes an upper bound that the branch can tolerate for a short duration under emergency or stressed conditions.

Although these two values may be treated as identical in simplified analyses, they are intentionally distinguished here to enable a graded severity assessment of overload conditions. Specifically, P_{ij}^{rated} is used as the threshold for the onset of overload, whereas P_{ij}^{max} defines the upper bound beyond which the operating condition is considered critical.

This distinction allows the severity function to quantify the extent of overload in a continuous manner rather than as a binary condition.

3.5 Power Quality Assessment

3.5.1 Power Quality Challenges and Standards

Power quality has increasingly become an important concern due to its direct impact on the proper functioning of electrical equipment and the reliability of power systems. The rapid growth of industrialization and advancements in science and technology have significantly raised both the capacity and complexity of electrical power systems, leading to heightened sensitivity among users toward variations in power quality. Modern electrical equipment often employs high-performance and energy-efficient technologies, making them particularly susceptible to disturbances caused by voltage fluctuations and harmonic distortions. Consequently, maintaining stable and high-quality electricity supply has emerged as an essential requirement for ensuring safe and reliable operations in industrial processes and economic activities.

Recent developments in computing, networking technologies, and market dynamics have further complicated the management of power quality. Industrial users now demand greater customization and flexibility, which has intensified the challenge of optimizing electrical systems to meet diverse user needs. Issues like voltage sags, harmonics, and frequency deviations not only pose operational risks but also cause substantial economic losses annually. Despite significant progress in power quality management techniques and monitoring methods, ongoing challenges remain, driven by evolving user demands and technological complexity. Therefore, systematic and comprehensive approaches to power quality monitoring, evaluation, and control are necessary. Developing robust theoretical frameworks and advanced technological solutions is essential for enhancing competitiveness, achieving stable operation of power networks, and ensuring the provision of reliable, high-quality power services.

The International Electrotechnical Commission (IEC), headquartered in Geneva, is the leading international authority on electric power quality standards. Its Electromagnetic Compatibility (EMC) Standards series, which addresses power quality issues, is structured into the following parts [224]:

1. **General (IEC 61000-1-x)**: Introduces fundamental EMC principles and

defines essential terms and concepts.

2. **Environment (IEC 61000-2-x)**: Characterizes and classifies operational environments for equipment, providing guidelines on compatibility levels for various disturbances.
3. **Limits (IEC 61000-3-x)**: Specifies maximum permissible disturbance levels from equipment and immunity limits for sensitive devices.
4. **Testing and Measurement Techniques (IEC 61000-4-x)**: Provides guidelines for designing measurement and monitoring equipment and details testing procedures to ensure compliance.
5. **Installation and Mitigation Guidelines (IEC 61000-5-x)**: Recommends installation practices to minimize emissions and enhance immunity and describes methods for resolving power quality issues.
6. **Generic Standards (IEC 61000-6-x)**: Establishes standards for specific equipment categories or environments, encompassing both emission and immunity requirements.

The evaluation of power quality hinges on several measurable parameters, each governed by established standards to ensure system reliability:

3.5.2 Fundamental Requirement and Characteristics of Power Quality

It is well known that electrical energy is a widely applicable form of energy that can be converted into other types of energy and various electrical forms required in different fields. For example, electrical energy can be directly transformed into thermal, light, and mechanical energy for consumption. It can also be converted into non-power frequency and non-sinusoidal waveforms to serve as a fundamental power source for modern industry, communications, computing, and daily life.

To ensure the safe, economic transmission, distribution, and utilization of electrical energy, an ideal power supply system should exhibit the following fundamental characteristics:

1. The system should supply AC power to users at a single, constant nominal grid frequency (50 Hz or 60 Hz, with 50 Hz adopted in UK) and at specific voltage

levels (e.g., 110 kV, 35 kV, 10 kV, and 380V/220V in distribution systems). The waveform of the supplied AC power should follow a sinusoidal function, and these operational parameters should remain unaffected by the characteristics of the electrical load.

2. The three-phase AC voltage and load current should remain balanced at all times. Electrical equipment should draw power with maximum transmission efficiency, achieving a unit power factor, while ensuring that different electrical loads do not interfere with each other.
3. The power supply should be sufficient, ensuring uninterrupted electricity delivery to users. The operation of electrical equipment must remain stable, and at every moment, the power supply and demand in the system should be balanced.

Electrical energy, often referred to as an electric product, shares fundamental attributes with other industrial products, such as quality classification, measurement, standardization, and control. However, due to its singular form and the distinctive nature of its production, transmission, and consumption, power quality issues differ significantly from conventional product quality. The key characteristics of power quality are as follows:

1. **Dynamic Variation**: Power quality in an electrical system is continuously changing. The generation, transmission, and consumption of electrical energy form an interconnected process, maintaining dynamic equilibrium. Variations in grid structure and load conditions result in fluctuations in power quality indicators across different points in the system.
2. **System-Wide Interdependence**: Electrical energy cannot be stored efficiently, and its generation, transmission, and consumption occur simultaneously. Power quality issues at any stage of the system impact the entire network. If quality standards are not met, both power providers and consumers may experience operational risks, and in many cases, entities within the system act as both contributors to and victims of power quality disturbances.
3. **Propagation and Latent Hazards**: While electrical energy has a simple form, power quality disturbances are complex and may not always cause immediate

damage. Transmission lines serve as efficient conduits for disturbances, allowing them to propagate rapidly across the grid, potentially degrading the performance of connected equipment or even causing damage.

4. **User Influence on Power Quality**: In some cases, power quality is more affected by end users than by power producers or suppliers. Electrical loads determine current magnitude and waveform based on operational needs, often introducing harmonic distortion. Thus, users play a crucial role in maintaining power quality.
5. **Complexity of Comprehensive Evaluation**: Power quality assessment involves multiple interrelated parameters. While individual indicators can be compared to standard values, the combined effects of different disturbances on system performance and equipment reliability are complex. Sensitivity to voltage fluctuations varies across devices, making comprehensive technical and economic evaluations challenging. Currently, no universally accepted quantitative assessment method exists.
6. **Power Quality Management as a Systemic Approach**: Ensuring high-quality power supply requires coordinated efforts from equipment manufacturers, power utilities, consumers, standardization bodies, and regulatory agencies. Establishing clear, applicable quality standards and agreements tailored to different user requirements enables effective control and compliance. A structured approach to power quality management optimizes both technical performance and economic efficiency, ensuring a stable and reliable electrical environment.

3.5.3 Analysis of the Proposed Evaluation Index System

This study proposes a comprehensive evaluation index system to identify power quality weak points in distribution networks, leveraging three-phase harmonic power flow calculations. The system integrates six indicators assessing node voltage deviation, three-phase unbalance, harmonic distortion, and overrun risks, reflecting the complexities introduced by distributed generation. The indicators, their types, and significance are detailed in Table 3-5.

Table 3-5 Power Quality Risk Assessment Indicators

Indicator	Name	Type	Significance
P1	Three-Phase Voltage Imbalance	Negative	Reflects fundamental voltage unbalance
P2	Node Voltage Deviation Rate	Negative	Measures deviation from rated voltage
P3	Average Harmonic Voltage Distortion Rate	Negative	Quantifies harmonic impact on fundamental voltage
P4	Harmonic Voltage Three-Phase Imbalance Degree	Negative	Assesses harmonic voltage unbalance
P5	Maximum Over-limit Risk Value of Node Voltage	Negative	Evaluates voltage limit violation risk
P6	Active Power Over-limit Risk Value of Node Injection Branch	Negative	Assesses branch power limit violation risk

The selected indicators are designed to fully represent the characteristics of a distribution network system that incorporates three-phase harmonics, ensuring both representativeness and the ability to capture differentiated impacts. These indicators are categorized based on their relationship with power quality: those positively correlated with power quality are classified as positive indicators, those negatively correlated as negative (reverse) indicators, and those with an optimal intermediate value as interval indicators. This framework enables a robust and nuanced assessment of power quality across the network.

In this study, all selected indicators are negatively correlated with power quality, meaning that higher values indicate poorer performance. Therefore, only negative indicators are considered in the proposed evaluation framework. Positive and interval-type indicators are not included, as the selected metrics are sufficient to capture the key characteristics of power quality degradation in the studied distribution network.

1. Three-Phase Voltage Imbalance (P1)

This indicator measures the imbalance in three-phase fundamental voltages, noting that such unbalances increase line and transformer losses, impacting power quality.

$$P1 = \frac{\max(|V_A - V_{avg}|,|V_B - V_{avg}|,|V_C - V_{avg}|)}{V_{avg}} \tag{3.100}$$

Where $V_{avg} = \frac{V_A + V_B + V_C}{3}$, and V_A, V_B, V_C are the fundamental voltage magnitudes of phases A, B, and C, respectively.

2. Node Voltage Deviation Rate (P2)

This indicator quantifies the deviation of actual node voltage from the rated voltage, normalized by the rated voltage. This indicator quantifies the deviation of the actual node voltage from the rated voltage. In this study, a voltage range of 0.93–1.07 p.u. is adopted. This slightly extended range, compared to the typical operational limit of 0.95–1.05 p.u., is used to capture a wider spectrum of probabilistic variations under uncertainty and to better reflect potential extreme operating conditions.

$$P2 = \frac{|V_{act} - V_{rated}|}{V_{rated}} * 100\% \tag{3.101}$$

Where V_{act} is the actual fundamental voltage magnitude, and V_{rated} is the rated voltage at the node.

3. Average Harmonic Voltage Distortion Rate (P3)

This indicator averages the total harmonic distortion (THD) across the three phases to assess harmonic pollution.

$$P3 = \frac{1}{3} \sum_{x=A,B,C} \sqrt{\sum_{h=2}^{50} \left(\frac{V_{x,h}}{V_{x,1}} \right)^2} \tag{3.102}$$

Where THD_x is the THD for phase x (A, B, C), $V_{x,1}$ is the fundamental voltage, and $V_{x,h}$ is the h -th harmonic voltage.

4. Harmonic Voltage Three-Phase Imbalance Degree(P4)

This indicator assesses the imbalance in harmonic voltages across the three phases, similar to P1.

$$P4 = \frac{\max(|V_{A,h} - V_{avg,h}|, |V_{B,h} - V_{avg,h}|, |V_{C,h} - V_{avg,h}|)}{V_{avg,h}} \tag{3.103}$$

Where $V_{avg,h} = \frac{V_{A,h} + V_{B,h} + V_{C,h}}{3}$, and $V_{A,h}, V_{B,h}, V_{C,h}$ are the h -th harmonic voltage magnitudes.

5. Maximum Over-limit Risk Value of Node Voltage (P5)

This indicator evaluates the risk of node voltages exceeding upper or lower limits, incorporating probability and severity.

$$\begin{aligned} &P5 = \max(R_{i,A}, R_{i,B}, R_{i,C}) \\ &R_{i,x} = \int_{V_{up}} f_{up}(V) \cdot s_{up}(V) dV + \int_{V_{low}} f_{low}(V) \cdot s_{low}(V) dV \end{aligned} \tag{3.104}$$

Where $R_{i,x}$ is the risk for phase x at node i , $f_{up/low}$ and $s_{up/low}$ are the probability density and severity functions for upper/lower limit overruns, and $V_{up/low}$ are the limit thresholds.

6. Active Power Over-limit Risk Value of Node Injection Branch (P6)

This indicator assesses the risk of active power flows in branches exceeding limits, similar to P5.

$$\begin{aligned} &P6 = \max(R_{i,A}, R_{i,B}, R_{i,C}) \\ &R_{i,x} = \int_{P_{up}} f_{up}(P) \cdot s_{up}(P) dP + \int_{P_{low}} f_{low}(P) \cdot s_{low}(P) dP \end{aligned} \tag{3.105}$$

Where $R_{i,x}$ is the risk for phase x in the branch connected to node i, and $P_{up/low}$ are power limits.

3.5.4 Design of a Comprehensive Evaluation Model for Power Quality Weak Points

Given the complexity and multiplicity of indicators involved in evaluating power quality weak points, this study proposes a hybrid evaluation framework that integrates the Analytic Hierarchy Process (AHP), Criteria Importance Through Intercriteria Correlation (CRITIC), and Technique for Order Preference by Similarity to Ideal Solution (TOPSIS). This approach, termed the AHP-CRITIC-TOPSIS combined weighting method, is designed to assign higher weights to indicators exhibiting significant numerical variability, thereby emphasizing their importance in identifying power quality weak points. The TOPSIS model complements this by providing a multi-criteria ranking that overcomes the limitations of single-criterion assessments, ensuring a comprehensive, objective reflection of the actual situation and reducing the likelihood of identical evaluation outcomes [225].

The methodology is structured into three systematic steps, as illustrated in Figure 3-9.

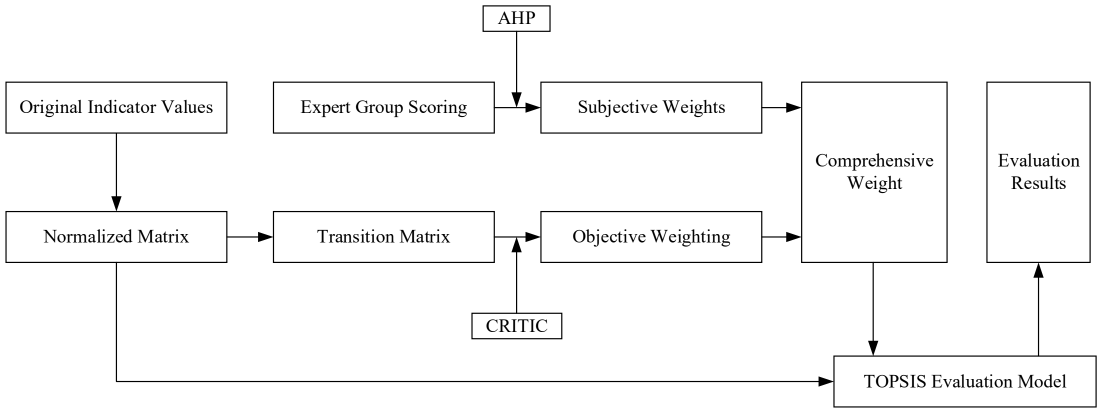

Figure 3-9 Comprehensive Evaluation Model Flowchart

1. Preprocessing of raw data using Grey Relational Analysis (GRA).

2. Determination of comprehensive indicator weights via the AHP-CRITIC combined weighting method.

3. Construction of a weighted decision matrix and evaluation using the TOPSIS method.

Each step is detailed below with rigorous explanations, mathematical formulations, and justifications to ensure clarity, precision, and academic integrity.

Step 1: Preprocessing of Raw Data

The initial step standardizes the raw data to address variations in scales and units across indicators, employing Grey Relational Analysis (GRA) for normalization and transformation into a comparable format.

1. Data Normalization Using GRA

The raw data matrix $X=[x_{ij}]_{m\times n}$ comprises m scenario (evaluation objects, e.g., power quality scenarios) and n indicators (e.g., voltage deviation, harmonic distortion). Here, x_{ij} represents the original value of the j-th indicator for the i-th scheme. A reference value x_{0j} is established for each indicator j based on its type:

Positive indicators (larger values are preferable, e.g., power supply reliability): $x_{0j}=\max_i x_{ij}$.

Negative indicators (smaller values are preferable, e.g., power loss): $x_{0j}=\min_i x_{ij}$.

Interval indicators (an optimal value within a range is desired, e.g., voltage within a tolerance band): x_{0j} is the most favorable value within the specified interval, typically the midpoint or a predefined optimal value.

The normalized value r_{ij} is calculated using the GRA formula:

$$r_{ij}=\frac{\min_i|x_{ij}-x_{0j}|+\xi\cdot\max_i|x_{ij}-x_{0j}|}{|x_{ij}-x_{0j}|+\xi\cdot\max_i|x_{ij}-x_{0j}|} \tag{3.106}$$

Where ξ is the distinguishing coefficient, set to 0.5 to balance resolution and stability. This yields a normalized matrix $R=[r_{ij}]_{m\times n}$, where $r_{ij}\in[0,1]$ reflects the similarity of each indicator value to its ideal reference, with higher values indicating better performance.

2. Transformation to an Intermediate Matrix

To prepare the data for weighting and ranking, the normalized matrix R is standardized into an intermediate matrix $P=[p_{ij}]_{m\times n}$ using vector normalization:

$$p_{ij}=\frac{r_{ij}}{\sqrt{\sum_{i=1}^{m}r_{ij}^2}} \tag{3.107}$$

This ensures that each column Euclidean norm equals 1, eliminating unit dependencies and facilitating multi-criteria analysis.

Step 2: Determination of Comprehensive Indicator Weights

This step calculates comprehensive weights by integrating subjective weights from AHP with objective weights from an improved CRITIC method, balancing expert judgment with data-driven insights [226].

1. Subjective Weighting Using AHP

The AHP method leverages expert knowledge to assign subjective weights. A hierarchical structure is established, with the evaluation of power quality weak points as the goal and the n indicators as criteria. Experts perform pairwise comparisons to assess the relative importance of each indicator, forming a judgment matrix $A = [a_{jk}]_{n \times n}$, where a_{jk} denotes the importance of indicator j over k on a 1-9 scale (see Table 3-6 for the indicator scale).

Table 3-6 Indicator Scale for AHP Pairwise Comparisons

Scale	Description
1.0	Indicators j and k are equally important
1.2	j is slightly more important than k
1.4	j is noticeably more important than k
1.6	j is strongly more important than k
1.8	j is extremely more important than k
1.1, 1.3, 1.5, 1.7	Intermediate values between adjacent judgments

The eigenvector corresponding to the maximum eigenvalue $\lambda_{\max}$ of A is computed and normalized to yield the subjective weight vector $w_{\text{AHP}} = [w_{\text{AHP},1}, \ldots, w_{\text{AHP},n}]$, where $\sum_{j=1}^{n} w_{\text{AHP},j} = 1$. Consistency is verified using the Consistency Ratio (CR):

$$\text{CR} = \frac{\text{CI}}{\text{RI}} \qquad \text{CI} = \frac{\lambda_{\max} - n}{n-1} \tag{3.108}$$

Where RI is the random index for n criteria. A CR < 0.1 ensures acceptable consistency. For multiple experts (e.g., k experts), individual weights are aggregated using the weighted arithmetic mean:

$$w_{\mathrm{AHP},j} = \sum_{e=1}^{k} \beta_e \cdot w_{\mathrm{AHP},j,e}, \quad \sum_{e=1}^{k} \beta_e = 1 \tag{3.109}$$

Where $w_{\mathrm{AHP},j,e}$ is the weight from expert e, and β_e is their assigned credibility weight.

2. Objective Weighting Using Improved CRITIC [227]

The CRITIC method is enhanced to account for variability, inter-indicator conflict, and redundancy. For the intermediate matrix P:

Variability: The coefficient of variation $\sigma_j / \bar{p}_j$ (where σ_j is the standard deviation and $\bar{p}_j$ is the mean of column j) measures contrast intensity.

Conflict: The absolute Pearson correlation coefficient $|\rho_{jk}|$ between indicators j and k quantifies interdependencies, with $\sum_{k=1}^{n}(1-|\rho_{jk}|)$ reflecting conflict.

Redundancy: Information entropy $e_j = -\frac{1}{\ln m}\sum_{i=1}^{m} p_{ij} \ln p_{ij}$ (where p_{ij} is adjusted to avoid undefined logarithms) captures dispersion, and the inverse entropy $1-e_j$ emphasizes variability.

The information content c_j is:

$$c_j = \frac{\sigma_j}{\bar{p}_j} \cdot \sum_{k=1}^{n}(1-|\rho_{jk}|)\cdot(1-e_j) \tag{3.110}$$

The objective weight is:

$$w_{\mathrm{CRITIC},j} = \frac{c_j}{\sum_{j=1}^{n} c_j}, \quad \sum_{j=1}^{n} w_{\mathrm{CRITIC},j} = 1 \tag{3.111}$$

This improvement ensures that indicators with high variability, low correlation, and significant information content are prioritized.

3. Comprehensive Weighting

The comprehensive weight vector $w = [w_1, \ldots, w_n]$ integrates subjective and objective weights:

$$w_j = \alpha \cdot w_{\text{AHP},j} + (1-\alpha) \cdot w_{\text{CRITIC},j} \tag{3.112}$$

Where α (typically 0.5) balances expert input and data properties, adjustable based on context-specific needs.

Step 3: Construction of the Weighted Decision Matrix and TOPSIS Evaluation

This step constructs a weighted decision matrix and applies TOPSIS to rank schemes and identify weak points.

1. Weighted Decision Matrix

The intermediate matrix P is transformed into a weighted decision matrix $V = [v_{ij}]_{m \times n}$:

$$v_{ij} = w_j \cdot p_{ij} \tag{3.113}$$

2. TOPSIS Evaluation

The positive ideal solution (PIS) V^+ and negative ideal solution (NIS) V^- are defined:

Benefit indicators: $v_j^+ = \max_i v_{ij}, v_j^- = \min_i v_{ij}$.

Cost indicators: $v_j^+ = \min_i v_{ij}, v_j^- = \max_i v_{ij}$.

Interval indicators: v_j^+ is the value closest to the interval's center, v_j^- is the farthest.

Euclidean distances from PIS (S_i^+) and NIS (S_i^-) are:

$$S_i^+ = \sqrt{\sum_{j=1}^{n} (v_{ij} - v_j^+)^2}, \quad S_i^- = \sqrt{\sum_{j=1}^{n} (v_{ij} - v_j^-)^2} \tag{3.114}$$

The closeness coefficient C_i is:

$$C_i = \frac{S_i^-}{S_i^+ + S_i^-}, \quad C_i \in [0,1] \tag{3.115}$$

Schemes are ranked by descending C_i, with lower values indicating weaker performance (i.e., power quality weak points).

This AHP–CRITIC–TOPSIS model provides a robust and systematic framework for power quality assessment. The GRA stage ensures consistent and standardized processing of input data, improving comparability across indicators. The combined AHP–CRITIC weighting method integrates both subjective expert judgement and objective data characteristics, thereby balancing interpretability with statistical variability. Finally, the TOPSIS method enables precise ranking of alternatives by evaluating their relative closeness to the ideal solution, which allows weak points within the network to be clearly identified and prioritised for improvement.

3.6 Optimization Methods for Active Power Filters [228]

3.6.1 Harmonic Mitigation Strategies: Active and Passive Approaches

Harmonic distortion poses a significant challenge in power systems due to the proliferation of nonlinear loads, such as power electronic devices and renewable energy interfaces. These harmonics can degrade power quality, leading to equipment malfunctions, increased thermal stress, and reduced system efficiency [6]. Consequently, effective harmonic mitigation is imperative to ensure the reliability and stability of electrical networks. Harmonic governance strategies are broadly classified into two categories: active mitigation and passive mitigation.

Active harmonic mitigation aims to suppress harmonic generation at its source by optimizing the operational conditions of harmonic-producing equipment or redesigning their configurations [229]. One prominent technique is the application of multi-pulse technology, where the waveforms of multiple harmonic sources are superimposed to achieve partial cancellation of lower-order harmonic components. For example, in a multi-pulse rectifier system, phase-shifting transformers can be employed to align harmonic currents in opposition, effectively reducing the total harmonic distortion (THD). Additionally, the operational states of harmonic sources can be strategically managed based on their harmonic characteristics. Devices exhibiting complementary harmonic cancellation properties—where the harmonic currents of one source counteract those of another—should be operated concurrently to maximize suppression. Conversely, equipment with mutually reinforcing harmonic profiles, which amplify distortion when operated together, should be spatially dispersed or scheduled alternately to minimize cumulative harmonic effects. These proactive measures reduce the harmonic burden on the power system without requiring additional filtering infrastructure.

In contrast, passive harmonic mitigation involves the deployment of external devices within the distribution network to filter or compensate for harmonic distortions. These devices are categorized into three primary types [230]:

Passive Filters (PF): Comprising inductors, capacitors, and resistors, PFs are tuned to specific harmonic frequencies, providing a low-impedance path that diverts unwanted currents from the main system. While it is cost-effective and simple to implement, their fixed tuning limits adaptability, and they may introduce resonance risks under varying load conditions.

Active Power Filters (APF): APFs leverage power electronics to dynamically inject compensating currents that neutralize harmonic distortions in real-time. Their ability to adapt to fluctuating harmonic profiles and mitigate a broad spectrum of frequencies distinguishes them from PFs. Over the past decades, advancements in control algorithms and semiconductor technology have enhanced the maturity and efficacy of APFs, positioning them as a preferred solution for harmonic suppression.

Unified Power Quality Conditioners (UPQC): UPQCs integrate series and shunt active filters to simultaneously address voltage and current distortions, offering a holistic approach to power quality enhancement. This dual functionality makes UPQCs particularly suitable for complex networks with diverse power quality issues.

The evolution of APF technology, in particular, has been driven by its flexibility and efficiency, establishing it as a leading method for harmonic mitigation in contemporary power systems. Its real-time responsiveness and capacity to handle dynamic loads underscore its growing adoption across industrial and utility applications [231].

3.6.2 Configuration of Shunt Active Power Filters

Shunt APF represent a sophisticated approach to enhancing power quality in electrical networks, particularly in addressing harmonic distortions. Unlike conventional passive inductor/capacitor (LC) filters, which are constrained to absorbing harmonic components at fixed frequencies, APFs provide dynamic, targeted compensation. By isolating harmonic and reactive components from the load current and injecting compensatory currents of precise magnitude and phase, APFs effectively neutralize distorted current components, thereby improving the overall power quality of the grid. Owing to their better controllability and adaptability, APFs have become a cornerstone of power quality management strategies.

Historically, the deployment of active power filters (APFs) has followed the "polluter pays" principle, leading to decentralized configurations in which each harmonic source is compensated individually at its point of connection. Although this approach is suitable for simpler systems, it exhibits notable limitations in microgrids with multiple harmonic sources. In these complex settings, APF configuration must address two key and interdependent aspects: optimal placement (i.e., determining suitable locations) and capacity sizing (i.e., determining appropriate capacities). These considerations are vital for attaining effective harmonic mitigation while maintaining economic feasibility and system stability.

The optimal configuration of APFs in multi-harmonic source microgrids hinges on resolving two key issues: determining the installation location and specifying the required capacity (capacity sizing). These decisions directly influence the filter harmonic suppression performance and its interaction with the broader network.

In this study, only shunt APFs are considered. This choice is motivated by their effectiveness in mitigating current harmonics, which are the dominant source of power quality issues in distribution networks due to nonlinear loads and inverter-based generation. By compensating harmonic currents at the point of common coupling, shunt APFs can indirectly reduce voltage distortion across the network, making them particularly suitable for system-level harmonic analysis.

In contrast, series APFs are primarily designed for voltage harmonic compensation and are more applicable in cases where voltage distortion is the dominant concern, which is not the main focus of this work. Hybrid APFs, while offering improved performance through combined active and passive compensation, introduce additional modelling complexity, parameter tuning requirements, and resonance considerations. These factors make them less suitable for the large-scale optimization framework developed in this study.

Therefore, to maintain model tractability while capturing the dominant harmonic mitigation mechanism, this work focuses exclusively on shunt APFs.

3.6.2.1 APF Placement

The placement of an APF within a power grid is a critical determinant of its ability to mitigate harmonic currents effectively. Strategic placement enables the filter to absorb harmonic distortions efficiently, reducing harmonic losses, preventing maloperation of protective relays, and minimizing the risk of system resonance. Conversely, suboptimal placement can result in overcompensation at certain nodes, degrading power quality in areas of the network that were previously stable. In power grid with a single harmonic source, the ideal placement is straightforward: installing the APF at the harmonic source node ensures direct elimination of distortions before they propagate through the network. However, in multi-harmonic source systems, a single APF must compensate for multiple distortion sources simultaneously, rendering perfect compensation across all harmonics unfeasible. Consequently, placement must be optimized to direct the compensation current predominantly toward the primary harmonic sources while avoiding overcompensation at non-harmonic nodes.

Mathematically, APF placement constitutes a mixed-integer nonlinear programming problem due to the discrete nature of node selection within the power grid topology. Current methodologies for addressing this challenge fall into two categories: theoretical analysis and intelligent optimization algorithms. Theoretical approaches, such as voltage sensitivity analysis, can identify optimal compensation points but rely heavily on accurate mathematical models of the power network--models that are often impractical to derive with precision in real-world power grid. As a result, intelligent algorithms, including genetic algorithms (GA) and particle swarm optimization (PSO), have emerged as preferred solutions. These algorithms require adaptation to accommodate the discrete variables inherent in the placement problem, enhancing their applicability to power grid configurations.

3.6.2.2 APF Capacity Sizing

The capacity of an APF directly governs its harmonic mitigation capability: larger capacities provide greater compensation margins, ensuring more robust suppression of distortions. However, the cost of an APF is approximately linear with its capacity, necessitating a careful trade-off between performance and economic feasibility. In single harmonic source systems, capacity sizing is relatively simple, as the APF capacity can be matched directly to the harmonic source output. In contrast, multi-harmonic source systems present a more complex scenario. The compensation current from a centrally placed APF disperses throughout the network, preventing precise allocation to individual harmonic sources. As a result, capacity cannot be determined by simply aggregating the capacities of all harmonic sources. Moreover, oversized capacities risk overcompensation, which can exacerbate power quality issues rather than resolve them.

Unlike placement, which involves discrete variables, capacity sizing is a continuous optimization problem, making it amenable to techniques such as PSO. However, the high-dimensional and nonlinear nature of this optimization task demands careful algorithm design to prevent issues such as premature convergence or entrapment in local optima.

The configuration of APFs in power grid with multiple harmonic sources entails a dual optimization challenge: determining the optimal placement to balance compensation across diverse sources and sizing the capacity to achieve effective harmonic mitigation without incurring excessive costs. Placement requires navigating the discrete topology of the network, while capacity sizing involves optimizing a continuous variable within economic constraints. Intelligent optimization algorithms, tailored to handle both mixed-integer and nonlinear problems, are indispensable for addressing these challenges. The theoretical foundation for developing a comprehensive methodology to optimize APF configuration in power grid will be elaborated in subsequent sections of this thesis.

3.6.3 Configuration Model of Active Power Filters in Power Grids

APFs are essential devices in power systems, categorized based on their connectivity to the grid into two primary configurations: series and shunt (parallel) structures. Series APFs are integrated between the power source and the load through a transformer, primarily designed to suppress harmonic voltages within the grid. Conversely, shunt APFs, which operate as voltage-source inverters, are connected directly in parallel with the power system, functioning as controlled current sources. Given that harmonic pollution in power grids predominantly originates from harmonic currents produced by nonlinear devices, APFs are particularly effective in addressing current distortions, which subsequently mitigate voltage distortions. As a result, APFs have become the prevailing approach for harmonic mitigation in power systems.

The filter employs circuit to detect harmonic and reactive components within the distorted load current. Subsequently, a compensation current generation circuit tracks these components, generating a compensatory current equal in magnitude but opposite in phase. This current is injected into the grid via an LCL filter, neutralizing the distorted components and yielding a sinusoidal fundamental active current, thereby enhancing overall power quality.

Mathematically, the grid current i_s comprises the load current i_L and the APF compensation current i_c:

$$i_s = i_L + i_c \tag{3.116}$$

In cases where the load includes nonlinear or reactive elements, the load current i_L consists of the fundamental active current i_p, harmonic components i_h, and reactive components i_q:

$$i_L = i_p + i_h + i_q \tag{3.117}$$

The APF injects a compensation current defined as:

$$i_c = -(i_h + i_q) \tag{3.118}$$

Substituting this into the grid current equation, we obtain:

$$i_s = i_p \tag{3.119}$$

This ensures that only the fundamental active current flows back into the grid, effectively eliminating harmonic and reactive distortions.

In traditional decentralized harmonic mitigation strategies, each harmonic source is paired with an individual APF in a "one-to-one" configuration. However, in centralized compensation approaches for systems with multiple harmonic sources, a single high-capacity APF is installed at a designated bus, providing compensation to multiple harmonic sources in a "one-to-many" arrangement. Here, the APF can be modeled as a controllable current source that injects "anti-harmonic" currents into the grid. The compensation current matrix is expressed as:

$$\mathbf{I}_h^{\mathrm{APF}} = [I_h^{\mathrm{APF1}}, I_h^{\mathrm{APF2}}, \ldots, I_h^{\mathrm{APF}n}] \tag{3.120}$$

Where $I_h^{\mathrm{APF}m} = 0$ if no APF is deployed at node m. The harmonic voltage at the nodes following compensation is calculated as:

$$\mathbf{U}_h = \mathbf{Y}^{-1}(\mathbf{I}_h - \mathbf{M}_{\mathrm{APF}}\mathbf{I}_h^{\mathrm{APF}}) \tag{3.121}$$

Where $\mathbf{Y}$ represents the admittance matrix, $\mathbf{I}_h$ is the harmonic current injection vector from the loads, and $\mathbf{M}_{\mathrm{APF}}$ is the APF placement vector, with elements set to 1 at nodes hosting an APF and 0 otherwise.

In a power grid with a single harmonic source, configuring $\mathbf{M}_{\mathrm{APF}}\mathbf{I}_h^{\mathrm{APF}} = \mathbf{I}_h$ results in $\mathbf{U}_h = 0$, achieving complete harmonic elimination. However, in systems with multiple harmonic sources, exact compensation across all sources is infeasible due to the distributed nature of harmonic injections. Nevertheless, optimizing the placement vector $\mathbf{M}_{\mathrm{APF}}$ and the capacity vector $\mathbf{I}_h^{\mathrm{APF}}$ can minimize the harmonic voltage distortion $\mathbf{U}_h$, thereby enhancing power quality across the grid.

This subsection establishes a model for configuring Shunt APF within power grids, highlighting their critical role in harmonic suppression. By conceptualizing the APF as a controlled current source, this framework supports the evaluation of both decentralized and centralized compensation strategies. The mathematical analysis reveals the limitations of achieving full compensation in multi-harmonic source systems, laying the groundwork for subsequent optimization techniques to determine the optimal placement and capacity of APFs in complex power grid environments.

In this study, the APF is modelled primarily for harmonic current compensation. Although APFs are capable of simultaneously compensating reactive power, reactive current compensation is not explicitly considered in the proposed model.

This assumption is made for two main reasons. First, the primary focus of this work is on harmonic distortion and its impact on power quality, particularly in terms of voltage distortion indices and harmonic-related risks. Including reactive power compensation would introduce additional control variables and coupling effects, significantly increasing model complexity without directly contributing to the core objectives of harmonic analysis.

Second, in many practical distribution systems, reactive power compensation is typically addressed by other devices, such as capacitor banks or voltage regulation equipment, and can therefore be treated as decoupled from harmonic mitigation in steady-state analysis.

Under this assumption, the APF is simplified as a controllable current source that injects only harmonic compensation currents, allowing a more tractable formulation for subsequent optimization of filter placement and capacity.

3.6.4 Double-Layer Economic Optimization Model for APF Harmonic Governance [232]

To achieve an optimal configuration of APFs in distribution networks for harmonic mitigation, this study proposes a double-layer optimization framework that balances economic costs with technical performance. The outer layer focuses on minimizing the total economic cost of APF deployment, while the inner layer aims to optimize harmonic suppression across the network. This section outlines the objective functions and constraints for both layers, ensuring compliance with power quality standards, operational safety, and economic feasibility.

3.6.4.1 Outer Layer Optimization Model

The outer layer optimization targets the minimization of the total economic cost associated with APF deployment, encompassing both the initial investment and the subsequent operation and maintenance expenses. This cost-centric approach ensures the economic viability of harmonic governance strategies in distribution networks. The objective function is formulated as:

$$\min C_{\text{total}} = C_{\text{ins}} + C_{\text{inv}} \tag{3.122}$$

Where:

C_{ins} : Installation cost of the APFs,

C_{inv} : Equivalent cost of investment, operation, and maintenance.

In this study, the equivalent cost includes both the initial investment cost and the operation and maintenance (O&M) cost converted into an annualized form. The O&M cost is treated as a recurring expense and is aggregated over the lifetime of the APF. To ensure consistency with the investment cost, both components are expressed as equivalent annual costs using a capital recovery factor.

These cost components are further detailed as:

$$C_{\text{ins}} = p_{\text{ins}} \cdot N_{\text{APF}} \tag{3.123}$$

$$C_{\text{inv}} = p_{\text{inv}} \cdot \sum_{i=1}^{N} S_{\text{APF},i} \tag{3.124}$$

Where:

p_{ins}: Installation cost per APF unit (in £),

p_{inv}: Cost per unit capacity of the APF (in monetary units per kVA),

N_{APF}: Total number of APF units installed,

$S_{\text{APF},i}$: Capacity of the APF at node i (in kVA),

N: Total number of nodes in the distribution network.

This formulation captures both fixed costs (proportional to the number of APF units) and variable costs (proportional to the installed capacity), providing a holistic economic evaluation.

The outer layer optimization is subject to constraints that ensure power quality compliance and practical feasibility:

1. Total Harmonic Voltage Distortion (THD) Constraint:

Post-APF deployment, the total harmonic voltage distortion at each node must meet national power quality standards:

$$\text{THD}_{U_n} \leq \text{THD}_{U_{\max}} \tag{3.125}$$

Where:

THD_{U_n}: Total harmonic voltage distortion at node n,

$\mathrm{THD}_{U_{\max}}$: Maximum allowable harmonic voltage distortion per regulatory standards (e.g., IEEE Standard 519).

2. Individual Harmonic Voltage Content Constraint:

The harmonic ratio for each harmonic order at every node must also comply with specified limits:

$$\mathrm{HR}_{U_{n,h}} \le \mathrm{HR}_{U_{h,\max}} \tag{3.126}$$

Where:

$\mathrm{HR}_{U_{n,h}}$: Harmonic ratio of the h -th harmonic at node n ,

$\mathrm{HR}_{U_{h,\max}}$: Maximum allowable harmonic ratio for the h -th harmonic.

3. APF Capacity Constraint:

The capacity of each APF is determined by the harmonic currents it must compensate. While larger capacities enhance redundancy and harmonic suppression, they also increase costs due to the higher expense of components like insulated gate bipolar transistors (IGBTs) and circuit breakers. The rated capacity is calculated as:

$$S_{\mathrm{APF},i} = \sqrt{\sum_{h=1}^{H} (I_{c_h,i})^2} \tag{3.127}$$

Where:

$I_{c_h,i}$: Compensation current for the h -th harmonic at node i (in A),

H : Highest harmonic order considered for compensation.

This constraint ensures that the APF capacity is sufficient for effective harmonic mitigation without leading to excessive and uneconomical oversizing.

3.6.4.2 Inner Layer Optimization Model

The inner layer optimization seeks to maximize the harmonic mitigation effectiveness across the distribution network. The objective is to minimize the root mean square (RMS) of the total harmonic voltage distortion across all nodes, ensuring a uniform improvement in power quality. The objective function is defined as:

$$\min \sqrt{\frac{1}{N}\sum_{n=1}^{N}(\mathrm{THD}_{U_n})^2} \tag{3.128}$$

Where:

N : Total number of nodes in the network,

THD_{U_n} : Total harmonic voltage distortion at node n .

This RMS-based metric prioritizes a balanced reduction of harmonic distortion throughout the network, aiming for an optimal comprehensive compensation effect.

The inner layer incorporates constraints to ensure the safe, stable, and physically consistent operation of the distribution network:

1.System Operational Safety Constraints:

Voltage and current magnitudes must remain within permissible operational limits:

$$\begin{aligned} &U_{\min} \le U_n \le U_{\max} \quad \forall n \in N \\ &I_{ij} \le I_{\max} \quad \forall \text{ branches } ij \end{aligned} \tag{3.129}$$

Where:

U_n : Voltage magnitude at node n (in kV),

$U_{\min}, U_{\max}$: Minimum and maximum allowable voltage magnitudes (in kV),

I_{ij} : Current magnitude in branch ij (in A),

$I_{\max}$: Maximum allowable branch current (in A).

2. AC/DC Power Flow Constraints:

Power flow equations must be satisfied for both AC and DC sections of the network:

$$\begin{aligned} P_{ij} &= \frac{U_i U_j}{Z_{ij}}\cos(\theta_{ij} + \delta_i - \delta_j) \\ Q_{ij} &= \frac{U_i U_j}{Z_{ij}}\sin(\theta_{ij} + \delta_i - \delta_j) \end{aligned} \tag{3.130}$$

Where:

P_{ij}, Q_{ij} : Active and reactive power flows in branch ij ,

U_i, U_j : Voltage magnitudes at nodes i and j (in kV),

Z_{ij}, θ_{ij} : Impedance magnitude and angle of branch ij ,

δ_i, δ_j : Voltage phase angles at nodes i and j (in radians).

Nodal power balance equations are also enforced:

$$\begin{aligned} P_i &= P_{\mathrm{DG},i} - P_{\mathrm{L},i} = \sum_{j \in \mathcal{N}(i)} P_{ij} \\ Q_i &= Q_{\mathrm{DG},i} - Q_{\mathrm{L},i} = \sum_{j \in \mathcal{N}(i)} Q_{ij} \end{aligned} \tag{3.131}$$

Where:

$P_{\mathrm{DG},i}, Q_{\mathrm{DG},i}$: Active and reactive power from distributed generation (DG) at node i (in (kW and kVar),

$P_{\mathrm{L},i}, Q_{\mathrm{L},i}$: Active and reactive load demands at node i (in (kW and kVar),

$\mathcal{N}(i)$: Set of nodes connected to node i .

3. Distributed Generation (DG) Operational Constraints:

DG units must operate within their rated capacities, and their total penetration must not destabilize the network:

$$\begin{aligned} &0 \le S_{\mathrm{DG},i} \le S_{\mathrm{DG},i}^{\mathrm{rated}} \quad \forall i \in N_{\mathrm{DG}} \\ &\sum_{i \in N_{\mathrm{DG}}} S_{\mathrm{DG},i} \le \lambda_{\max} \cdot P_{\mathrm{E}} \end{aligned} \tag{3.132}$$

Where:

$S_{\mathrm{DG},i}$: Apparent power output of the DG at node i ,

$S_{\mathrm{DG},i}^{\mathrm{rated}}$: Rated capacity of the DG at node i ,

N_{DG} : Set of nodes with DG installations,

$\lambda_{\max}$: Maximum allowable DG penetration rate,

P_{E} : Total rated active power of the distribution network.

This double-layer optimization model integrates economic and technical objectives for

APF harmonic governance in distribution networks. The outer layer minimizes the total cost of APF deployment, balancing installation and operational expenses, while adhering to power quality standards. The inner layer optimizes harmonic mitigation by reducing the RMS of voltage harmonic distortion across all nodes, subject to operational safety, power flow, and DG constraints. This framework provides a methodology for achieving cost-effective and high-quality power distribution, suitable for networks with significant harmonic pollution and distributed generation.

3.6.5 Particle Swarm Optimization: A Bio-Inspired Approach to Optimization [233]

3.6.5.1 Origins and Conceptual Framework

The evolution of optimization methodologies in the late 20th century marked a significant departure from conventional computational strategies toward biologically inspired paradigms. Among these, Swarm Intelligence (SI) emerged as a prominent field, drawing from the coordinated behaviours observed in natural collectives such as fish schools and insect societies. Within this domain, Particle Swarm Optimization (PSO), developed by J. Kennedy and R.C. Eberhart, stands out as a widely adopted algorithm [234]. PSO emulates the social dynamics of bird flocks foraging for food, representing potential solutions as particles that traverse a multidimensional search landscape. These particles iteratively refine their positions by leveraging both individual insights and shared swarm knowledge, guided by a fitness function that quantifies solution quality. This section outlines the operational mechanics of the standard PSO algorithm, its critical parameters, inherent shortcomings, and advanced modifications aimed at enhancing its efficacy.

In the standard PSO model, a swarm comprises multiple particles, each defined at iteration k by its velocity v_i^k and position x_i^k within a D-dimensional problem space, where x_i^k denotes a prospective solution. The algorithm updates these attributes iteratively using the following equations:

$$v_i^{k+1} = \omega v_i^k + c_1 \cdot r_1 \cdot (p_{bi}^k - x_i^k) + c_2 \cdot r_2 \cdot (g_b^k - x_i^k) \tag{3.133}$$

$$x_i^{k+1} = x_i^k + v_i^{k+1} \tag{3.134}$$

Where:

ω: The inertia weight, which moderates the influence of the particle prior velocity.

c_1: The cognitive coefficient, governing the particle attraction to its personal best position p_{bi}^k.

c_2: The social coefficient, dictating the particle alignment with the swarm global best position g_b^k.

r_1 and r_2: Random variables drawn uniformly from [0,1], injecting stochastic variation into the updates.

These equations integrate three fundamental influences:

1. Inertia Term (ωv_i^k): Maintains the particle's momentum from its previous trajectory.

2. Cognitive Term ($c_1 \cdot r_1 \cdot (p_{bi}^k - x_i^k)$): Drives the particle toward its historically best-known position.

3. Social Term ($c_2 \cdot r_2 \cdot (g_b^k - x_i^k)$): Pulls the particle toward the swarm's collectively optimal solution.

The process repeats until a predefined stopping condition is satisfied, such as reaching a maximum iteration count or achieving an acceptable fitness threshold.

3.6.5.2 Core Parameters Shaping PSO Performance

The success of PSO hinges on the careful calibration of several parameters, which collectively determine the algorithm's balance between exploration (searching new regions) and exploitation (refining known solutions):

1. Swarm Size (N)

The number of particles influences the algorithm's capacity to survey the search domain. A larger swarm bolsters wider exploration but escalates computational cost, whereas a smaller swarm risks may miss optimal solutions. Common swarm sizes range between 40 and 100 particles.

2. Inertia Weight (ω)

This parameter regulates the persistence of a particle's prior velocity. A higher ω favors expansive exploration, while a lower value emphasizes localized refinement. Dynamic adjustment of ω is often employed to optimize this trade-off over time.

3. Acceleration Coefficients (c_1 and c_2)

The coefficients c_1 and c_2 dictate the weight of individual versus collective experience. Nullifying c_1 diminishes a particle self-directed search, risking premature convergence, while setting $c_2 = 0$ isolates particles, undermining swarm synergy. Typically, values such as $c_1 = c_2 = 2$ are adopted for balance.

4. Velocity Constraint ($v_{\max}$)

A cap on velocity limits the magnitude of positional shifts, preventing particles from overshooting promising areas. An overly high $v_{\max}$ may cause erratic movement, while a restrictive cap can confine the swarm to suboptimal zones. This parameter is often scaled to the problem domain's bounds.

3.6.5.3 Challenges in Standard PSO and Mitigation Strategies

While the standard PSO algorithm is computationally efficient and conceptually straightforward, it encounters difficulties in complex optimization tasks:

Early Convergence: Particles may coalesce prematurely around local optima, particularly in problems with multiple peaks.

Search Stagnation: Over time, particle diversity diminishes, stalling progress toward the global optimum.

To overcome these issues, researchers have introduced refinements, especially for continuous, nonlinear problems like those in electrical engineering optimization:

1. Time-Varying Inertia Weight (TVIW)

The inertia weight is progressively reduced over iterations to shift from broad exploration to precise exploitation:

$$\omega(k) = \omega_{\text{start}} - \left(\omega_{\text{start}} - \omega_{\text{end}}\right) \cdot \frac{k}{k_{\text{total}}} \tag{3.135}$$

Where:

ω_{start} : Starting inertia weight (e.g., 0.9),

ω_{end} : Ending inertia weight (e.g., 0.4),

k : Current iteration,

k_{total} : Total iterations.

This approach promotes extensive searching initially and focused convergence later.

2. Dynamic Tuning of Acceleration Coefficients

The coefficients c_1 and c_2 are adjusted nonlinearly to enhance adaptability:

$$c_i(k) = c_{i,\text{init}} + (c_{i,\text{final}} - c_{i,\text{init}}) \cdot \left(1 - \cos\left(\frac{\pi k}{2k_{\text{total}}}\right)\right) \tag{3.136}$$

Where:

$c_{i,\text{init}}$: Initial value of c_i ,

$c_{i,\text{final}}$: Final value of c_i .

This method amplifies early diversity and ensures late-stage convergence.

These adaptations bolster PSO resilience, mitigating early entrapment and stagnation while expediting the identification of globally optimal solutions.

PSO harnesses the collective behaviour of natural swarms to address intricate optimization challenges. Though effective in its basic form, the standard algorithm is prone to premature convergence and reduced effectiveness in prolonged iterations. By implementing adaptive adjustments to parameters such as inertia weight and acceleration coefficients, PSO performance is markedly improved, rendering it more adept for demanding applications, including power system optimization. These enhancements strike an optimal balance between global exploration and local refinement, ensuring robust and efficient solution discovery.

3.7 Summary

This chapter outlines the methodological framework for analyzing uncertainties, harmonics, risks, and optimizations in power systems. It is structured into six sections: probabilistic and statistical foundations (3.1), distributed generation modeling (3.2), harmonic power flow analysis (3.3), risk assessment (3.4), power quality evaluation (3.5), and active power filter optimization (3.6).

The chapter introduces essential tools, including the three-point estimation method and MCS for probabilistic power flow; Newton-Raphson and correlation modeling for distributed generation; harmonic source models and calculation methods; state enumeration and MCS for risk indicators; a comprehensive index system for power quality; and particle swarm optimization for active power filters.

The probabilistic and harmonic power flow models developed here form the basis for Chapter 4, where the three-point estimation method is applied to evaluate uncertainty propagation in distribution networks. The probabilistic framework is further extended in Chapter 5 through a three-phase MCS analysis to study stochastic harmonic and risk characteristics. Finally, the optimization concepts introduced in this chapter support the design and configuration of active power filters in Chapter 6, improving system power quality and harmonic mitigation performance.

Chapter 4 Probabilistic Power Flow Calculation Using the Three-Point Estimation Method

4.1 Introduction

This chapter analyses probabilistic power flow in a radial distribution network with uncertain loads and distributed generation (PV and wind). A three-point estimation method (3PEM) with Copula/Nataf dependence is used to obtain statistics of voltages, branch powers, and losses with few deterministic runs.

The objectives of this chapter are to develop and evaluate a probabilistic analysis framework based on the 3PEM combined with Copula modelling. First, a clear 3PEM–Copula workflow is established for the IEEE 33-bus distribution system. The accuracy of the proposed approach is then verified through comparison with Monte Carlo Simulation (MCS), focusing on key statistical measures such as mean values and standard deviations.

In addition, the study is extended to probabilistic harmonic power flow analysis by incorporating harmonic sources at selected nodes (e.g., buses 18, 21, and 33), and by evaluating total harmonic distortion (THD) statistics across the network. The impact of input correlations, including load–load, load–PV, and load–wind relationships, on system performance indicators such as power losses, line flows, and voltage profiles is also quantified. Finally, an error analysis is conducted to assess the performance of 3PEM, highlighting the conditions under which it aligns closely with MCS results as well as scenarios where notable discrepancies arise.

The motivation for testing the 3PEM in this chapter is to investigate its effectiveness in addressing the computational challenges associated with probabilistic power flow analysis in distribution networks with multiple sources of uncertainty. Although MCS provides highly accurate results, its computational burden becomes prohibitive when a large number of uncertain variables and scenarios are involved.

Therefore, 3PEM is explored as a more efficient alternative that can significantly reduce the number of required power flow evaluations while still capturing key statistical characteristics of system outputs. This chapter aims to evaluate the accuracy and applicability of 3PEM under practical operating conditions, particularly in the presence of correlated uncertainties. The performance of 3PEM is validated through comparison with MCS results, ensuring that the proposed method maintains an acceptable level of accuracy while improving computational efficiency.

All simulations, programming, and numerical analyses in this study were conducted in MATLAB (R2021b) Update 7 environment.

4.2 Calculation process

Probabilistic power flow (PPF) analysis in distribution networks with uncertain loads and distributed generation (DG) requires modeling of stochastic inputs to capture their variability and interdependencies. The three-point estimation method (3PEM) addresses this by selecting three representative points from the probability distributions of these inputs, performing a limited number of deterministic power flow calculations based on those points, and using the results to approximate the probability distributions of output variables (e.g., node voltages, branch powers). This approach bridges the modeling of inputs to outputs by leveraging statistical moments to propagate uncertainty efficiently, without the computational burden of full MCS. This section details the computational procedure for PPF analysis using the 3PEM, leveraging statistical moments and dependency modeling via Copula functions. The method is validated against a flowchart and consists of the following steps:

Step 1: Input the Raw Data of the Distribution Network

The procedure begins with the input of the distribution network's raw data, including:

1. Network Topology and Line Parameters: The topological structure (nodes and branches) and electrical parameters (e.g., resistance, reactance) of the network.

2. Load Parameters: Statistical characteristics of nodal loads, represented by mean values and standard deviations to capture demand uncertainty.

3. DG Output Characteristics: Statistical distributions of DG outputs (e.g., wind, solar), including distribution type (e.g., normal, Weibull) and parameters (e.g., mean, variance).

These establish the foundation for probabilistic analysis.

Step 2: Compute the Spearman Rank Correlation Coefficient Matrix Using Copula

Dependencies among the m input random variables X_i (e.g., loads, DG outputs) are modeled using a multi-dimensional Copula function. The Spearman rank correlation coefficient matrix C_X is computed to quantify the monotonic relationships among X_i. Spearman correlation is selected for its robustness over Kendall correlation, with a Gaussian Copula typically employed for simplicity, though alternatives may be explored for complex dependencies.

Step 3: Compute the Correlation Coefficient Matrix of Standard Normal Variables

For each random variable X_i, calculate its mean μ_i and standard deviation σ_i. Transform X_i into independent standard normal variables Z_i using the inverse cumulative distribution function (CDF). Compute the correlation coefficient matrix C_Z of Z_i, preserving the dependency structure in the standard normal space.

Step 4: Perform Cholesky Decomposition

Decompose C_Z using Cholesky decomposition to obtain a lower triangular matrix B such that $C_Z = BB^T$. This matrix facilitates the generation of correlated standard normal variables, ensuring adherence to the specified correlation structure.

Step 5: Compute Estimation Points and Transform Back to the Original Space

To handle correlations properly, first work in the independent standard normal space. Apply the 2m+1 Point Estimate Method (PEM) to compute estimation points and weights. For each of the m variables, define two off-center points per variable (to match mean and variance, assuming zero skewness for simplicity) and one central point. The locations in the independent space U are set as follows: for the k-th variable's pair, $U_k = \pm\sqrt{3}$, $U_{i\neq k} = 0$; for the central point, all $U_i = 0$. Weights are

$w_{k,\pm} = 1/(2m)$for off-center points and $w_0 = 1 - 1/m$ for the central weight; in this formulation, the central weight is always non-negative for $m \geq 1$, and the sum of all weights equals 1. Therefore, no negative weight issue arises in this simplified implementation. Negative weights may arise in more general point estimation schemes that incorporate higher-order moments (e.g., skewness or kurtosis), but such effects are not present under the current zero-skewness assumption. Transform to correlated normal space: $Z_r = BU_r$. Then, transform back to the original space: $X_r = F_i^{-1}(\Phi(Z_r))$ (or $X_r = \mu + \sigma \cdot Z_r$ if normal), yielding the sample matrix X_r with $2m + 1$estimation points.

Step 6: Initialize the Counter

Set the iteration counter $j = 1$ to begin processing the estimation points.

Step 7: Compute Estimation Points for State Variables

For the j-th estimation point in X_r, compute three estimation points for each state variable (e.g., voltages, flows) using the mean, standard deviation, and position coefficients (0, ±1) of the input variables. These points represent the deterministic scenarios for power flow analysis.

Step 8: Perform Power Flow Calculations for Each Estimation Point

Conduct a deterministic power flow calculation for each estimation point in X_r, obtaining state variable values (e.g., voltage magnitudes, phase angles, branch flows). Record these results for all $2m+1$ points.

Step 9: Compute the Raw Moments of the Output Variables

Calculate the raw moments of output variables (e.g., mean, variance) using the power flow results and weights:

$$E[Y^k] = \sum_{r=1}^{2m+1} w_r Y_r^k$$

where Y_r is the output value at the r-th point, and w_r is its weight.

Step 10: Fit the Probability Distribution of the Output Variables

Fit the probability distribution of output variables using the Cornish-Fisher series expansion, based on the computed raw moments. This method approximates the cumulative distribution function, capturing the statistical behaviour of outputs.

Step 11: Repeat the Calculations

Increment $j = j + 1$ and repeat Steps 7–10 until $j > 2m + 1$ or a predefined accuracy (e.g., moment convergence) is achieved.

Step 12: Output the Final Results

Summarize the results to derive the final probability distributions of output variables, providing a comprehensive statistical description of the network under uncertainty.

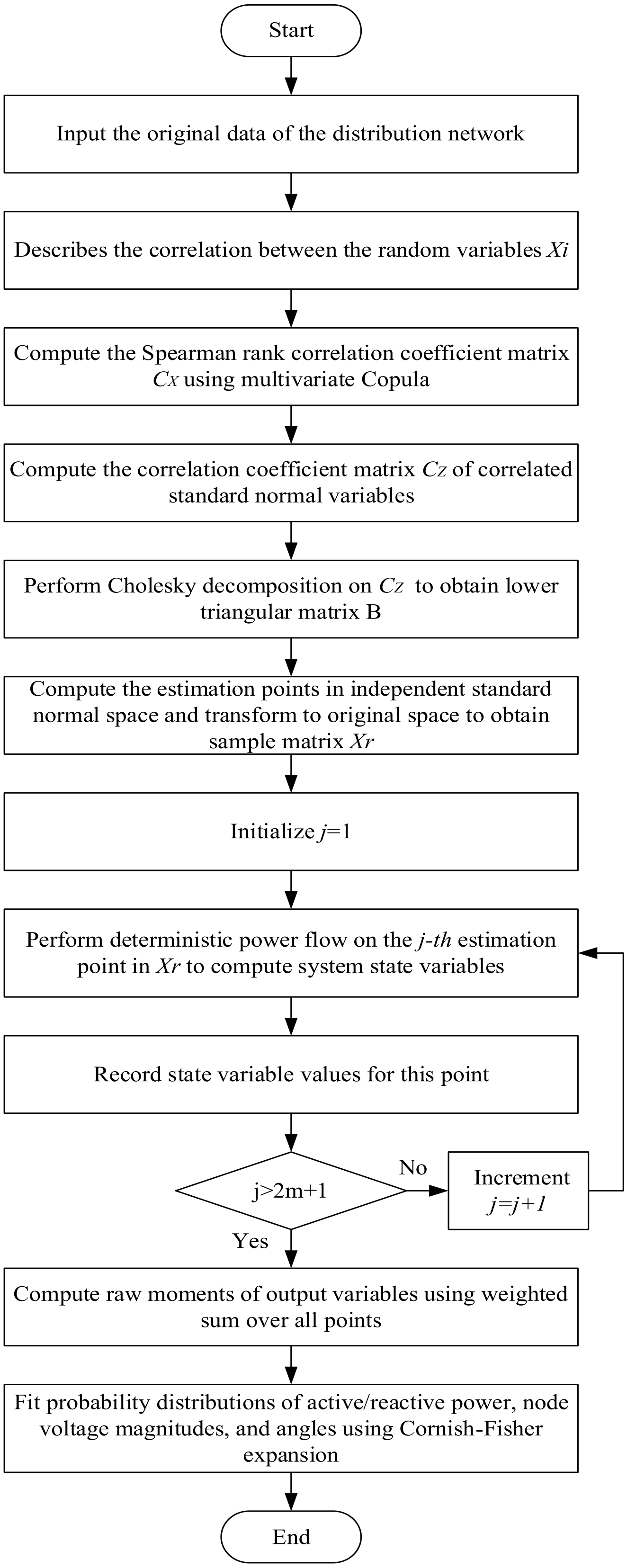

Figure 4-1 Flowchart of the Probabilistic Power Flow Analysis Using Copula and Nataf Transformation-Based 2m+1 Point Estimate Method

4.3 Example Illustration, Network Parameters, and Topology

The IEEE 33-node test system is utilized to validate the stochastic power flow model for distribution networks proposed in this study, which is based on the three-point estimation method (2m+1 PEM). The node topology is illustrated in the Figure 4-2. The base voltage V_B of the IEEE 33-node radial distribution system is 12.66 kV, and the base capacity is 100 MWA. Node 1 serves as the slack bus with a voltage of 1.00 per unit (p.u.) (phase angle 0°). Loads are assumed to follow a normal distribution, with means adopted from standard IEEE data and a standard deviation of 20% of the mean active power to capture demand uncertainty. A constant lagging power factor of 0.95 is assumed for all loads. The system comprises 32 branches. Detailed branch impedances and base nodal loads are as per Baran and Wu [235]. To evaluate the effectiveness of the proposed algorithm, its results are compared with those obtained from 10,000 MCS, assuming the same input distributions and using mean, variance, and distribution fits of output variables (e.g., voltages, flows) as metrics. Node loads and branch impedances are listed in Table AP 4 (adopted from standard datasets).

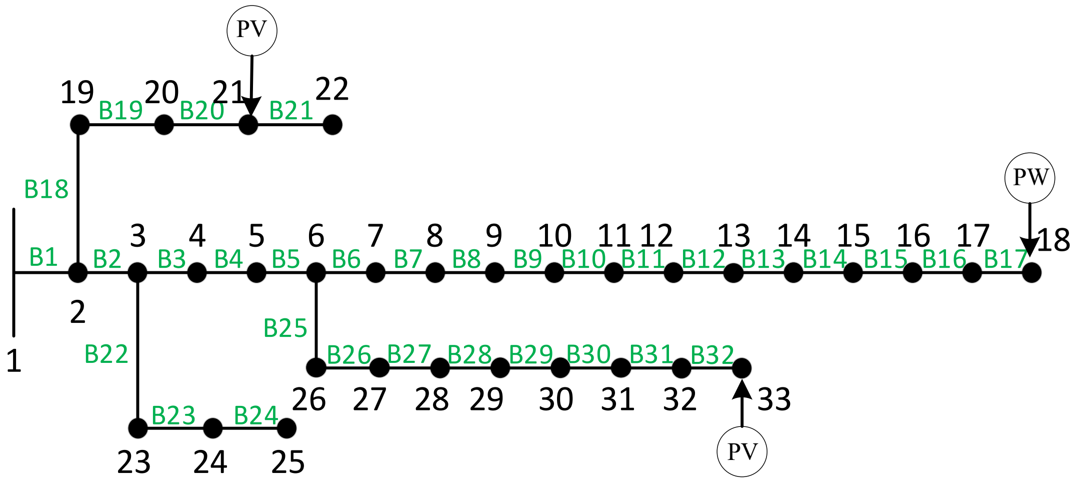

Figure 4-2 Topology of IEEE 33-bus System

The parameters of PV cell modules (modeled with Beta-distributed irradiance) and wind turbines (modeled with Weibull-distributed wind speeds) are presented in Table 4-1 and Table 4-2, respectively. Distributed generation sources are modeled as PQ nodes, with their output treated as negative load injections.

Table 4-1 Relevant Parameters of Photovoltaic Cells

Access Node	**Total Area (m^2)**	**Photoelectric Conversion Efficiency (%)**	**Mean Output (MW)**	**α**	**β**
21	3150	13.44	0.1230	3.1253	7.7432
33	3150	13.44	0.1230	2.7732	6.7782

Table 4-2 Relevant Parameters of Wind Turbines

Access Node	**Cut-in Wind Speed (m/s)**	**Cut-out Wind Speed (m/s)**	**Rated Wind Speed (m/s)**	**Rated Output (MW)**	**K**	**C**
18	4	25	15	0.2000	4.1416	11.8003

The parameters of the Beta and Weibull distributions used in this study are derived based on representative statistical characteristics of renewable energy sources reported in the literature, combined with typical operational profiles of photovoltaic generation and wind speed.

For photovoltaic systems, solar irradiance is commonly modeled using a Beta distribution due to its bounded nature and asymmetric variability. The shape parameters (α, β) are obtained by matching the mean and variance of normalized solar irradiance data, which are inferred from typical daily irradiance profiles under standard meteorological conditions. The corresponding PV output is then calculated based on panel area and conversion efficiency.

For wind power generation, wind speed is modeled using a two-parameter Weibull distribution, which is widely accepted for representing wind characteristics. The scale parameter (c) and shape parameter (k) are estimated based on typical wind speed distributions reported for similar distribution-level studies, ensuring realistic representation of variability. These parameters are consistent with commonly used values in probabilistic power flow and renewable integration studies.

It should be noted that the adopted distributions are not based on a specific measured dataset, but are selected to represent typical stochastic behaviour of renewable generation in distribution networks. This approach is widely used in probabilistic analysis to ensure generality and comparability of results.

4.4 Computational Results and Analysis

The moments of various orders for the output of photovoltaic and wind power sources are listed in Table 4-3. The first-order moment of each distributed generation source's output corresponds to its expected value, while the second-order moment represents the variance of the output fluctuations.

It should be noted that the first-order moments of PV and wind outputs appear as negative values because distributed generation is modelled as negative power injection (i.e., negative load) in the power flow formulation. Therefore, the negative sign reflects the modelling convention rather than negative physical generation.

Table 4-3 Moments of Distributed Generation Sources

Order of Moments	Moments of PV1 Output	Moments of PV2 Output	Moments of Wind Power Output
1st Order	-0.113715	-0.122872	-0.1202929
2nd Order	0.009102	0.007578	0.006281
3rd Order	0.000844	-0.001059	-0.000649
4th Order	0.000149	0.000171	7.8489e-05
5th Order	1.8848e-05	-2.9283e-05	-1.0006e-05

The first-order raw moment ($\mu_1 = E[X]$) is the mean, representing the expected value or central tendency of the variable.

The second-order raw moment ($\mu_2 = E[(X - E[X])^2$) is used to derive the variance, which measures dispersion around the mean.

The third-order raw moment ($\mu_3 = E[(X - E[X])^3$) is used to derive the third central moment, which measures skewness (asymmetry of the distribution; standardized skewness = third central / σ^3).

The fourth-order raw moment ($\mu_4 = E[(X - E[X])^4$) relates to the fourth central moment, describing kurtosis (tailedness; excess kurtosis = (fourth central / σ^4) - 3, where 0 indicates mesokurtic like normal, positive leptokurtic with heavy tails, negative platykurtic with light tails).

The fifth-order raw moment (μ_5) contributes to higher-order asymmetry assessments, useful for non-Gaussian distributions in Cornish-Fisher approximations.

The statistical moments of network loss are summarized in Table 4-4. The first-order moment (mean) is 0.166 MW, which is lower than the typical deterministic value of approximately 0.203 MW for the IEEE 33-bus system without distributed generation. This reduction (approximately 18%) reflects the impact of PV and wind integration in reducing network losses through local power injection.

The second-order raw moment corresponds to $E[X^2]$, from which the variance is calculated as $\mathrm{Var}(X) = E[X^2] - (E[X])^2$. Based on the obtained values, the variance is approximately 0.00059 MW^2, yielding a standard deviation of about 0.024 MW. This indicates moderate variability in network losses despite the uncertainty in distributed generation outputs, which can be attributed to the partial balancing effect between local generation and load demand.

Higher-order moments are used to characterize the shape of the distribution. The standardized skewness, derived from the third-order moment, is positive (approximately 2.8), indicating a right-skewed distribution with a higher probability of larger loss values under certain operating conditions. The excess kurtosis, derived from the fourth-order moment, is close to zero (approximately 0.1), suggesting a near-normal tail behaviour with slight deviation.

The fifth-order moment is small and positive, which is consistent with mild higher-order asymmetry. Overall, these results indicate that while the loss distribution is approximately symmetric in terms of tail behaviour, it exhibits noticeable skewness due to stochastic variations in distributed generation.

Compared with Monte Carlo Simulation (10,000 samples), the moments obtained using the point estimation method are expected to show close agreement, while requiring significantly fewer evaluations (2m+1 = 71 for m = 35), demonstrating the computational efficiency of the proposed approach.

Table 4-4 Moments of Network Loss

	1st Order	**2nd Order**	**3rd Order**	**4th Order**	**5th Order**
Network Loss (MW)	0.166344	0.028247	0.004889	0.000861	0.000154

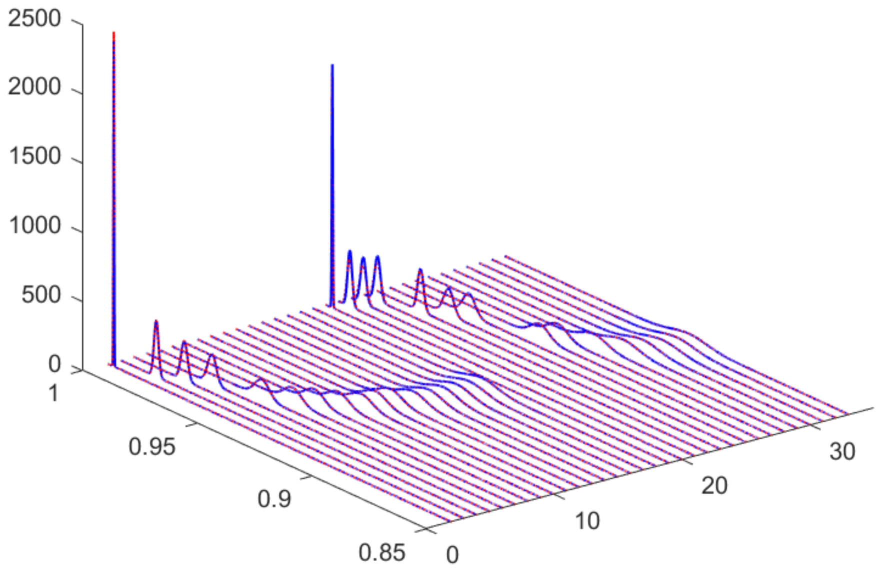

Figure 4-3 Node Voltage Probability Distributions

Figure 4-3 presents the probability density functions (PDFs) of nodal voltages across the IEEE 33-bus system. The x-axis represents node indices (1–33), the y-axis denotes voltage magnitude in per unit (p.u.), and the z-axis indicates probability density.

The voltage PDFs at head-end nodes (e.g., Nodes 1–3) exhibit highly concentrated peaks within the range of approximately 0.95–1.0 p.u., indicating low variability and strong voltage stability. This behaviour is attributed to the proximity of these nodes to the slack bus, where voltage regulation is most effective and less influenced by downstream uncertainties.

In contrast, nodes located further along the feeder exhibit broader distributions, reflecting increased sensitivity to stochastic load variations and distributed generation (DG) fluctuations. At DG-connected nodes (e.g., Node 18 for wind generation and Nodes 21 and 33 for photovoltaic systems), local power injections partially offset voltage drops along the feeder. As a result, the voltage distributions at these nodes remain relatively concentrated, typically centred within the range of 0.92–0.95 p.u., although with slightly increased dispersion compared to upstream nodes.

A close agreement is observed between the results obtained using MCS and the Nataf–3PEM approach, as indicated by the overlap between the blue solid lines MCS and red dashed lines 3PEM. This confirms the capability of the proposed method to accurately capture the probabilistic characteristics of nodal voltages.

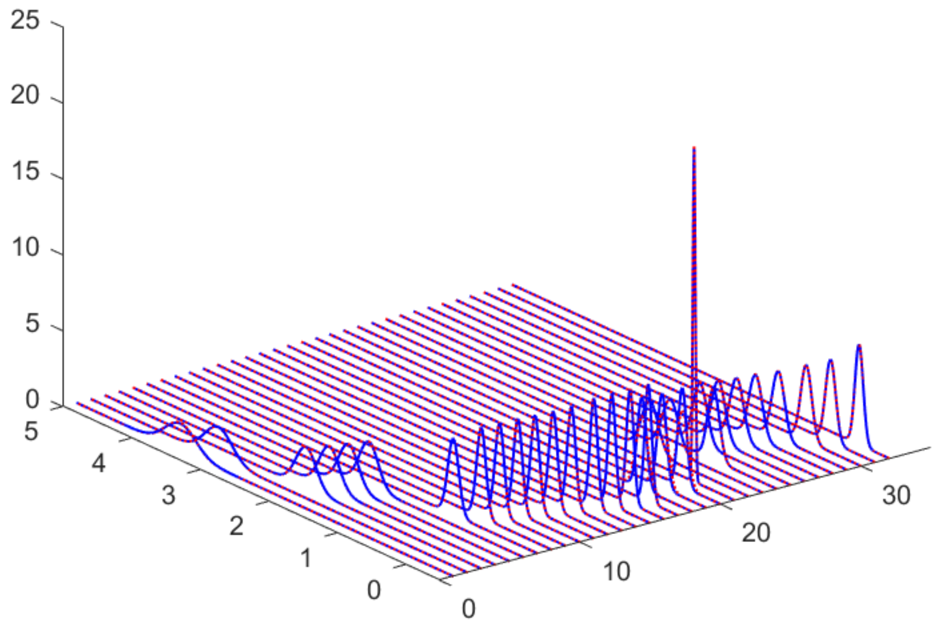

Figure 4-4 Branch Active Power Probability Distributions

Figure 4-4 illustrates the probability density functions of active power flows across the branches of the IEEE 33-bus system. The x-axis represents branch indices, the y-axis denotes active power flow (MW), and the z-axis corresponds to probability density.

Branches located near the source (head-end branches) exhibit relatively wider distributions of active power flow, reflecting their role in transmitting aggregated power to downstream nodes. The spread of these distributions indicates higher variability due to the cumulative effect of stochastic loads and distributed generation.

In contrast, branches located near the end of the feeder (tail-end branches) show more concentrated distributions with higher probability density peaks. These branches typically carry lower power levels and are influenced primarily by local load and generation conditions, resulting in reduced variability.

Overall, the probabilistic behaviour of branch power flows demonstrates the spatial propagation of uncertainty along the radial network, with variability decreasing toward the feeder end. The close overlap between MCS and 3PEM results further validates the accuracy of the proposed probabilistic modelling approach.

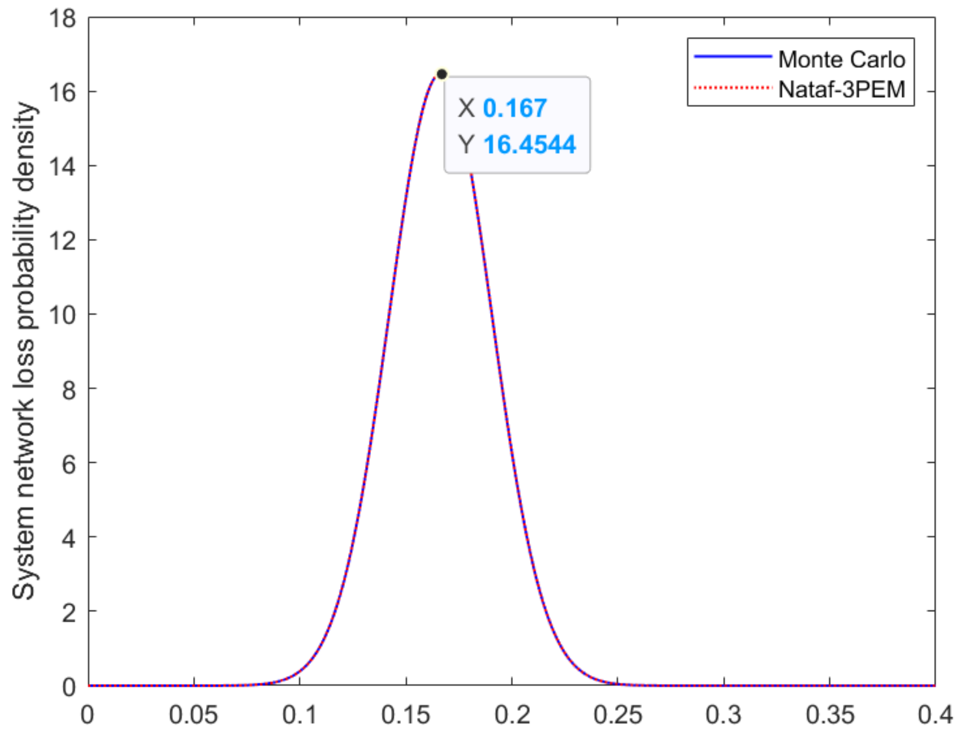

Figure 4-5 System Network Loss Probability Fluctuation Curve

Figure 4-5 presents the probability density function of total system network losses. The distribution exhibits a positively skewed shape, with a mean value of approximately 0.167 MW. Compared to the deterministic baseline value of approximately 0.203 MW (without distributed generation), this represents a reduction of around 18%, demonstrating the effectiveness of distributed generation in reducing network losses through localized power supply.

The positive skewness indicates that while most operating conditions result in moderate loss levels, there remains a non-negligible probability of higher losses under certain scenarios, such as reduced renewable generation or increased load demand. This observation is consistent with the higher-order moment analysis presented in Table 4-4.

The results obtained using the Nataf–3PEM method closely match those from MCS, with only minor deviations observed in the tails of the distribution. These differences are primarily due to the approximation of higher-order moments in the point estimation method. Nevertheless, the overall agreement confirms that the proposed method provides an accurate and computationally efficient alternative to full Monte Carlo simulation.

The statistical moments of nodal voltages across the IEEE 33-bus system are summarized in Table 4-5. The first-order moments, corresponding to the expected values of nodal voltages, range from approximately 0.997 p.u. at upstream nodes (e.g., Node 2) to 0.919 p.u. at downstream nodes (e.g., Node 33). This trend reflects the typical voltage drop along radial distribution feeders due to line impedance and load accumulation.

At nodes with DG, such as Node 18 (wind) and Node 21 (photovoltaic), the mean voltage levels are noticeably higher compared to adjacent nodes, indicating that local power injection partially compensates for voltage drops. As a result, DG contributes to voltage support and improves the overall voltage profile, particularly in the downstream sections of the network.

It is observed that several nodes, particularly in the mid- and end-sections of the feeder (e.g., Nodes 7–18 and 26–33), exhibit mean voltage values below 0.95 p.u. While these values do not necessarily indicate voltage limit violations, they suggest increased sensitivity to operating conditions and potential risk of undervoltage under adverse scenarios. These values represent statistical expectations derived from probabilistic analysis rather than deterministic steady-state operating points.

The second-order raw moments indicate that voltage variability remains relatively low across the system. The corresponding standard deviations are generally below 0.02 p.u., suggesting that voltage fluctuations are limited despite the presence of stochastic load and distributed generation. This indicates a relatively stable voltage profile under uncertainty.

Higher-order moments provide further insight into the distribution characteristics. The third-order moments indicate predominantly negative skewness, implying a slight bias toward lower voltage values and a higher likelihood of undervoltage conditions compared to overvoltage scenarios. The fourth-order moments suggest kurtosis values close to that of a normal distribution, with slight deviations indicating mildly platykurtic to near-mesokurtic behaviour.

Overall, the results show that voltage variability tends to increase toward the downstream nodes, while distributed generation plays a mitigating role by improving voltage levels and reducing the severity of voltage drops. The consistency of these statistical characteristics with the physical behaviour of radial distribution systems further supports the validity of the probabilistic modelling approach.

Table 4-5 Moments of Node Voltage

Node Index	**1st Order**	**2nd Order**	**3rd Order**	**4th Order**	**5th Order**
2	0.997334	0.994675	0.992023	0.989378	0.986741
3	0.984394	0.969032	0.953911	0.939027	0.924376
4	0.977766	0.956028	0.934776	0.913997	0.893683
5	0.971257	0.943343	0.916235	0.88991	0.864344
6	0.954999	0.912033	0.87101	0.83184	0.794441
7	0.947251	0.897299	0.849994	0.805197	0.762772

8	0.943253	0.889743	0.839284	0.7917	0.746829
9	0.938379	0.880573	0.826347	0.775477	0.727754
10	0.93397	0.872323	0.814766	0.761026	0.710849
11	0.933343	0.871152	0.813127	0.758987	0.708471
12	0.932286	0.869182	0.810371	0.755561	0.704478
13	0.928187	0.861561	0.799746	0.742391	0.689175
14	0.926779	0.858953	0.796121	0.737914	0.683989
15	0.926193	0.857869	0.794617	0.73606	0.681846
16	0.925816	0.857173	0.793654	0.734876	0.680481
17	0.925809	0.857166	0.793654	0.734886	0.680504
18	0.92618	0.857857	0.794618	0.736081	0.681894
19	0.996977	0.993964	0.990959	0.987964	0.984978
20	0.994952	0.989932	0.984938	0.979971	0.97503
21	0.994699	0.989427	0.984186	0.978975	0.973793
22	0.994063	0.988163	0.9823	0.976475	0.970686
23	0.980812	0.961995	0.94354	0.92544	0.90769
24	0.974149	0.948971	0.924448	0.900563	0.877299
25	0.970827	0.942513	0.915031	0.888357	0.862467
26	0.945533	0.894048	0.845382	0.799379	0.755893
27	0.943265	0.889768	0.839321	0.79175	0.746891
28	0.933095	0.870696	0.812498	0.758217	0.707586
29	0.925838	0.857218	0.793723	0.734967	0.680594
30	0.922812	0.851631	0.785984	0.725439	0.669595
31	0.919866	0.846207	0.778498	0.716252	0.659026

32	0.919359	0.845277	0.777218	0.714686	0.657229
33	0.919577	0.84568	0.777775	0.715371	0.65802

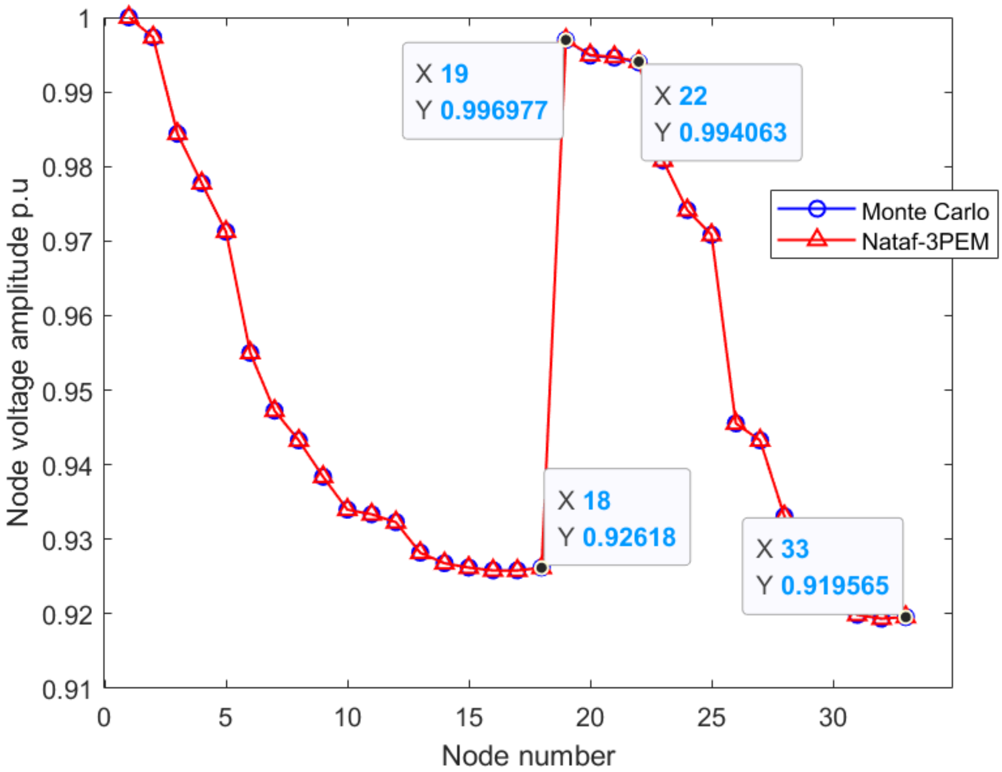

Figure 4-6 Comparison of Expected Value of Voltage Amplitude at Each Node

The node voltage profile shown in Figure 4-6 reflects the combined effects of network topology and distributed generation on voltage distribution across the IEEE 33-bus system. In this study, the primary reference for voltage regulation is the slack bus (Node 1), which maintains a fixed voltage of 1.0 p.u. Therefore, the voltage magnitude at each node is strongly influenced by its electrical distance from the slack bus rather than solely by the presence of local generation.

As expected in radial distribution networks, voltage magnitudes generally decrease along the feeder due to cumulative line impedance and power flow. Nodes located further from the slack bus, such as Node 18 and Node 33, exhibit lower voltage levels, with values of approximately 0.926 p.u. and 0.920 p.u., respectively. This reflects the significant voltage drop caused by the long electrical distance and accumulated load demand.

Although distributed generation is connected at certain nodes (e.g., wind generation at Node 18 and photovoltaic generation at Node 21), its impact on voltage support is limited by several factors. First, the magnitude of the injected power may not be sufficient to fully compensate for upstream voltage drops. Second, the effectiveness of voltage support depends on the local network impedance and the position of the generation within the feeder. For example, despite the presence of distributed generation at Node 18, its relatively distant location from the slack bus and the surrounding load conditions result in a net voltage level that remains relatively low.

In contrast, nodes such as Node 19 and Node 22 exhibit higher voltage magnitudes (approximately 0.997 p.u. and 0.994 p.u., respectively). This is primarily because these nodes are electrically closer to the slack bus and are also influenced by nearby distributed generation (e.g., the photovoltaic system at Node 21), which provides localized voltage support and partially offsets voltage drops in adjacent branches.

Overall, the voltage profile demonstrates that nodal voltage levels are governed by a combination of electrical distance from the slack bus, load distribution, and the location and capacity of distributed generation. The results highlight that while distributed generation can improve local voltage conditions, it does not uniformly eliminate voltage drops across the network.

The statistical moments of branch active power flows are summarized in Table 4-6. The first-order moments represent the expected values of branch power flows (in MW), which decrease progressively from upstream to downstream branches. For example, Branch 2 exhibits a high mean power flow of approximately 3.482 MW, reflecting its role in supplying the entire downstream network. In contrast, some downstream branches (e.g., Branch 33) exhibit small negative mean values (approximately −0.063 MW), indicating the occurrence of reverse power flow due to local distributed generation exceeding local demand.

The second-order raw moments correspond to $E[P^2]$ (in MW²), from which the variance can be derived as $\mathrm{Var}(P) = E[P^2] - (E[P])^2$. Based on these values, the standard deviation of branch power flows typically lies in the range of approximately 0.1–0.4 MW. This indicates that the relative variability of branch flows is non-negligible, particularly for upstream branches where both load aggregation and distributed generation uncertainties accumulate.

The uncertainty in branch power flows can be interpreted through the magnitude of the variance and higher-order moments. Branches with larger second-order moments (e.g., Branches 2–7) exhibit higher variability, reflecting the cumulative effect of stochastic load fluctuations and distributed generation along the feeder. In contrast, downstream branches generally show smaller variance, as they are influenced primarily by localized conditions.

The third-order moments indicate that the distributions of branch power flows are generally asymmetric. Positive skewness is observed in several heavily loaded branches, suggesting a higher probability of extreme high-flow events, which may be associated with potential overload conditions under certain scenarios. Conversely, near-zero or negative skewness in some downstream branches reflects more balanced or slightly reverse-flow-dominated behaviour.

The fourth-order moments suggest that the distributions are generally close to mesokurtic, with kurtosis values near those of a normal distribution, indicating limited presence of extreme outliers. However, slight deviations in kurtosis imply that tail behaviour may still be influenced by the interaction between stochastic loads and distributed generation.

Overall, the results demonstrate that uncertainty in branch power flows is spatially dependent and propagates along the network. It is highest in upstream branches due to aggregation effects and gradually decreases toward downstream sections, except in areas influenced by distributed generation, where local uncertainty may increase due to intermittent power injections.

Table 4-6 Moments of Branch Active Power

Branch Index	1st Order	2nd Order	3rd Order	4th Order	5th Order
2	3.481762	12.16975	42.701	150.3981	531.6822105
3	3.137685	9.884337	31.26043	99.24629	316.2658917

4	2.063883	4.28131	8.925675	18.6989	39.35634385
5	1.92802	3.737725	7.285312	14.27453	28.10913642
6	1.853292	3.454398	6.47504	12.20328	23.11882444
7	1.763338	3.127681	5.579759	10.00999	18.05354917
8	0.735115	0.546703	0.411183	0.312567	0.239953238
9	0.531773	0.287377	0.157741	0.087861	0.049597969
10	0.469217	0.224529	0.109485	0.054329	0.027387274
11	0.407143	0.169911	0.072591	0.031684	0.014092453
12	0.361839	0.134981	0.051812	0.020402	0.008212323
13	0.301385	0.094723	0.030931	0.010439	0.003619914
14	0.240149	0.061356	0.016544	0.00466	0.001357399
15	0.119857	0.017457	0.002878	0.000514	9.67945E-05
16	0.059776	0.006514	0.000787	0.000106	1.51242E-05
17	-0.00026	0.002792	4.5E-05	1.92E-05	6.00331E-07
18	-0.06029	0.006282	-0.00065	7.85E-05	-1.006E-05
19	0.234119	0.06172	0.017391	0.005104	0.001539965
20	0.14404	0.027325	0.005527	0.001177	0.000259884
21	0.053715	0.009103	0.000844	0.00015	1.88484E-05
22	0.090045	0.008433	0.000818	8.19E-05	8.43245E-06
23	0.939804	0.898313	0.87259	0.860365	0.859902682
24	0.846575	0.731243	0.643698	0.576557	0.524511418
25	0.421337	0.184669	0.08383	0.039281	0.018948408
26	0.821724	0.685294	0.57963	0.496681	0.430592733
27	0.759564	0.586762	0.460573	0.366836	0.295964342

28	0.696818	0.49511	0.358282	0.263573	0.196689622
29	0.627558	0.402813	0.264027	0.176302	0.119597941
30	0.501176	0.25929	0.138034	0.075282	0.041864291
31	0.298059	0.095201	0.032091	0.011243	0.004043117
32	0.147206	0.027067	0.00548	0.001164	0.000254302
33	-0.06287	0.007578	-0.00106	0.000172	-2.9237E-05

The statistical moments of branch reactive power flows are presented in Table 4-7. The first-order moments, representing the expected reactive power flows (in MVar), show a clear decreasing trend from upstream to downstream branches. High mean values are observed in upstream branches (e.g., approximately 2.26 MVar at Branch 2), reflecting their role in supplying reactive power to the network. In contrast, some downstream branches (e.g., Branch 33) exhibit small negative mean values, indicating localized reverse reactive power flow influenced by distributed generation.

The variability of reactive power flows can be assessed through the second-order moments, from which the variance and standard deviation are derived. Overall, the standard deviation of reactive power flows remains relatively moderate, typically within the range of approximately 0.1–0.3 MVar. This suggests that, although uncertainty is present due to stochastic loads and distributed generation, reactive power flows are comparatively stable, particularly in downstream sections where flows are smaller in magnitude.

From an uncertainty perspective, upstream branches exhibit higher variability due to the aggregation of load demand and reactive power requirements, while downstream branches are primarily influenced by local conditions. In regions with distributed generation (e.g., around Branches 18–22), variability may increase due to fluctuations in power injection and the associated reactive power behaviour, even though a constant power factor assumption (0.95 lagging) is applied in the model.

Overall, the probabilistic characteristics of reactive power flows closely follow those of active power flows, with uncertainty propagating along the feeder and being partially mitigated by distributed generation. These results confirm that the proposed probabilistic framework is capable of capturing both the magnitude and variability of reactive power flows in distribution networks under uncertainty.

Table 4-7 Moments of Branch Reactive Power

Branch Index	**1st Order**	**2nd Order**	**3rd Order**	**4th Order**	**5th Order**
2	2.261746	5.142538	11.75377	27.00224	62.34236
3	2.07774	4.342843	9.130748	19.30736	41.05241
4	1.557941	2.44859	3.881546	6.204356	9.996472
5	1.469863	2.181329	3.267575	4.939113	7.530496
6	1.432362	2.072153	3.026854	4.462839	6.639012
7	1.386504	1.941818	2.746266	3.920772	5.648289
8	0.356637	0.128433	0.046689	0.017125	0.006333
9	0.255533	0.066123	0.017319	0.004588	0.001228
10	0.233696	0.055399	0.013314	0.003241	0.000798
11	0.212226	0.045787	0.010035	0.002231	0.000503
12	0.182126	0.033879	0.006429	0.001242	0.000244
13	0.146976	0.02226	0.003466	0.000553	9E-05
14	0.111003	0.012912	0.001565	0.000196	2.53E-05
15	0.030618	0.001263	6.03E-05	3.15E-06	1.74E-07
16	0.020546	0.000742	3.01E-05	1.35E-06	6.44E-08
17	0.000517	0.000303	2.19E-06	2.29E-07	3.05E-09
18	-0.01952	0.000667	-2.2E-05	8.88E-07	-3.7E-08
19	0.118929	0.015017	0.001984	0.000271	3.79E-05
20	0.078854	0.007024	0.000671	6.69E-05	6.84E-06

21	0.038562	0.002218	0.000131	8.31E-06	5.44E-07
22	0.04006	0.001669	7.2E-05	3.21E-06	1.47E-07
23	0.457388	0.212738	0.100538	0.048222	0.023442
24	0.405182	0.167539	0.070613	0.030287	0.013196
25	0.201046	0.042052	0.009111	0.002038	0.000469
26	0.908384	0.84205	0.795711	0.76567	0.749376
27	0.882284	0.795221	0.73137	0.68553	0.654055
28	0.855886	0.749222	0.669922	0.611043	0.567754
29	0.827722	0.701243	0.607223	0.536661	0.483394
30	0.752162	0.581287	0.460689	0.373726	0.309773
31	0.150574	0.023688	0.003872	0.000653	0.000113
32	0.079731	0.007152	0.000695	7.1E-05	7.49E-06
33	-0.02036	0.000805	-3.7E-05	1.95E-06	-1.1E-07

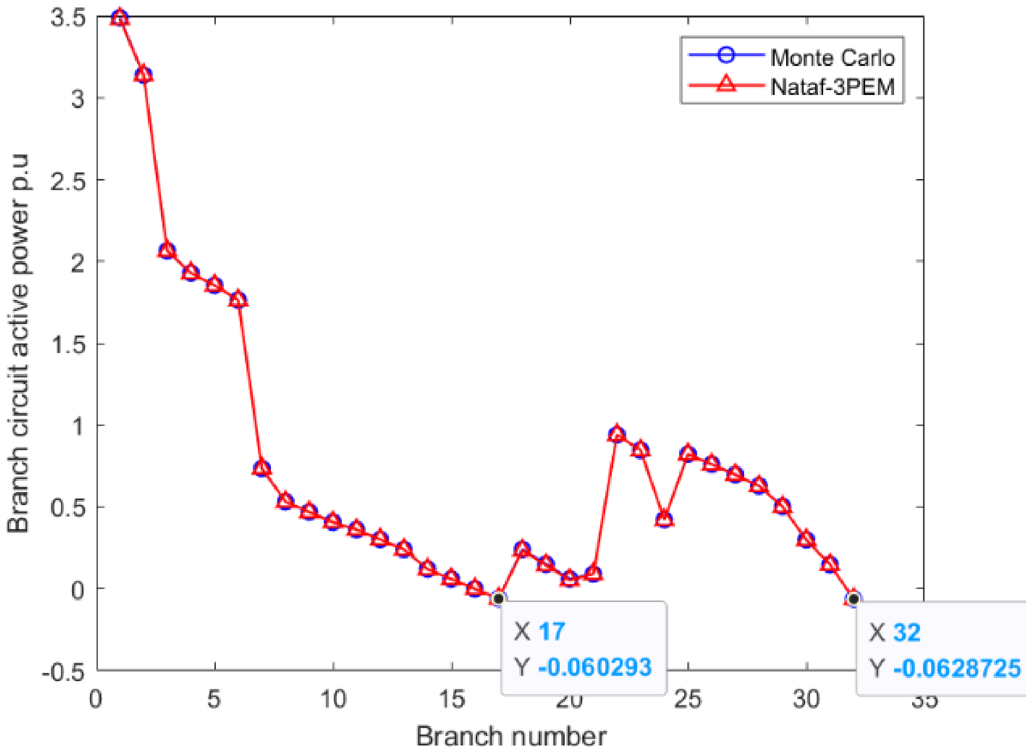

Figure 4-7 Comparison of Active Power Expected Values

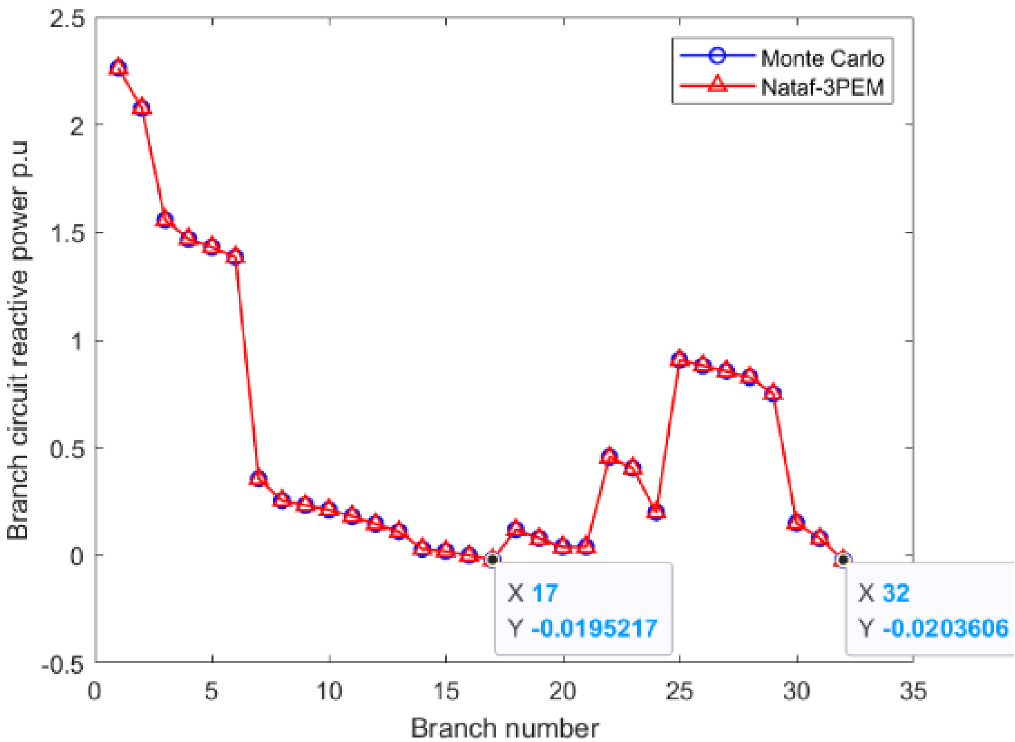

Figure 4-8 Comparison of Reactive Power Expected Values

Figure 4-7 and Figure 4-8 present the expected values of active and reactive power flows across all branches of the IEEE 33-bus system. The results show that most branches exhibit positive expected values, corresponding to conventional downstream power delivery from the slack bus to load points.

However, certain branches located at the network periphery (e.g., Branches 17 and 33) display negative expected values for both active and reactive power. This indicates the occurrence of reverse power flow, where locally generated power from distributed energy sources—such as wind and PV systems—exceeds the local demand and is injected back toward the upstream network.

This behaviour is consistent with the spatial distribution of distributed generation and highlights its impact on altering traditional unidirectional power flow patterns in radial distribution systems. In particular, reverse flow tends to occur in downstream branches with relatively high local generation and low load demand, leading to a net upstream power transfer.

A close agreement between the Monte Carlo and Nataf–3PEM results is observed in Figure 4-6, Figure 4-7 and Figure 4-8, confirming the accuracy of the proposed probabilistic approach in capturing the expected values of branch power flows. For completeness, the raw numerical data used to generate in Figure 4-6, Figure 4-7 and Figure 4-8 are provided in the Table AP 1.

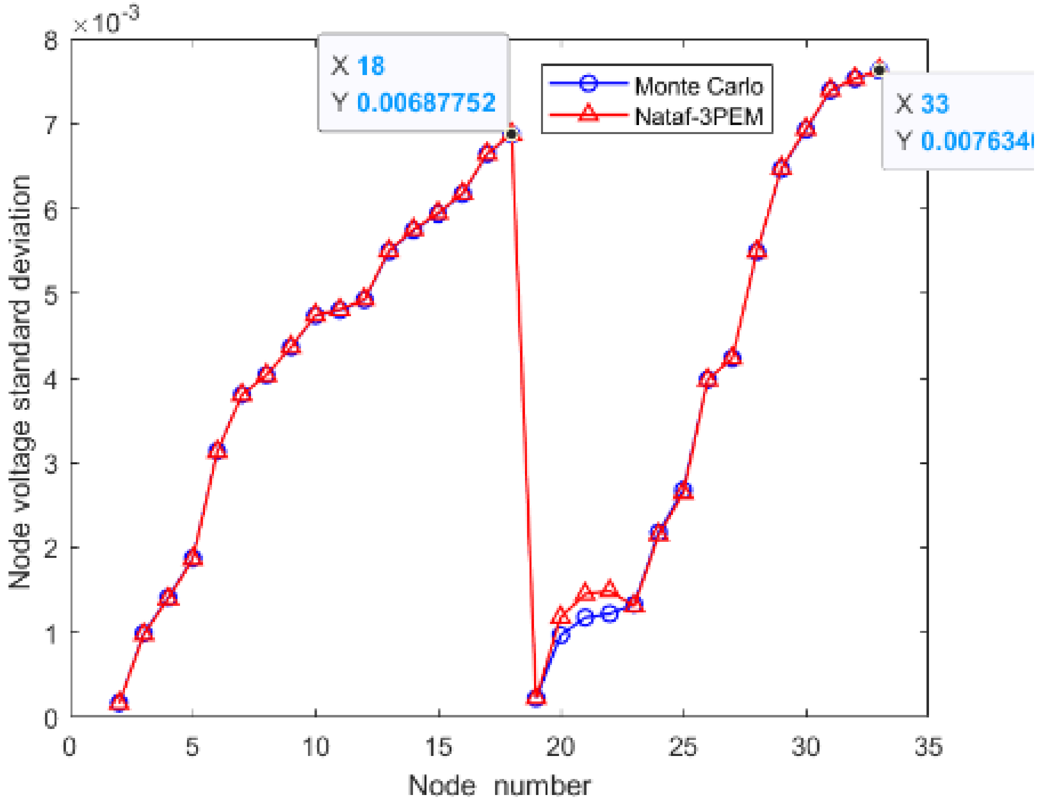

Figure 4-9 Comparison of Standard Deviation of Voltage Amplitude at Each Node

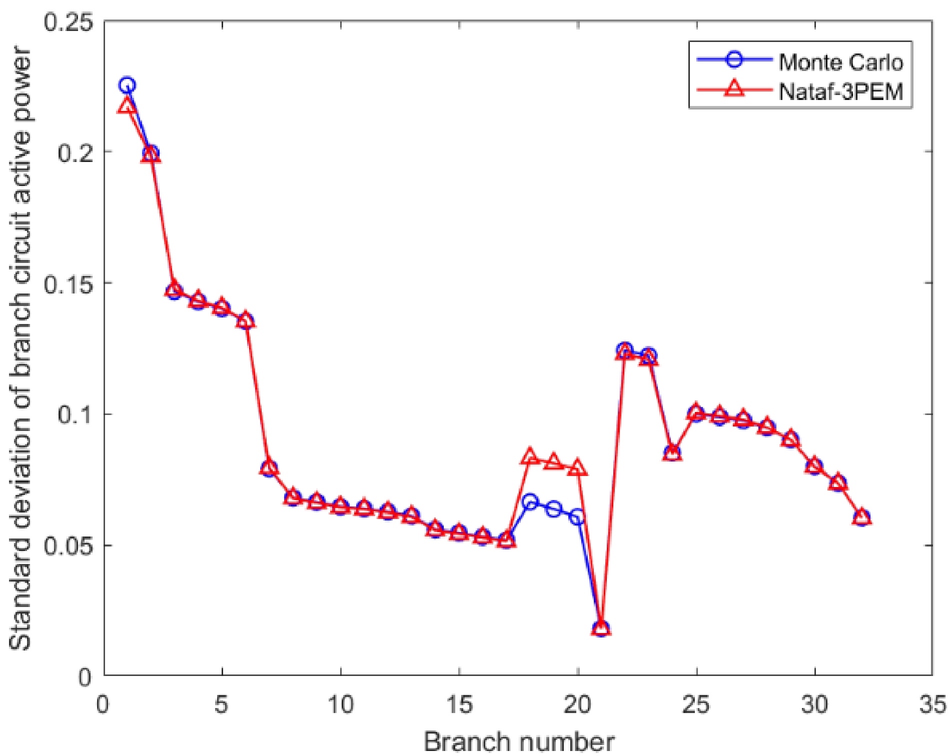

Figure 4-10 Comparison of Active Power Standard Deviation of Each Branch

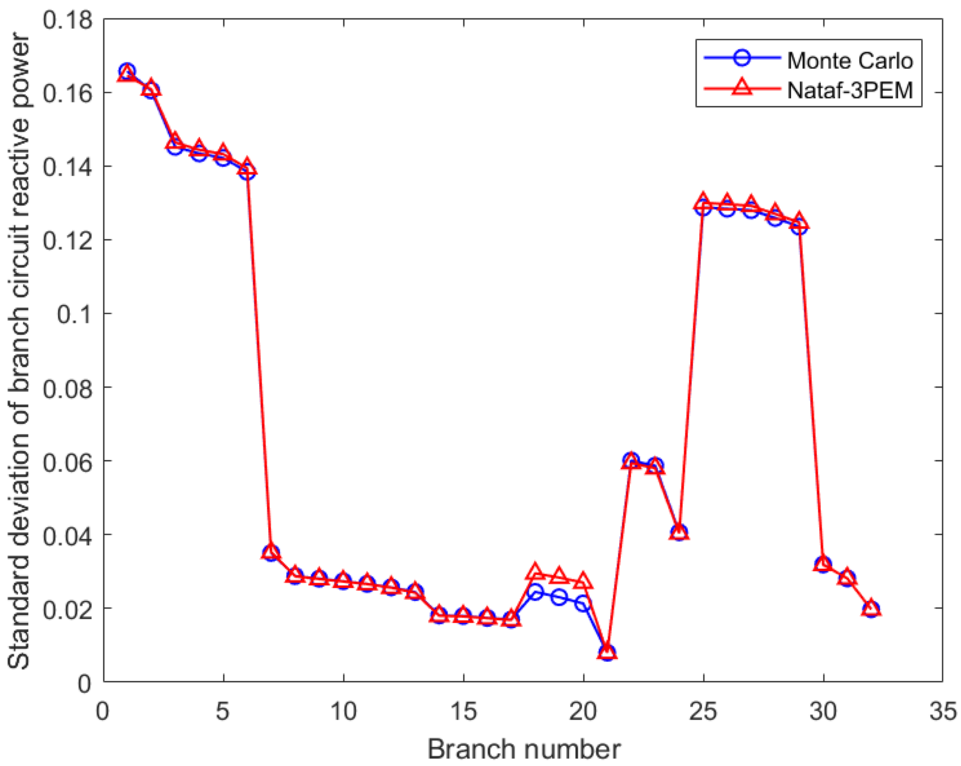

Figure 4-11 Comparison of Reactive Power Standard Deviation of Each Branch

Figure 4-9, Figure 4-10 and Figure 4-11 illustrate the standard deviations of node voltage magnitudes, as well as the standard deviations of active and reactive power flows across the distribution network.

A prominent feature observed in the results is that the standard deviation of both active and reactive power flows reaches its maximum at the initial branch. This is due to the upstream branch aggregating uncertainties from all downstream nodes in the radial network. As a result, fluctuations from stochastic loads and distributed generation accumulate toward the source side, leading to higher variability in the first few branches.

At the node level, higher voltage standard deviations are observed at nodes 18 and 33. These nodes are located at electrically distant positions from the slack bus and are influenced by local distributed generation (wind at node 18 and PV near node 33). The combination of long feeder distance and stochastic power injection increases voltage sensitivity, leading to larger fluctuations.

More importantly, localized discrepancies between the 3PEM and MCS can be observed, and these differences vary depending on the variable type and network location.

For voltage standard deviation (Figure 4-9), the differences are mainly concentrated at nodes 20–22. Referring to the network topology (Figure 4-2), this region corresponds to the connection point between the main feeder and a lateral branch containing a photovoltaic source at node 21. At this junction, power flow is influenced simultaneously by upstream supply, downstream loads, and local DG injection. This creates a nonlinear interaction between multiple stochastic variables. Since PEM approximates the system response using a limited number of estimation points, it cannot fully capture these nonlinear coupling effects, whereas MCS, through extensive sampling, provides a more accurate estimation. As a result, small deviations in voltage standard deviation appear in this region.

For active power standard deviation (Figure 4-10), the main differences occur in branches 18–20. These branches are directly associated with the wind generation connected at node 18 and the transition region toward the upstream network. In this area, the direction and magnitude of power flow are highly sensitive to wind power fluctuations, and reverse power flow may occur under certain scenarios. This introduces strong variability and nonlinearity in branch power flows. PEM tends to smooth such variations due to its moment-based approximation, while MCS captures the full range of stochastic behaviour, leading to noticeable differences in standard deviation.

For reactive power standard deviation (Figure 4-11), the discrepancies again appear mainly at nodes 20–22. Reactive power flows are indirectly affected by voltage magnitude and local load conditions. In this region, the interaction between PV generation (operating under PQ control assumptions) and local load demand leads to coupled variations in voltage and reactive power. Any approximation error in voltage estimation from PEM propagates into reactive power results, amplifying the differences when compared to MCS.

Overall, the differences between PEM and MCS are localized in regions with strong interactions between distributed generation, network topology, and power flow coupling. Outside these regions, the agreement between the two methods remains very close, confirming that the proposed PEM approach provides an efficient and sufficiently accurate approximation for probabilistic analysis in distribution networks. For completeness and transparency, the raw data corresponding to Figure 4-9, Figure 4-10 and Figure 4-11 are included in the Table AP 2.

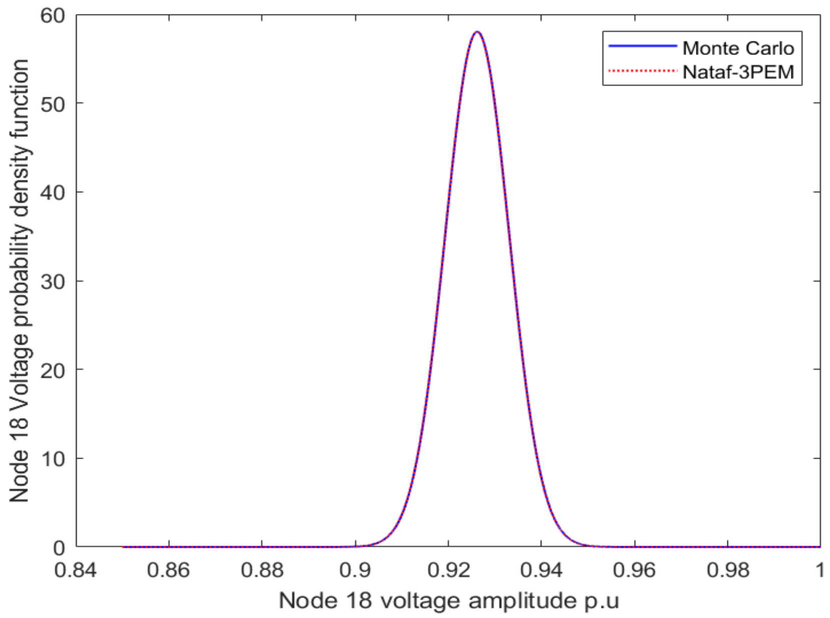

Figure 4-12 Node 18 Voltage Probability Distribution

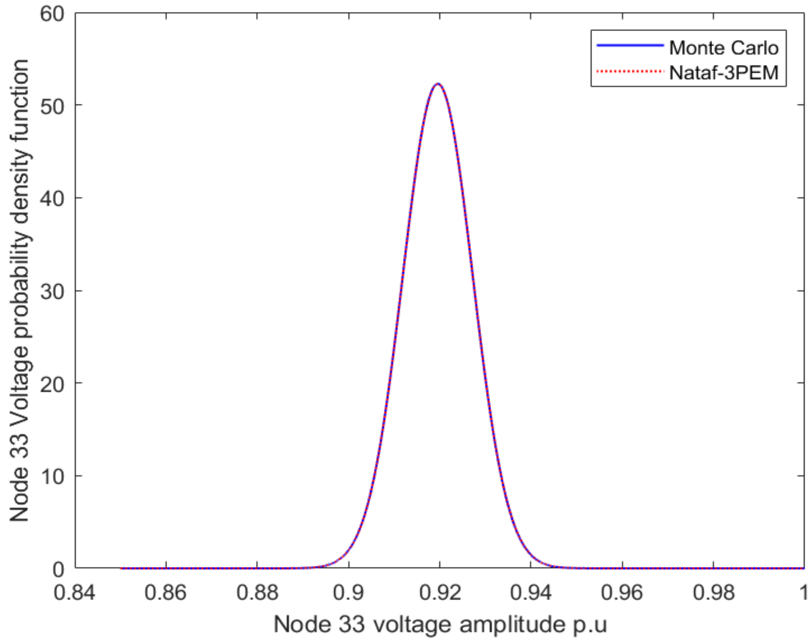

Figure 4-13 Node 33 Voltage Probability Distribution

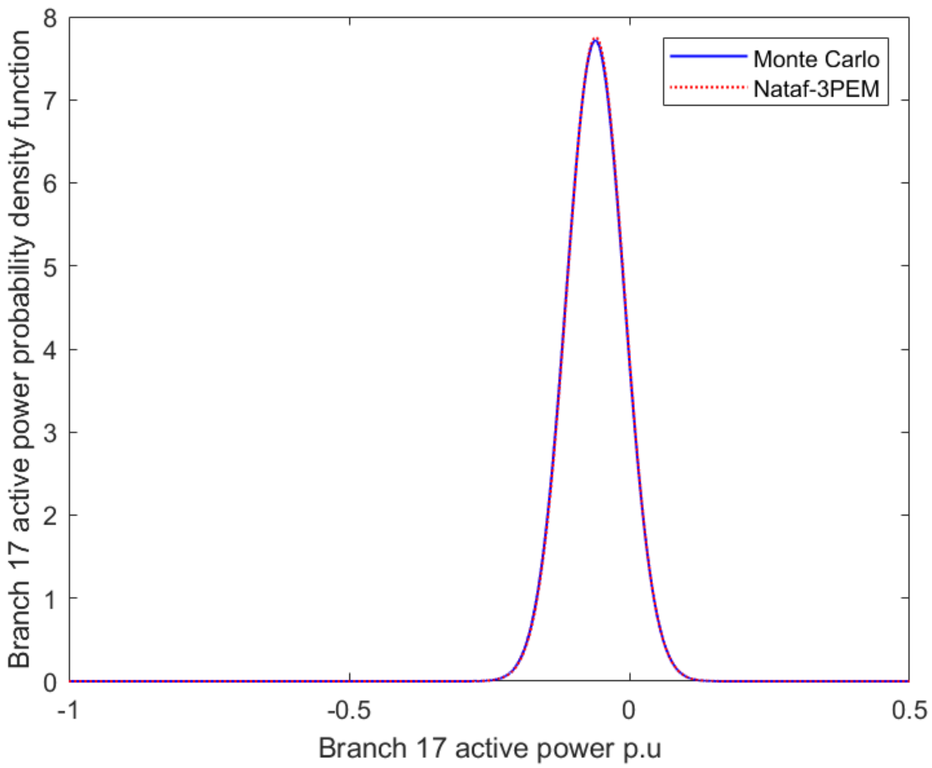

Figure 4-14 Branch 17 Active Power Probability Distribution

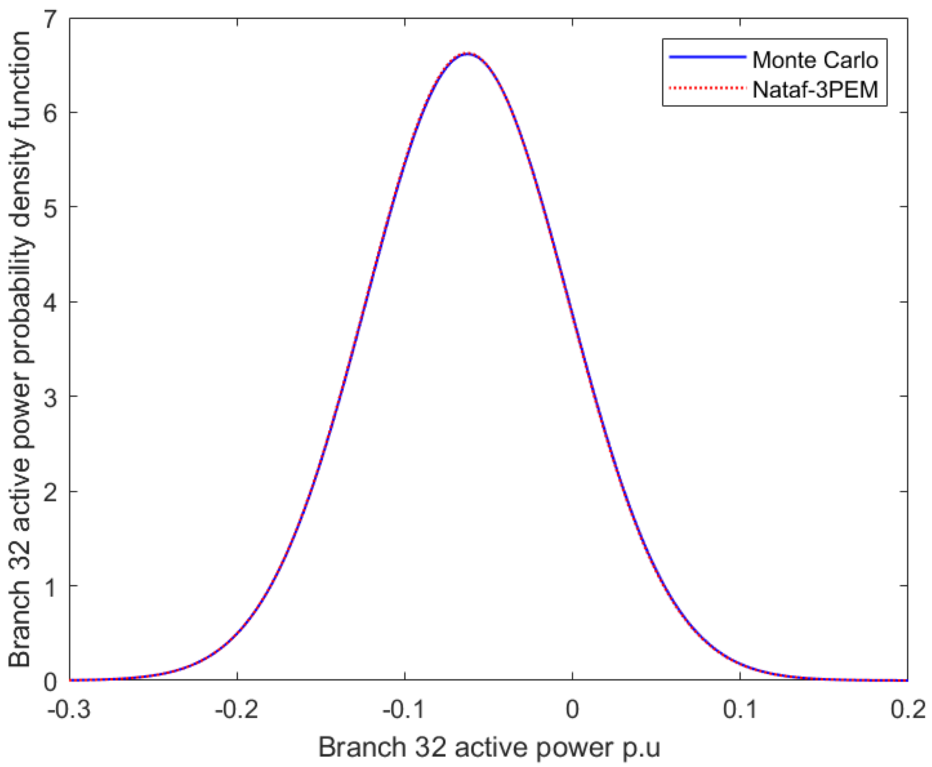

Figure 4-15 Branch 32 Active Power Probability Distribution

Figure 4-12 to Figure 4-15 present the probability distributions of voltage at Nodes 18 and 33, and active power at Branches 17 and 32. These nodes and branches are deliberately selected as representative cases to illustrate distinct operating conditions within the network.

Nodes 18 and 33 are chosen because they correspond to electrically critical locations with distributed generation integration. Node 18 is directly connected to wind generation, representing a source-dominated node with strong stochastic injection. In contrast, Node 33 is located at the feeder end with photovoltaic integration and is electrically distant from the slack bus, making it more vulnerable to voltage drops and fluctuations. These two nodes therefore capture two typical but fundamentally different uncertainty propagation mechanisms: generation-driven variability (Node 18) and weak-grid sensitivity (Node 33).

Similarly, Branches 17 and 32 are selected to represent different power flow regimes. Branch 17 is located near the wind generation node and is directly affected by fluctuations in wind output, often exhibiting reverse power flow behaviour. Branch 32, on the other hand, is situated near the end of the feeder and reflects the cumulative effects of upstream uncertainties combined with local photovoltaic injection. These two branches therefore illustrate the contrasting characteristics of power flow variability in DG-dominated and downstream-accumulated regions of the network.

From Figure 4-13, it can be observed that the voltage distribution at Node 33 is centred around a relatively low mean value (approximately 0.92 p.u.) with a certain spread. Given that typical operational voltage limits in distribution systems are commonly set within the range of 0.93–1.07 p.u. in this study, this distribution indicates a non-negligible probability of voltage values falling below the lower acceptable limit. This suggests a potential risk of undervoltage at Node 33 under certain operating conditions.

This phenomenon can be attributed to the combined effects of electrical distance from the slack bus, cumulative voltage drops along the feeder, and the variability of local photovoltaic generation. While PV generation can provide local voltage support, its intermittent nature may not consistently compensate for voltage drops, especially during low generation periods. Therefore, Node 33 represents a weak point in the network in terms of voltage regulation, which further justifies its selection for detailed probabilistic analysis.

The results also indicate that the expected active power values for both Branches 17 and 32 are negative, confirming the presence of reverse power flow due to the integration of distributed renewable generation. In addition, Branch 32 exhibits a wider probability distribution compared to Branch 17, indicating higher variability. This reflects the combined influence of upstream uncertainty propagation and local generation effects at the feeder end, whereas Branch 17 is primarily influenced by local wind generation variability.

4.5 Analysis of Probabilistic Harmonic Power Flow Results

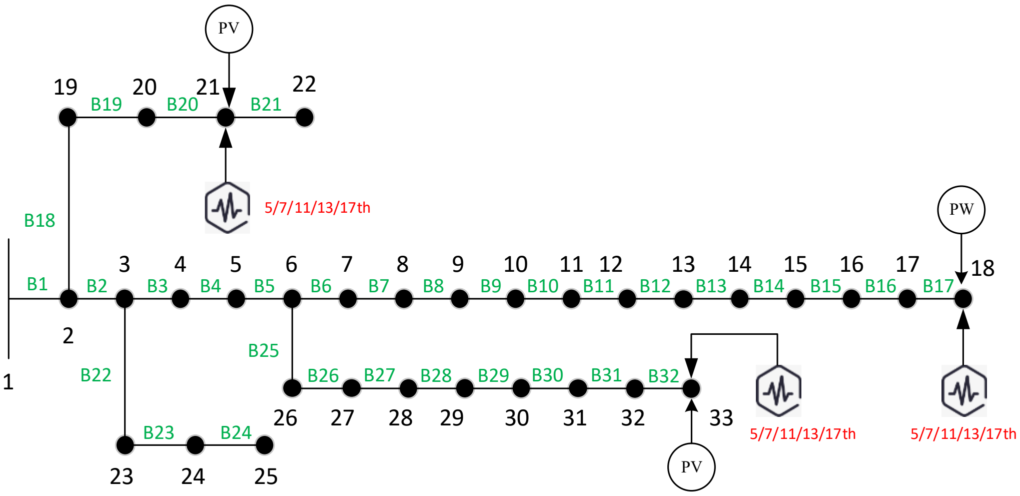

Figure 4-16 Topology of System IEEE 33-bus with Harmonic Source

As illustrated in the Figure 4-16, harmonic sources are integrated at nodes 18, 21, and 33 within the distribution network. This figure depicts the topological structure of the test system, a modified IEEE 33-bus radial distribution network, with PV and wind power (PW) generation units connected at specific nodes to simulate realistic renewable energy integration. This setup facilitates the evaluation of harmonic propagation under uncertain conditions arising from variable renewable outputs and nonlinear loads.

In this study, the harmonic sources represent the combined effect of harmonics generated by both nonlinear loads and power-electronic interfaced renewable generation units. Specifically, nonlinear loads are considered the primary sources of harmonic currents in the network, while PV and wind power (PW) units contribute additional harmonic components due to the switching behaviour of their inverter interfaces.

Therefore, the harmonic injections at nodes 18, 21, and 33 are modelled as equivalent current sources that aggregate the harmonic contributions from local nonlinear loads and renewable generation. This modelling approach reflects a practical scenario in modern distribution networks, where both load-side and generation-side power electronic devices jointly influence harmonic distortion levels.

Table 4-8 Node Voltage Magnitudes at Different Harmonic Orders

Node Index	**5th**	**7th**	**11th**	**13th**	**17th**
18	0.2001	0.1409	0.0908	0.0706	0.0519
21	0.1978	0.1342	0.0858	0.0686	0.0521
33	0.2002	0.1409	0.0908	0.0706	0.0519

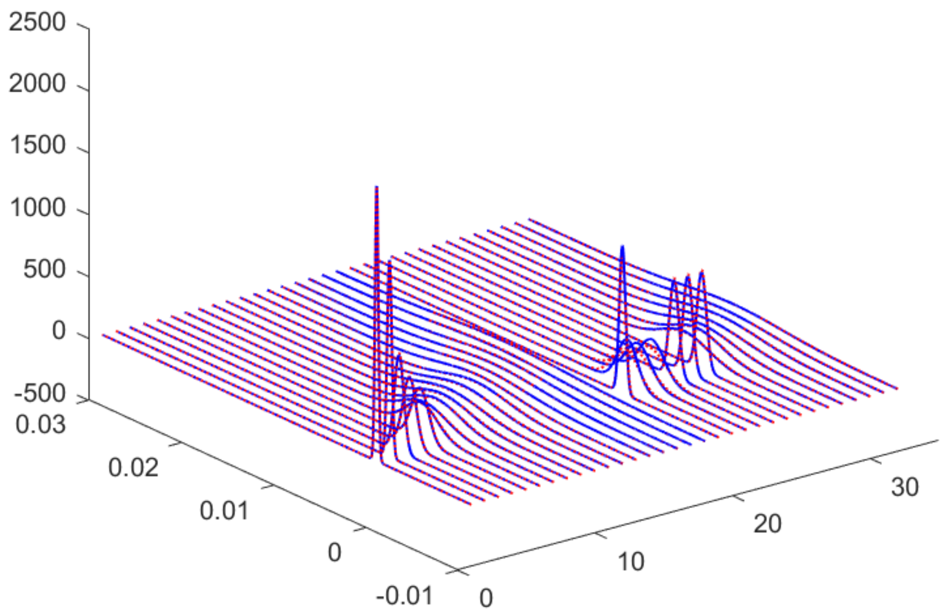

Figure 4-17 Comparison of Probability Distributions of Total Harmonic Distortion at Each Node

The Figure 4-17 presents a comparative 3D surface plot of the probability distributions of total harmonic distortion (THD) in voltage across all nodes, obtained using two methodologies: the 3PEM and MCS as the benchmark. The blue solid lines represent the results obtained from the MCS, while the red dashed lines correspond to the 3PEM calculations. The THD is defined as the ratio of the root-mean-square (RMS) value of the harmonic components to the RMS value of the fundamental component, expressed in per unit (p.u.). Notably, nodes proximate to the harmonic sources (e.g., nodes 18, 21, and 33) exhibit higher expected THD values, accompanied by larger standard deviations and broader fluctuation ranges. This is attributable to the direct injection of harmonic currents, which amplify voltage distortions locally. In contrast, nodes electrically distant from the sources (e.g., nodes 1 and 2 near the root) display lower expected THD values, with narrower fluctuation intervals, smaller standard deviations, and higher probability density peaks. Consequently, the probability distributions at distant nodes appear "tall and narrow," indicating concentrated and less variable distortions, whereas those at nearer nodes are "short and broad," reflecting greater uncertainty and spread due to harmonic propagation effects.

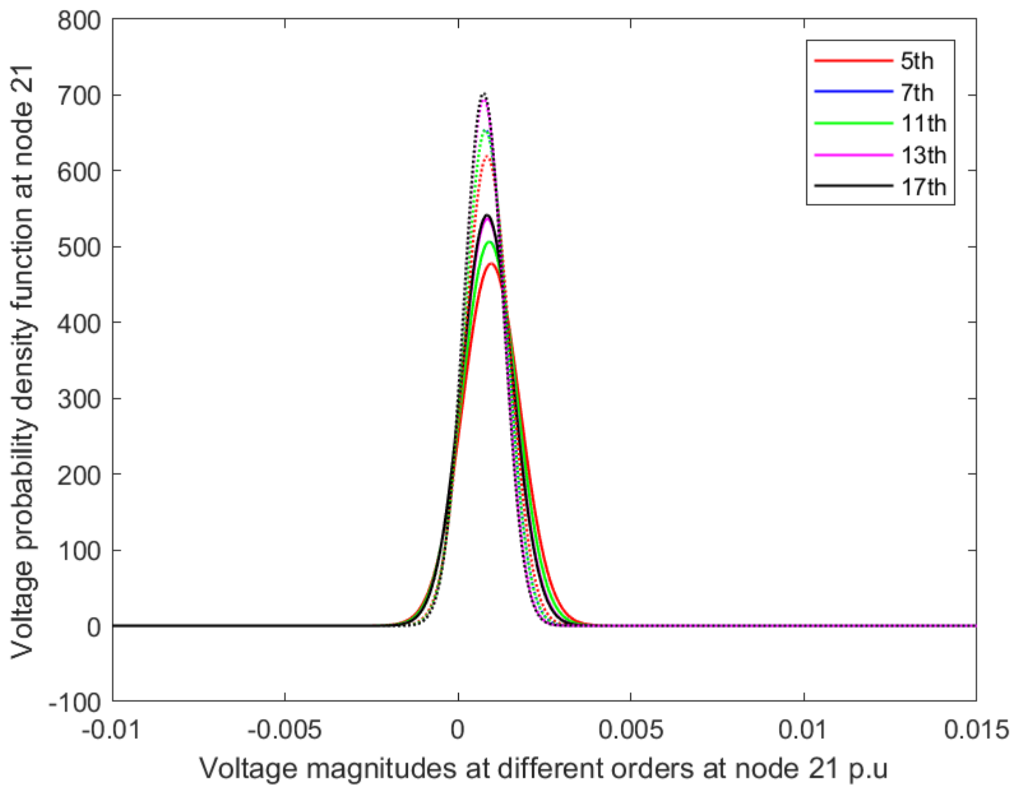

Figure 4-18 Node 21 Voltage Probability Density Functions

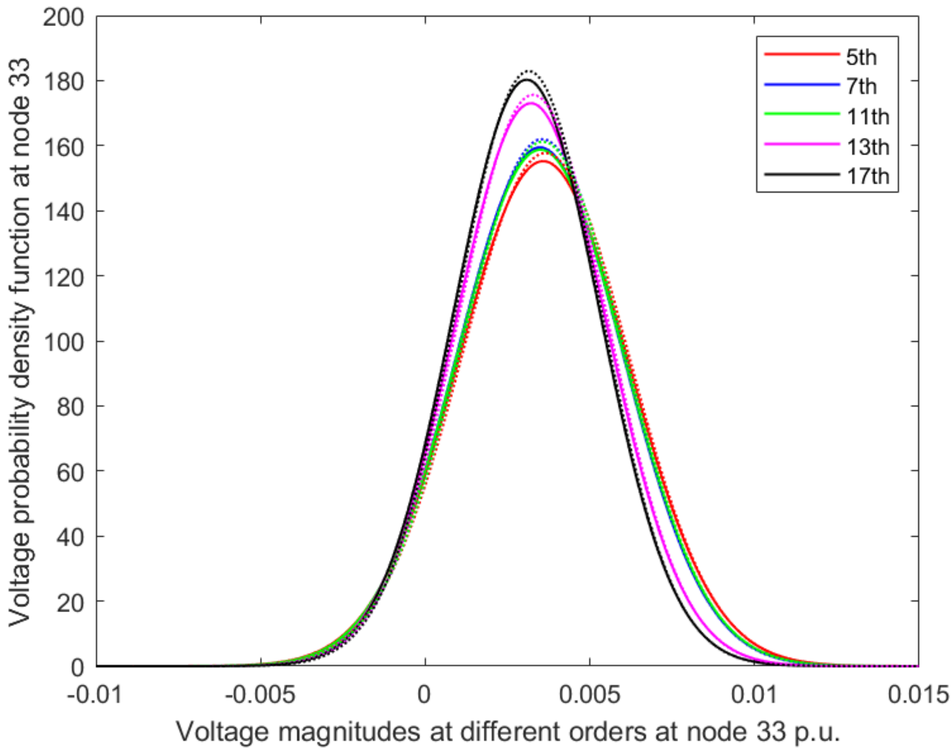

Figure 4-19 Node 33 Voltage Probability Density Functions

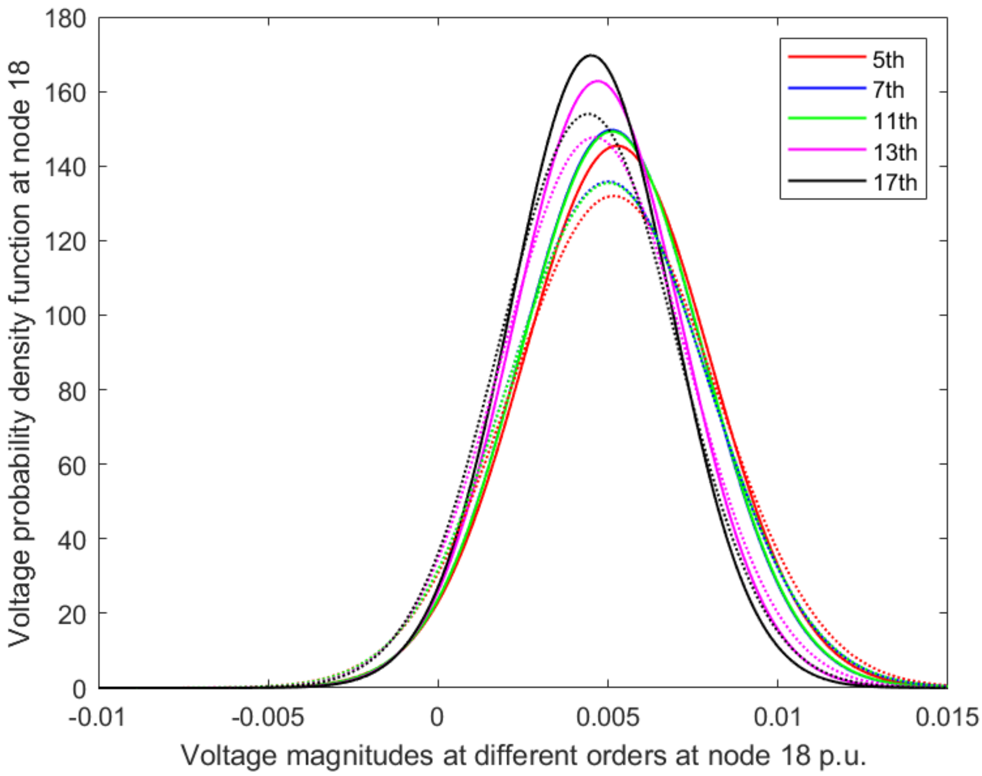

Figure 4-20 Node 18 Voltage Probability Density Functions

Figure 4-18, Figure 4-19 and Figure 4-20 illustrate the probability density functions (PDFs) of voltage magnitudes for selected harmonic orders (5th, 7th, 11th, 13th, and 17th) at nodes 21, 33, and 18, respectively, with solid lines representing 3PEM results and dashed lines denoting MCS outcomes. Across these nodes, the 5th-order harmonic consistently shows the highest expected voltage magnitude and the largest standard deviation, while the 17th-order harmonic exhibits the lowest values in both metrics. This trend aligns with the harmonic current injection characteristics: lower-order harmonics typically have higher content ratios in the fundamental current waveform, as dictated by the spectral properties of common nonlinear devices (e.g., rectifiers and inverters in PV/PW systems). As the harmonic order increases, the injection magnitude diminishes, leading to reduced distortion levels and variability.

A key observation is the close agreement between 3PEM and MCS results, with minimal discrepancies in PDF shapes and statistical moments. This validates that 3PEM is an efficient approximation for probabilistic harmonic analysis, offering reduced computational burden compared to the sampling-intensive MCS while maintaining accuracy under Gaussian or near-Gaussian uncertainty assumptions. However, potential limitations include 3PEM's sensitivity to non-Gaussian distributions in renewable generation uncertainties, which could necessitate hybrid approaches in more complex scenarios.

4.6 Effect of correlation on calculation results

This section investigates the impact of statistical dependence among uncertain inputs on probabilistic power flow (PPF) results in the modified IEEE 33-bus distribution network. The dependencies are modelled simultaneously using a unified correlation structure within the Nataf transformation framework. Specifically, a Spearman rank correlation matrix C_X is constructed to describe the joint dependence among all uncertain variables, including nodal loads, PV generation, and wind turbine outputs. This multivariate correlation matrix is then mapped into the standard normal space via a Gaussian Copula, enabling consistent integration within the 2m+1 PEM. Therefore, the dependence modelling is not pairwise or independent but fully coupled across all variables.

In the base modelling assumptions, load–load and load–PV correlations are taken as positive, reflecting coincident demand patterns and the partial alignment between solar generation and daytime electricity consumption. In contrast, load–wind correlations are assumed to be negative, representing the tendency for wind generation to peak during off-peak demand periods. To evaluate the overall sensitivity of system performance to correlation strength, a parametric analysis is conducted in which a uniform correlation magnitude (from 0 to 0.6) is applied. It should be noted that the parameter shown in Figure 4-21 to Figure 4-24 represents the absolute level of dependence strength, while the sign of specific relationships (e.g., load–wind turbine negative correlation) is preserved within the correlation matrix structure. Thus, increasing the correlation coefficient corresponds to strengthening both positive and negative dependencies proportionally, rather than implying that all correlations become positive.

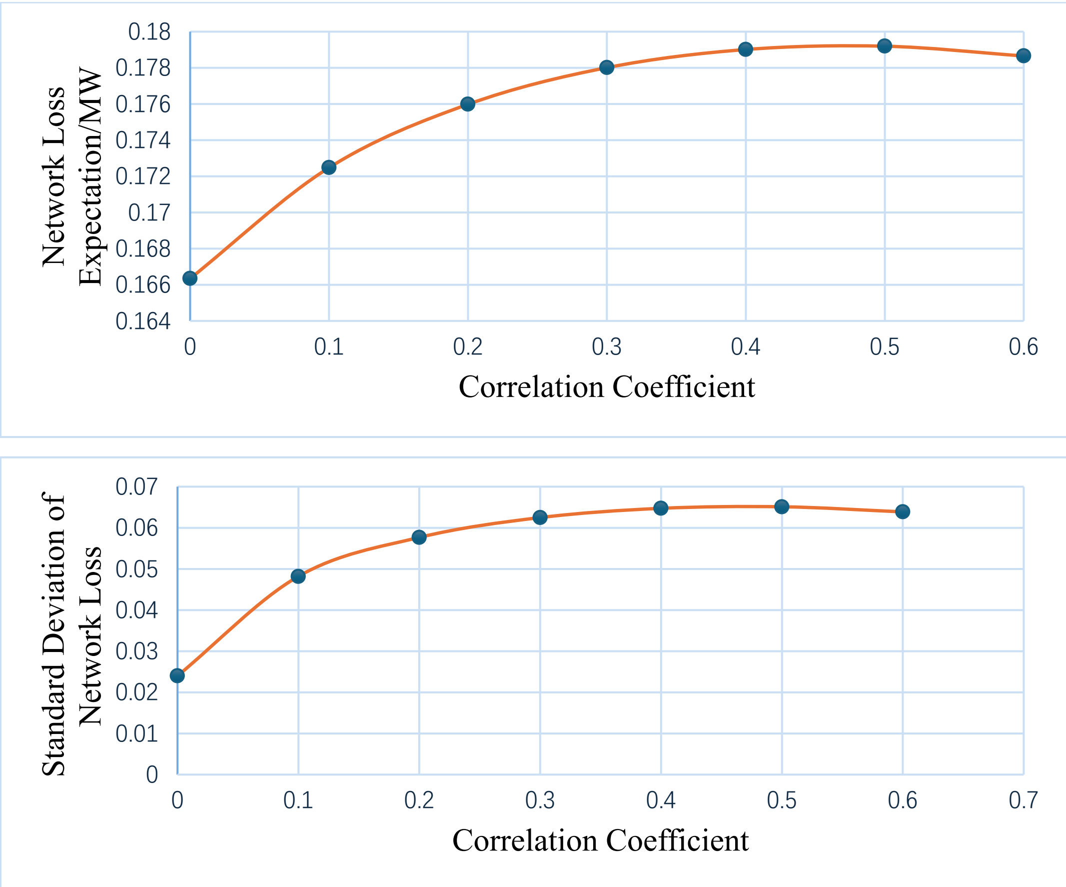

Figure 4-21 Fluctuation Curve of Expected Value of Network Loss and Standard Deviation of Network Loss with Correlation Coefficient

As shown in Figure 4-21, both the expected value and the standard deviation of network losses increase with the correlation coefficient. This trend reflects the growing likelihood of simultaneous high-load conditions under stronger positive dependencies among loads. The variance amplification is mainly driven by covariance terms in the aggregated power demand.

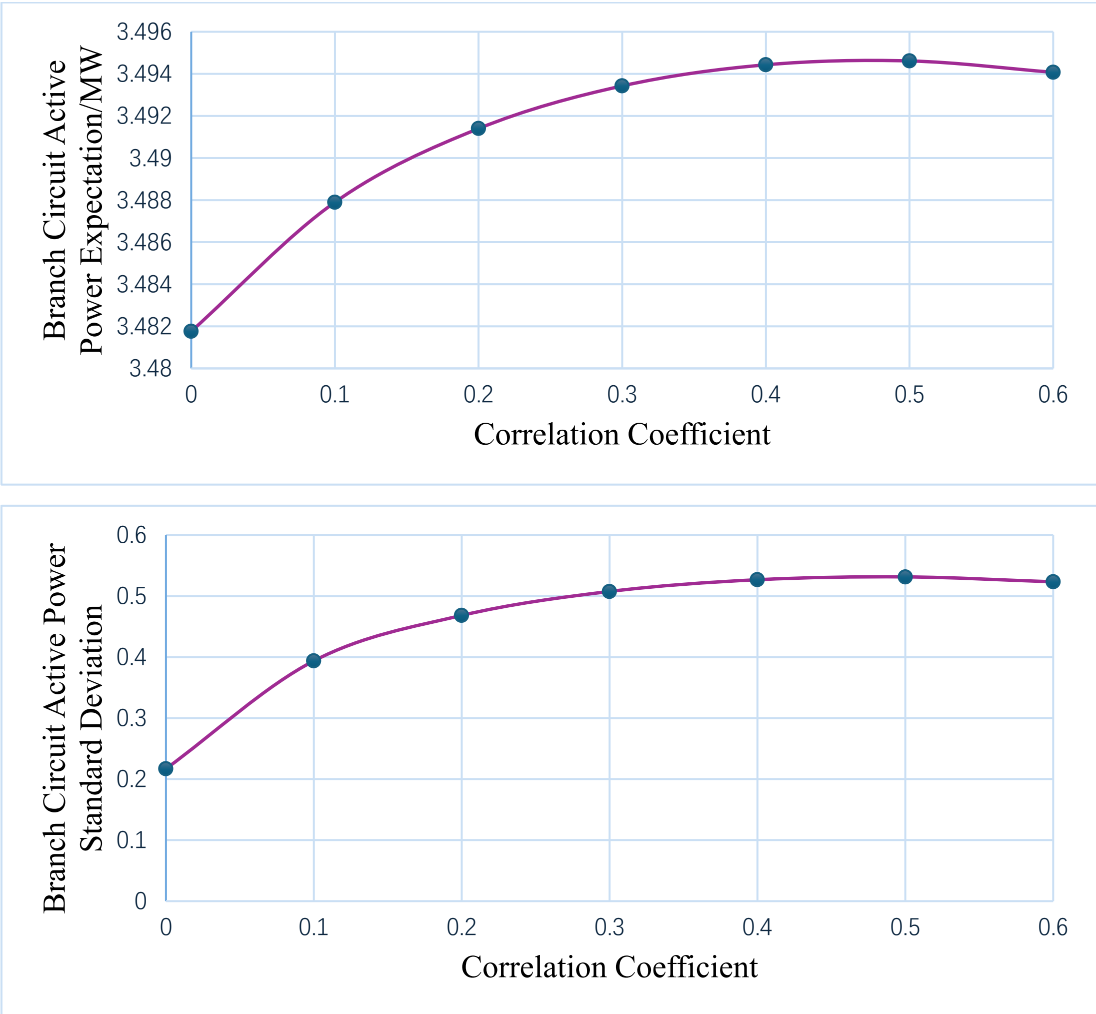

Figure 4-22 Fluctuation Curve of Expected Value of Branch Active Power and Standard Deviation of Branch Active Power with Correlation Coefficient

Figure 4-22 presents the variation of branch active power statistics with correlation strength. A similar increasing trend is observed for both the expected value and standard deviation. This indicates that correlated load fluctuations propagate through the network and intensify power flow variability, particularly in upstream branches.

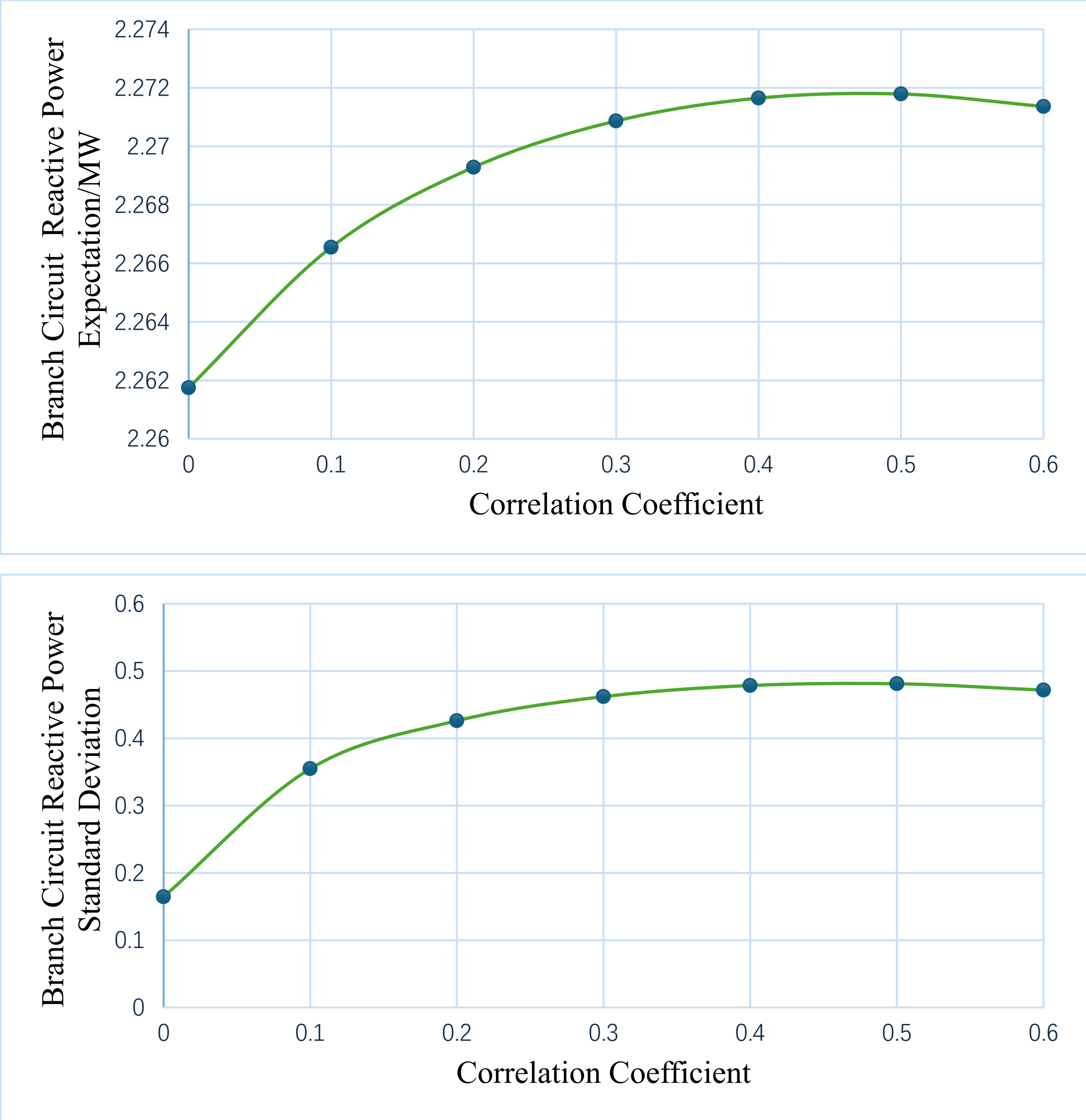

Figure 4-23 Fluctuation Curve of Expected Value of Branch Reactive Power and Standard Deviation of Branch Reactive Power with Correlation Coefficient

As illustrated in Figure 4-23, the expected value and standard deviation of branch reactive power also increase with correlation. This behaviour is consistent with active power trends, as reactive demand is directly linked to load levels under the assumed constant power factor.

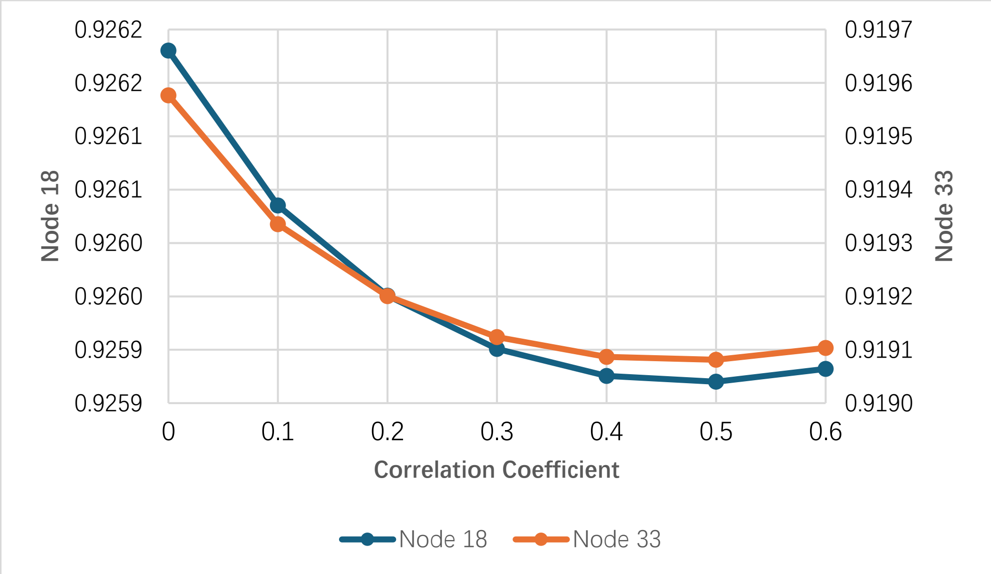

Figure 4-24 Relationship of Expected Voltage between Nodes 18 and 33 and Correlation Coefficients

Figure 4-24 shows the relationship between correlation strength and node voltage magnitudes at Nodes 18 and 33. A slight decreasing trend is observed as correlation increases, indicating that stronger load synchronisation leads to more severe voltage drops, particularly at downstream nodes.

The effect of wind power requires further clarification. Although wind generation is negatively correlated with load, its mitigating influence on system stress is relatively limited in this case study. This is primarily due to its comparatively small installed capacity (0.2 MW), which is significantly lower than the total system load (approximately 3.7 MW). As a result, even though the negative correlation tends to reduce coincident peaks, its impact is dominated by the stronger positive load–load correlations. Consequently, the overall system behaviour still shows an increasing trend in both expected values and variability as correlation strength increases.

The results also indicate a slight non-monotonic behaviour at higher correlation levels (e.g., beyond 0.4–0.5), where some variables begin to stabilise or slightly decrease. This suggests that the combined effects of positive and negative dependencies introduce partial balancing mechanisms within the system.

It is acknowledged that the relatively small capacities of PV and WT units in this study limit the observable impact of their correlations with load. For a more comprehensive assessment of renewable-load interaction effects, future studies may consider higher penetration levels of distributed generation to better capture the influence of negative correlations, particularly for wind power.

For completeness and transparency, the raw data corresponding to Figure 4-21 to Figure 4-24 are included in the Table AP 3.

4.7 Algorithm error analysis

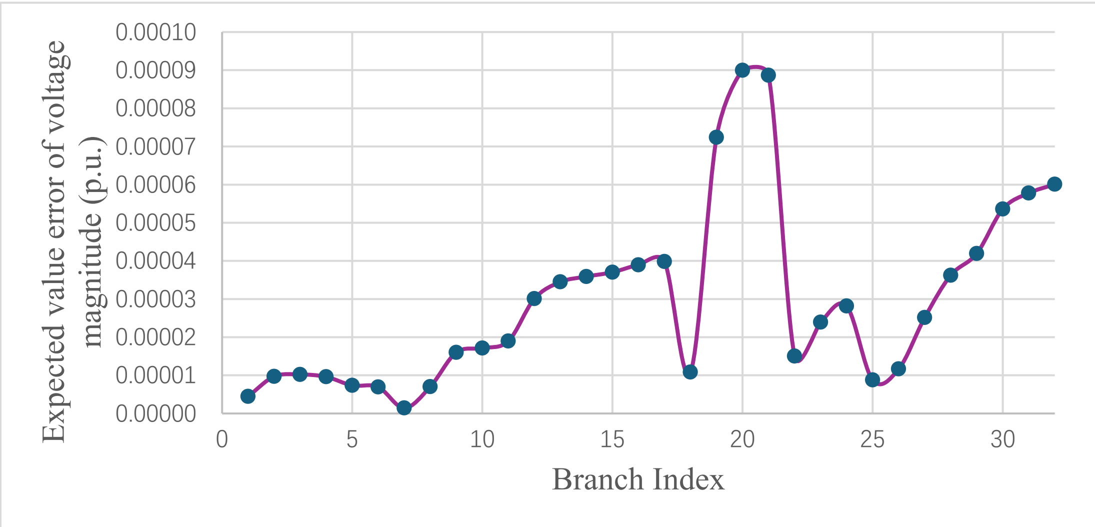

Figure 4-25 Expected Value Error of Node Voltage Magnitude (p.u.)

Figure 4-25 presents the expected value error of node voltage magnitude obtained by the 3PEM method compared with MCS. It can be observed that the error remains consistently low across all nodes, generally within the order of $10^{-4}$to 10^{-3}p.u. A gradual increase in error is observed along the feeder, with higher deviations occurring at downstream nodes, reflecting the cumulative effect of uncertainty propagation through the radial network.

A noticeable local variation appears around nodes 18–22, where distributed generation (PV and wind) is connected. The interaction between stochastic generation and load introduces additional nonlinearity, which slightly reduces the approximation accuracy of 3PEM. Nevertheless, the overall error level remains very small, demonstrating that 3PEM provides highly accurate estimates of voltage expected values across the entire network.

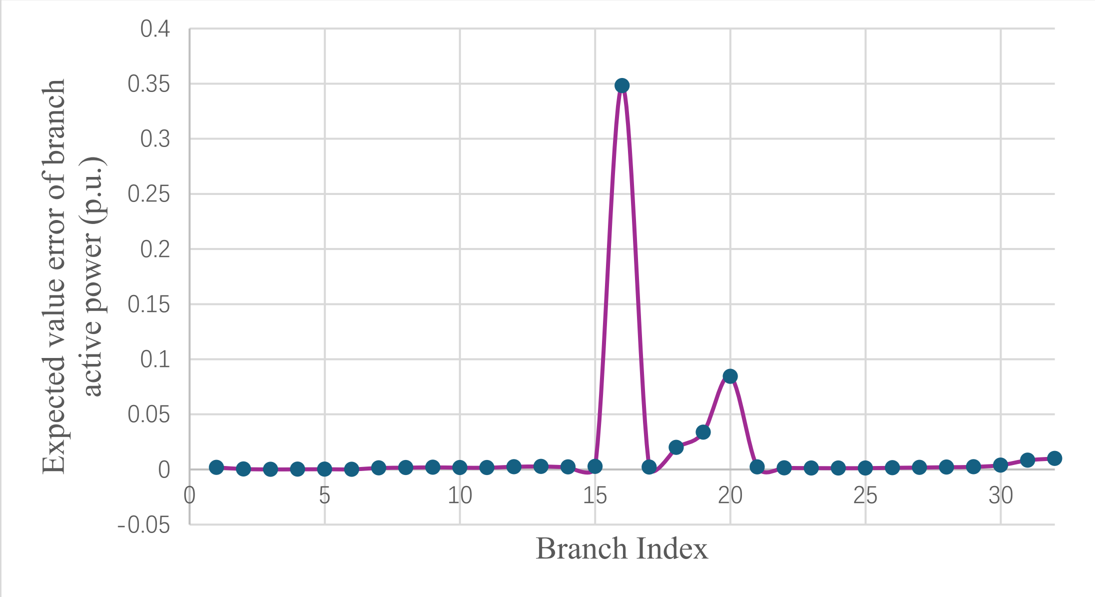

Figure 4-26 Expected Value Error of Branch Active Power (p.u.)

Figure 4-26 illustrates the expected value error of branch active power. Compared with voltage, the error in active power is more pronounced, with a significant peak observed around branch 16, where the error reaches approximately 0.35 p.u. This branch is located near the junction of multiple feeders and distributed generation units, where power flow direction and magnitude are highly sensitive to stochastic inputs.

The elevated error in this region can be attributed to stronger nonlinear interactions between load fluctuations and renewable generation, which are more difficult to approximate accurately using the limited number of evaluation points in 3PEM. Away from this critical region, the error rapidly decreases and remains close to zero across most branches. This indicates that the approximation error is highly localised and mainly associated with structurally sensitive parts of the network.

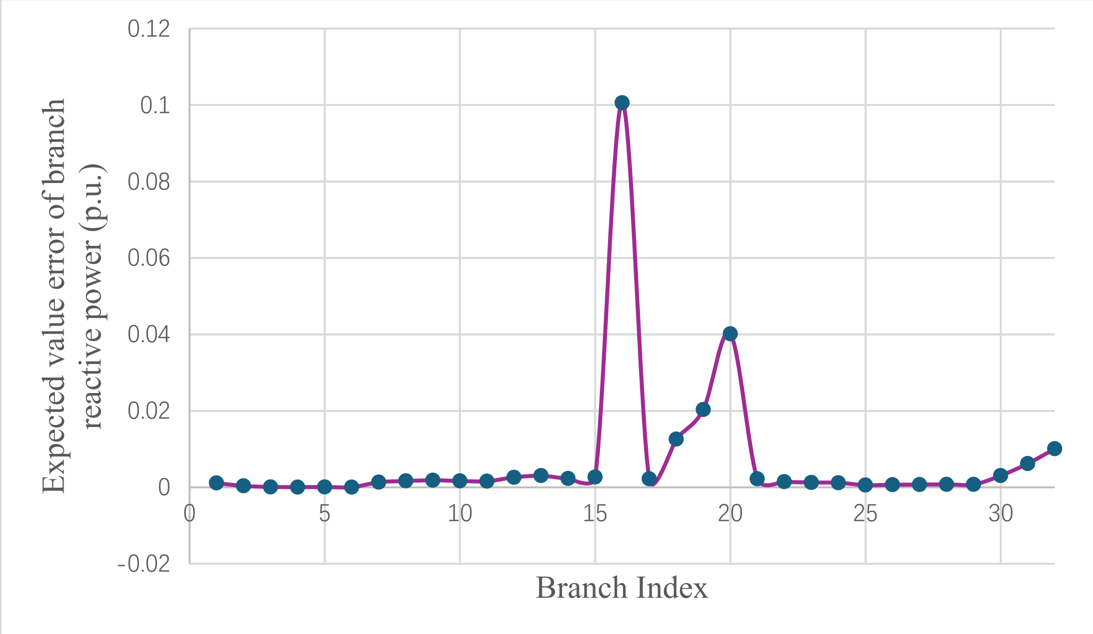

Figure 4-27 Expected Value Error of Branch Reactive Power (p.u.)

Figure 4-27 shows the expected value error of branch reactive power. The overall error level is lower than that of active power, with the majority of values remaining below 0.1 p.u. Similar to the active power case, a local peak appears around branch 16–20, corresponding to the region influenced by distributed generation and branching structure.

Reactive power is inherently linked to voltage magnitude and is less sensitive to directional changes compared to active power. As a result, its approximation error remains more stable and exhibits smoother spatial variation. The observed results indicate that 3PEM is capable of capturing the expected behaviour of reactive power with satisfactory accuracy, even under uncertain operating conditions.

Overall, the results demonstrate that the 3PEM method achieves high accuracy in estimating expected values of voltage, active power, and reactive power. The observed discrepancies are mainly localised around network regions with strong nonlinearity and high uncertainty, confirming the effectiveness and robustness of the proposed approach.

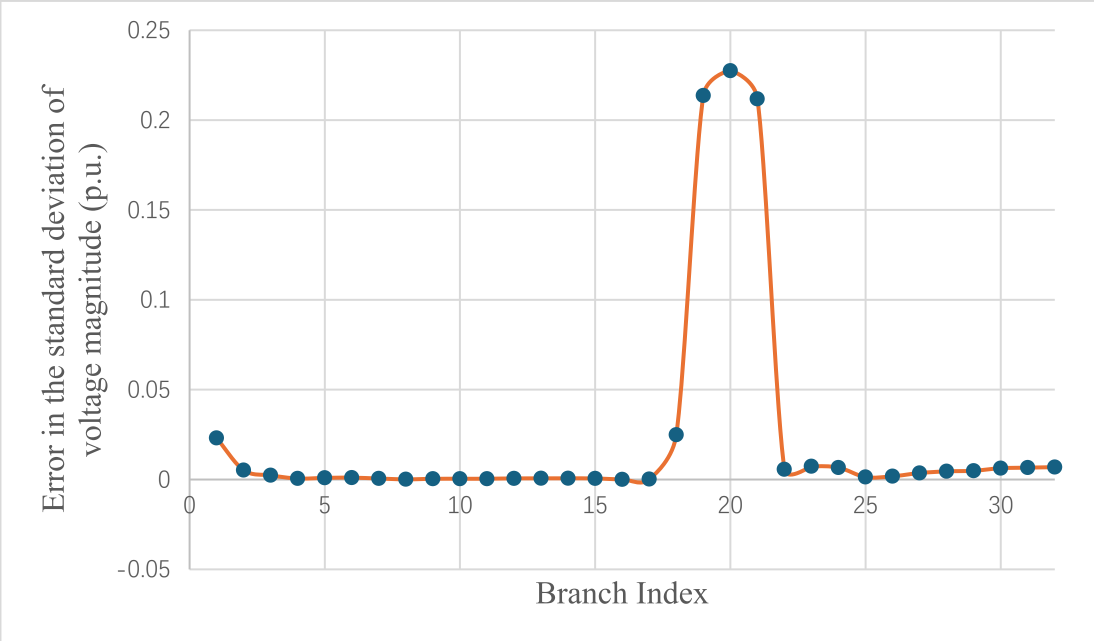

Figure 4-28 Error in the Standard Deviation of Node Voltage Magnitude (p.u.)

Figure 4-28 presents the error in the standard deviation of node voltage magnitude obtained using the 3PEM method compared with MCS. It can be observed that the error remains close to zero across most nodes, indicating that 3PEM provides a reliable estimation of voltage variability.

However, a noticeable peak appears around nodes 18–21, where the error reaches approximately 0.22 p.u. This region corresponds to the location of distributed generation and network branching, where uncertainty interactions are more complex. The increased error can be attributed to the higher-order nonlinear effects introduced by the combination of stochastic load and renewable generation.

Despite this local deviation, the overall error distribution remains low and well-contained, demonstrating that 3PEM maintains good accuracy in capturing the standard deviation of voltage across the network.

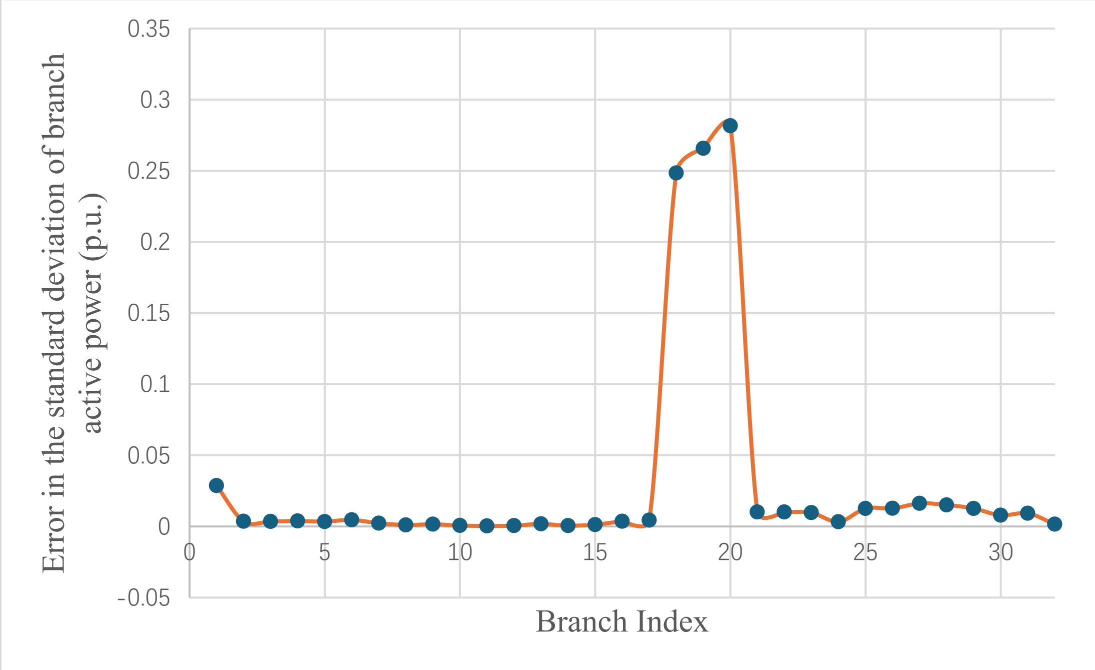

Figure 4-29 Error in the Standard Deviation of Branch Active Power (p.u.)

Figure 4-29 illustrates the error in the standard deviation of branch active power. Compared with voltage, the error magnitude is significantly higher, with a pronounced peak observed around branch 18–20, reaching approximately 0.28 p.u.

This behaviour is mainly associated with the strong sensitivity of active power flows to uncertainty, particularly in regions where power direction and magnitude are influenced by distributed generation. In these branches, small variations in input variables can lead to amplified fluctuations in power flow, making it more challenging for 3PEM to accurately approximate second-order statistics.

Outside this critical region, the error remains very small, indicating that the deviation is highly localised and primarily driven by network topology and nonlinear interactions.

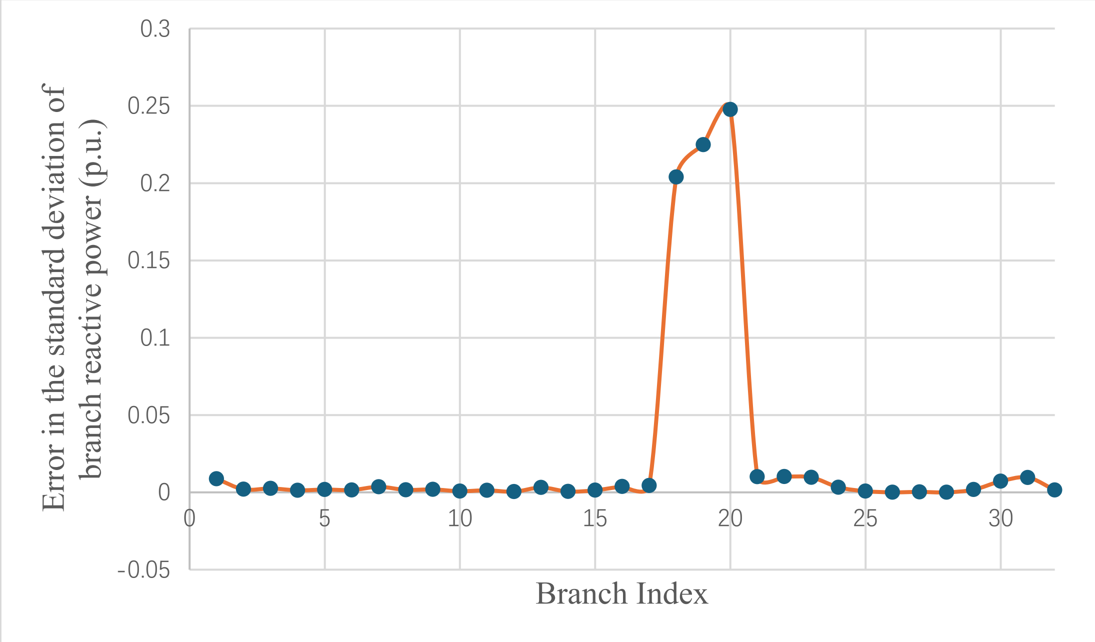

Figure 4-30 Error in the Standard Deviation of Branch Reactive Power (p.u.)

Figure 4-30 shows the error in the standard deviation of branch reactive power. The overall pattern is similar to that of active power, with a localised peak around branches 18–20, where the error reaches approximately 0.25 p.u.

Reactive power variability is closely related to voltage fluctuations and load characteristics. Although it exhibits nonlinear behaviour, its sensitivity is generally lower than that of active power. As a result, the error magnitude is slightly lower and the variation trend is smoother.

The results indicate that 3PEM is capable of capturing the variability of reactive power with reasonable accuracy, while minor discrepancies arise in regions with strong coupling between voltage and power flow uncertainties.

Overall, the results indicate that the 3PEM method provides satisfactory accuracy in estimating both the expected values and standard deviations of key system variables. The observed discrepancies are mainly concentrated in regions with strong nonlinearity and high uncertainty, confirming the effectiveness and robustness of the proposed method.

Table 4-9 Relative Error Comparison of Calculation Results with MCS as Reference

Branch Index	**Node voltage expected value**	**Node voltage standard deviation**	**Branch active power expected value**	**Branch active power standard deviation**	**Branch reactive power expected value**	**Branch reactive power standard deviation**
1	2.95E-06	0.020345	0.001178	0.026179	0.000868	0.003553
2	2.75E-06	0.001758	0.000113	0.007295	0.000252	0.003626
3	2.20E-06	0.001203	0.000232	0.00278	0.000289	0.003003
4	1.19E-06	0.000122	0.000312	0.004356	0.00025	0.004457
5	1.98E-06	0.001778	0.000437	0.004427	0.000185	0.004546
6	1.51E-06	0.002403	0.00038	0.004511	0.000229	0.004393
7	4.76E-06	0.001502	0.000852	0.00407	0.000239	0.001595
8	5.51E-06	9.87E-05	0.000365	0.004424	0.000508	0.000627
9	7.13E-06	0.001385	0.000609	0.006887	0.000426	0.002276
10	7.63E-06	0.001589	0.00093	0.006983	0.000326	0.002466

11	8.42E-06	0.001965	0.000902	0.00823	0.000569	0.00519
12	1.20E-05	0.003009	0.001281	0.005769	0.000469	0.001944
13	1.40E-05	0.00332	0.002147	0.002549	5.29E-05	0.002427
14	1.97E-05	0.003828	0.008608	0.002832	0.01137	0.002399
15	2.68E-05	0.004201	0.018018	0.002171	0.017294	0.002027
16	4.06E-05	0.004544	0.795477	0.00179	1.892132	0.001944
17	4.67E-05	0.004588	0.014831	0.003656	0.015073	0.003663
18	8.87E-06	0.028403	0.018468	0.252813	0.011717	0.206195
19	6.23E-05	0.224609	0.029538	0.278494	0.017456	0.237779
20	7.82E-05	0.240418	0.076951	0.301104	0.0362	0.269034
21	7.70E-05	0.226735	0.001975	0.013307	0.001976	0.013292
22	3.75E-06	0.00208	0.000264	0.004834	0.000279	0.004604
23	4.91E-06	0.005478	0.000165	0.006296	0.000165	0.006319
24	7.97E-06	0.007574	0.000891	0.012178	0.000891	0.012176

25	1.64E-06	0.002777	0.000294	0.004582	0.000343	0.005959
26	2.05E-06	0.003286	0.000439	0.006174	0.00031	0.006337
27	1.80E-06	0.004894	0.000326	0.005908	0.000371	0.006089
28	2.34E-06	0.005638	0.000513	0.00647	0.000346	0.00569
29	1.91E-06	0.00626	0.000156	0.010939	0.00057	0.008372
30	4.24E-06	0.007348	0.000817	0.001963	0.000432	0.004345
31	4.38E-06	0.007579	0.000437	0.002818	0.000241	0.004323
32	5.67E-06	0.007455	0.005383	0.001338	0.005474	0.001275

Table 4-9 presents the relative errors between the Nataf–3PEM and MCS results, with MCS taken as the reference. Overall, the errors for most nodes and branches remain very small, particularly for expected values of node voltages and branch powers, which are generally on the order of 10^{-6} to 10^{-4}. This confirms that the 3PEM method provides accurate estimates of first-order statistical moments under correlated uncertainties.

However, relatively larger errors are observed in specific regions of the network, most notably at nodes 18–21 and the corresponding downstream branches. For example, the relative error of voltage standard deviation reaches approximately 0.24 at node 20, and the standard deviation errors of branch active and reactive power exceed 0.25 in the same region. These higher errors can be attributed to the following factors.

First, these nodes are located near the points of renewable integration and branching structures in the network. As shown in the system topology, nodes 18, 21, and 33 are associated with distributed generation sources. The combination of renewable output variability and load uncertainty leads to stronger nonlinear interactions in these areas. Since 3PEM approximates the system response using a limited number of estimation points, it may not fully capture these nonlinear effects, resulting in larger deviations compared to MCS.

Second, the radial topology of the distribution network amplifies uncertainty propagation. In particular, branches around nodes 18–20 act as transition points between the main feeder and lateral branches. At these locations, power flows are influenced by both upstream aggregation and downstream variability, leading to higher sensitivity of second-order statistics (i.e., standard deviations). This increased sensitivity makes the approximation error of 3PEM more pronounced.

Third, the errors are significantly larger for standard deviations than for expected values. This is because standard deviation depends not only on the mean but also on higher-order moments of the distribution. The 3PEM method, based on a limited number of deterministic sampling points, is inherently more accurate for estimating first-order moments than second-order moments, especially when the underlying distributions deviate from Gaussian behaviour due to nonlinear power flow equations and correlated inputs.

Finally, in a few branches (e.g., branch 16), relatively large errors in active and reactive power expected values are observed. These are mainly associated with localised power injections or reversals, where the magnitude of the reference value is relatively small or changes sign. Under such conditions, even small absolute deviations can lead to large relative errors.

Overall, although higher errors appear at specific nodes and branches, they are confined to regions with strong nonlinearity and high uncertainty coupling. The results demonstrate that 3PEM maintains good accuracy across the majority of the network, while highlighting its limitations in capturing second-order statistics in highly sensitive areas.

Table 4-10 summarises the maximum relative errors observed for each variable. Most variables exhibit low maximum errors, particularly for node voltage expected values, which remain on the order of 10^{-6}, indicating excellent agreement between 3PEM and MCS.

However, a relatively large maximum error (greater than 1) is observed for the branch reactive power expected value. This phenomenon is primarily attributed to the nature of the relative error metric. Specifically, when the reference value obtained from MCS is close to zero, even a small absolute deviation can result in a disproportionately large relative error. In such cases, the magnitude of the error is amplified due to the small denominator, rather than reflecting a significant discrepancy in absolute terms.

This situation typically occurs in branches with low reactive power flow or near power flow reversal conditions, where the expected value is small or changes sign. Therefore, the large relative error does not indicate a failure of the 3PEM method, but rather highlights a limitation of relative error metrics when applied to quantities with small magnitudes.

Overall, when considering both the relative error distribution and the absolute error magnitudes presented earlier, the 3PEM method demonstrates good accuracy across the network, with larger relative errors confined to a small number of low-magnitude cases.

Table 4-10 Maximum Relative Errors for Each Variable

Variable	Maximum relative errors (p.u.)
Node Voltage Expected Value	0.0000782
Node Voltage Standard Deviation	0.240418
Branch Active Power Expected Value	0.795477
Branch Active Power Standard Deviation	0.301104
Branch Reactive Power Expected Value	1.892132
Branch Reactive Power Standard Deviation	0.269034

Table 4-11 Comparison of 3PEM and MCS

Calculation Method	Calculation Time (s)	Standard Variance (p.u.)
3PEM	8.416725	0.0244
MCS	22.122795	0.0254

Table 4-11 presents a comparative evaluation of the computational efficiency and statistical consistency of the Nataf–3PEM and MCS methods. The results show that 3PEM requires 8.42 s for computation, whereas MCS requires 22.12 s under the same simulation settings. This confirms that 3PEM achieves significantly higher computational efficiency, reducing execution time by approximately 62% compared to MCS. The improvement is primarily due to the deterministic nature of 3PEM, which avoids the need for large-scale random sampling and repeated power flow calculations.

In terms of statistical performance, the standard deviations obtained by the two methods are highly consistent, with values of 0.0244 p.u. for 3PEM and 0.0254 p.u. for MCS. The difference between the two is less than 4%, indicating that 3PEM accurately captures the variability of system responses under uncertainty. This agreement demonstrates that 3PEM is capable of reproducing second-order statistical characteristics with high fidelity, despite using a significantly reduced number of evaluation points.

Overall, the results highlight that 3PEM provides a favourable balance between computational efficiency and accuracy. While MCS remains a benchmark due to its robustness, its computational burden becomes significant for large-scale or real-time applications. In contrast, 3PEM offers a practical and efficient alternative for probabilistic power flow and harmonic analysis, particularly in scenarios where rapid evaluation is required.

4.8 Summary

A 3PEM–Copula/Nataf framework for probabilistic studies on the IEEE 33-bus network was established and systematically evaluated. The method produced results closely matching MCS in terms of the means and standard deviations of node voltages, branch active and reactive power, and network losses, while requiring significantly fewer power flow evaluations. This demonstrates its effectiveness as a computationally efficient alternative for uncertainty quantification.

In the harmonic setting with sources located at nodes 18, 21, and 33, the THD distributions across buses were successfully obtained. It was observed that buses closer to harmonic injection points exhibited higher THD levels and greater variability, reflecting the spatial propagation characteristics of harmonic distortion.

Correlation analysis further revealed that positive dependence among loads, as well as between load and PV generation, tends to increase both expected losses and variability, while potentially reducing voltages at weak-end buses. The magnitude of these effects depends strongly on the placement and capacity of distributed generation.

Error analysis indicated that the 3PEM–Copula approach maintains high accuracy for most buses and branches, with relatively larger deviations observed near feeder ends and at DG or harmonic injection points, where system nonlinearity is more pronounced. Under well-defined input statistics and dependence structures, the method provides a reliable and efficient tool for probabilistic assessment, including harmonic scenarios.

Building on the efficient approximation capability demonstrated in this chapter, Chapter 5 extends the analysis to a more comprehensive MCS-based framework for three-phase stochastic harmonic power flow studies on the IEEE 33-bus system. This allows a more detailed statistical characterisation of uncertainties, including phase unbalance effects, full probabilistic distributions of voltages, power flows, and THD, as well as quantitative risk indicators for limit violations. In addition, multi-criteria weighting methods—combining subjective analytic hierarchy process (AHP) with objective techniques—are introduced to support comprehensive power quality evaluation. This provides a solid foundation for identifying system vulnerabilities and guiding targeted mitigation strategies in renewable-integrated distribution networks.

Chapter 5 Three-Phase Monte Carlo Analysis of Stochastic Harmonic and Risk Characteristics in Distribution Networks

5.1 Introduction

Following the development and validation of the 3PEM–Nataf framework in Chapter 4, which provided an efficient single-phase probabilistic approximation of power flow and harmonic behaviour, this chapter advances the analysis toward a more detailed and realistic representation of distribution networks.

Building upon the probabilistic modelling framework established in the previous chapter, this chapter focuses on a comprehensive Monte Carlo Simulation (MCS)-based three-phase stochastic harmonic power flow analysis for the IEEE 33-bus distribution system. The approach aims to capture the combined effects of uncertainties in loads, renewable generation, and harmonic injections in an unbalanced three-phase network, yielding probabilistic distributions of key variables such as node voltages, branch flows, and total harmonic distortion.

This analysis is important because it quantifies phase-specific behaviours and harmonic propagation under realistic uncertainty conditions, which are essential for assessing power quality and operational reliability in distribution networks with high renewable penetration [236], [237]. The results include probabilistic risk indicators for voltage and active power limit violations, as well as a multi-criteria weighting scheme for comprehensive power quality evaluation.

The main objectives of this chapter are to establish a systematic MCS-based framework for combined fundamental and harmonic power flow analysis under stochastic conditions. This includes examining the probabilistic distributions of three-phase node voltages, branch power flows, and total harmonic distortion (THD) across the network. In addition, the chapter aims to quantify operational reliability by evaluating voltage and power limit risk indicators, including over-limit probabilities and associated risk values. Finally, multi-criteria indicator weights are derived and compared using both the subjective Analytic Hierarchy Process (AHP) and the objective Criteria Importance Through Intercriteria Correlation (CRITIC) methods, enabling a comprehensive assessment of power quality.

In Chapter 4, the 3PEM combined with the Nataf transformation was developed and validated as an efficient probabilistic power flow approach, particularly suitable for rapid estimation of statistical moments in simplified or single-phase scenarios. However, the scope of this chapter extends beyond moment-based approximation and requires a more detailed probabilistic characterization of system behaviour.

Specifically, Chapter 5 focuses on three-phase unbalanced distribution networks with harmonic interactions, where the objectives include obtaining full probabilistic distributions of both fundamental and harmonic quantities, evaluating voltage and power flow uncertainties under complex operating conditions, and calculating risk-based indices for subsequent multi-criteria assessment. In such contexts, the limitations of 3PEM become more evident, as it primarily captures low-order statistical moments and may not adequately represent nonlinear coupling effects, distribution asymmetry, and tail behaviours introduced by harmonic distortion and phase unbalance.

Therefore, MCS is adopted in this chapter as the primary analysis tool. Although computationally more intensive, MCS does not rely on moment-based approximations and is capable of capturing the complete probabilistic characteristics of system variables, including non-Gaussian distributions and complex dependencies. This makes it more suitable as a benchmark method for probabilistic harmonic power flow analysis under unbalanced conditions and for accurate risk quantification.

By incorporating harmonic phenomena into probabilistic power flow and extending to risk quantification and weighting in unbalanced systems, this chapter provides a detailed benchmark for evaluating uncertainty impacts in three-phase distribution networks. The outcomes serve as an analytical basis for identifying vulnerable points and informing mitigation strategies in renewable-integrated grids.

5.2 Monte Carlo-based three-phase stochastic harmonic power flow progress

This subsection presents a systematic 12-step procedure for conducting a MCS-based three-phase stochastic harmonic power flow analysis within the IEEE 33-bus distribution network. The methodology addresses uncertainties in load demand, wind power generation, and PV power output, while also accounting for harmonic distortions introduced by nonlinear devices. By integrating stochastic modelling, power flow computations, and statistical analysis, this process evaluates the probabilistic behaviour of the distribution system under diverse operating conditions.

Step 1: Read IEEE 33-Bus System Parameters

The initial step involves obtaining the essential parameters of the IEEE 33-bus distribution network. These parameters encompass:

Three-phase fundamental parameters: Base voltage, system frequency, and network topology.

Node load parameters: Active and reactive power demands at each bus, reflecting the unbalanced characteristics inherent in distribution systems.

Branch impedance parameters: Resistance, reactance, and mutual coupling coefficients for each line segment, modeled in a three-phase configuration.

Distributed generation (DG) access parameters: Locations, types, and rated capacities of DG units integrated into the network.

Harmonic source specifications: Locations of nonlinear loads or devices injecting harmonics, along with their harmonic current spectra, focusing on the 5th, 7th, 11th, 13th and 17th orders, as these are predominant in power systems per IEEE Standard 519.

These parameters are derived from the standard IEEE 33-bus test system dataset and adjusted to represent the three-phase, unbalanced nature of distribution networks.

Step 2: Sample Load Active and Reactive Power

To capture load demand uncertainty, active and reactive power at each node are sampled using a normal distribution, justified by its ability to model natural load variability based on historical data. The sampling is defined as:

$$P_{L,i} \sim \mathcal{N}(\mu_{P,i}, \sigma_{P,i}^2), \quad Q_{L,i} \sim \mathcal{N}(\mu_{Q,i}, \sigma_{Q,i}^2)$$

where $\mu_{P,i}$ and $\mu_{Q,i}$ denote the mean active and reactive power demands, and $\sigma_{P,i}$ and

$\sigma_{Q,i}$ represent the corresponding standard deviations, estimated from historical data or forecasting models.

In this study, these sampled values correspond to the total load at each node. The inter-phase imbalance is modelled by allocating the total nodal load unevenly across the three phases according to predefined phase distribution ratios, which reflect typical unbalanced loading conditions in distribution systems. This approach enables the representation of phase asymmetry without introducing additional stochastic variables for each phase.

Regarding the relationship between active and reactive power, $Q_{L,i}$ is not treated as an independent random variable. Instead, it is derived from the sampled active power using a fixed power factor assumption, i.e., $Q_{L,i} = P_{L,i}\tan(\phi_i)$, where ϕ_i is the load power factor angle. As a result, a deterministic dependence between P and Q is imposed, and no additional stochastic correlation modelling between active and reactive power is introduced in this work.

Step 3: Sample Wind Speed and Compute Power Output

For wind farms connected to the network, wind speed is sampled using the Weibull distribution, widely recognized for its suitability in modelling wind speed variability.

Step 4: Sample Solar Irradiance and Compute Power Output

For PV systems, solar irradiance is sampled using the Beta distribution, which effectively captures the bounded and skewed nature of irradiance data.

Step 5: Generate Monte Carlo Scenarios

The MCS generates 10,000 scenarios, each comprising a unique combination of sampled load, wind, and PV power values. These scenarios assume independence among stochastic variables for computational efficiency. The sample size of 10,000 is determined through convergence analysis, ensuring statistical stability of output variables' moments within acceptable tolerances. The simulation begins with scenario index $m=1$.

Step 6: Modify Three-Phase System Parameters for the m-th Scenario

For each scenario m, the three-phase system parameters are updated to incorporate:

Load injections: Adjusted based on sampled active and reactive power values.

DG injections: Modified according to the computed wind and PV power outputs.

This ensures the system model reflects the specific conditions of the m-th scenario.

Step 7: Calculate Three-Phase Fundamental Power Flow

The fundamental power flow for the m-th scenario is solved using the Newton–Raphson method in polar coordinates, which is suitable for capturing nonlinear behaviour and mutual coupling effects in unbalanced systems. In this study, the three-phase imbalance is explicitly modelled by representing each node with phase-specific load and generation values. Specifically, the total nodal load obtained from the stochastic sampling process is distributed across the three phases using predefined phase allocation factors:

$$P_i^{(a)},\ P_i^{(b)},\ P_i^{(c)} \text{and} Q_i^{(a)},\ Q_i^{(b)},\ Q_i^{(c)}$$

$$P_i^{(a)} + P_i^{(b)} + P_i^{(c)} = P_{L,i}, Q_i^{(a)} + Q_i^{(b)} + Q_i^{(c)} = Q_{L,i}$$

Where unequal phase allocation ratios are applied to represent realistic load asymmetry in distribution systems.

In addition, mutual coupling between phases is incorporated into the three-phase admittance matrix, allowing inter-phase interactions to be captured during the solution process. Based on this formulation, the three-phase Newton–Raphson power flow computes phase-wise voltage magnitudes and angles at each node, as well as active and reactive power flows in each branch.

Step 8: Calculate Harmonic Injection Currents and Solve Harmonic Power Flow

Harmonic distortions from nonlinear devices are modeled by calculating harmonic injection currents based on the fundamental currents from Step 7 and the specified harmonic spectra (5th, 7th, 11th, and 13th orders). The harmonic power flow is solved using the direct method (decoupled harmonic analysis), expressed for each harmonic order h as:

$$Y_h V_h = I_h$$

Where Y_h is the harmonic admittance matrix, V_h is the harmonic voltage vector, and

I_h is the harmonic current injection vector. This approach assumes negligible harmonic interactions, a valid approximation for distribution systems with moderate harmonic levels. The solution yields harmonic voltage magnitudes, as well as harmonic currents for each specified order.

Step 9: Record and Save Results for the m-th Scenario

Results from the fundamental and harmonic power flow calculations for the m-th scenario are stored, including fundamental voltage magnitudes and branch power flows, as well as harmonic voltages and currents for each considered harmonic order. The total harmonic distortion (THD) at each node is also recorded, which is calculated according to the definition given in Equation (X), where the contribution of all harmonic components is normalised by the corresponding fundamental voltage.

Step 10: Check Completion and Proceed

After storing results for the m-th scenario, the simulation evaluates:

If $m < 10,000$, increment m by 1 and return to Step 6 for the next scenario.

If $m = 10,000$, proceed to statistical analysis.

Step 11: Statistical Analysis of Monte Carlo Results

Upon completion of all Monte Carlo scenarios, the statistical characteristics of the output variables (e.g., node voltages, branch power flows, and THD) are obtained directly from the simulated samples. The mean and standard deviation are calculated to describe the central tendency and variability of each variable.

For visualisation purposes, probability distributions can be illustrated using smooth curves (e.g., kernel-based or histogram-based representations) to aid interpretation of the results. These representations are used only for graphical analysis, while all quantitative assessments are based on the raw MCS samples.

Step 12: Calculate Risk Indices for Limit Violations

Risk indices are computed to quantify the likelihood of operational limit violations:

Voltage limit violations: Probability of node voltages exceeding the standard range (0.93–1.07 p.u.), expressed as:

$$P(V_i > 1.07\text{p.u.}) \quad \text{or} \quad P(V_i < 0.93\text{p.u.})$$

Branch power limit violations: Probability of branch power flows exceeding thermal ratings, calculated as:

$$P(P_b > P_{b,\max})$$

Where $P_{b,\max}$ is the maximum allowable power flow in branch b. These indices assess system reliability under stochastic conditions, guiding mitigation strategies.

Additionally, the loads in the IEEE 33-node system are set to be unbalanced: phase C has the highest load, phase B the lowest, and phase A retains the original load values.

Figure 5-1 shows a flowchart of the 12-step process described above, which provides a structured framework for Monte Carlo-based three-phase stochastic harmonic power flow analysis in the IEEE 33-bus distribution network. By combining stochastic modelling of loads and renewable generation with detailed fundamental and harmonic power flow calculations, the approach captures the probabilistic behaviour of modern distribution systems.

Statistical characteristics of the outputs are obtained directly from the Monte Carlo samples, and risk indices are further evaluated to quantify the likelihood and severity of operational limit violations. These features enhance the practical relevance of the results, supporting system planning and operational decision-making.

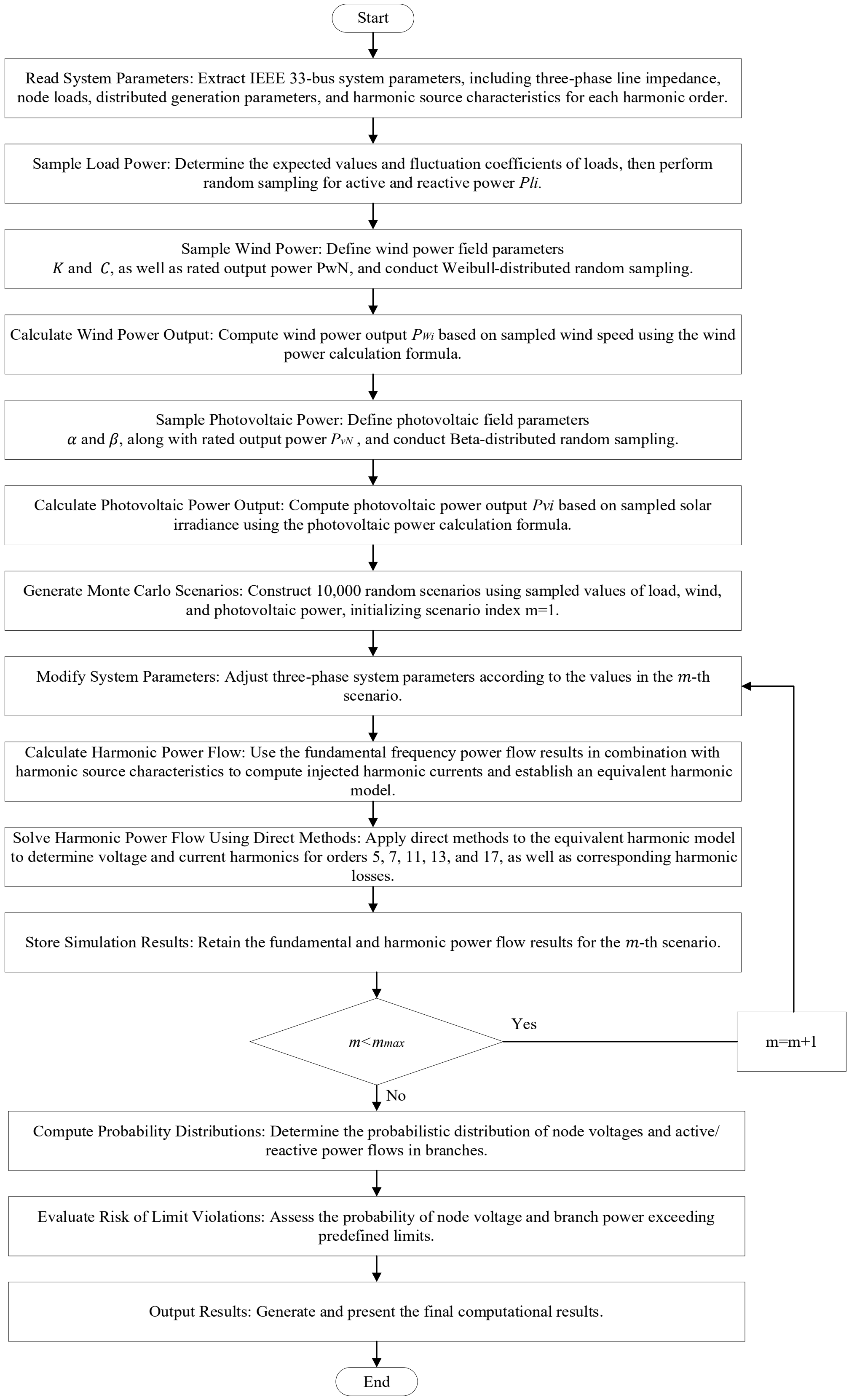

Figure 5-1 Flowchart of Monte Carlo-Based Three-Phase Stochastic Harmonic Power Flow Calculation in Distribution Networks

5.3 Network parameters and topology

The IEEE 33-bus radial distribution test system is employed to validate the Monte Carlo-based three-phase stochastic harmonic power flow model. This benchmark system, originally proposed by Baran and Wu (1989), is widely used for distribution network studies due to its radial topology and representative loading profile [238].

The network consists of 33 buses and 32 branches. Bus 1 is the slack bus with a fixed voltage of 1.00 p.u. The nominal line voltage is 12.66 kV, and the three-phase base power is 100 MVA (unless otherwise specified for per-unit calculations). The total nominal load is $3715\,\mathrm{kW} + 2300\,\mathrm{kVAr}$.

Node loads and branch impedances are listed in Table AP 4 (adopted from standard datasets). Impedances are given in ohms (Ω), with the base impedance calculated as $Z_{\mathrm{base}} = \dfrac{(12.66\,\mathrm{kV})^2}{100\,\mathrm{MVA}} \approx 1.6028\,\Omega$ for per-unit conversion if needed. Note: Load values represent total three-phase demands; for three-phase unbalanced modeling, loads are assumed equally distributed across phases unless specified otherwise, consistent with common extensions of the IEEE 33-bus system for unbalanced studies.

The topology is shown in Figure 5-2, including the placement of distributed generation (DG) and harmonic sources. A PV farm (rated 200 kW) is connected at bus 18, and a wind farm (rated 200 kW) at bus 33. Harmonic injections (nonlinear loads) are placed at buses 12, 22, 25, and 29, with dominant orders of the 5th, 7th, 11th, 13th, and 17th harmonics (based on typical spectra for power electronic devices and IEEE Standard 519).

Load uncertainty is modeled with a 20% standard deviation on nominal active and reactive power values (normal distribution). Voltage limits are set to 0.93 p.u. (lower) and 1.07 p.u. (upper) for compliance assessment. The MCS uses 10,000 scenarios, as detailed in Section 5.2.

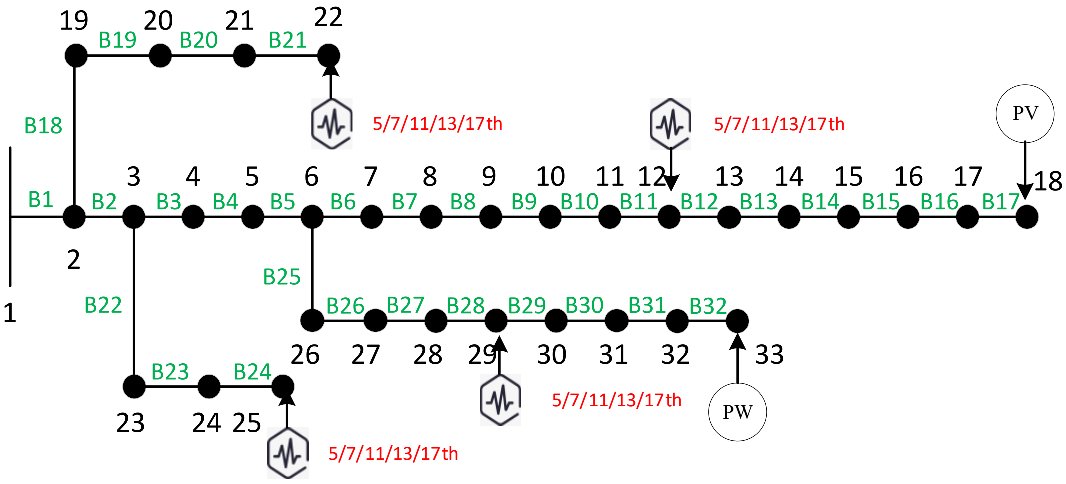

Figure 5-2 Topology of IEEE 33-bus System

Compared with the case study presented in Chapter 4, the network topology in Chapter 5 has been modified to better support three-phase stochastic harmonic analysis and to reflect a more realistic and distributed pattern of harmonic injection. In Chapter 4 (Figure 4-16), harmonic sources are primarily assigned to a limited number of nodes (e.g., nodes 18, 21, and 33), and they are co-located with distributed generation (DG) units. This configuration is suitable for validating the harmonic power flow model and analysing localised harmonic effects under correlated uncertainties. However, it implicitly assumes that harmonic injections originate from DG locations, which may not fully represent practical distribution systems where harmonics are mainly introduced by nonlinear loads.

In contrast, the topology in Chapter 5 (Figure 5-2) adopts a more distributed configuration. Harmonic sources are relocated to multiple nodes (e.g., nodes 12, 22, 25, and 29) along different feeder sections, rather than being concentrated on DG buses. This modification allows a clearer representation of harmonic propagation and interaction across the network. Meanwhile, the placement and types of DG units are adjusted to avoid co-locating all uncertainties at a small number of nodes and to better reflect diverse generation characteristics. In this study, DG units are not treated as dominant harmonic sources; instead, harmonic injections are modelled independently to represent nonlinear load behaviour. This separation enables a clearer distinction between the effects of renewable generation uncertainty and harmonic distortion.

Furthermore, the feeder structure is reorganised to better align with the requirements of three-phase modelling, where phase-wise quantities are explicitly considered. This supports a more consistent implementation of Monte Carlo simulation under unbalanced operating conditions and improves the representation of inter-phase interactions.

Overall, these modifications shift the focus from a relatively localised harmonic assessment in Chapter 4 to a more system-level investigation in Chapter 5, where spatial distribution, interaction effects, and stochastic variability can be jointly analysed. Importantly, this revised topology also provides a suitable foundation for the subsequent risk indicator analysis, as it enables variations in harmonic distortion, power flow, and voltage profiles to be evaluated across different parts of the network under uncertainty, thereby supporting a more comprehensive and meaningful assessment of system risk.

5.4 Probabilistic fundamental power flow result

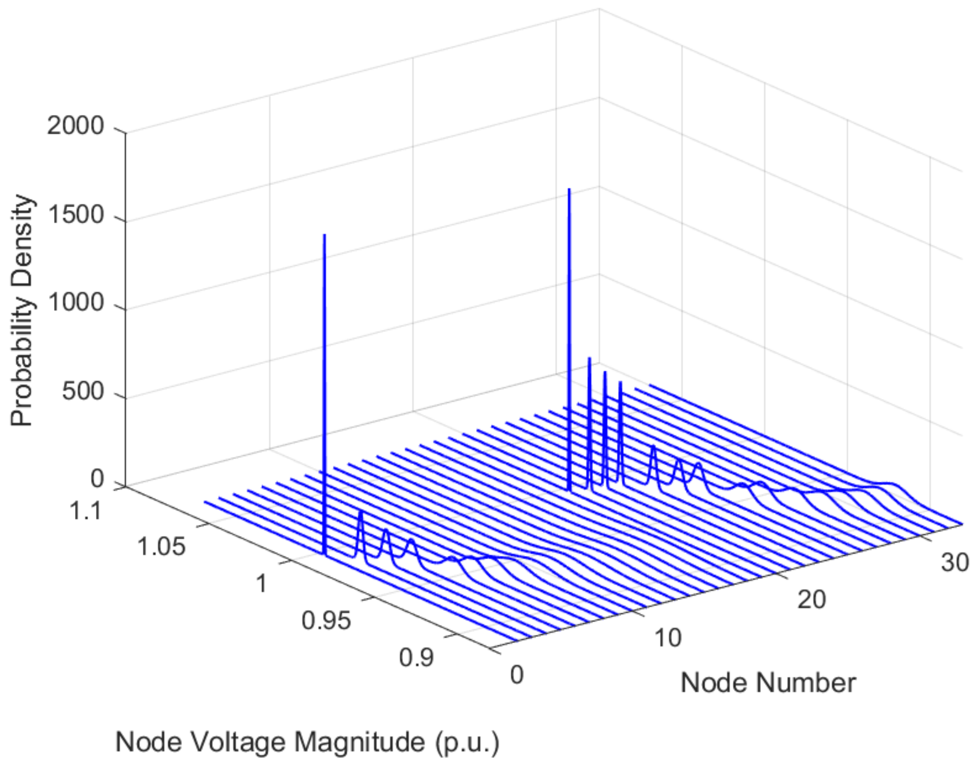

Figure 5-3 Phase-A Node Voltage Magnitude Probability Distribution

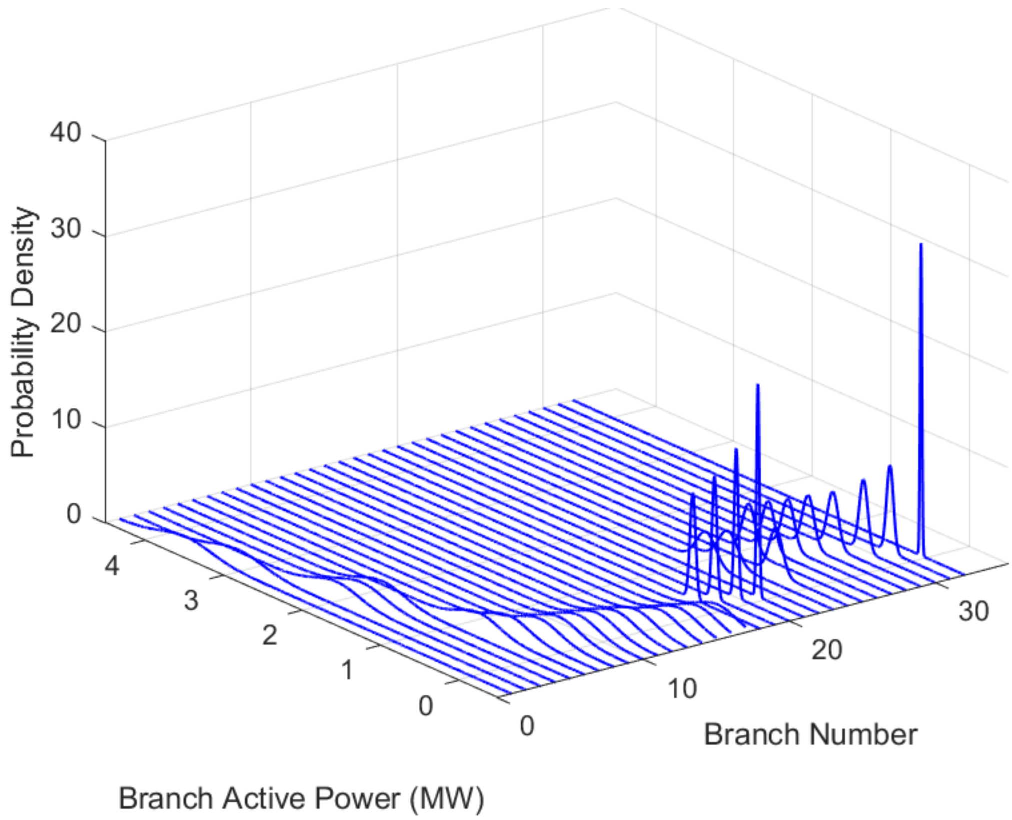

Figure 5-4 Phase-A Branch Active Power (MW) Probability Distribution

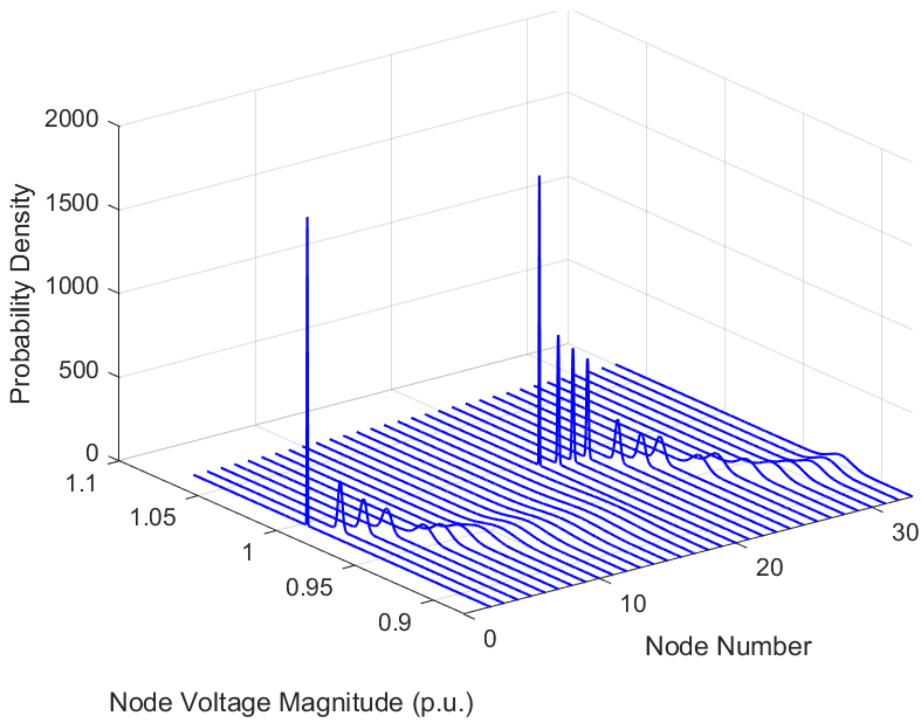

Figure 5-5 Phase-B Node Voltage Magnitude Probability Distribution

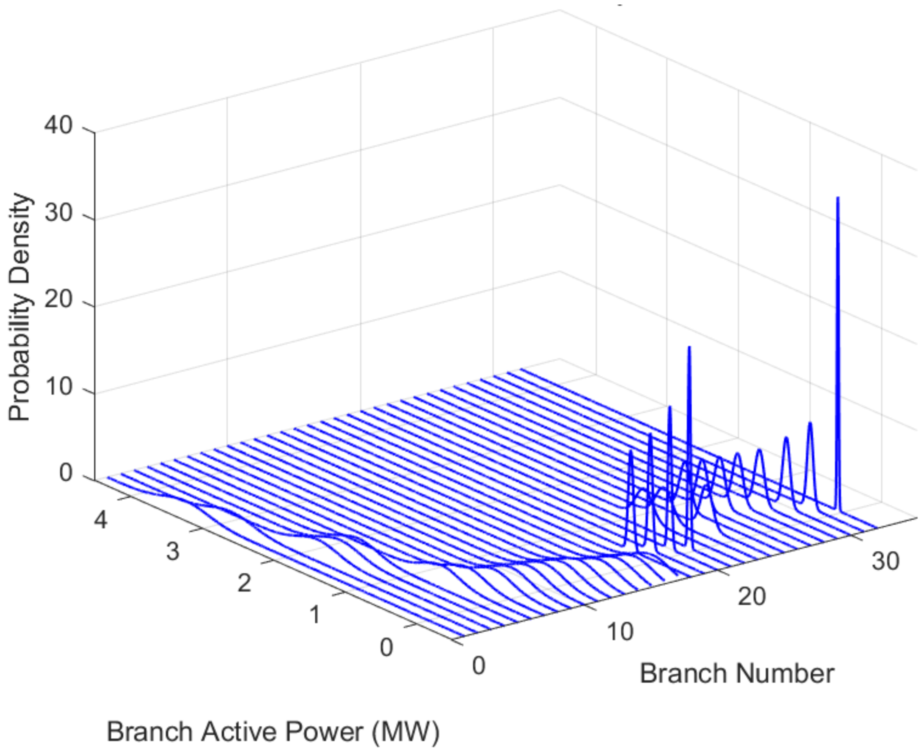

Figure 5-6 Phase-B Branch Active Power (MW) Probability Distribution

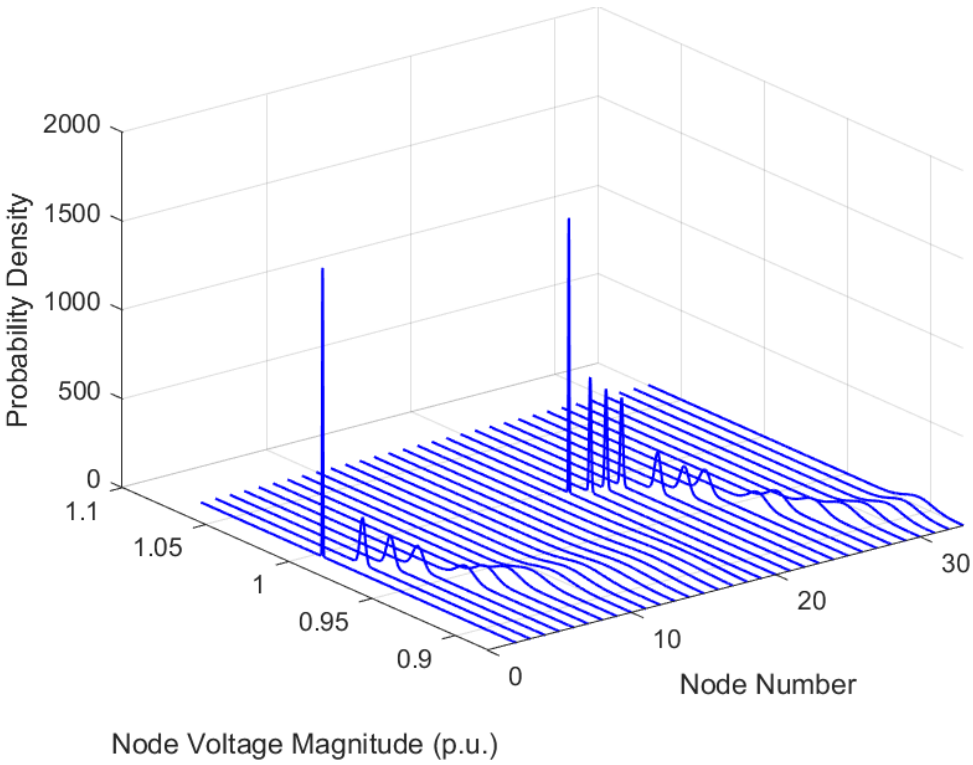

Figure 5-7 Phase-C Node Voltage Magnitude Probability Distribution

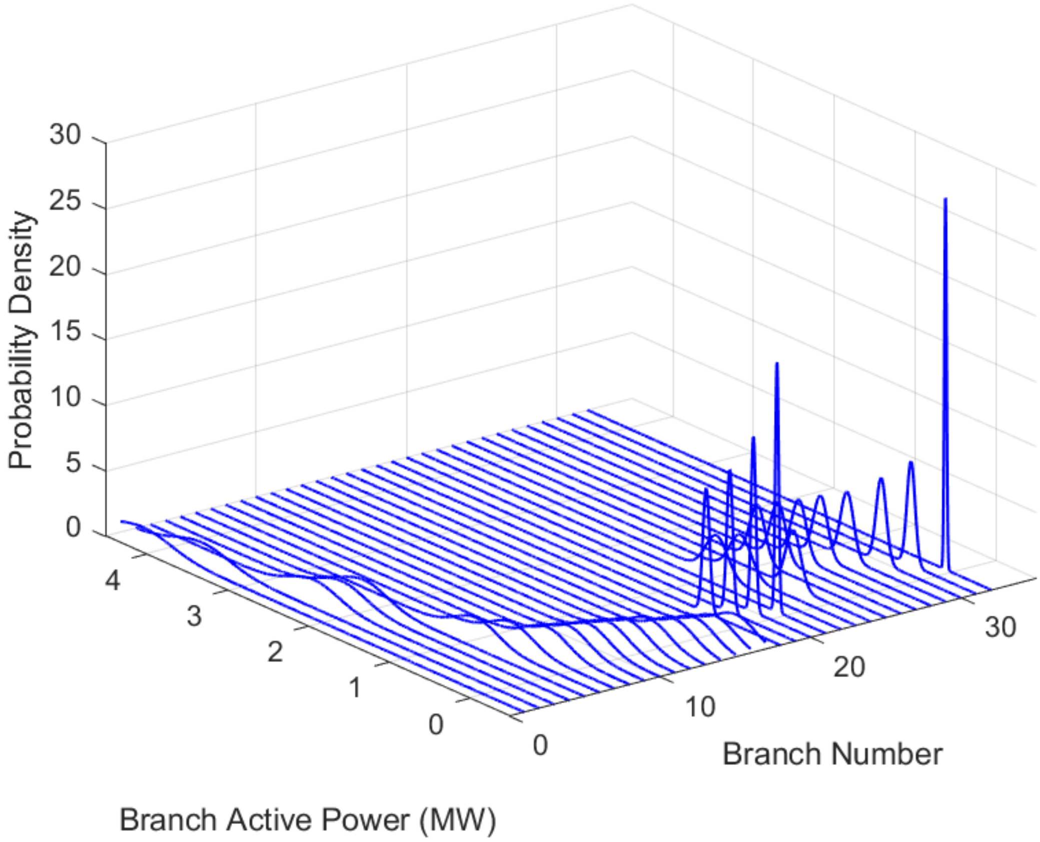

Figure 5-8 Phase-C Branch Active Power (MW) Probability Distribution

Figure 5-3, Figure 5-5 and Figure 5-7 illustrate the PDFs of node voltage magnitudes for phases A, B, and C, respectively, while Figure 5-4, Figure 5-6 and Figure 5-8 depict the corresponding PDFs for branch active power flows. These 3D visualizations illustrate the distribution across nodes/branches (x-axis), power/voltage values (y-axis), and probability density (z-axis), based on 10,000 MCS scenarios.

The probability distributions of branch reactive power were also computed in this study but are not presented here for brevity. This is because the reactive power exhibits similar spatial patterns and statistical characteristics to active power, as both are derived from the same power flow solutions and are strongly coupled through network equations. Therefore, including additional 3D plots for reactive power would not provide substantially new insights but would increase redundancy in the presentation. Instead, the key statistical properties of reactive power are discussed in subsequent sections.

Across all phases, voltage magnitudes exhibit a clear spatial trend: buses proximal to the slack bus (bus 1) display higher expected values and lower variability, while distant buses show reduced expectations and increased fluctuations. For phase A, the expected voltage at bus 2 is 0.9972 p.u. ($\sigma = 0.0002$ p.u.), dropping to 0.9208 p.u. ($\sigma = 0.0072$ p.u.) at bus 33. This drop arises from cumulative line losses and the amplified sensitivity of downstream voltages to stochastic load perturbations, as voltage drops are proportional to branch impedances and currents (per the approximate relation $\Delta V \approx I \cdot Z$). The PDFs transition from narrow peaks near the source (indicating stability due to slack bus regulation) to broader distributions at the ends, with some tails extending below 0.93 p.u., contributing to an overall system-wide voltage violation probability of approximately 61.83% (computed via empirical cumulative distribution functions integrated over limit bounds).

Figure 5-4 presents the probability distribution of active power flow in each branch for phase A. Branches close to the source carry higher expected power and exhibit greater fluctuation, as they must supply the combined power demands of downstream branches and loads. On the other hand, end branches only transfer local load power, leading to smaller expected values and reduced variability.

The trends for phases B and C are consistent with those observed in phase A. In both cases, the voltage profiles show similar spatial characteristics, with head nodes maintaining more stable and higher voltage levels due to the regulation effect of the source. Similarly, the branch active power distributions of phases B and C reflect higher expected power and variability at the source end, while end branches carry lower power with smaller fluctuations.

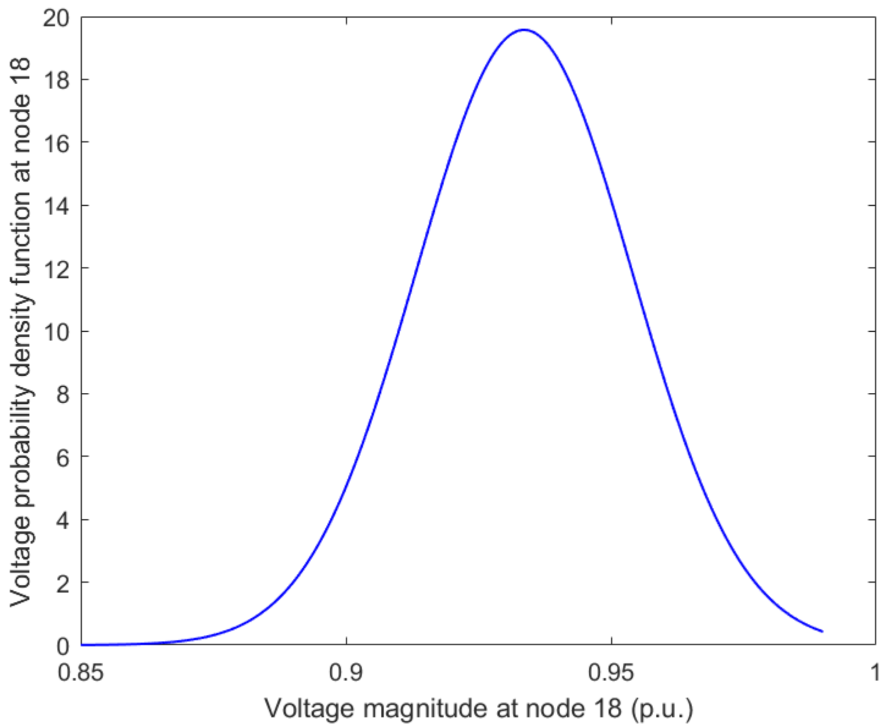

Figure 5-9 Phase-A Node 18 Voltage Magnitude Probability Distribution

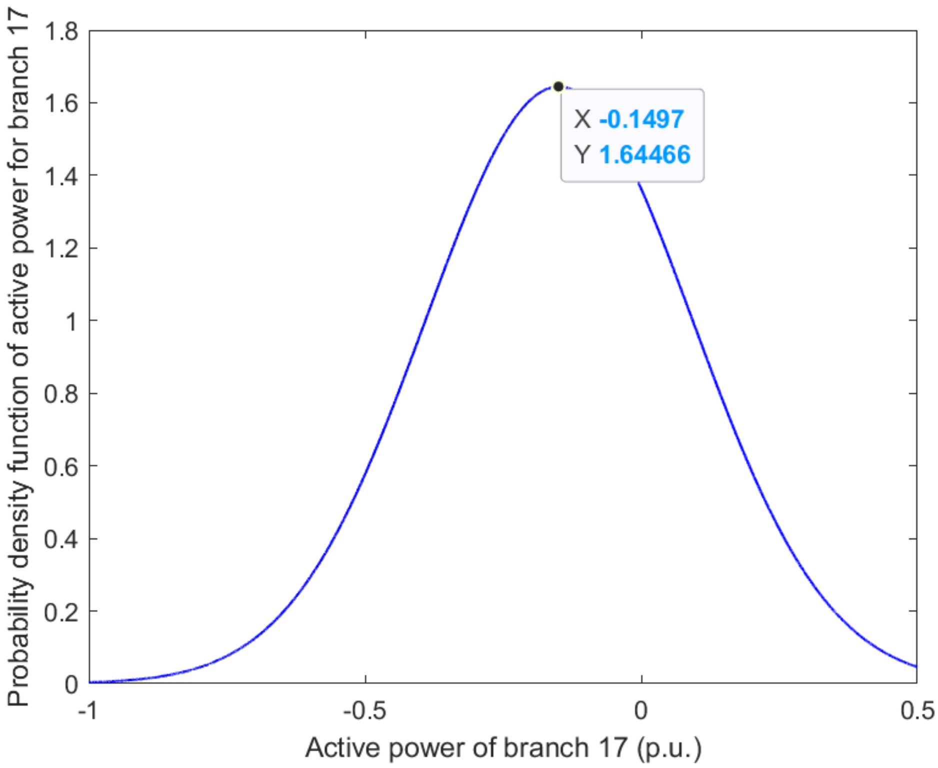

Figure 5-10 Phase-A Branch 17 Active Power (MW) Probability Distribution

Figure 5-9 shows the probability density function of the voltage magnitude at node 18 (Phase A). The distribution exhibits a clear unimodal and approximately symmetric shape, indicating that the voltage variations are relatively stable under stochastic inputs. The peak of the curve corresponds to the most probable operating voltage, while the spread reflects the level of uncertainty introduced by load and generation variability.

Figure 5-10 presents the probability density function of active power for branch 17 (Phase A). A similar unimodal distribution is observed, with the peak indicating the most likely power flow value. The wider spread compared to voltage suggests that branch power is more sensitive to stochastic variations in system conditions. The distribution also reflects the influence of network topology and nearby sources on power flow variability.

Table 5-1 Expected Value and Standard Deviation of Voltage at Each Node

Node Index	Phase A Node Voltage		Phase B Node Voltage		Phase C Node Voltage	
	Expectation (p.u.)	Standard deviation (p.u.)	Expectation (p.u.)	Standard deviation (p.u.)	Expectation (p.u.)	Standard deviation (p.u.)
1	1.0000		1.0000		1.0000	
2	0.9972	0.0002	0.9974	0.0002	0.9967	0.0002
3	0.9840	0.0014	0.9851	0.0013	0.9814	0.0015
4	0.9772	0.0021	0.9788	0.0020	0.9733	0.0023
5	0.9705	0.0029	0.9726	0.0028	0.9653	0.0032
6	0.9537	0.0048	0.9572	0.0046	0.9454	0.0052
7	0.9508	0.0053	0.9546	0.0051	0.9417	0.0057
8	0.9472	0.0064	0.9513	0.0062	0.9373	0.0069

9	0.9428	0.0082	0.9475	0.0079	0.9321	0.0086
10	0.9389	0.0100	0.9441	0.0097	0.9274	0.0105
11	0.9384	0.0104	0.9436	0.0100	0.9268	0.0108
12	0.9375	0.0110	0.9429	0.0106	0.9258	0.0114
13	0.9341	0.0136	0.9400	0.0132	0.9216	0.0140
14	0.9329	0.0146	0.9390	0.0142	0.9201	0.0151
15	0.9326	0.0157	0.9388	0.0152	0.9196	0.0161
16	0.9326	0.0169	0.9389	0.0165	0.9194	0.0174
17	0.9331	0.0193	0.9395	0.0189	0.9196	0.0199
18	0.9338	0.0206	0.9402	0.0201	0.9202	0.0211
19	0.9967	0.0002	0.9969	0.0002	0.9961	0.0003
20	0.9931	0.0005	0.9934	0.0005	0.9919	0.0006
21	0.9924	0.0006	0.9928	0.0006	0.9911	0.0007

22	0.9918	0.0007	0.9921	0.0007	0.9904	0.0008
23	0.9804	0.0016	0.9816	0.0016	0.9774	0.0018
24	0.9738	0.0024	0.9752	0.0022	0.9699	0.0026
25	0.9704	0.0028	0.9720	0.0027	0.9662	0.0031
26	0.9518	0.0049	0.9554	0.0047	0.9431	0.0054
27	0.9493	0.0051	0.9530	0.0048	0.9402	0.0056
28	0.9378	0.0059	0.9423	0.0056	0.9269	0.0066
29	0.9297	0.0066	0.9345	0.0062	0.9174	0.0074
30	0.9261	0.0069	0.9311	0.0065	0.9132	0.0078
31	0.9220	0.0072	0.9272	0.0068	0.9083	0.0081
32	0.9210	0.0072	0.9263	0.0068	0.9072	0.0082
33	0.9208	0.0072	0.9260	0.0068	0.9069	0.0082

Table 5-2 Expected Value and Standard Deviation of Branch Active Power

Branch Index	**Phase A Active Power**		**Phase B Active Power**		**Phase C Active Power**	
	Expected value (MW)	**Standard deviation (MW)**	**Expected value (MW)**	**Standard deviation (MW)**	**Expected value (MW)**	**Standard deviation (MW)**
1	3.6536	0.319089	3.39658	0.304087	4.22168	0.339686
2	3.180809	0.315037	2.951699	0.300254	3.675628	0.334171
3	2.105042	0.283127	1.926063	0.27105	2.47884	0.295126
4	1.968041	0.279117	1.799632	0.26728	2.322735	0.289439
5	1.892468	0.275629	1.729572	0.264102	2.233013	0.284867
6	0.848803	0.255492	0.757943	0.247921	1.027944	0.258777
7	0.647298	0.251478	0.578808	0.244856	0.776257	0.25301
8	0.444463	0.247033	0.388902	0.240693	0.521506	0.245771

9	0.38199	0.245566	0.331886	0.239576	0.45217	0.244009
10	0.320137	0.244509	0.275253	0.23857	0.383411	0.242667
11	0.274951	0.244212	0.23502	0.23828	0.330971	0.242268
12	0.214579	0.243738	0.179348	0.237843	0.26329	0.241681
13	0.153123	0.243177	0.123407	0.237554	0.194109	0.240584
14	0.032598	0.241564	0.013064	0.236989	0.063771	0.23915
15	-0.02773	0.241288	-0.04123	0.236901	-0.0014	0.23904
16	-0.08819	0.241612	-0.09654	0.237378	-0.0678	0.239098
17	-0.14882	0.242567	-0.15222	0.238211	-0.13441	0.239728
18	0.361878	0.036318	0.345317	0.034509	0.421336	0.041944
19	0.271521	0.031255	0.259089	0.029641	0.316686	0.036566
20	0.180687	0.025526	0.172078	0.024119	0.210332	0.029716
21	0.090394	0.018239	0.085964	0.017217	0.105129	0.021182

22	0.939618	0.122938	0.900155	0.116522	1.037027	0.134764
23	0.846618	0.120896	0.811324	0.114537	0.928027	0.131955
24	0.420584	0.084955	0.403317	0.080521	0.462191	0.091798
25	0.951557	0.078949	0.889956	0.07414	1.093963	0.09243
26	0.889051	0.077409	0.833708	0.072752	1.023511	0.090741
27	0.825756	0.075756	0.776727	0.071336	0.952026	0.088752
28	0.754462	0.072633	0.711662	0.068532	0.870935	0.084695
29	0.626472	0.067067	0.593322	0.063445	0.728619	0.077907
30	0.422447	0.053487	0.403154	0.050173	0.492903	0.062224
31	0.27066	0.043942	0.256812	0.040867	0.310363	0.049952
32	0.059947	0.011971	0.055883	0.011404	0.069878	0.014158

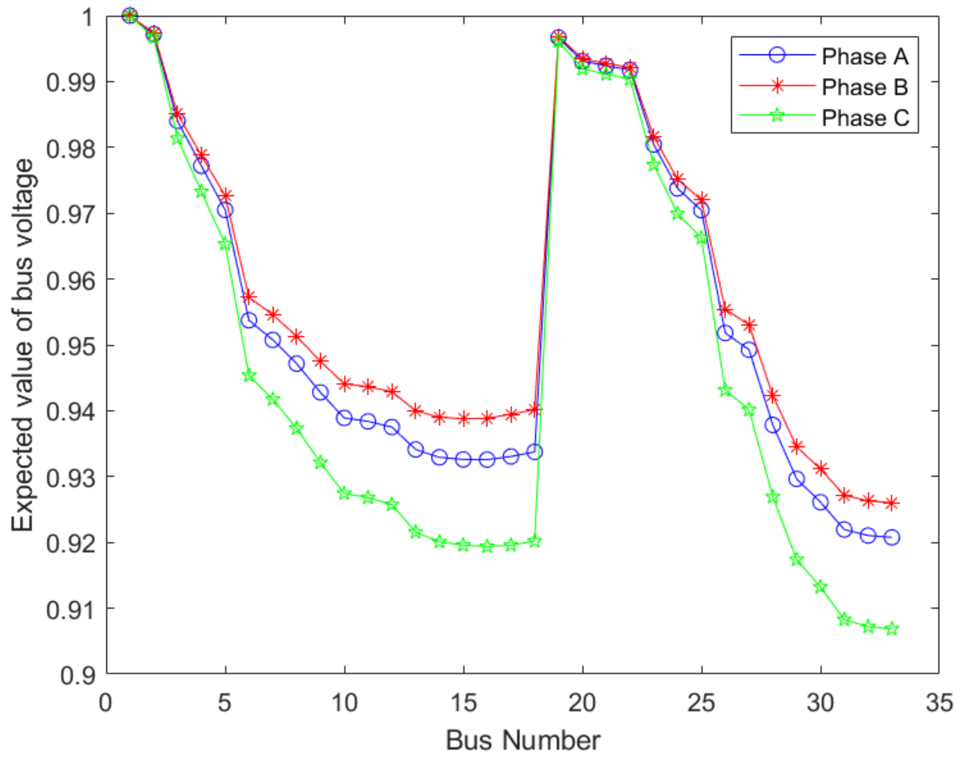

Figure 5-11 Expected Value of Three-Phase Voltage

Figure 5-11 shows the expected (mean) three-phase node voltage magnitudes across the IEEE 33-bus system, highlighting the impact of unbalanced PV generation and loads. The PV system at bus 18 injects 200 kW into phases A and B only (phase C receives zero PV output), while loads are unbalanced: phase C carries the highest demand, phase B the lowest, and phase A uses nominal values. In this case, the system includes a three-phase unbalanced PV generation connected at node 18. The PV unit injects a total active power of 200 kW, which is equally distributed between phases A and B, while phase C has no PV output.

Under the combined influence of unbalanced PV generation and phase-dependent load conditions, clear differences in voltage magnitudes are observed among the three phases. Phase C consistently exhibits the lowest voltage levels, which can be attributed to the absence of local generation and relatively higher effective loading. In contrast, phases A and B show higher voltage magnitudes due to the presence of local PV injection.

The voltage rise is most noticeable at node 19, which is electrically downstream of the PV connection point (node 18). This reflects the radial structure of the network, where injected power propagates along the feeder and leads to increased voltage levels in subsequent nodes.

Overall, the results demonstrate that phase imbalance in both generation and loading conditions leads to uneven voltage profiles across the network, with the magnitude and location of voltage deviations strongly influenced by feeder topology and power flow direction.

Under these conditions, phase-specific asymmetries emerge. Phase C, burdened by higher load without local generation support, exhibits the lowest mean voltages throughout the feeder (e.g., $\mu = 0.9069$ p.u. at bus 33). Phase B benefits from lighter loading and PV injection, resulting in relatively higher voltages (e.g., $\mu = 0.9260$ p.u. at bus 33). Phase A shows intermediate values, closer to a balanced baseline. The effect is most evident near bus 18, where local PV injection causes a modest voltage rise in phases A and B (up to approximately 0.94 p.u. in some segments), while phase C remains unaffected by DG.

These phase differences arise from the combined effects of uneven load distribution and single-phase PV support, which can lead to increased neutral currents, higher losses, and additional challenges for voltage regulation in unbalanced systems.

Compared with the deterministic load flow results for the standard IEEE 33-bus system (without DG), where the minimum voltage magnitude is typically around 0.903–0.91 p.u. at bus 33, the stochastic modelling framework introduces variability around the mean operating point rather than changing only the mean values. This variability is reflected in the standard deviation of voltage magnitudes.

In particular, nodes that are electrically distant from the slack bus and close to uncertain injections exhibit larger standard deviations. For example, node 18 shows a relatively higher standard deviation (approximately 0.007–0.008 p.u., as reported in Table 5-2), indicating increased sensitivity to uncertainties in both load demand and renewable generation. This demonstrates that stochastic effects are not uniform across the network but are strongly influenced by electrical distance and local operating conditions.

Limitations of the current analysis include the assumption of fixed PV output (ignoring solar irradiance variability modeled elsewhere) and independence among stochastic variables; correlations could be incorporated in future extensions using methods like the Nataf transformation from Chapter 4. More efficient probabilistic power flow techniques, such as point estimate methods, may also improve computational scalability.

In summary, the probabilistic fundamental power flow results demonstrate spatially dependent and phase-specific variations in voltage and power flow. Proximal buses remain relatively stable due to slack bus regulation, while distal buses show greater sensitivity to uncertainties. Phase unbalances from asymmetric generation and loading further complicate voltage profiles, emphasizing the value of three-phase probabilistic analysis for reliability assessment in renewable-integrated unbalanced distribution networks.

5.5 Probabilistic harmonic power flow results

Harmonic power flow analysis was conducted to evaluate the propagation and probabilistic characteristics of voltage distortions in the IEEE 33-bus system, incorporating the stochastic load model from Section 5.3. Harmonic sources were modeled at buses 12, 22, 25, and 29, injecting fixed-magnitude currents for the 5th, 7th, 11th, 13th, and 17th orders.

The total harmonic distortion (THD) of the voltage at node i is defined as:

$$THD_{V_i} = \frac{\sqrt{\sum_{h=2}^{H} |V_i^h|^2}}{|V_i^1|} \times 100\%, \quad i = 1, 2, \ldots, n$$

where V_i^1 Is the fundamental voltage and current components, and $|V_i^h|$ is the h-th order harmonic components. Here, n is the total number of nodes, and m is the total number of branches; n = 33 buses and m = 32.

The Figure 5-12 shows the probability density function (PDF) of the voltage THD across all nodes in the IEEE 33-bus system. The nodes with harmonic sources (nodes 12, 22, 25, and 29) exhibit relatively high expected THD values and larger variances. This is due to the high harmonic current injection at these nodes, which leads to significant voltage distortion and greater fluctuation. In contrast, nodes farther from the harmonic sources (e.g., nodes 1 and 19) show lower expected THD and smaller variation, as the harmonic currents arriving at these locations are attenuated by the network impedance. As a result, the local harmonic voltage distortion is weaker and more stable.

Table 5-3 presents the mean and standard deviation of the voltage THD across all three phases for each node, highlighting the spatial impact of harmonic sources in the system.

The PDFs generally approximate skewed Gaussians, with tails toward higher THD under heavy load scenarios. System-wide, expected THD remains below IEEE Standard 519 limits (<5% for voltages <69 kV), but probabilistic tails indicate a ~5–10% risk of exceeding 3% at source buses (estimated via CDF integration, assuming lognormal fits for conservatism). Phases B and C show comparable trends (Table 5-3), with slight asymmetries due to unbalanced fundamental conditions, e.g., phase C's higher loads yielding marginally elevated THD variances (σ up to 0.0030 at bus 25).

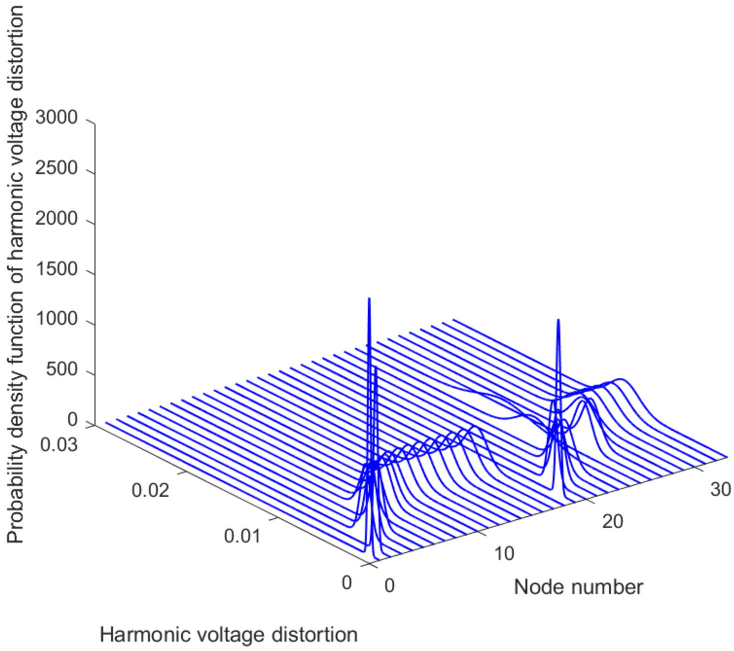

Figure 5-12 Probability Distribution of Harmonic Voltage Distortion Rate at Each Node

Table 5-3 Expected Value of Harmonic Voltage Distortion Rate at Each Node and Standard Deviation of Fluctuation

Node Index	**Phase A of Harmonic Voltage Distortion**		**Phase B of Harmonic Voltage Distortion**		**Phase C of Harmonic Voltage Distortion**	
	Expected value (p.u.)	**Standard deviation (p.u.)**	**Expected value (p.u.)**	**Standard deviation (p.u.)**	**Expected value (p.u.)**	**Standard deviation (p.u.)**
1	0.0012	0.0002	0.0011	0.0001	0.0013	0.0002
2	0.0017	0.0002	0.0016	0.0002	0.0019	0.0002
3	0.0040	0.0006	0.0038	0.0005	0.0045	0.0006
4	0.0046	0.0006	0.0043	0.0006	0.0051	0.0006
5	0.0051	0.0006	0.0049	0.0006	0.0058	0.0007

6	0.0073	0.0008	0.0068	0.0008	0.0082	0.0010
7	0.0078	0.0009	0.0073	0.0008	0.0089	0.0010
8	0.0081	0.0009	0.0076	0.0009	0.0092	0.0010
9	0.0088	0.0010	0.0083	0.0009	0.0100	0.0012
10	0.0096	0.0011	0.0090	0.0010	0.0109	0.0013
11	0.0097	0.0011	0.0091	0.0010	0.0110	0.0013
12	0.0098	0.0011	0.0092	0.0011	0.0112	0.0013
13	0.0098	0.0011	0.0092	0.0011	0.0111	0.0013
14	0.0097	0.0011	0.0091	0.0011	0.0111	0.0013
15	0.0097	0.0011	0.0091	0.0011	0.0111	0.0013
16	0.0097	0.0011	0.0091	0.0011	0.0111	0.0013
17	0.0097	0.0011	0.0091	0.0011	0.0110	0.0013
18	0.0096	0.0011	0.0091	0.0011	0.0110	0.0013
19	0.0019	0.0002	0.0018	0.0002	0.0021	0.0003
20	0.0037	0.0005	0.0035	0.0005	0.0042	0.0006
21	0.0043	0.0006	0.0041	0.0006	0.0049	0.0007
22	0.0055	0.0008	0.0053	0.0008	0.0064	0.0010
23	0.0060	0.0009	0.0057	0.0009	0.0067	0.0010
24	0.0105	0.0018	0.0101	0.0018	0.0117	0.0020
25	0.0150	0.0028	0.0144	0.0026	0.0168	0.0030
26	0.0075	0.0009	0.0070	0.0008	0.0084	0.0010
27	0.0078	0.0009	0.0073	0.0009	0.0088	0.0010

28	0.0098	0.0013	0.0091	0.0012	0.0111	0.0014
29	0.0113	0.0015	0.0105	0.0014	0.0128	0.0017
30	0.0113	0.0015	0.0105	0.0014	0.0128	0.0017
31	0.0113	0.0015	0.0105	0.0014	0.0128	0.0017
32	0.0113	0.0015	0.0105	0.0014	0.0128	0.0017
33	0.0113	0.0015	0.0105	0.0014	0.0128	0.0017

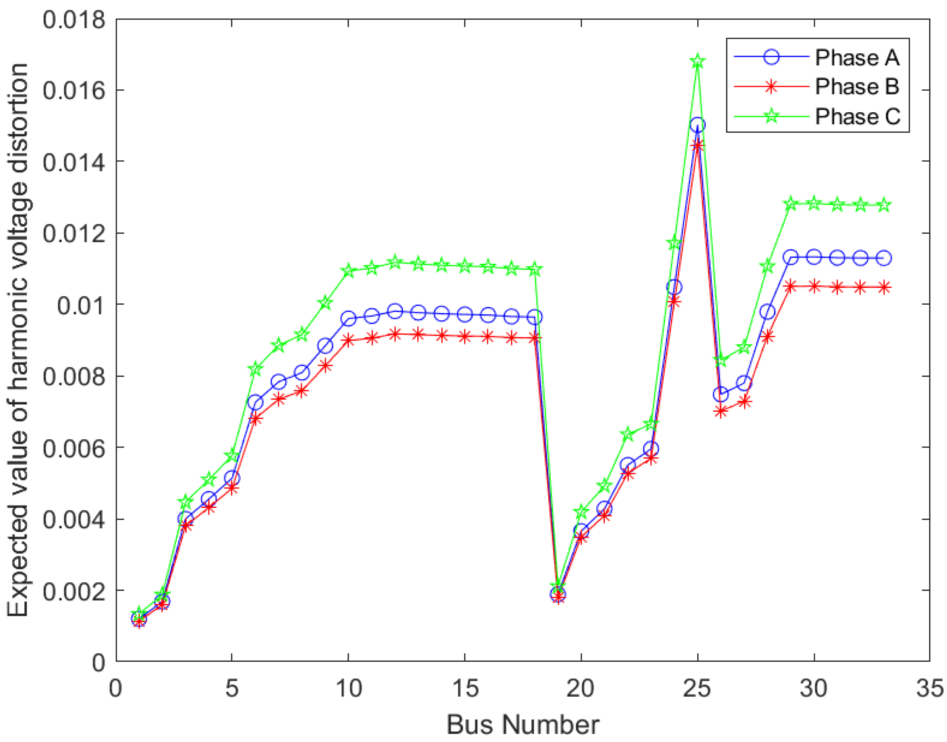

Figure 5-13 Expected Value of Three-Phase Harmonic Voltage Distortion at Each Node

Figure 5-13 shows the expected values of three-phase voltage THD at all buses. The overall variation of THD across the network is strongly affected by the locations of harmonic sources, the feeder topology, and the underlying fundamental voltage profile. In general, THD increases along feeder sections that are electrically influenced by harmonic injections and tends to remain lower in buses that are closer to the slack bus or more strongly supported by the upstream network.

A clear phase-dependent pattern can be observed, with Phase C generally exhibiting the highest THD, followed by Phase A, while Phase B remains the lowest over most of the network. This reflects the influence of three-phase unbalance in both the fundamental operating point and the harmonic propagation process. Since THD is defined as the ratio between the harmonic voltage magnitude and the corresponding fundamental voltage magnitude, phase differences in both harmonic response and fundamental voltage contribute to the unequal THD levels.

The THD values rise progressively along the feeder from the upstream section toward buses 10–18, where they reach a relatively stable elevated level. A sharp reduction is then observed around bus 19, which marks the transition to another feeder section that is more strongly supported by the upstream network. Beyond this point, THD increases again and reaches its highest value around bus 25. This indicates that the lower lateral feeder is particularly sensitive to harmonic propagation, most likely due to its electrical distance from the source and the accumulation of harmonic effects in that section.

A further local peak is observed around bus 25, after which THD decreases and then rises again toward buses 29–33. The relatively high THD in the downstream buses does not necessarily imply that the local harmonic injection is strongest there; rather, it reflects the combined effect of harmonic propagation and the lower fundamental voltage magnitudes in the weak-end portion of the feeder. In other words, even when the harmonic voltage component is not maximal, THD can still become relatively large if the corresponding fundamental voltage is small.

The case of bus 22 is also notable. Although it is defined as a harmonic source bus, its THD level is only moderate compared with buses such as 25 and the downstream buses near 29–33. This suggests that the local network conditions at bus 22, including its stronger upstream support and relatively higher fundamental voltage level, reduce the resulting THD ratio. Therefore, the distribution of THD across the network is not determined solely by whether a bus is a harmonic source, but by the interaction between source location, feeder impedance, propagation path, and local fundamental voltage magnitude.

Overall, Figure 5-13 indicates that voltage THD in the network is spatially non-uniform and phase-dependent. The highest distortion occurs in feeder sections that combine harmonic injection, weak voltage support, and greater electrical distance from the slack bus, while buses with stronger upstream support tend to exhibit lower THD values.

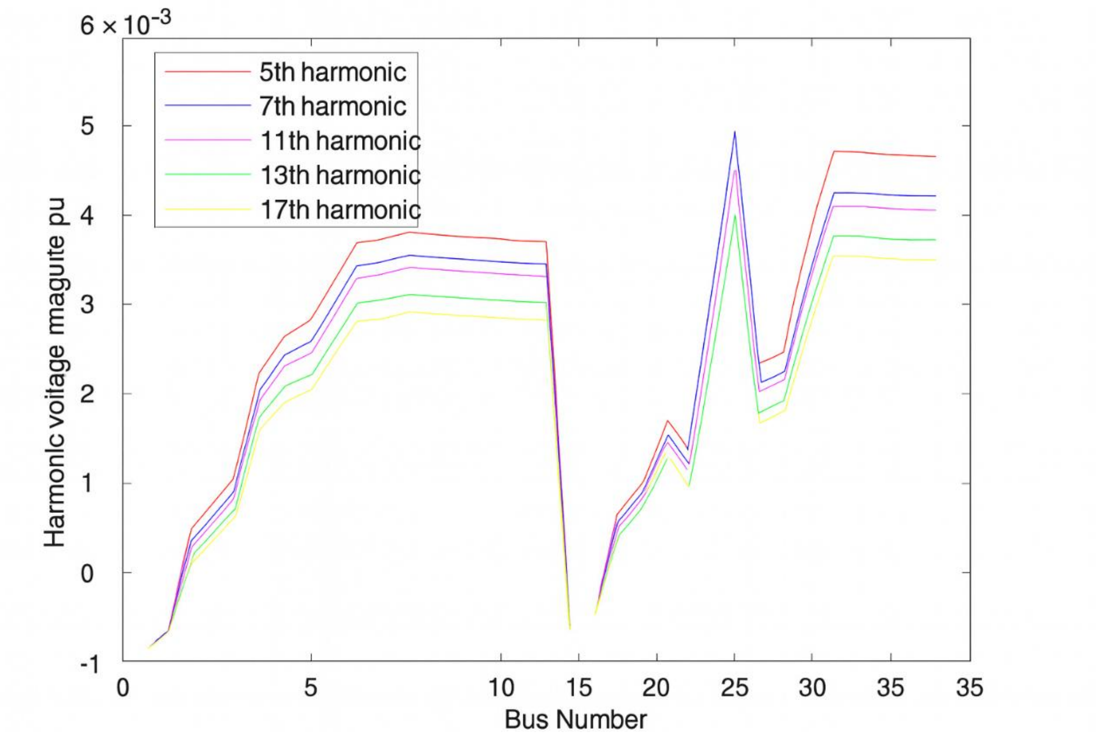

Figure 5-14 Harmonic Voltage Magnitude

Figure 5-14 presents the harmonic voltage magnitudes for different harmonic orders across all buses. A consistent ordering of harmonic magnitudes can be observed throughout most of the network, with the 5th harmonic exhibiting the highest magnitude, followed by the 7th, 11th, 13th, and 17th harmonics. This indicates that lower-order harmonics contribute more significantly to the overall harmonic distortion in the system.

The spatial variation of harmonic voltages shows a clear dependence on feeder topology. Harmonic magnitudes increase progressively along the feeder sections, particularly in the upstream portion (buses 1–12), where the values gradually rise and then stabilise. A sharp drop is observed around bus 15, which corresponds to a transition point between feeder sections with different electrical characteristics. Beyond this point, harmonic voltages increase again and reach a pronounced peak around bus 25, indicating strong harmonic accumulation in this part of the network.

Downstream of bus 25, the harmonic voltage magnitudes decrease locally and then increase again toward the end of the feeder (buses 29–33). This pattern suggests that harmonic propagation is influenced by both network impedance distribution and the location of harmonic injections. In particular, buses located further from the slack bus and within weaker feeder sections tend to exhibit higher harmonic voltage magnitudes due to reduced voltage support and cumulative effects along the line.

Across different harmonic orders, the shapes of the curves are similar, indicating that the network structure governs the spatial distribution, while the magnitude differences are mainly determined by the injected harmonic currents at each frequency. The absence of monotonic behaviour across the network reflects the interaction between multiple harmonic sources and the non-uniform electrical characteristics of the feeder.

Overall, the results demonstrate that harmonic voltage magnitudes are strongly dependent on both harmonic order and network location, with lower-order harmonics dominating and certain feeder sections showing higher susceptibility to harmonic accumulation.

5.6 Risk indicator calculation results

This section evaluates the probabilistic risks of voltage and active power limit violations in the IEEE 33-bus distribution network under the stochastic scenarios defined in Section 5.2. The assessment uses two quantitative indicators—over-limit probability and risk value—to measure the likelihood and expected severity of operational limit violations, enabling identification of vulnerable nodes and branches for mitigation.

For a variable x (e.g., voltage V_i at node i or apparent power S_l in branch l), the over-limit probability represents the fraction of MCS samples that exceed predefined limits. For voltage, the limits are set as V < 0.93 p.u. or V > 1.07 p.u. For branch loading, the limit is defined in terms of apparent power capacity ($S_l > S_l^{\max}$), which reflects the thermal constraint of the branch.

In this study, the same capacity limit is applied to all branches for consistency, with $S_l^{\max}$ derived from the base-case loading level. The violation check is performed for each branch across all Monte Carlo samples.

The risk value expresses the expected severity of violations:

$$\text{Risk} = \mathbb{E}[\mid x - x_{\text{lim}} \mid \mid x \notin [x_{\min}, x_{\max}]] \times P(x \notin [x_{\min}, x_{\max}])$$

Figure 5-15 and Figure 5-16 illustrate the probability density functions (PDFs) for Node 33 voltage and Branch loading (represented here using active power for illustration), respectively.. The blue, red, and green curves correspond to Phases A, B, and C. Table 5-5 and Table 5-6 list the detailed over-limit probabilities and risk values for each node and branch across all three phases.

5.6.1 Voltage Risk Assessment

Table 5-4 presents the voltage limit-violation probability and corresponding risk index for each node and each phase, based directly on the Monte Carlo samples. The results show a clear phase-dependent and location-dependent pattern of voltage vulnerability. In general, Phase C exhibits the highest violation probabilities and risk indices across the network, followed by Phase A, while Phase B remains the least vulnerable. This ranking is consistent with the three-phase voltage profiles reported earlier, where

Phase C maintains the lowest expected voltage level over much of the feeder and is therefore more prone to falling below the lower voltage limit of 0.93 p.u.

A strong spatial trend is also evident. For nodes 1–6, and again for nodes 19–25, the violation probabilities are essentially zero in all three phases, indicating that these parts of the network remain sufficiently supported under stochastic operating conditions. In contrast, significant undervoltage risk emerges in the downstream sections. Along the feeder segment around nodes 10–18, the violation probability increases progressively, particularly in Phase C, where it rises from 0.5105 at node 10 to around 0.6859 at node 18. A similar pattern appears again in the downstream end section around nodes 28–33, where Phase C reaches very high probabilities, peaking at 0.8613 at node 32 and remaining at 0.8471 at node 33. These results indicate that the weakest parts of the network are concentrated in electrically remote sections with lower voltage support.

The risk index follows the same overall trend as the violation probability, but it also reflects the severity of violations rather than their frequency alone. This distinction is important. For example, in Phase C, the highest risk index is observed at node 18 (0.01253), although the highest violation probability occurs at node 32 (0.8613). This indicates that violations at node 18, while slightly less frequent than those at node 32, are on average more severe when they occur. The same tendency can be observed in Phases A and B, where node 18 also gives the largest risk indices within each phase. Therefore, the most critical node is not necessarily the one with the highest violation probability, but the one where the combined effect of frequency and severity is greatest.

Table 5-4 Voltage Limit-Violation Probability and Risk Index for Each Node

Node Index	**Phase A Voltage**		**Phase B Voltage**		**Phase C Voltage**	
	Over-Limit Probability	**Risk Index**	**Over-Limit Probability**	**Risk Index**	**Over-Limit Probability**	**Risk Index**
1	0	0	0	0	0	0
2	0	0	0	0	0	0
3	0	0	0	0	0	0
4	0	0	0	0	0	0
5	0	0	0	0	0	0
6	0	0	0	0	0	0
7	0	0	0	0	0.0009	1.82E-06
8	0	0	0	0	0.0219	4.63E-05
9	0.0015	1.59E-06	0	0	0.2327	0.00083

10	0.0418	8.9E-05	0.0017	1.86E-06	0.5105	0.003312
11	0.0558	0.000134	0.0029	3.94E-06	0.5386	0.003797
12	0.0944	0.000254	0.0068	1.12E-05	0.5825	0.004678
13	0.3068	0.001479	0.08	0.000217	0.6898	0.00864
14	0.3783	0.002239	0.1375	0.000452	0.7141	0.010172
15	0.411	0.002723	0.1761	0.000652	0.7161	0.010979
16	0.4358	0.003186	0.2097	0.00088	0.7126	0.011653
17	0.4519	0.003834	0.2517	0.001264	0.6992	0.012476
18	0.4474	0.003959	0.2578	0.001368	0.6859	0.012533
19	0	0	0	0	0	0
20	0	0	0	0	0	0
21	0	0	0	0	0	0
22	0	0	0	0	0	0

23	0	0	0	0	0	0
24	0	0	0	0	0	0
25	0	0	0	0	0	0
26	0	0	0	0	0.0004	3.7E-07
27	0	0	0	0	0.0019	4.04E-06
28	0.0068	1.37E-05	0	0	0.2751	0.001217
29	0.1273	0.000493	0.0269	6.95E-05	0.6767	0.005758
30	0.2305	0.001137	0.0742	0.000251	0.7862	0.008461
31	0.34	0.002066	0.1392	0.000612	0.8549	0.011288
32	0.3565	0.002258	0.1523	0.000703	0.8613	0.01175
33	0.3392	0.002177	0.1446	0.000682	0.8471	0.011434

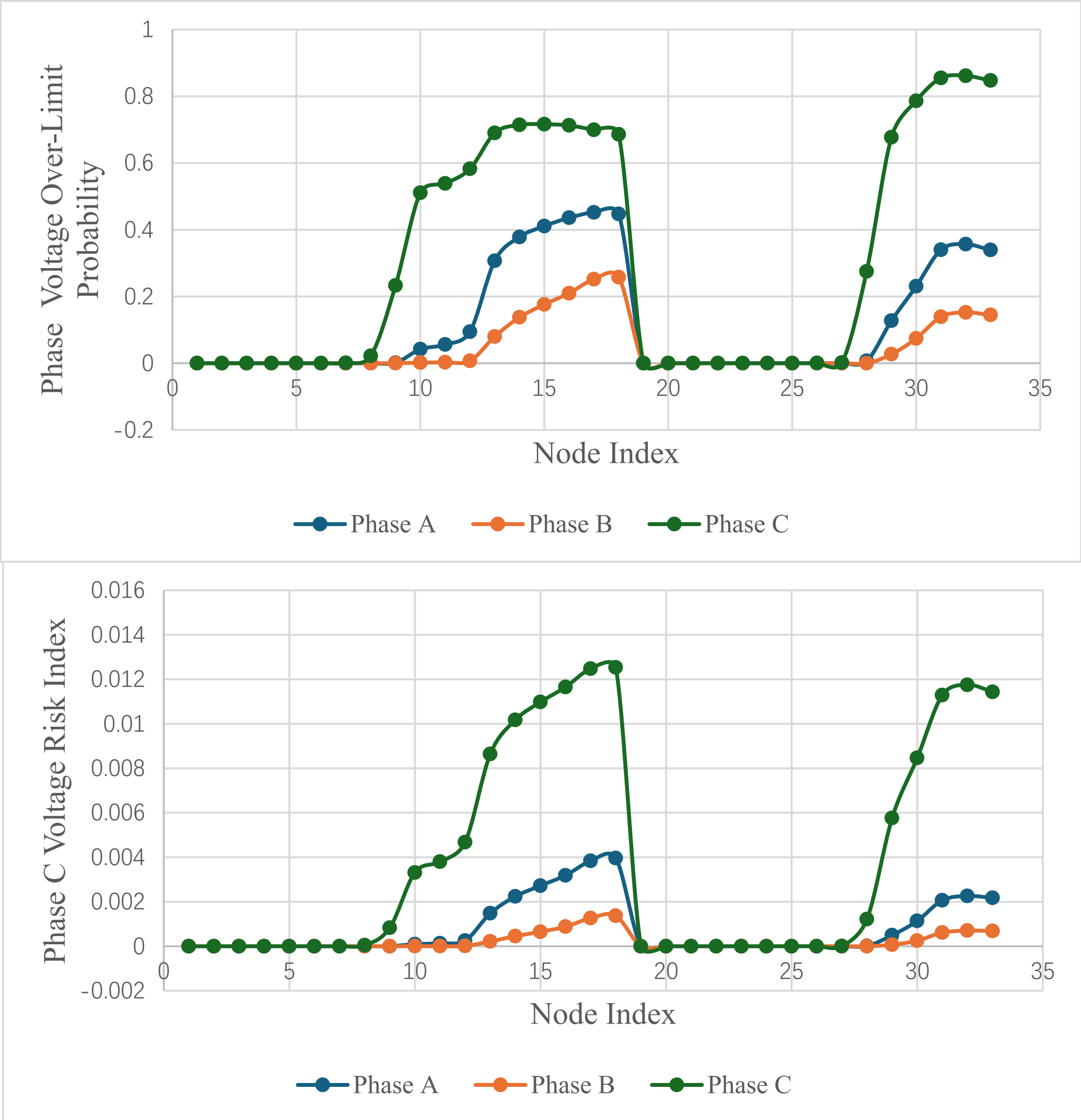

Figure 5-15 Voltage Limit-Violation Probability and Risk Index Across Nodes for Three Phases

The trends of voltage limit-violation probability and corresponding risk index across all nodes are further illustrated in Figure 5-15, which provides a direct comparison of the three phases and highlights both spatial variation and phase-dependent differences in system vulnerability.

From the upper subplot, the violation probability remains negligible in the upstream region (nodes 1–9) and the middle section around nodes 19–25, indicating that voltage levels in these areas are consistently maintained within acceptable limits under stochastic operating conditions. In contrast, two distinct high-risk regions can be observed. The first is located around nodes 10–18, where the violation probability increases progressively along the feeder, reaching peak values at node 18. The second region appears in the downstream end section (nodes 28 – 33), where violation probabilities rise again and attain their highest levels, particularly in Phase C.

A clear phase-dependent pattern is evident. Phase C consistently shows the highest violation probability across both high-risk regions, followed by Phase A, while Phase B remains the least affected. This confirms that Phase C is the most vulnerable phase in the system, mainly due to its lower voltage profile and lack of sufficient local support compared to the other phases.

The lower subplot shows the corresponding risk index, which reflects not only the frequency but also the severity of voltage violations. While the spatial pattern broadly follows that of the violation probability, the peak risk is observed around node 18 rather than at the very end nodes. This indicates that although the downstream nodes (e.g., node 32) experience very frequent violations, the deviations at node 18 tend to be more severe when they occur. As a result, node 18 emerges as the most critical location when both probability and severity are considered.

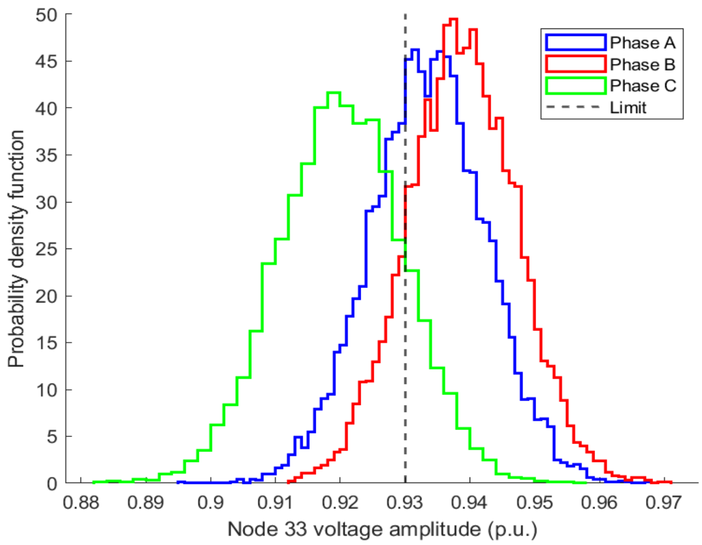

Figure 5-16 Empirical Probability Density of Node 33 Voltage

Figure 5-16 provides a representative example through the empirical probability density distributions of node 33 voltage in the three phases. The dashed vertical line marks the lower voltage limit of 0.93 p.u. The distribution of Phase C lies predominantly to the left of this threshold, which is fully consistent with its very high under-limit probability of 0.8471 in Table 5-4. Phase A straddles the limit more substantially, corresponding to a moderate violation probability of 0.3392, while Phase B is centred further to the right of the threshold and therefore shows the lowest probability of violation at node 33 (0.1446). This figure clearly illustrates how the relative position of each phase distribution with respect to the limit determines the resulting violation probability and risk level.

Overall, the results demonstrate that voltage risk in the system is highly phase-dependent and spatially non-uniform. The most severe vulnerability is concentrated in the downstream buses and is dominated by Phase C, confirming that three-phase stochastic analysis is necessary to identify weak phases and critical locations that would be masked in single-phase or deterministic studies.

5.6.2 Active Power Risk Assessment

Table 5-5 presents the branch active-power limit-violation probability and the corresponding risk index for all branches and all three phases. The results show that non-zero branch violation risk is concentrated almost entirely in the first two upstream branches, while all remaining branches have zero violation probability and zero risk index under the adopted branch active-power limits. This indicates that, within the present case study, branch overload risk is dominated by the heavily loaded source-side branches, whereas downstream branches remain well below the prescribed thresholds in all Monte Carlo samples.

This pattern is consistent with the branch power magnitudes obtained from the simulations. As shown by the maximum sampled branch active power values, the first two branches reach substantially higher loading levels than the rest of the network, while branch power decreases rapidly along the feeder. Consequently, only the upstream branches are able to exceed the adopted limits, and the remaining branches exhibit zero overload probability. Therefore, the prevalence of zero values in Table 5-5 does not indicate a computational error, but rather reflects the combined effect of radial feeder power distribution and the selected branch loading thresholds.

To further interpret the prevalence of zero violation probabilities, reports the maximum active power observed for each branch across all Monte Carlo scenarios. It can be seen that only the first two branches reach loading levels close to or exceeding the prescribed limits, while all remaining branches operate well below these thresholds. This confirms that the absence of overload risk in downstream branches is a result of the network loading profile rather than a computational issue.

To further interpret the prevalence of zero violation probabilities in Table 5-6 reports the maximum active power observed for each branch across all Monte Carlo scenarios. It can be seen that only the first two branches reach loading levels close to or exceeding the prescribed limits, while all remaining branches operate well below these thresholds. This confirms that the absence of overload risk in downstream branches is a result of the network loading profile rather than a computational issue.

Table 5-5 Branch Active-Power Limit-Violation Probability and Risk Index for Each Branch

Branch Index	**Phase A Branch Active Power**		**Phase B Branch Active Power**		**Phase C Branch Active Power**	
	Over-Limit Probability	**Risk Index**	**Over-Limit Probability**	**Risk Index**	**Over-Limit Probability**	**Risk Index**
1	0.3573	0.0188	0.0837	0.0026	0.8791	0.1267
2	0.0141	0.0003	0.0003	0.0000	0.3821	0.0221
3	0.0000	0.0000	0.0000	0.0000	0.0000	0.0000
4	0.0000	0.0000	0.0000	0.0000	0.0000	0.0000
5	0.0000	0.0000	0.0000	0.0000	0.0000	0.0000
6	0.0000	0.0000	0.0000	0.0000	0.0000	0.0000
7	0.0000	0.0000	0.0000	0.0000	0.0000	0.0000
8	0.0000	0.0000	0.0000	0.0000	0.0000	0.0000

9	0.0000	0.0000	0.0000	0.0000	0.0000	0.0000
10	0.0000	0.0000	0.0000	0.0000	0.0000	0.0000
11	0.0000	0.0000	0.0000	0.0000	0.0000	0.0000
12	0.0000	0.0000	0.0000	0.0000	0.0000	0.0000
13	0.0000	0.0000	0.0000	0.0000	0.0000	0.0000
14	0.0000	0.0000	0.0000	0.0000	0.0000	0.0000
15	0.0000	0.0000	0.0000	0.0000	0.0000	0.0000
16	0.0000	0.0000	0.0000	0.0000	0.0000	0.0000
17	0.0000	0.0000	0.0000	0.0000	0.0000	0.0000
18	0.0000	0.0000	0.0000	0.0000	0.0000	0.0000
19	0.0000	0.0000	0.0000	0.0000	0.0000	0.0000
20	0.0000	0.0000	0.0000	0.0000	0.0000	0.0000
21	0.0000	0.0000	0.0000	0.0000	0.0000	0.0000

22	0.0000	0.0000	0.0000	0.0000	0.0000	0.0000
23	0.0000	0.0000	0.0000	0.0000	0.0000	0.0000
24	0.0000	0.0000	0.0000	0.0000	0.0000	0.0000
25	0.0000	0.0000	0.0000	0.0000	0.0000	0.0000
26	0.0000	0.0000	0.0000	0.0000	0.0000	0.0000
27	0.0000	0.0000	0.0000	0.0000	0.0000	0.0000
28	0.0000	0.0000	0.0000	0.0000	0.0000	0.0000
29	0.0000	0.0000	0.0000	0.0000	0.0000	0.0000
30	0.0000	0.0000	0.0000	0.0000	0.0000	0.0000
31	0.0000	0.0000	0.0000	0.0000	0.0000	0.0000
32	0.0000	0.0000	0.0000	0.0000	0.0000	0.0000

Table 5-6 Statistical Summary of Branch Active Power (Min, Mean, Max) Across Monte Carlo Scenarios

Branch Index	**Minimum (MW)**	**Mean (MW)**	**Maximum (MW)**	**Branch Index**	**Minimum (MW)**	**Mean (MW)**	**Maximum (MW)**
1	0	0	4.951935	**17**	0	0	0.160603
2	0	0	4.397413	**18**	0	0	0.603454
3	0	0	3.073124	**19**	0	0	0.459345
4	0	0	2.903333	**20**	0	0	0.339353
5	0	0	2.794286	**21**	0	0	0.182418
6	0	0	1.537042	**22**	0	0	1.547348
7	0	0	1.257334	**23**	0	0	1.464222
8	0	0	0.926449	**24**	0	0	0.799919
9	0	0	0.846988	**25**	0	0	1.34246
10	0	0	0.766048	**26**	0	0	1.239252
11	0	0	0.708221	**27**	0	0	1.165775
12	0	0	0.656815	**28**	0	0	1.0709
13	0	0	0.568423	**29**	0	0	0.924276
14	0	0	0.385975	**30**	0	0	0.652295
15	0	0	0.312838	**31**	0	0	0.444484
16	0	0	0.243097	**32**	0	0	0.106481

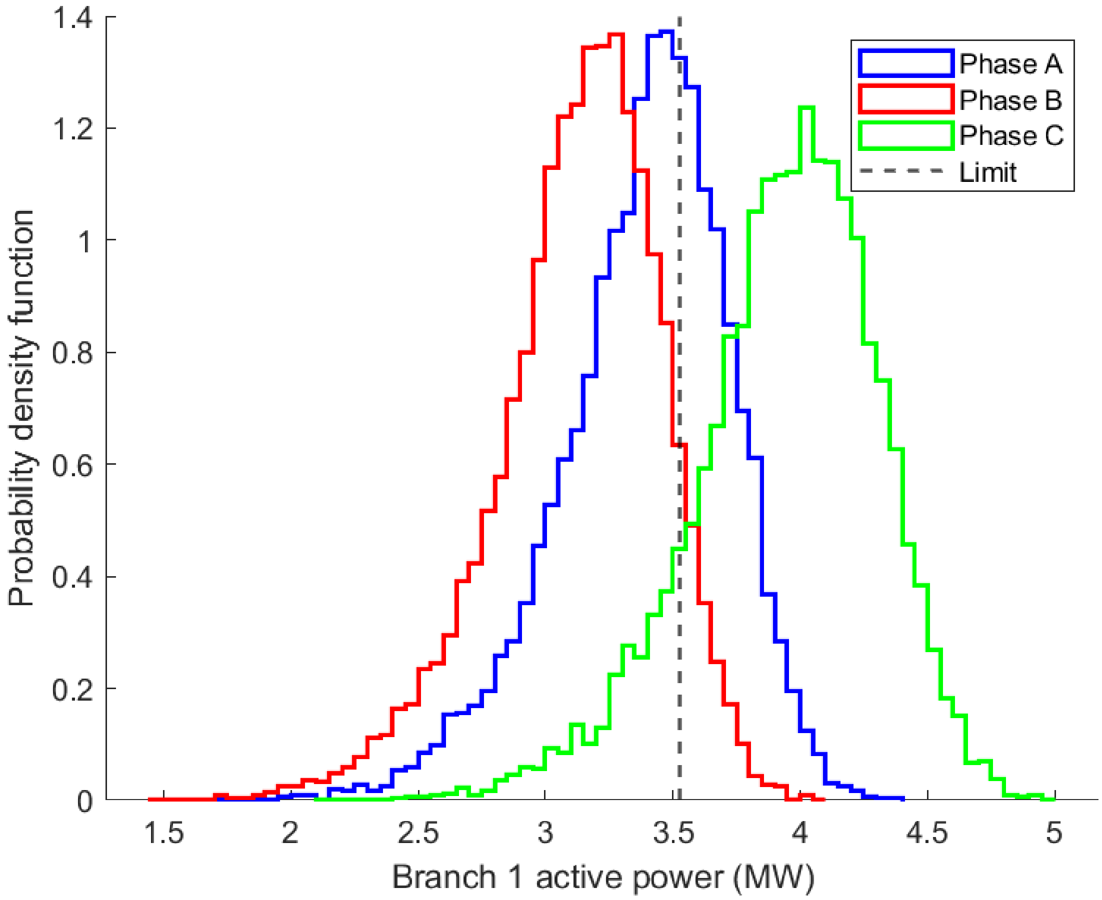

Figure 5-17 Empirical Probability Density of Branch 1 Active Power for Phases A, B, and C

Figure 5-17 provides a representative example through the empirical probability density distributions of Branch 1 active power for the three phases. The dashed vertical line indicates the branch active-power limit. Phase C is centred furthest to the right and has the largest fraction of samples above the threshold, which explains its highest over-limit probability and risk index. Phase A lies closer to the limit and shows moderate risk, whereas Phase B is mainly located to the left of the threshold and therefore has the lowest probability of violation. This confirms that the branch risk level is determined by the relative position and spread of the phase-wise power distributions with respect to the limit.

Overall, the branch active-power risk assessment reveals a highly localised pattern, with overload vulnerability concentrated in the upstream part of the network. It also shows a clear phase dependence, with Phase C being the most critical phase in the most heavily loaded branches.

5.6.3 Discussion and implications

The voltage and branch active-power risk assessments reveal different but complementary aspects of system vulnerability. The voltage risk results show a strongly phase-dependent and location-dependent pattern, with Phase C consistently exhibiting the highest violation probabilities and risk indices, particularly in the downstream sections of the feeder. This indicates that the most critical voltage weakness is associated with the weakest phase in electrically remote parts of the network, where voltage support is limited and stochastic variations in load and generation have a greater impact.

In contrast, the branch active-power risk is highly concentrated in the first two upstream branches, while all remaining branches show zero violation probability under the adopted loading thresholds. This suggests that, for the present case study, branch overload risk is dominated by the heavily loaded source-side branches rather than by downstream sections. The corresponding probability density distributions further confirm that the three phases do not contribute equally to this risk, with Phase C again showing the highest loading vulnerability in the most critical branch.

Taken together, these results demonstrate that different risk indicators highlight different forms of weakness in the network. Voltage risk is mainly associated with downstream weak-bus conditions, whereas branch loading risk is concentrated in upstream high-transfer branches. This distinction is important for practical mitigation. Measures aimed at improving voltage performance, such as phase balancing, reactive power compensation, or local voltage support, should be targeted at the most vulnerable downstream buses and phases. By contrast, measures intended to reduce branch loading risk should focus on relieving the most heavily loaded upstream branches through feeder reconfiguration, demand redistribution, or improved coordination of distributed generation.

Overall, the probabilistic risk framework provides more informative guidance than deterministic analysis alone, because it captures not only whether a limit may be violated, but also how frequently and how severely such violations occur under uncertainty. This makes the framework useful for supporting risk-aware planning and operation of unbalanced distribution systems.

5.7 Calculation Results for Indicator Weights

The correspondence between P1–P6 and the six evaluation indicators is as follows:

- P1: Three-phase Voltage Imbalance
- P2: Node Voltage Deviation Rate
- P3: Average Harmonic Voltage Distortion Rate
- P4: Harmonic Voltage Three-phase Imbalance Degree
- P5: Maximum Over-limit Risk Value of Node Voltage
- P6: Active Power Over-limit Risk Value of Node Injection Branch

According to the formulas in Chapter 3 for identifying weak power quality nodes, the indicator values for each node and branch are obtained as summarized in the Table 5-7. The calculations focus on four main aspects: three-phase imbalance, harmonic voltage distortion, over-limit risk, and voltage deviation.

Table 5-7 Raw Data of Power Quality Indicators for Nodes and Branches

Node Index	P1	P2	P3	P4	P5	P6
2	0.00063699	0.002889	0.001226	0.162856	0	82.5793
3	0.00372471	0.016509	0.00172	0.163045	2E-247	37.5289
4	0.00558008	0.023555	0.004094	0.162511	6.73E-77	0.00305
5	0.00745807	0.030488	0.004659	0.168486	2.08E-28	0.00024
6	0.01229657	0.047847	0.005258	0.173899	0.017888	4.28E-05
7	0.01335919	0.050938	0.007424	0.187615	0.289331	1.33E-20
8	0.01459261	0.054678	0.008015	0.190126	3.252613	1.13E-25
9	0.01606901	0.059132	0.008279	0.192185	15.68631	3.95E-32
10	0.01744805	0.063106	0.009056	0.196694	34.95804	4.54E-34
11	0.01764332	0.063639	0.009842	0.200727	38.14427	6.29E-36
12	0.01797096	0.064515	0.009916	0.201165	43.73292	3.33E-37
13	0.01933931	0.067991	0.010057	0.201976	67.04726	6.55E-39
14	0.01984869	0.069205	0.010019	0.200684	75.10086	7.22E-41
15	0.02013843	0.069544	0.009989	0.199769	78.4067	1.68E-44
16	0.02039241	0.069593	0.009969	0.199223	80.19781	3.76E-46
17	0.02074365	0.069145	0.009954	0.198777	80.18604	6.95E-48
18	0.0208074	0.068453	0.009911	0.197607	78.21247	3.67E-49
19	0.00074937	0.003438	0.009895	0.197394	0	0

20	0.00151218	0.007159	0.001931	0.167223	0	0
21	0.00166392	0.007891	0.003777	0.184399	0	0
22	0.00180137	0.008554	0.004428	0.187206	0	0
23	0.00430677	0.020191	0.005705	0.191115	1.6E-149	3.64E-54
24	0.00537234	0.027029	0.006111	0.15691	5.85E-52	2.27E-62
25	0.00590797	0.030442	0.010776	0.152642	1.38E-30	1.4E-178
26	0.01278153	0.049832	0.015456	0.151665	0.085168	1.3E-111
27	0.01341577	0.052474	0.007651	0.188751	0.473376	7.8E-123
28	0.0161878	0.064283	0.007971	0.19017	27.5615	3.8E-136
29	0.01822387	0.072771	0.009998	0.196921	79.75904	1.9E-160
30	0.01912997	0.076463	0.011554	0.201316	105.5861	5.3E-213
31	0.02029602	0.080808	0.011564	0.201418	136.8973	0
32	0.02054981	0.081761	0.011539	0.200623	143.7549	0
33	0.02063151	0.082055	0.011532	0.200463	145.8752	0

Following the preprocessing of the original indicator data through dimensionless and normalization techniques, the resulting normalized matrix is shown in Table 5-8. All indicator values are scaled within the range 0 to 1 using the min–max normalization method for negative indicators (where smaller values indicate better performance), expressed as:

$$r_{ij} = \frac{\max_j - x_{ij}}{\max_j - \min_j}$$

This transformation assigns 1 to the best (lowest) raw value and 0 to the worst (highest), allowing direct comparison across indicators of different types.

Normalization is an essential step in multi-criteria decision-making, especially when indicators have different units or scales (for example, deviation rates expressed as percentages versus risk values expressed as absolute numbers). Transforming all indicators into a common range reduces the effect of unit differences and makes integration into weighting and ranking models fair and consistent. This process follows standard practice in operations research and improves the robustness of the following evaluation.

Interpreting the Normalized Values:

- Values closer to 1 indicate superior performance, signifying that the indicator is closer to its ideal (minimal) state relative to the dataset.
- Values closer to 0 denote inferior performance, highlighting areas of potential weakness where the indicator deviates significantly from the optimal.

This standardized representation not only streamlines the computational process but also offers an intuitive metric for preliminary assessment, allowing researchers to identify outliers and trends prior to advanced weighting.

Table 5-8 Normalized Data on Power Quality Indicators for Nodes and Branches

Node Index	**P1**	**P2**	**P3**	**P4**	**P5**	**P6**
2	1	1	1	0.777565	1	0
3	0.846918	0.827947	0.965316	0.773795	1	0.54554
4	0.754933	0.738955	0.798486	0.784421	1	0.999963
5	0.661827	0.65138	0.75872	0.665663	1	0.999997
6	0.421946	0.4321	0.716665	0.55807	0.999877	0.999999

7	0.369264	0.393057	0.564456	0.285433	0.998017	1
8	0.308114	0.345823	0.522896	0.235526	0.977703	1
9	0.234918	0.289563	0.504363	0.1946	0.892468	1
10	0.166548	0.239359	0.449768	0.104973	0.760356	1
11	0.156867	0.232623	0.394495	0.024813	0.738514	1
12	0.140623	0.221561	0.389295	0.016106	0.700203	1
13	0.072784	0.177658	0.379411	0	0.540379	1
14	0.04753	0.162318	0.382103	0.025677	0.48517	1
15	0.033166	0.158034	0.384169	0.043852	0.462508	1
16	0.020574	0.157413	0.385591	0.054716	0.45023	1
17	0.00316	0.163082	0.386665	0.063576	0.450311	1
18	0	0.171817	0.389624	0.086834	0.46384	1
19	0.994429	0.993061	0.39075	0.091062	1	1
20	0.95661	0.946062	0.95044	0.69075	1	1
21	0.949087	0.936815	0.820767	0.349358	1	1
22	0.942273	0.928431	0.775	0.293576	1	1
23	0.818061	0.781443	0.685242	0.215877	1	1
24	0.765233	0.695073	0.656715	0.895752	1	1
25	0.738678	0.651952	0.328841	0.980582	1	1
26	0.397903	0.407036	0	1	0.999416	1
27	0.366459	0.373659	0.548485	0.262869	0.996755	1
28	0.229028	0.224498	0.526005	0.234649	0.811061	1

29	0.128085	0.117279	0.383518	0.100472	0.453238	1
30	0.083163	0.070638	0.274179	0.013108	0.276188	1
31	0.025353	0.01576	0.273469	0.011077	0.061545	1
32	0.012771	0.003721	0.275262	0.026884	0.014535	1
33	0.00872	0	0.275755	0.030058	0	1

The information entropy and redundant entropy values, calculated using objective weighting methods such as the entropy weight method and the improved CRITIC method, are listed in Table 5-9. These parameters describe the information content of each indicator by representing data variability, uncertainty, and overlap between indicators.

Information entropy is defined as:

$$e_j = -\sum_{i=1}^{m} p_{ij} \ln p_{ij}, \text{ where } p_{ij} = \frac{r_{ij}}{\sum_{i=1}^{m} r_{ij}}, m = 32$$

A lower entropy value means higher information contribution because of greater data variability. Redundant entropy, introduced in the improved CRITIC method, measures the shared information between indicators. A smaller redundancy value means the indicator contributes more uniquely to the overall assessment.

Indicators with high information entropy and low redundant entropy are prioritised since they offer distinct and meaningful insight into power quality behaviour while reducing multicollinearity in the model.

Table 5-9 Information Entropy and Redundant Entropy Values of Each Indicator

Indicator Number	Information Entropy	Redundant Entropy
P1	2.8255	0.1494
P2	2.9881	0.1005
P3	2.7369	0.1761
P4	2.5898	0.2204
P5	2.1556	0.3511
P6	0.3998	0.8797

5.7.1 Subjective weight determination based on the analytic hierarchy process (AHP)

The subjective weights were determined using the Analytic Hierarchy Process (AHP) based on five independent groups of evaluators (Table 5-10 to Table 5-14). In this study, the term *expert group* refers to evaluators with relevant background and experience in power systems, particularly in power quality analysis and distribution network operation. Each group independently performed pairwise comparisons of the selected indicators using the same evaluation criteria, providing one judgement matrix per group. The use of multiple groups aims to reduce individual bias and reflect variations in professional judgement rather than relying on a single source of subjective assessment.

Each pairwise comparison matrix represents the relative importance of the indicators and was constructed using a modified comparison scale ranging from 1.0 to 1.8. This restrained scale allows sufficient discrimination between indicators while limiting extreme judgements that may lead to inconsistency. For each group, the principal eigenvector associated with the maximum eigenvalue was calculated and normalised to obtain the corresponding subjective weight vector. The consistency of each matrix was evaluated using the Consistency Ratio (CR = CI / RI), and all CR values were below the commonly accepted threshold of 0.1, indicating acceptable consistency.

The final subjective weights were obtained by taking the arithmetic mean of the weight vectors from the five groups, assuming equal credibility among groups for simplicity (Equation 3.107). Although small differences exist among the group assessments, the overall ranking of indicators remains consistent, indicating a stable perception of relative importance across groups. This approach provides a balanced and transparent basis for deriving subjective weights to be combined with objective weighting methods in the subsequent analysis.

Table 5-10 Suppose the Judgement Matrix Given by Group 1

Group 1	**P1**	**P2**	**P3**	**P4**	**P5**	**P6**
P1	1	0.9	0.9	0.99	0.825	1.32
P2	1.1111	1	1	1.1	0.9167	1.4667
P3	1.1111	1	1	1.1	0.9167	1.4667
P4	1.0101	0.9091	0.9091	1	0.8333	1.3333
P5	1.2121	1.0909	1.0909	1.2	1	1.6
P6	0.7576	0.6818	0.6818	0.75	0.625	1

Table 5-11 Suppose the Judgement Matrix Given by Group 2

Group 2	**P1**	**P2**	**P3**	**P4**	**P5**	**P6**
P1	1	0.8333	0.9167	0.8333	0.641	0.8974
P2	1.2	1	1.1	1	0.7692	1.0769
P3	1.0909	0.9091	1	0.9091	0.6993	0.979
P4	1.2	1	1.1	1	0.7692	1.0769
P5	1.56	1.3	1.43	1.3	1	1.4
P6	1.1143	0.9286	1.0214	0.9286	0.7143	1

Table 5-12 Suppose the Judgement Matrix Given by Group 3

Group 3	**P1**	**P2**	**P3**	**P4**	**P5**	**P6**
P1	1	0.7143	0.7143	0.5952	0.3968	0.4762
P2	1.4	1	1	0.8333	0.5556	0.6667
P3	1.4	1	1	0.8333	0.5556	0.6667
P4	1.68	1.2	1.2	1	0.6667	0.8
P5	2.52	1.8	1.8	1.5	1	1.2
P6	2.1	1.5	1.5	1.25	0.8333	1

Table 5-13 Suppose the Judgement Matrix Given by Group 4

Group 4	**P1**	**P2**	**P3**	**P4**	**P5**	**P6**
P1	1	0.8333	0.7576	0.7576	0.6313	0.6944
P2	1.2	1	0.9091	0.9091	0.7576	0.8333
P3	1.32	1.1	1	1	0.8333	0.9167
P4	1.32	1.1	1	1	0.8333	0.9167
P5	1.584	1.32	1.2	1.2	1	1.1
P6	1.44	1.2	1.0909	1.0909	0.9091	1

Table 5-14 Suppose the Judgement Matrix Given by Group 5

Group 5	**P1**	**P2**	**P3**	**P4**	**P5**	**P6**
P1	1	1	1.1	1	1	1.1
P2	1	1	1.1	1	1	1.1
P3	0.9091	0.9091	1	0.9091	0.9091	1
P4	1	1	1.1	1	1	1.1
P5	1	1	1.1	1	1	1.1
P6	0.9091	0.9091	1	0.9091	0.9091	1

The subjective weights were determined using the Analytic Hierarchy Process (AHP) based on five independent groups of evaluators (Table 5-10 to Table 5-14). In this study, the term expert group refers to individuals with relevant academic or professional experience in power systems, particularly in power quality assessment, distribution network operation, and renewable energy integration. The selection of multiple groups aimed to ensure diversity in perspectives, including both research-oriented and practice-oriented viewpoints, thereby reducing the bias associated with relying on a single source of judgement.

To ensure consistency and comparability across groups, all evaluators were provided with the same set of indicator definitions, evaluation criteria, and instructions for pairwise comparison. Each group independently constructed a judgement matrix based on their understanding of the relative importance of the selected indicators. No interaction between groups was allowed during this process, ensuring that each matrix reflects an independent assessment and captures variability in expert judgement.

Each pairwise comparison matrix was constructed using a modified comparison scale centred around 1.0, where a value of 1 indicates equal importance, and values greater than 1 indicate increasing relative importance of one indicator over another. The scale was designed to be restrained to reduce extreme judgements and improve consistency, typically ranging from 1.0 to 1.8. However, in some cases, values exceeding this nominal range (e.g., above 2.0) appear in the judgement matrices, reflecting stronger perceived importance differences by individual expert groups. This flexible scaling approach allows experts to express relative importance more accurately while maintaining acceptable consistency levels.

For each group, the principal eigenvector corresponding to the maximum eigenvalue of the judgement matrix was calculated and normalised to obtain the subjective weight vector. The consistency of each judgement matrix was evaluated using the consistency ratio (CR), defined as CR = CI / RI. All calculated CR values were below the commonly accepted threshold of 0.1, indicating that the pairwise comparisons are logically consistent and acceptable for further analysis.

The final subjective weights were obtained by taking the arithmetic mean of the weight vectors from the five expert groups, assuming equal credibility among groups.

Although minor differences exist among the individual group assessments, the overall ranking of indicators remains consistent across groups, indicating stability in the perceived relative importance of the indicators.

This approach ensures that the derived subjective weights reflect both expert knowledge and variability in professional judgement, providing a transparent and balanced basis for integration with objective weighting methods in the subsequent AHP–CRITIC analysis.

5.7.2 Objective and comprehensive weights

Table 5-15 presents the subjective (AHP) and objective weights (Entropy Weight Method and improved CRITIC) for the six indicators, alongside their combinations (AHP-Entropy and AHP-CRITIC). The comprehensive weights were determined using Equation 3.110, $w_j = \alpha w_{sub,j} + (1-\alpha) w_{obj,j}$,where $\alpha = 0.5$ is adopted in this study to assign equal importance to subjective judgement and objective data characteristics. Other values of α may be considered in future work to reflect different decision preferences.

Under the AHP–CRITIC scheme, indicator P4 (harmonic voltage three-phase imbalance degree) receives the highest weight (0.2522), indicating that it plays a particularly influential role in identifying power quality weak points under harmonic power flow conditions. This prominence is supported by its elevated objective weights (Entropy: 0.3597; CRITIC: 0.3557), reflecting substantial data variability and low redundancy, as evidenced by its information entropy (2.5898) and redundant entropy (0.2204) in Table 5-9. Such metrics indicate that P4 captures unique fluctuations critical to power quality assessment, potentially due to its sensitivity to asymmetric harmonic injections in the grid.

In contrast, P6 (active power over-limit risk value of node injection branch) receives the lowest comprehensive weight (0.1211), consistent with its minimal objective contributions (Entropy: 0.0217; CRITIC: 0.0831). This suggests limited discriminatory power, possibly arising from skewed data distribution (e.g., many near-zero values indicating low risk across nodes), as reflected in its low information entropy (0.3998).

Subjective AHP weighting emphasizes P5 (maximum over-limit risk value of node voltage, 0.2071), aligning with expert prioritization of voltage stability risks in practical grid operations. However, objective methods assign lower weights to P5 (Entropy: 0.0832; CRITIC: 0.1211), revealing a discrepancy where data variability downplays its role compared to expert intuition. The AHP-CRITIC combination moderates this to 0.1638, demonstrating the method's ability to reconcile subjective biases with empirical evidence.

Comparing AHP-Entropy and AHP-CRITIC illuminates methodological nuances. AHP-Entropy assigns higher weight to P4 (0.2691) than AHP-CRITIC (0.2522), likely due to Entropy's focus on variance alone, which may amplify indicators with compressed ranges (e.g., P4's pre-normalized values). This vulnerability can lead to overemphasis on low-variance indicators, potentially overlooking interdependencies. Conversely, the improved CRITIC incorporates conflict (via Pearson correlations) and redundancy (via inverse entropy), yielding a more resilient distribution—e.g., tempering P2's weight and mitigating AHP's overreliance on P1 (reducing from 0.1397 to 0.1586 in AHP-CRITIC). This enhancement promotes objectivity, as visualized in the pie charts (Figure 5-19), where AHP-CRITIC exhibits a balanced allocation, avoiding the subjective skew toward P1 and P5 in AHP-Entropy.

Overall, the AHP-CRITIC method provides a superior hybrid framework by integrating human expertise with data-driven metrics, minimizing biases and enhancing the model's applicability to real-world power systems. Future sensitivity analyses could explore varying α to optimize for specific grid configurations, further validating the framework's adaptability.

Table 5-15 Subjective (AHP) And Objective Weights for the Six Indicators

Indicator Number	**AHP**	**Entropy Weight Method**	**CRITIC**	**AHP-Entropy Weight Method**	**AHP-CRITIC**
P1	0.1397	0.2788	0.1778	0.2165	0.163
P2	0.1619	0.1915	0.1409	0.1932	0.1562
P3	0.1588	0.0647	0.1211	0.1112	0.1434
P4	0.1672	0.3597	0.3557	0.2691	0.2522
P5	0.2071	0.0832	0.1211	0.144	0.1638
P6	0.1649	0.0217	0.0831	0.0657	0.1211

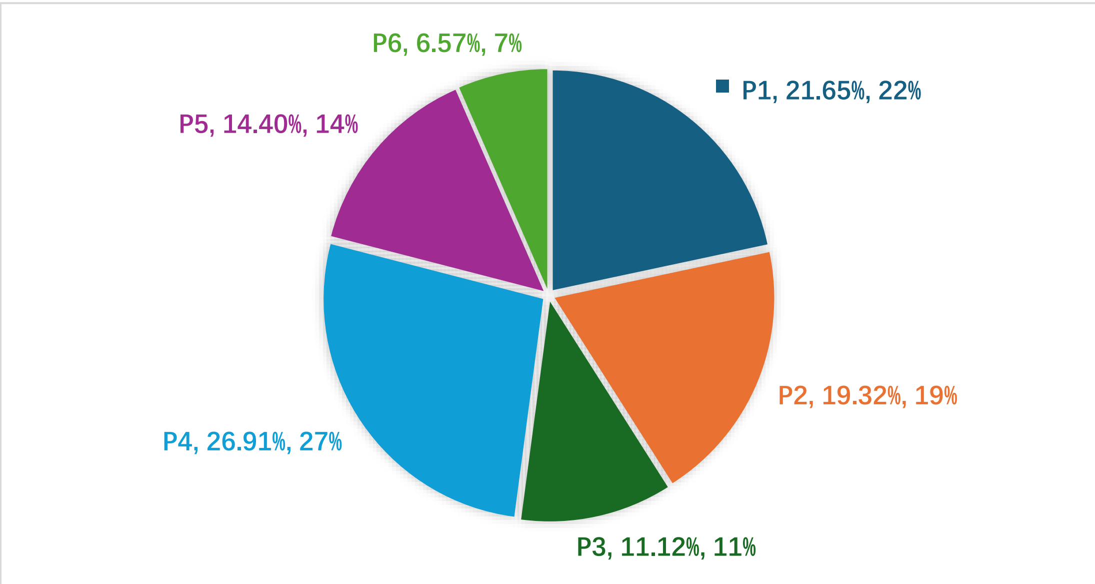

Figure 5-18 Weight Distributions Under Combined AHP-Entropy Weighting Method

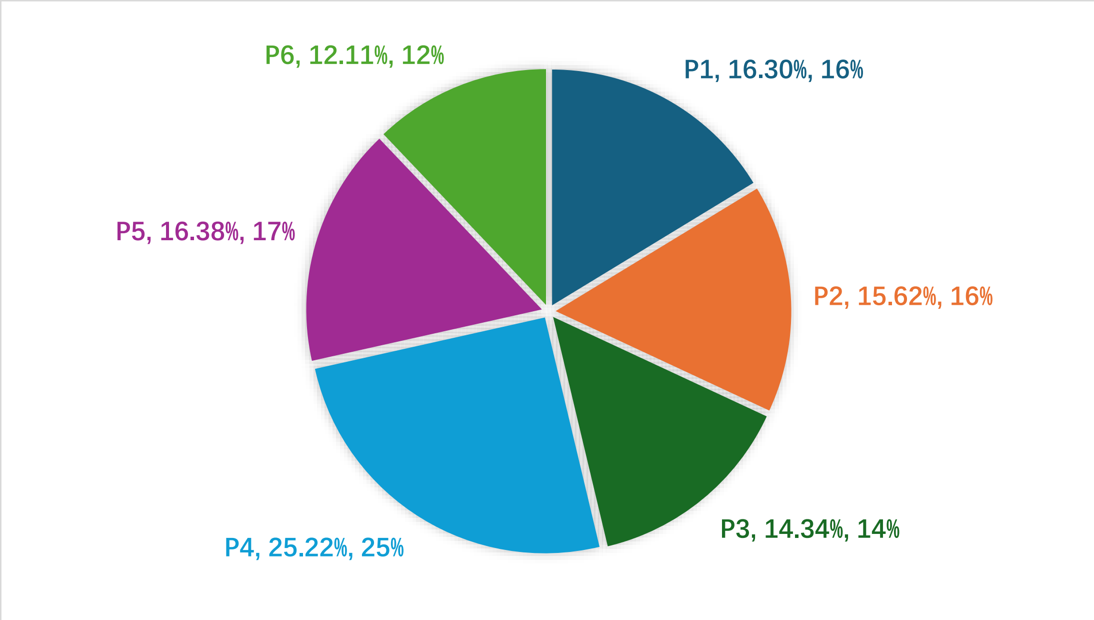

Figure 5-19 Weight Distributions Under Combined AHP-CRITIC Method

Figure 5-18 and Figure 5-19 present two pie charts illustrating the weight distributions under the combined AHP-Entropy and AHP-CRITIC methods, providing a visual comparison of how the hybrid approaches allocate importance across the six indicators (P1 to P6). These visualizations facilitate an intuitive understanding of the methodological differences and their impact on indicator prioritization.

In Figure 5-18, depicting the AHP-Entropy Weighting Method, the largest slice is attributed to P4 (harmonic voltage three-phase imbalance degree) at 26.91%, underscoring its dominant role as per the entropy-based objective weighting, which emphasizes indicators with higher variability. This is followed by P1 (three-phase voltage imbalance) at 21.65% and P2 (node voltage deviation rate) at 19.32%, reflecting a blend where subjective AHP inputs elevate P1 and P2, while entropy amplifies P4 due to its data dispersion. Smaller allocations include P5 (maximum over-limit risk value of node voltage) at 14.40%, P3 (average harmonic voltage distortion rate) at 11.12%, and P6 (active power over-limit risk value of node injection branch) at 6.57%, indicating lower perceived informational content for these under entropy metrics. This distribution highlights a potential overemphasis on variance-driven indicators, as entropy may disproportionately favour those with narrower but more uniform data ranges, leading to a skewed allocation that diminishes the role of risk-related metrics like P6.

In contrast, Figure 5-19 representing the AHP-CRITIC Method, shows a more balanced distribution, with P4 still prominent at 25.22% but moderated compared to AHP-Entropy. P5 receives 16.38%, P1 16.30%, P2 15.62%, P3 14.34%, and P6 12.11%, demonstrating CRITIC's incorporation of inter-indicator correlations and redundancies, which tempers extreme weights and promotes equilibrium. For instance, P6's weight increases from 6.57% in AHP-Entropy to 12.11%, better accounting for its unique contributions despite low variance, while P1 decreases from 21.65% to 16.30%, mitigating subjective overemphasis. This visual comparison affirms the superiority of AHP-CRITIC in achieving a more robust, less biased weight profile, as the slices are more evenly distributed, reducing the risk of overlooking interconnected power quality factors in grid assessments.

5.8 Summary

This chapter presented a detailed Monte Carlo-based three-phase stochastic harmonic power flow study for the IEEE 33-bus distribution network, integrating uncertainty in loads, PV and wind generation, and harmonic sources. The proposed framework offers a statistically complete reference for analysing voltage and power variability as well as harmonic distortion in complex unbalanced systems.

The simulation results showed that voltage deviations and power fluctuations increase along the feeder, with the most severe effects observed in the downstream sections and in the heavily loaded phase. Harmonic analysis revealed that THD peaks at the injection nodes and decreases with electrical distance, verifying the expected spatial propagation characteristics.

Risk evaluation results demonstrated that Phase C is the most critical, exhibiting both the highest under-voltage and overload probabilities due to its heavy load and absence of local generation. The derived over-limit probabilities and risk values clearly outlined the spatial pattern of vulnerability across the feeder.

The multi-indicator weighting analysis, combining AHP and CRITIC methods, further identified the relative influence of various factors. It was found that three-phase harmonic voltage imbalance and voltage risk indicators play dominant roles in determining power quality weakness.

Overall, this chapter provides a complete and data-driven framework for stochastic and harmonic assessment of distribution systems. The developed MCS-based model not only validates earlier probabilistic approaches but also delivers a practical reference for risk-based planning, reliability assessment, and mitigation of power quality issues in networks with renewable and nonlinear sources.

Building upon the insights from Chapter 5, which identified the locations and severity of power quality weaknesses, Chapter 6 offers transitions from assessment to active mitigation of harmonic distortion. It uses an improved Particle Swarm Optimization (PSO) framework to determine the most effective placement and sizing of Active Power Filters (APFs).

Chapter 6 Optimization of Active Power Filter Configuration Using Improved Particle Swarm Optimization

6.1 Introduction

Building on the probabilistic and harmonic analysis presented in Chapter 5, which identified network buses with high voltage distortion and power quality weaknesses, this chapter moves from system assessment to mitigation planning. The focus is placed on the configuration optimization of Active Power Filters (APFs) in distribution networks subject to harmonic distortion from nonlinear loads and distributed generation.

The objective of this chapter is to determine suitable APF installation locations and capacities that reduce voltage harmonic distortion while limiting overall compensation cost, subject to practical system constraints. Compliance with commonly used harmonic standards, including limits on voltage total harmonic distortion (THDU), is explicitly considered in the optimization formulation.

To address this problem, a Particle Swarm Optimization (PSO)–based method is employed and adapted for the APF configuration task. The proposed approach introduces a subpopulation-based search mechanism intended to improve convergence behaviour in high-dimensional decision spaces. In this framework, particles are grouped during the search process to guide exploration, while all candidate solutions retain a complete encoding of APF locations and capacities. Subpopulation screening is applied to adjust the search strategy rather than to remove decision variables, and the final solution is obtained from the global best particle satisfying all constraints.

The optimization procedure is coupled with harmonic power flow analysis to evaluate system performance under candidate APF configurations. Operational constraints, including THDU limits and APF capacity bounds at each bus, are incorporated to ensure feasible solutions. Simulation studies are carried out on a modified IEEE 33-bus distribution system with multiple harmonic sources. The following sections describe the optimization formulation, the PSO-based solution procedure, and the resulting improvements in harmonic voltage distortion before and after APF compensation.

In this chapter, voltage THDU is selected as the primary power quality metric in the APF optimisation model. This choice is motivated by the fact that the main function of the APF in this study is harmonic compensation, and THDU provides the most direct and comprehensive indicator of harmonic voltage distortion at the network level. Although other power quality indices, such as voltage deviation, phase unbalance, and risk-based indicators, were evaluated in Chapter 5, they are not included as explicit optimisation objectives here in order to maintain a focused and tractable optimisation framework. Instead, this chapter concentrates on the dominant harmonic mitigation objective, while the broader impact of APF deployment on overall power quality is examined through post-optimisation assessment.

It should also be noted that, although Chapter 5 examined stochastic harmonic behaviour in a three-phase unbalanced framework, the optimisation model in this chapter is formulated in a simplified network representation that focuses on system-level harmonic mitigation rather than detailed phase-specific balancing. This simplification is adopted to keep the APF placement and sizing problem computationally tractable, while still preserving the dominant harmonic propagation characteristics required for optimisation. The effectiveness of the obtained APF configuration is then evaluated in terms of network-level harmonic voltage reduction.

6.2 Optimization steps for power filter configuration based on improved particle swarm optimization

This section outlines the proposed improved Particle Swarm Optimization (PSO) algorithm for determining the optimal locations and capacities of shunt Active Power Filters (APFs) in a distribution network to minimize harmonic distortion and compensation costs while satisfying system constraints (IEEE Standard 519). The algorithm extends standard PSO [239] by incorporating node-based niche partitioning (subpopulation division) and periodic performance-based subpopulation elimination to enhance exploration, mitigate premature convergence, and improve computational efficiency in high-dimensional, constrained problems [240] [241].

The key enhancement lies in dividing particles into subpopulations (niches) corresponding to network node clusters, allowing parallel search in different regions of the solution space. Underperforming subpopulations are dynamically eliminated after evaluation periods to concentrate resources on promising areas. To ensure the final solution addresses the full system (not partial sub-configurations), a shared global best is maintained, and elite particles from eliminated subpopulations are reintegrated or used to influence remaining groups. This contrasts with independent subproblem decomposition approaches and aligns with dynamic multi-swarm or niche PSO variants adapted for engineering optimization [242].

The algorithm proceeds in the following steps.

Step 1: Initialize the Particle Swarm and Divide into Small Niches

Divide the nodes into small niches (referred to as subpopulations) based on node numbers. For each particle j in subpopulation i, initialize its velocity v_{ij} and position x_{ij}. Here, x_{ij} represents the position of the particle in the solution space (a potential configuration of the power filter), and v_{ij} represents its velocity, which directs its movement during optimization.

Step 2: Evaluate Initial Fitness and Determine Individual and Subpopulation Best Values

Calculate the initial fitness of each particle using a predefined fitness function, which integrates both the objective function (e.g., minimizing harmonic distortion) and constraints. These constraints include harmonic voltage and current distortion rates, derived from the harmonic analysis algorithm. This ensures that solutions remain feasible within the power system's operational limits.

Assign this fitness value as the particle's individual best value p_b. Then, within each subpopulation, identify the particle with the highest fitness and designate its fitness as the subpopulation best value s_b. Additionally, define w_g as the worst fitness value among the best solutions (s_b) of all subpopulations in each iteration. This step establishes a baseline for tracking progress throughout the optimization.

Step 3: Update Particle Positions and Velocities, and Recalculate Fitness

Update the position x_{ij} and velocity v_{ij} of each particle using its individual best p_b and the subpopulation best s_b. Recalculate the fitness for each particle using the fitness function.

Step 4: Recalculate Individual and Subpopulation Best Values

Based on the updated fitness values, recalculate the individual best value p_b for each particle and the subpopulation best value s_b for each subpopulation. This step ensures that the algorithm continuously tracks the best-known solutions as it iterates.

Step 5: Check Iteration Count for Subpopulation Elimination

After every m iterations (i.e., when the iteration number gen satisfies $\mathrm{mod}(gen, m) = 0$), compare the subpopulation best values s_b across all subpopulations. Identify the minimum s_b, denoted as s_{bi}, which represents the worst-performing subpopulation among the best values. Eliminate subpopulation i, meaning all particles in this subpopulation are excluded from subsequent iterations.

This elimination reflects the evolutionary progress of each subpopulation, reducing redundant computations and enhancing efficiency by focusing on more promising regions of the solution space.

Step 6: Update the Population by Removing Eliminated Particles

Remove the particles from the eliminated subpopulations and update the overall population accordingly. This step ensures that only the most effective subpopulations continue to evolve, aiding convergence toward an optimal solution.

Step 7: Check Termination Condition

Check if the current iteration number gen exceeds the maximum number of iterations N. If $gen > N$, terminate the algorithm and output the optimization results, including the optimal installation location and capacity of the shunt Active Power Filter (APF), along with the corresponding optimal fitness value. If the maximum iteration count has not been reached, return to Step 3 and continue the iterative process.

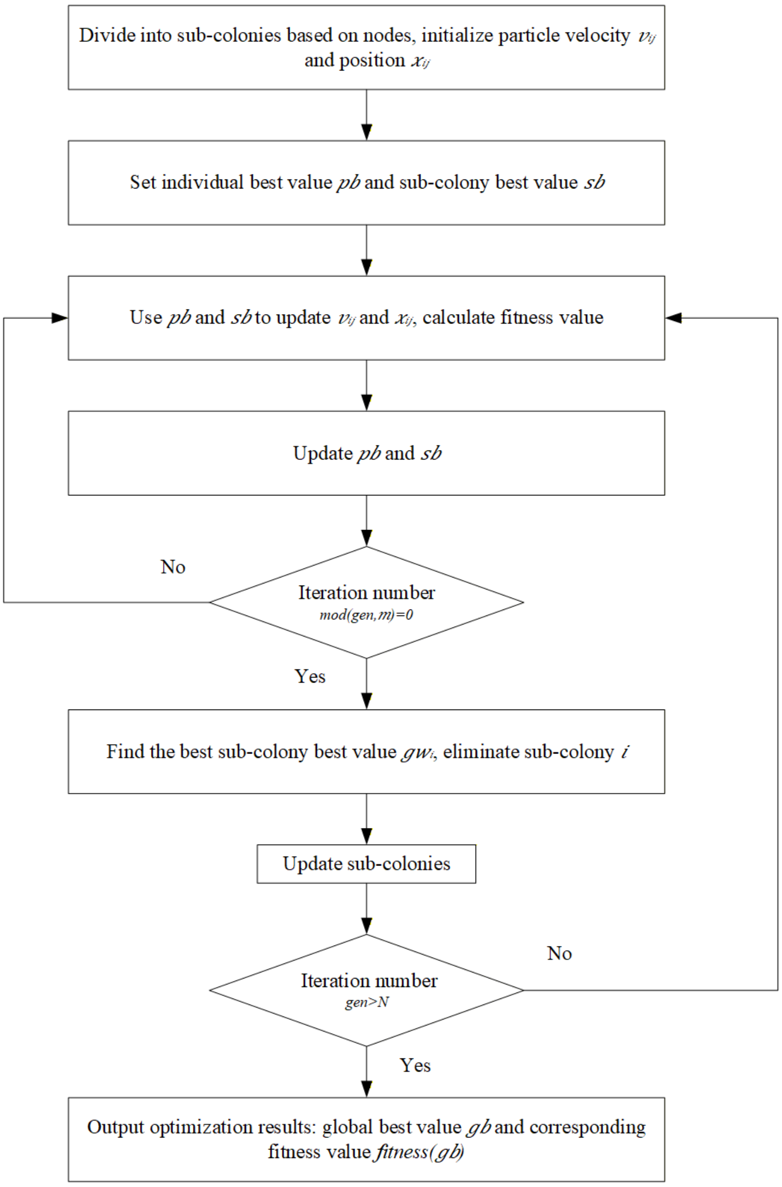

Figure 6-1 Flowchart of the Two-Layer Optimization Configuration of the APF

Figure 6-1 illustrates the flowchart of the proposed two-layer PSO-based optimization process for APF configuration, including particle initialization, sub-colony division, iterative updating of individual and group best values, periodic elimination of inferior sub-colonies, and final determination of the global optimal solution.

6.3 APF Optimization Configuration Results

In this section, the results of the proposed optimization framework for active power filter (APF) configuration in the distribution network are presented. The analysis encompasses the harmonic source parameters, system constraints, optimal APF placement and sizing, improvements in harmonic voltage distortion rates, variations in individual harmonic voltage contents, and the convergence behaviour of the particle swarm optimization (PSO) algorithm. All simulations were conducted using the IEEE 33-bus test system adapted for distribution network operation with distributed harmonic sources. The objective was to minimize the total harmonic governance cost while ensuring compliance with national grid harmonic standards, such as those specified in IEEE Standard 519, which limit total harmonic distortion in voltage (THDU) to below 5% for low-voltage systems.

6.3.1 Harmonic Source Parameters

The harmonic current injection rates at various buses, representing the primary sources of distortion in the distribution network, are detailed in Table 6-1. These rates are expressed as percentages of the fundamental current for the dominant harmonic orders (5th, 7th, 11th, 13th, and 17th), which are typical in systems with nonlinear loads such as rectifiers and inverters. For instance, bus 22 exhibits the highest 5th harmonic content at 0.2978%, while bus 33 shows elevated levels across multiple orders, peaking at 0.3209% for the 11th harmonic. These parameters were derived from load flow simulations incorporating realistic nonlinear device models, ensuring that the optimization accounts for the spatial distribution of harmonic pollution. Notably, buses closer to the substation (e.g., bus 6) display lower distortion rates, reflecting the attenuating effect of impedance on harmonic propagation.

The case study is based on a modified IEEE 33-bus distribution system in which multiple harmonic sources are assigned to selected buses to represent the spatially distributed effects of nonlinear loads and converter-based devices. The injected harmonic current spectra are specified for the dominant odd harmonic orders, namely the 5th, 7th, 11th, 13th, and 17th components, which are commonly observed in practical distribution systems with rectifiers, inverters, and other nonlinear equipment.

The harmonic source magnitudes used in this chapter are defined as percentages of the corresponding fundamental current and are derived from representative harmonic spectra reported in the literature and adapted to the selected buses according to their load and operating characteristics. This design enables the optimisation study to capture both the local severity of harmonic injections and their network-wide propagation effects.

The selected harmonic-injection buses are distributed along the feeder in order to represent both upstream and downstream harmonic interactions and to create a non-uniform harmonic distortion profile suitable for APF placement analysis.

Table 6-1 Harmonic Current Content Rates (%) for Selected Orders at Various Buses

Harmonic Injection Node	**5th**	**7th**	**11th**	**13th**	**17th**
6	0.0211	0.0136	0.0077	0.0063	0.0047
8	0.233	0.144	0.078	0.06	0.052
9	0.0218	0.0134	0.0082	0.0067	0.0054
10	0.0201	0.0147	0.0081	0.0067	0.0052
11	0.32	0.33	0.21	0.19	0.049
14	0.211	0.126	0.077	0.063	0.047
18	0.2201	0.1309	0.1008	0.0606	0.0419
19	0.0218	0.0134	0.0082	0.0067	0.0054
20	0.0201	0.0147	0.0081	0.0067	0.0052
21	0.0191	0.0147	0.0078	0.0065	0.0049
22	0.2978	0.3042	0.1858	0.1686	0.0521
23	0.0191	0.0147	0.0078	0.0065	0.0049
24	0.0186	0.0131	0.0076	0.0063	0.0053

25	0.1964	0.3033	0.1858	0.1675	0.0508
26	0.0211	0.0136	0.0077	0.0063	0.0047
29	0.3141	0.3211	0.1898	0.1716	0.0512
33	0.3101	0.3209	0.1932	0.1676	0.0609

Table 6-1 highlights the concentration of harmonic sources at downstream buses, necessitating targeted APF placement to mitigate propagation effects.

6.3.2 System constraints

To ensure feasible and practical optimization outcomes, system constraints were imposed on the maximum allowable THDU post-optimization and the maximum APF capacity per bus. These are summarized in Table 6-2. The THDU threshold was set to 3% for most buses to provide a safety margin below the 5% national standard, promoting robust power quality. If the optimized THDU exceeds this threshold, the solution is deemed suboptimal, requiring increased investment for additional compensation. Similarly, APF capacity limits prevent overloading at any single bus and demand the necessity of capacity redistribution, potentially elevating overall costs due to additional devices or infrastructure.

It should be noted that the maximum APF capacity at each bus is not arbitrarily assigned, but is determined based on practical engineering considerations and system characteristics.

First, the capacity limits are constrained by realistic equipment ratings of commercially available APF devices. In practical applications, APFs are typically designed within a certain capacity range due to limitations in converter ratings, thermal performance, and installation space.

Second, the capacity limits are scaled according to the local load demand and network conditions at each bus. In this study, the maximum allowable APF capacity is defined as a proportion of the nodal load level, ensuring that the allocated compensation capacity remains physically meaningful and consistent with the scale of power consumption at that location. This prevents unrealistically large compensation devices being assigned to nodes with relatively small loads.

Third, these limits also serve as boundary constraints in the optimization process. By restricting the search space of APF capacity, the optimization algorithm is guided toward feasible and economically realistic solutions, avoiding excessive compensation that would not be practical in real-world deployment.

Therefore, the specified APF capacity limits reflect a combination of equipment constraints, local system characteristics, and optimization requirements, ensuring that the obtained solutions are both technically feasible and practically implementable.

Table 6-2 System Constraints on Maximum THDU (p.u.) And APF Capacity (MVA)

Node Number	**Max THDU (p.u.)**	**Max APF Capacity MVA)**
1	0.0250	0
2	0.0250	26
3	0.0250	23
4	0.0250	31
5	0.0300	34
6	0.0300	28
7	0.0300	53
8	0.0300	53
9	0.0300	26
10	0.0330	21
11	0.0330	16
12	0.0330	22
13	0.0330	34

14	0.0330	44
15	0.0330	16
16	0.0330	33
17	0.0330	34
18	0.0330	21
19	0.0200	24
20	0.0200	31
21	0.0200	28
22	0.0200	24
23	0.0300	30
24	0.0300	110
25	0.0300	113
26	0.0330	27
27	0.0330	27
28	0.0330	23
29	0.0330	33
30	0.0330	58
31	0.0330	45
32	0.0330	54
33	0.0330	22

6.3.3 Optimal APF Configuration

The optimized configuration places APFs at buses 5, 14, 25, and 33, selected from the IEEE 33-bus system due to their proximity to major harmonic sources and strategic positions for mitigating upstream and downstream distortions. Table 6-3 summarizes the compensation harmonic currents (in per unit, p.u., relative to the fundamental), capacities (in MVA), and individual compensation costs (in £). The total governance cost converges to £81,104.15, representing a cost-effective solution that reduces the number of APFs while ensuring system-wide compliance.

In the proposed APF optimisation framework, the compensation cost reported in Table 6-3 and Figure 6-2 is derived from the objective function of the particle swarm optimisation (PSO) algorithm. The cost is formulated as a governance cost index that combines installation expenditure, capacity-related investment, and constraint enforcement. It is used to compare alternative APF allocation schemes under identical modelling assumptions, rather than to represent exact market procurement prices.

The total compensation cost is defined as

$$C_{\text{total}} = C_{\text{inst}} + C_{\text{cap}} + C_{\text{pen}},$$

where C_{inst}, C_{cap}, and C_{pen} denote the fixed installation cost, capacity-dependent cost, and penalty cost associated with harmonic constraint violations, respectively.

- Fixed installation cost

The fixed installation cost represents site-independent expenses associated with deploying an APF, including equipment installation, commissioning, protection, and integration with the existing distribution network. This term is expressed as

$$C_{\text{inst}} = c_{\text{inst}} N_{\text{APF}},$$

where N_{APF} is the total number of installed APFs, and c_{inst} is the unit installation cost per device. In this study, $c_{\text{inst}} = 3000$(£/unit) is adopted as a representative constant value. This term encourages solutions with fewer devices, provided that harmonic constraints are satisfied.

- Capacity-dependent cost

The capacity-dependent cost reflects the increase in equipment cost with APF rating, accounting for converter size, semiconductor devices, thermal design, and filter components. Let S_i denote the rated compensation capacity of the APF installed at bus i, as obtained from the optimisation process. The capacity-related cost is defined as

$$C_{\mathrm{cap}} = c_{\mathrm{cap}} \sum_{i=1}^{N_{\mathrm{APF}}} S_i$$

where c_{cap} is the unit cost coefficient. In the numerical implementation, APF capacities are converted to an equivalent kVA scale, and a linear cost coefficient of $c_{\mathrm{cap}} = 360$(£/kVA) is applied. This formulation penalises excessive oversizing and promotes economically balanced capacity allocation across the network.

- Harmonic constraint penalty

To ensure compliance with the post-mitigation harmonic voltage distortion limits specified in Table 6-2, a penalty term is introduced for any violation of the THDU constraints. Let THDU_k and $\mathrm{THDU}_k^{\max}$ denote the resulting and allowable total harmonic distortion at bus k, respectively. The number of violating buses is defined as

$$N_{\mathrm{viol}} = \sum_{k=1}^{N_{\mathrm{bus}}} \mathbb{I}\left(\mathrm{THDU}_k > \mathrm{THDU}_k^{\max}\right),$$

where $\mathbb{I}(\cdot)$ is the indicator function. The corresponding penalty cost is

$$C_{\mathrm{pen}} = \lambda\, N_{\mathrm{viol}},$$

with a penalty coefficient $\lambda = 5 \times 10^5$. This large penalty ensures that infeasible solutions with harmonic limit violations are strongly discouraged during optimisation, effectively enforcing THDU compliance across all buses.

The PSO algorithm minimises C_{total} as the objective function. Figure 6-2 illustrates the convergence of the global best objective value over successive iterations. Once all harmonic constraints are satisfied ($N_{\mathrm{viol}} = 0$), further reductions in the objective value are driven by improved trade-offs between the number of APFs and their allocated capacities. The final converged cost therefore corresponds to the optimal APF configuration reported in Table 6-3.

Table 6-3 Optimal APF Allocation Results

APF Node Number	**Compensation Harmonic Current (p.u.)**	**Compensation Capacity (MVA)**	**Compensation Cost (£)**
25	0.628	0.0855	33763.32
14	0.962	0.0392	17102.25
33	1.183	0.0443	18958.58
5	0.261	0.0230	11280
Total	-	-	81104.15

It should be noted that the relationship between the compensation current and the required APF capacity is not strictly proportional. Although the compensation current reflects the magnitude of harmonic distortion at a given node, the APF capacity is determined by multiple factors rather than the current magnitude alone.

First, the required APF capacity depends on both the compensation current and the local voltage level at the installation node. Since APF capacity is essentially related to the apparent power required for compensation, it is influenced by the product of voltage and current. In practical distribution networks, node voltages are not uniform and typically decrease along radial feeders. As a result, a node with a relatively large compensation current but lower voltage may not require the highest APF capacity.

Second, the compensation current reported in Table 6-3 represents the magnitude of harmonic components at individual nodes, whereas the APF capacity reflects the overall compensation requirement from a system perspective. Due to the network coupling effect, harmonic currents injected at one node can propagate through the network and influence voltage distortion at multiple locations. Therefore, the optimization process determines APF capacities based on their global impact on system-wide harmonic mitigation, rather than matching local harmonic current magnitudes directly.

Third, the optimal APF configuration is obtained through a system-level optimization process that considers both power quality improvement and economic cost. This introduces a trade-off between minimizing harmonic distortion and limiting investment and operational costs. As a result, the allocated APF capacity at each node is not solely driven by the local compensation current, but by its contribution to the overall objective function.

Therefore, the observed difference between compensation current and APF capacity is a natural outcome of voltage variation, network interactions, and optimization trade-offs, rather than an inconsistency in the results.

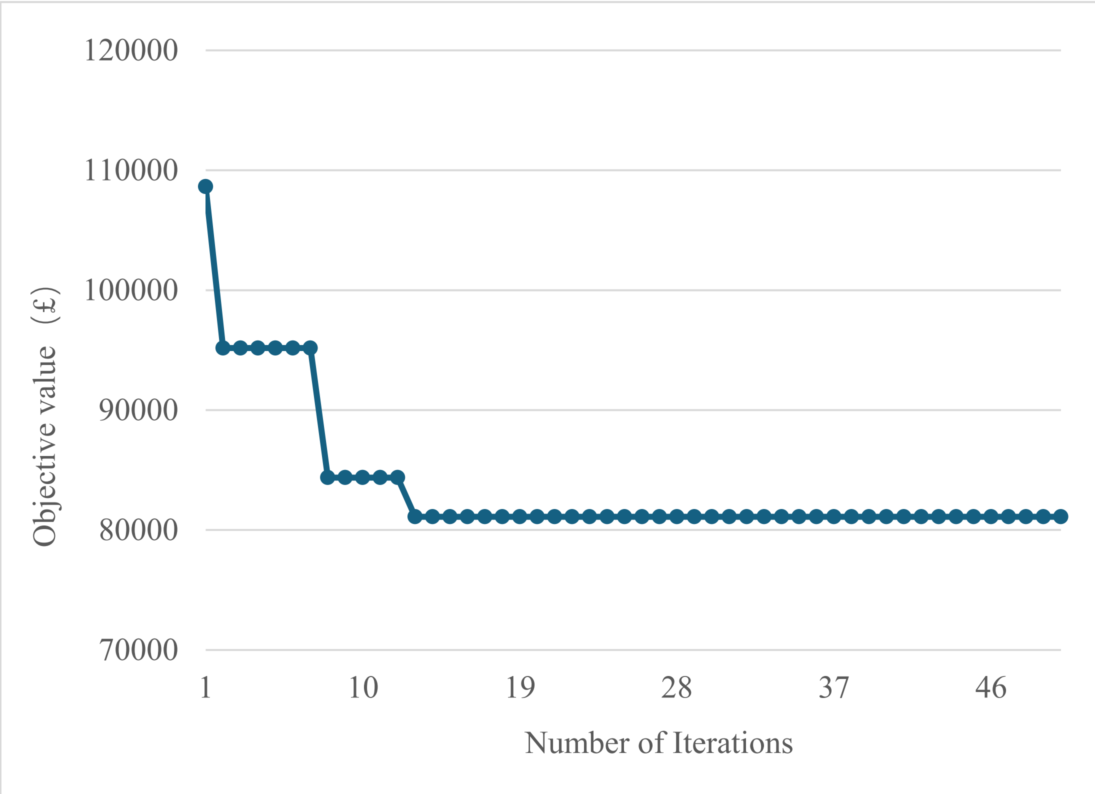

Figure 6-2 Compensation Cost by Iteration

Bus 25 demands the largest capacity (0.0855 MVA) and incurs the highest individual cost (£33,763.32), attributable to its elevated aggregate harmonic content across multiple orders (as per Table 6-4), necessitating substantial local filtering. Conversely, bus 5 handles a smaller load with a compensation current of 0.261 p.u., reflecting its role in addressing lower-magnitude distortions from upstream propagation.

A key feature of this configuration is the adoption of an over-compensation strategy at bus 33, where the injected compensation current (1.183 p.u.) exceeds the local harmonic injection rate. This deliberate over-injection generates counteracting harmonic currents that propagate through the network, potentially inducing slight over-compensation at non-critical buses. To quantify this, consider the harmonic current balance at a generic bus k:

$$I_{h,k}^{\text{net}} = I_{h,k}^{\text{source}} - I_{h,k}^{\text{APF}} + \sum_{m \neq k} I_{h,m \to k}^{\text{prop}}$$

Where $I_{h,k}^{\text{APF}}$ is the APF-injected current, and $I_{h,m \to k}^{\text{prop}}$ represents propagated currents from adjacent buses m. In over-compensation, $I_{h,k}^{\text{APF}} > I_{h,k}^{\text{source}} + | \sum I_{h,m \to k}^{\text{prop}} |$ at bus 33, resulting in a net negative (cancelling) current that flows to other buses, reducing their THDU at the expense of minor local over-correction.

Over-compensation, as implemented here, is a strategic deviation from conventional one-to-one harmonic cancellation, where APF currents precisely match local injections. Instead, it leverages the interconnected nature of the distribution network to achieve global optimization. The rationale stems from multi-objective optimization theory, balancing cost minimization with constraint satisfaction. Mathematically, this is incorporated into the PSO fitness function by allowing a tolerance band for individual bus THDU (e.g., permitting up to 10% over-correction if the system average THDU decreases by >20%), subject to the binding constraint that all buses remain below 3% THDU.

6.3.4 Variations in harmonic voltage distortion rates

Figure 6-3 illustrate the THDU at all buses before and after APF implementation. Prior to optimisation, several downstream buses exhibit elevated distortion levels, with buses 14 and 33 showing the highest THDU values (exceeding 0.08 p.u.), thereby surpassing the prescribed planning limits and indicating the need for harmonic mitigation. This non-uniform distribution reflects the cumulative propagation of harmonic currents from multiple nonlinear sources toward the feeder end.

Following the optimised APF deployment, THDU levels are substantially reduced across the entire network. All bus voltages comply with the imposed post-mitigation threshold of 3%, with the maximum residual THDU observed at bus 29 (0.0319 p.u.). This uniform suppression demonstrates the effectiveness of the proposed APF configuration in limiting harmonic propagation and reducing the risk of resonance, insulation stress, and equipment overheating.

A detailed quantitative comparison is provided in Table 6-4. The average THDU across the system decreases from 0.0476 p.u. to 0.0202 p.u., corresponding to a mean reduction of 54.11%. In addition, the standard deviation of THDU is reduced from 0.0229 p.u. to 0.0086 p.u., indicating a more homogeneous power quality profile after compensation. The largest improvement is observed at bus 18, where THDU is reduced by 71.34% (from 0.0595 p.u. to 0.0171 p.u.). In contrast, the smallest improvement occurs at bus 22 (20.44%), reflecting its relatively low initial distortion and limited margin for further reduction.

A moderate positive correlation ($r = 0.3745$) is observed between the pre-compensation THDU and the percentage reduction achieved, indicating that the optimisation strategy prioritises buses with higher initial distortion levels. This effect is further reinforced by the over-compensation strategy applied at bus 33, where the injected harmonic current exceeds the local harmonic generation. The resulting surplus compensating current propagates to neighbouring buses, producing additional THDU reductions of approximately 15–20% in buses 29–32, while introducing only marginal residual distortion variations (<0.008 p.u.) in upstream low-distortion buses. This trade-off enables system-wide compliance with harmonic limits using a reduced number of APFs, thereby supporting the overall cost minimisation objective.

Table 6-4 THDU Comparison and Improvement Before and After APF Compensation

Node Index	THDU Before (p.u.)	THDU After (p.u.)	Improvement (%)
1	0.005278	0.002576	51.1961
2	0.007401	0.003612	51.1931
3	0.018185	0.008334	54.1693
4	0.021577	0.010043	53.4549
5	0.025219	0.011876	52.9105
6	0.038433	0.018520	51.8122
7	0.049608	0.024070	51.4793
8	0.052421	0.025673	51.0241
9	0.056813	0.026669	53.0575
10	0.061239	0.027567	54.9845
11	0.061706	0.027673	55.1539
12	0.062179	0.027459	55.8383
13	0.065542	0.024992	61.8691
14	0.067639	0.023456	65.3220
15	0.066232	0.022354	66.2493
16	0.064853	0.021269	67.2039
17	0.060687	0.017976	70.3788

18	0.059492	0.017052	71.3366
19	0.008026	0.004242	47.1451
20	0.013265	0.009510	28.3023
21	0.015016	0.011270	24.9495
22	0.018285	0.014547	20.4412
23	0.026242	0.011504	56.1603
24	0.044938	0.018772	58.2265
25	0.063360	0.025577	59.6327
26	0.050694	0.024521	51.6302
27	0.052201	0.025126	51.8667
28	0.061664	0.028915	53.1091
29	0.069061	0.031886	53.8293
30	0.070433	0.031491	55.2894
31	0.075426	0.029990	60.2389
32	0.077438	0.029473	61.9401
33	0.080635	0.028813	64.2672

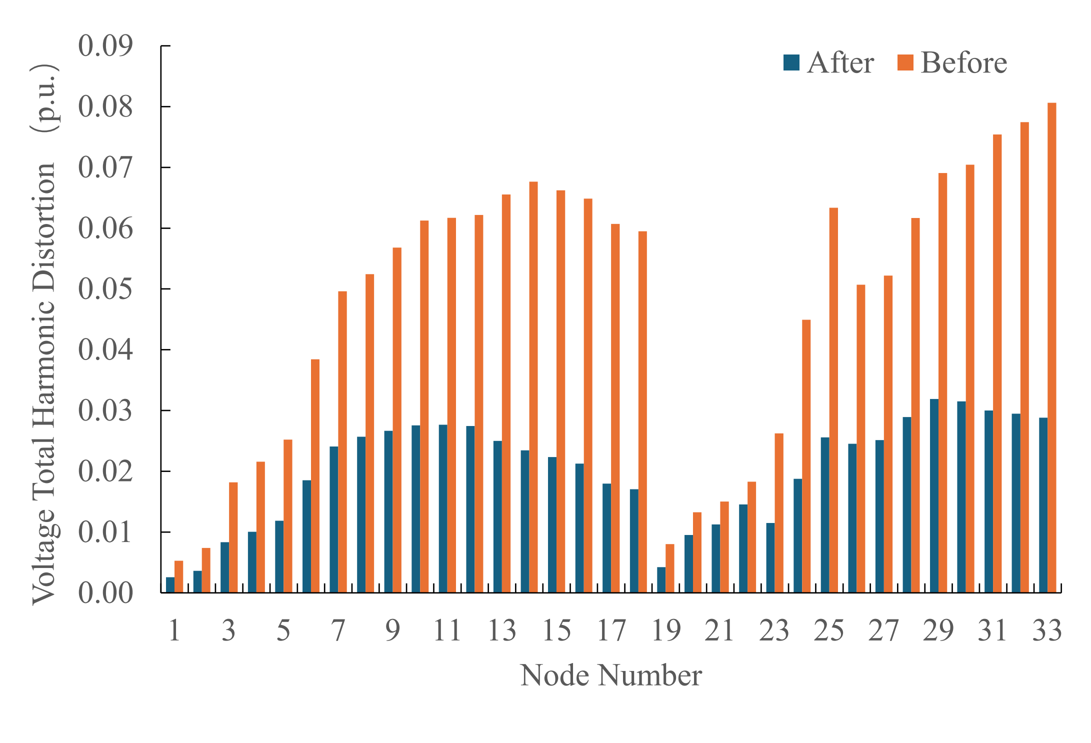

Figure 6-3 THDU Before and After APF Implementation

6.3.5 Variations in individual harmonic voltage components

The variations in individual harmonic voltage ratios before and after APF compensation are summarized in Table 6-5, covering the dominant odd harmonic orders (5th, 7th, 11th, 13th, and 17th). These results provide granular insight into the frequency-selective performance of the proposed optimization strategy, complementing the aggregate THDu assessment presented previously.

Prior to optimization, the network exhibits distinct downstream amplification of harmonic voltages. As evidenced in the pre-compensation data, buses near the feeder end (notably buses 29–33) display the highest HRU values across all considered orders. Specifically, bus 33 records peak values of 0.0354 p.u. (5th) and 0.0438 p.u. (7th), reflecting the cumulative interaction between concentrated harmonic injections and the increasing inductive reactance of the long feeder lines. This spatial trend indicates a high susceptibility to resonance and localized insulation stress in the absence of active mitigation.

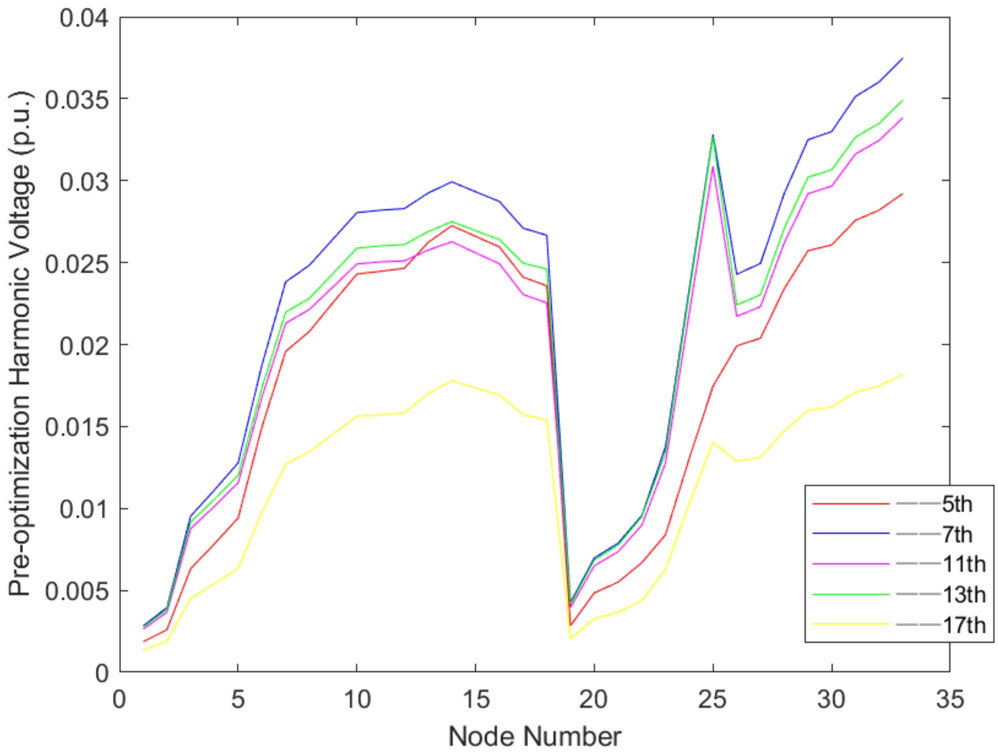

Figure 6-4 Pre-Optimization Harmonic Voltage

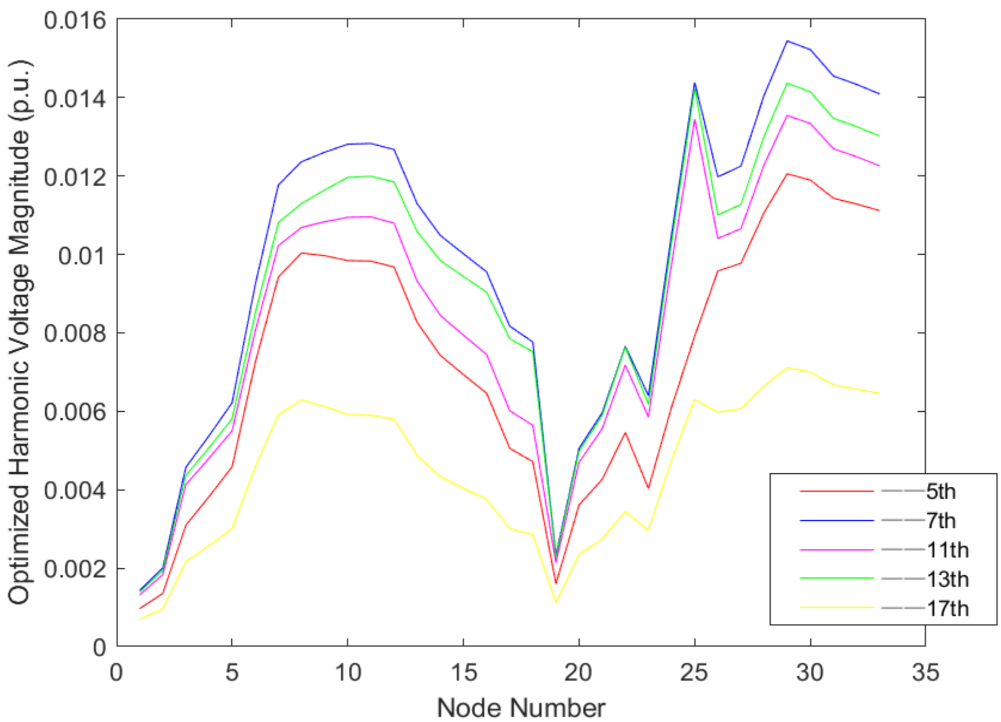

Figure 6-5 Optimized Harmonic Voltage Magnitude

Following the optimized APF deployment, substantial mitigation is achieved across the entire frequency spectrum. As illustrated in Figure 6-4 and Figure 6-5, the harmonic voltage profiles are significantly flattened, with peak HRU values suppressed to below 0.016 p.u. for all orders. The most pronounced reductions are observed in the lower-order harmonics (5th and 7th), which typically dominate the distortion spectrum in distribution networks containing power-electronic loads. System-wide, the average attenuation ranges from 56% to 60% across the five harmonic orders, confirming the broadband efficacy of the APF configuration.

A comparative analysis reveals that lower-order harmonics exhibit marginally higher mitigation ratios than higher-order components. This is attributable to the optimization algorithm prioritizing the dominant low-frequency components which contribute most heavily to the objective function. Nevertheless, higher-order harmonics (11th–17th) also experience consistent suppression without evidence of secondary amplification or control instabilities, verifying that the solution effectively dampens harmonic propagation without inducing adverse resonance at higher frequencies.

Bus-specific analysis further highlights the "over-compensation" mechanism inherent in the optimal solution. High-distortion nodes (e.g., buses 22, 25, 29, and 33) benefit from reductions exceeding 60%. Notably, the strategy involves injecting surplus canceling currents at key locations (like bus 33), which propagate upstream. This results in noticeable improvements even in upstream buses (1–10) that have lower baseline distortions. This propagation effect allows the limited number of APFs to enforce global compliance effectively, validating the economic efficiency of the proposed siting and sizing approach.

Table 6-5 HRU (p.u.) For Harmonic Orders Before and After APF

Node Index	**5th**		**7th**		**11th**		**13th**		**17th**	
	Before	**After**	**Before**	**After**	**Before**	**After**	**Before**	**After**	**Before**	**After**
1	0.0011	0.0005	0.0012	0.0005	0.0011	0.0005	0.0011	0.0005	0.0007	0.0003
2	0.0015	0.0006	0.0017	0.0008	0.0015	0.0007	0.0015	0.0007	0.0010	0.0004
3	0.0039	0.0016	0.0044	0.0019	0.0038	0.0017	0.0039	0.0018	0.0024	0.0010
4	0.0058	0.0024	0.0065	0.0028	0.0056	0.0025	0.0058	0.0027	0.0035	0.0014
5	0.0079	0.0032	0.0087	0.0038	0.0076	0.0034	0.0077	0.0036	0.0048	0.0019
6	0.0152	0.0062	0.0169	0.0074	0.0148	0.0065	0.0151	0.0070	0.0093	0.0037
7	0.0212	0.0086	0.0239	0.0103	0.0210	0.0092	0.0215	0.0099	0.0132	0.0052
8	0.0229	0.0093	0.0254	0.0110	0.0222	0.0098	0.0227	0.0105	0.0142	0.0056
9	0.0245	0.0110	0.0270	0.0129	0.0237	0.0114	0.0243	0.0123	0.0152	0.0067
10	0.0261	0.0127	0.0287	0.0147	0.0251	0.0130	0.0260	0.0142	0.0161	0.0078

11	0.0262	0.0129	0.0289	0.0149	0.0252	0.0132	0.0261	0.0143	0.0162	0.0079
12	0.0264	0.0131	0.0290	0.0150	0.0253	0.0133	0.0262	0.0145	0.0163	0.0080
13	0.0274	0.0143	0.0296	0.0159	0.0256	0.0139	0.0268	0.0153	0.0171	0.0089
14	0.0280	0.0150	0.0300	0.0164	0.0258	0.0143	0.0271	0.0158	0.0176	0.0096
15	0.0273	0.0144	0.0294	0.0159	0.0251	0.0137	0.0266	0.0153	0.0171	0.0092
16	0.0266	0.0138	0.0288	0.0154	0.0244	0.0131	0.0260	0.0148	0.0167	0.0088
17	0.0245	0.0119	0.0269	0.0137	0.0223	0.0112	0.0244	0.0134	0.0153	0.0076
18	0.0239	0.0114	0.0264	0.0132	0.0217	0.0107	0.0240	0.0129	0.0149	0.0073
19	0.0015	0.0007	0.0017	0.0008	0.0015	0.0007	0.0016	0.0007	0.0010	0.0004
20	0.0017	0.0008	0.0019	0.0009	0.0017	0.0008	0.0017	0.0009	0.0011	0.0006
21	0.0017	0.0008	0.0019	0.0009	0.0016	0.0008	0.0017	0.0009	0.0011	0.0006
22	0.0017	0.0008	0.0019	0.0009	0.0016	0.0008	0.0017	0.0009	0.0011	0.0005
23	0.0039	0.0016	0.0044	0.0019	0.0038	0.0017	0.0039	0.0018	0.0024	0.0010
24	0.0039	0.0016	0.0043	0.0019	0.0038	0.0017	0.0039	0.0018	0.0024	0.0010

25	0.0039	0.0016	0.0043	0.0019	0.0038	0.0017	0.0039	0.0018	0.0024	0.0010
26	0.0218	0.0089	0.0246	0.0107	0.0217	0.0095	0.0222	0.0102	0.0135	0.0053
27	0.0225	0.0092	0.0257	0.0111	0.0226	0.0099	0.0232	0.0106	0.0139	0.0055
28	0.0273	0.0111	0.0323	0.0138	0.0287	0.0124	0.0295	0.0132	0.0164	0.0065
29	0.0309	0.0127	0.0375	0.0160	0.0334	0.0143	0.0344	0.0152	0.0184	0.0074
30	0.0315	0.0129	0.0382	0.0163	0.0341	0.0146	0.0351	0.0155	0.0187	0.0075
31	0.0334	0.0137	0.0409	0.0174	0.0366	0.0156	0.0377	0.0165	0.0199	0.0080
32	0.0342	0.0140	0.0420	0.0179	0.0376	0.0161	0.0387	0.0169	0.0204	0.0082
33	0.0354	0.0145	0.0438	0.0186	0.0392	0.0167	0.0404	0.0176	0.0212	0.0085

6.4 Summary

This chapter developed and validated an optimisation framework for Active Power Filter (APF) configuration in a distribution network using an enhanced Particle Swarm Optimisation (PSO) algorithm. By introducing niche-based subpopulation evolution and periodic elimination, the algorithm improves convergence stability and solution diversity when solving the mixed discrete–continuous APF placement and sizing problem.

Using the IEEE 33-bus test system with distributed harmonic sources, the framework jointly minimises harmonic distortion and a composite governance cost that accounts for APF installation, capacity allocation, and harmonic constraint enforcement. The optimal solution places APFs at buses 5, 14, 25, and 33, reducing the average system-wide THDU from 0.047612 to 0.020206, corresponding to a 54.1% improvement, while ensuring all buses comply with post-mitigation harmonic limits.

Consistent suppression is achieved across all dominant harmonic orders, with reductions exceeding 55% for the 5th and 7th components. The over-compensation strategy applied at bus 33 enhances network-wide mitigation by propagating cancelling currents to downstream buses, enabling compliance with a reduced number of APFs.

Overall, the results demonstrate that the proposed framework achieves an effective balance between power quality improvement and economic efficiency, providing a scalable basis for coordinated and adaptive APF deployment in future distribution network applications.

Chapter 7 Conclusion and Future Work

7.1 Conclusion

In an era of accelerating renewable energy integration, modern distribution networks face unprecedented challenges from stochastic variability, three-phase unbalance, and harmonic distortion. Traditional deterministic methods are no longer sufficient, as they often fail to capture the complex interactions between these factors, leading to suboptimal planning and inadequate mitigation.

This thesis has systematically addressed these gaps by establishing a unified probabilistic framework that spans from efficient uncertainty quantification and three-phase stochastic harmonic propagation to economically optimised mitigation. By integrating advanced probabilistic techniques—specifically dependence-aware point estimation and hybrid multi-criteria weighting—with bio-inspired global optimisation, this research provides a comprehensive, uncertainty-respecting toolkit for assessing operational risks in RES-rich, unbalanced distribution systems.

The achieved outcomes demonstrate that it is possible to:

- Obtain high-fidelity statistical characterizations of system states with significantly reduced computational cost;
- Quantitatively reveal phase-specific vulnerability patterns that single-phase or deterministic models overlook;
- Realise cost-effective global harmonic suppression through topology-aware active filter deployment.

These advancements collectively contribute toward more resilient, reliable, and economically viable operation of future active distribution networks, providing both the analytical insight and practical tools necessary to support the transition to high-renewable, low-carbon power systems.

7.2 Summary of Original Contributions

1. Dependence-Aware Probabilistic Power Flow Framework

"The thesis proposes and validates an integrated Three-Point Estimation Method (3PEM) enhanced by Nataf transformations to explicitly model rank correlations among uncertain inputs (loads, wind, and PV generation). This dependence-aware approach significantly improves the fidelity of estimated moments for node voltages, branch powers, and network losses compared with independent-variable assumptions, while requiring far fewer deterministic power-flow runs than Monte Carlo Simulation (MCS). The framework is further extended to probabilistic harmonic power flow, enabling fast yet accurate screening of Total Harmonic Distortion (THD) distributions under correlated uncertainties, representing a novel combination that fills a methodological gap in existing literature."

This thesis developed and validated a systematic probabilistic power flow (PPF) framework that explicitly accounts for the stochastic dependence among uncertain system inputs. By integrating the Three-Point Estimation Method (3PEM) with the Nataf transformation, the proposed approach effectively maps non-Gaussian correlated variables—including nodal loads, wind power, and PV generation—into an independent standard normal space via a Gaussian Copula. This enables the explicit modeling of rank correlations while preserving the marginal distribution characteristics of each resource (e.g., Weibull for wind and Beta for PV)."

Evaluated on the IEEE 33-bus radial distribution system, the proposed framework demonstrates high numerical fidelity and computational efficiency:

- Accuracy and Precision: The method characterizes the first five statistical moments of bus voltages, branch power flows, and total system losses. Validation against a 10,000-sample MCS benchmark reveals relative errors in expected values within 0.01% and standard deviations generally below 5%, with minor discrepancies observed only in high-order moment approximations at the distribution tails.

- Computational Superiority: By requiring only 2m+1 deterministic evaluations (where m denotes the number of correlated uncertain variables), the framework achieves an orders-of-magnitude reduction in computational burden compared to MCS, rendering it suitable for real-time uncertainty screening.

A key contribution is the quantification of how inter-variable correlations alter the system's physical operating state. The analysis reveals that positive correlations among load demands and PV generation can significantly exacerbate expected network losses and broaden voltage variability, particularly at the end-of-feeder nodes (e.g., nodes 18 and 33). Conversely, negative load–wind correlations provide a degree of stochastic mitigation, though the efficacy is constrained by the installed capacity of the resources.

Furthermore, the framework was extended to probabilistic harmonic power flow, addressing a significant methodological gap. By incorporating stochastic harmonic injectors at critical buses, the model provides a fast yet accurate estimation of THD probability distributions. The results demonstrate that while harmonic distortion exhibits higher expected values and broader variance near injection points (predominantly the 5th and 7th harmonics), the impact attenuates and concentrates as it propagates toward upstream buses.

In summary, this dependence-aware framework provides a robust and computationally tractable tool for risk-informed planning and operation, enabling distribution system operators to move beyond the limitations of independence assumptions toward a more realistic, uncertainty-respecting assessment of modern active networks.

2. ***Comprehensive Three-Phase Stochastic Harmonic Risk Assessment with Hybrid Weighting***

"A three-phase Monte Carlo-based stochastic harmonic power flow model (10,000 scenarios) is developed, incorporating realistic harmonic injection spectra and unbalanced loading conditions. This framework enables a detailed and data-driven characterisation of how uncertainty and harmonic distortions propagate across phases in radial distribution networks. In addition, a hybrid weighting scheme combining the

Analytic Hierarchy Process (AHP) with an improved CRITIC method (incorporating redundancy entropy) is proposed to balance expert judgment with objective data information, leading to a robust prioritisation of power quality weak points, with particular emphasis on three-phase harmonic voltage imbalance under renewable penetration. The results reveal a clear downstream amplification of uncertainty and systematically higher violation risks in the most heavily loaded phase, highlighting behaviours that cannot be captured by deterministic or single-phase analyses."

This contribution is reflected in the establishing of a comprehensive three-phase stochastic harmonic power flow and operational risk assessment framework to characterize the multifaceted uncertainties in modern distribution networks. By integrating large-scale MCS (10,000 scenarios), the framework provides a statistically complete description of the interaction between three-phase unbalance, stochastic load/resource variations, and non-linear harmonic injections (specifically the 5th through 17th orders).

The empirical findings on an unbalanced IEEE 33-bus system yield several critical insights into system physics:

- Spatial and Phase-Dependent Propagation: Uncertainty and harmonic distortion propagate unevenly across the network. A pronounced "downstream widening" effect of voltage uncertainty was observed, where tail-end buses exhibit significantly higher variance compared to upstream locations.
- Phase-Specific Vulnerability: The framework quantitatively reveals that the most heavily loaded phase suffers from systematically elevated risks of both under-voltage and branch overload. These phase-specific patterns—and the associated "probabilistic tails" of voltage violations—are effectively masked in traditional deterministic or single-phase analyses.
- • Harmonic Interaction: The analysis shows that THD varies significantly across the network, with higher values generally observed in feeder sections that are electrically distant from the slack bus or weakly supported. The spatial

distribution of THD is influenced by the combined effects of harmonic source locations, feeder impedance characteristics, and variations in fundamental voltage magnitude. Differences across phases further highlight that harmonic distortion is not uniformly distributed, reinforcing the importance of three-phase modelling for accurately capturing distortion patterns in unbalanced distribution systems.

To translate these analytical insights into actionable planning, a hybrid subjective–objective weighting scheme was developed. This scheme synthesizes the Analytic Hierarchy Process (AHP) with an improved Criteria Importance Through Intercriteria Correlation (CRITIC) method incorporating redundancy entropy, effectively balancing domain expertise with the inherent information content of the data. The resulting assessment identifies three-phase harmonic voltage imbalance as the most influential factor in weak-point prioritization within renewable-rich systems.

Overall, this contribution provides a granular and mathematically rigorous basis for identifying critical nodes and vulnerable phases, supporting risk-informed power quality management in active distribution networks.

3. Enhanced Optimization Strategy for Active Power Filter Placement and Sizing

"An improved Particle Swarm Optimization (PSO) algorithm incorporating niche division and periodic subpopulation elimination is introduced to solve the multi-objective APF configuration problem. By strategically allowing controlled over-compensation at selected buses, the method exploits network topology to achieve global harmonic suppression more efficiently than conventional local-matching approaches. Case studies on the IEEE 33-bus system demonstrate that the proposed approach significantly reduces voltage harmonic distortion while meeting IEEE 519 requirements, achieving an effective balance between harmonic mitigation performance and overall investment cost."

This contribution is reflected in the introduction of an improved PSO algorithm specifically designed for the multi-objective configuration of shunt APFs in harmonic-constrained distribution networks. The enhancement incorporates niche-based subpopulation division (grouping particles according to network nodes) and periodic elimination of underperforming subpopulations. These mechanisms promote broader exploration, reduce the risk of premature convergence, and enhance solution diversity in the mixed discrete continuous search space of APF locations and capacities.

The optimization employs a double-layer model that simultaneously minimizes a composite governance cost (installation + capacity + constraint penalties) while strictly enforcing post-mitigation THDU limits. Harmonic power flow calculations are embedded to evaluate candidate configurations under operating conditions.

Applied to the IEEE 33-bus system with multiple distributed harmonic sources, the algorithm identifies an optimal placement at buses 5, 14, 25, and 33. A distinctive feature is the controlled over-compensation strategy at bus 33, where injected compensating currents exceed local harmonic levels. This generates propagating cancellation effects that benefit downstream buses, enabling effective global compliance with fewer APFs than conventional approaches.

Results demonstrate substantial harmonic mitigation: average system-wide THDU is reduced from 4.76% to 2.02% (a 54.1% improvement), with all buses satisfying the 3% threshold. Dominant low-order harmonics (5th and 7th) experience reductions exceeding 55%, and individual harmonic voltage components are consistently suppressed across the network. The over-compensation mechanism effectively exploits feeder topology to achieve more efficient system-wide suppression than local-matching or standard PSO methods.

This enhanced PSO-based framework provides a practical, cost-effective solution that balances stringent power quality compliance with investment minimization, serving as a scalable tool for coordinated harmonic mitigation in renewable-integrated distribution systems where probabilistic weak-point identification (from Chapter 5) directly informs targeted APF deployment.

7.3 Future work

The work presented in this thesis provides a probabilistic foundation for harmonic analysis and mitigation in distribution networks, but several practical extensions remain worthwhile:

1. Inclusion of Voltage Phase Angles in Probabilistic Analysis

The current probabilistic models (Chapters 4 and 5) focus primarily on voltage magnitudes, branch powers, and THD, with limited attention to phase angles. Future work could extend the 3PEM and MCS frameworks to compute statistical moments and distributions of fundamental and harmonic phase angles. This would allow evaluation of angle-dependent effects, such as branch power-angle relationships, maximum angle differences for stability margins, and their influence on harmonic cancellation across phases. Such analysis would be particularly useful in unbalanced networks where phase shifts affect neutral currents and overall distortion patterns.

2. Incorporation of Temporal Dependencies and Seasonal Patterns

The present correlation modeling relies on static rank correlations within individual scenarios. A natural next step is to account for time-varying dependencies between load, wind, and PV outputs across hours or seasons. This could be achieved by extending the Copula framework with simple autoregressive structures or by generating correlated time-series scenarios using historical data. The resulting multi-period probabilistic assessment would better capture how harmonic risks evolve over daily cycles or under seasonal renewable variability.

3. Utilization of Existing Distributed Energy Resources (DER) Inverters for Harmonic Support

Instead of relying exclusively on dedicated APFs (Chapter 6), future studies could investigate how grid-tied DER inverters (PV, battery, or EV chargers) can provide supplementary harmonic compensation using their existing control loops. This would involve formulating a coordinated allocation problem that balances active/reactive power delivery with selective harmonic current injection, subject to inverter capacity and availability constraints. Building on the weak-point identification of Chapter 5, such an approach could reduce the need for additional hardware while maintaining acceptable THDU levels.

4. Transition Toward Online or Adaptive Mitigation Strategies

The current APF optimization is offline and planning oriented. A practical extension would be to develop adaptive control rules or simple feedback mechanisms that adjust APF reference currents in real time based on measured THD or voltage distortion levels. This could start with rule-based or model-predictive approaches before considering more advanced techniques, enabling better response to sudden changes in load, generation, or network topology.

5. Advanced Dependency Modelling for Multi-Variable Uncertainty

In this study, the dependencies among uncertain inputs are represented using a Nataf transformation based on a Gaussian Copula. While this approach provides an efficient way to model monotonic dependencies, it may have limitations in capturing more complex or non-linear dependency structures.

Future research could explore the use of alternative Copula models, such as Vine Copulas or non-Gaussian Copulas, to better characterise high-dimensional and asymmetric dependencies among loads and renewable sources. This would further improve the accuracy of probabilistic power flow analysis, particularly in systems with high renewable penetration and strong non-linear interactions.

Appendix

Table AP 1 Expected Value Distribution of the State Variable

Node Index	Node Voltage Expectation	Branch Active power Expectation	Branch Reactive power Expectation
1	1	3.481762411	2.261745627
2	0.99733388	3.13768454	2.077739516
3	0.984393904	2.063882735	1.557941481
4	0.977765914	1.928019656	1.469862575
5	0.971256834	1.853292213	1.432361669
6	0.954999188	1.763338428	1.386504182
7	0.947250778	0.735115444	0.356637244
8	0.943253219	0.53177295	0.255532643
9	0.938378571	0.469217006	0.233696333
10	0.933970274	0.407143244	0.212226413
11	0.933343077	0.361839322	0.182125931
12	0.932286133	0.301385488	0.146975876
13	0.928186702	0.240149339	0.1110033
14	0.926779347	0.119856856	0.030618298
15	0.926192925	0.059775942	0.020546278
16	0.92581552	-0.000263828	0.000517233
17	0.925808924	-0.060292954	-0.019521659
18	0.926180272	0.234118823	0.118929371
19	0.996977243	0.144039877	0.078854036
20	0.994952491	0.053715474	0.038561723

21	0.994698561	0.090045171	0.040059725
22	0.994062667	0.939803669	0.457388434
23	0.980812376	0.846574951	0.405182287
24	0.974148824	0.421337133	0.201046277
25	0.970827413	0.821724017	0.908384044
26	0.945532911	0.759564491	0.882284065
27	0.943265468	0.696818428	0.855885922
28	0.93309478	0.627558459	0.827721571
29	0.92583825	0.501176382	0.752161609
30	0.92281232	0.298058652	0.150573652
31	0.919865588	0.147206363	0.079731326
32	0.919358804	-0.062872504	-0.020360623
33	0.919576794		

Table AP 2 Standard Deviation Distribution of State Variables

Node Index	Nodal voltage standard deviation	Branch active power standard deviation	Branch reactive power standard deviation
1		0.216971	0.164454
2	0.000165	0.198173	0.160752
3	0.000979	0.147304	0.146317
4	0.001402	0.143058	0.144338
5	0.001866	0.140378	0.143154
6	0.003132	0.135345	0.13937
7	0.003804	0.079423	0.035249
8	0.004036	0.067781	0.028738
9	0.004367	0.066063	0.028013
10	0.004744	0.064388	0.027335
11	0.004809	0.063662	0.026638
12	0.004931	0.062365	0.025651
13	0.005504	0.060702	0.024294
14	0.005753	0.055604	0.018046
15	0.005947	0.054225	0.017875
16	0.006181	0.052835	0.017388
17	0.006649	0.051444	0.016908
18	0.006878	0.083119	0.029542
19	0.00023	0.081102	0.028395
20	0.00118	0.07885	0.027033
21	0.001455	0.018017	0.008023

22	0.001492	0.122808	0.059448
23	0.001314	0.12064	0.058024
24	0.002153	0.08452	0.040407
25	0.002646	0.100317	0.129957
26	0.003982	0.099113	0.129601
27	0.004235	0.097747	0.129157
28	0.005495	0.094782	0.126965
29	0.006476	0.090068	0.124658
30	0.006939	0.079764	0.031873
31	0.007399	0.073469	0.028188
32	0.007534	0.06021	0.019769
33	0.007635		

Table AP 3 Impact of Correlation Coefficient on Network Loss, Branch Power Statistics, And Voltage Magnitudes

Correlation coefficient	Expected value of network loss	Standard deviation of network loss	Expected value of branch active power	Standard deviation of branch active power	Expected value of branch reactive power	Standard deviation of branch reactive power	Node 18 voltage magnitude	Node 33 voltage magnitude
0	0.166344	0.024006	3.481762	0.216971	2.261746	0.164454	0.926180	0.919577
0.1	0.172478	0.048194	3.487896	0.393736	2.266548	0.354774	0.926035	0.919335
0.2	0.175982	0.057660	3.491399	0.468243	2.269285	0.426072	0.925951	0.919200
0.3	0.178009	0.062487	3.493427	0.507514	2.270867	0.461945	0.925901	0.919124
0.4	0.179012	0.064731	3.494430	0.526753	2.271648	0.478426	0.925876	0.919087
0.5	0.179196	0.065109	3.494614	0.531405	2.271789	0.481027	0.925870	0.919081
0.6	0.178656	0.063874	3.494074	0.523354	2.271364	0.471628	0.925882	0.919104

Table AP 4 Node Load and Branch Impedance Parameters for IEEE 33-bus System

Node i	**Node j**	**Branch impedance (p.u.)**	**Node j load (kW + j kVAr)**	**Node i**	**Node j**	**Branch impedance (p.u.)**	**Node j load (kW + j kVAr)**
0	1	0.0922+j0.047	100+j60	16	17	0.3720+j0.5740	90+j40
1	2	0.4930+j0.2511	90+j40	1	18	0.1640+j0.1565	90+j40
2	3	0.3660+j0.1864	120+j80	18	19	1.5042+j1.3554	90+j40
3	4	0.3811+j0.1941	60+j30	19	20	0.4095+j0.4784	90+j40
4	5	0.8190+j0.7070	60+j20	20	21	0.7089+j0.9373	90+j40
5	6	0.1872+j0.6188	200+j100	2	22	0.4512+j0.3083	90+j50
6	7	0.7114+j0.2351	200+j100	22	23	0.8980+j0.7091	420+j200
7	8	1.0300+j0.7400	60+j20	23	24	0.8960+j0.7011	420+j200
8	9	1.0440+j0.7400	60+j20	5	25	0.2030+j0.1034	60+j25
9	10	0.1966+j0.0650	45+j30	25	26	0.2842+j0.1447	60+j25
10	11	0.3744+j0.1238	60+j35	26	27	1.0590+j0.9337	60+j20

<table>
<tr><td>11</td><td>12</td><td>1.4680+j1.1550</td><td>60+j35</td><td>27</td><td>28</td><td>0.8042+j0.7006</td><td>120+j70</td></tr>
<tr><td>12</td><td>13</td><td>0.5416+j0.7129</td><td>120+j80</td><td>28</td><td>29</td><td>0.5075+j0.2585</td><td>200+j600</td></tr>
<tr><td>13</td><td>14</td><td>0.5910+j0.5260</td><td>60+j10</td><td>29</td><td>30</td><td>0.9744+j0.9630</td><td>150+j70</td></tr>
<tr><td>14</td><td>15</td><td>0.7463+j0.5450</td><td>60+j20</td><td>30</td><td>31</td><td>0.3105+j0.3619</td><td>210+j100</td></tr>
<tr><td>15</td><td>16</td><td>1.2890+j1.7210</td><td>60+j20</td><td>31</td><td>32</td><td>0.3410+j0.5362</td><td>60+j40</td></tr>
<tr><td>7</td><td>20</td><td>2+j2</td><td rowspan="5">Note</td><td colspan="4" rowspan="5">The network consists of 32 branches. The reference voltage at the source end is 12.66 kV. The three-phase power base is set to 100 MVA, and the total network load is 5084.26 + j2547.32 kVA. The line impedance is given in ohms (Ω), with the base impedance calculated as:Z=(12.66*10^3)^2/100^7=1.602756Ω</td></tr>
<tr><td>8</td><td>14</td><td>2+j2</td></tr>
<tr><td>11</td><td>21</td><td>2+j2</td></tr>
<tr><td>17</td><td>32</td><td>0.5+j0.5</td></tr>
<tr><td>24</td><td>28</td><td>0.5+j0.5</td></tr>
</table>

Reference

[1] ‘Net Zero by 2050 – Analysis’, IEA. Accessed: Jan. 24, 2026. [Online]. Available: https://www.iea.org/reports/net-zero-by-2050

[2] B. R. Prusty and D. Jena, ‘A critical review on probabilistic load flow studies in uncertainty constrained power systems with photovoltaic generation and a new approach’, *Renew. Sustain. Energy Rev.*, vol. 69, pp. 1286–1302, Mar. 2017, doi: 10.1016/j.rser.2016.12.044.

[3] Z. Hu, Y. Han, A. Zalhaf, S. Zhou, J. Jonsen, and P. Yang, ‘Harmonic Sources Modeling and Characterization in Modern Power Systems: A Comprehensive Overview’, *Electr. Power Syst. Res.*, vol. 218, p. 109234, Feb. 2023, doi: 10.1016/j.epsr.2023.109234.

[4] ‘IEEE Standards Association’, IEEE Standards Association. Accessed: Jan. 24, 2026. [Online]. Available: https://standards.ieee.org/ieee/519/10677/

[5] ‘An analysis of the August 9th 2019 GB transmission system frequency incident - ScienceDirect’. Accessed: Jan. 24, 2026. [Online]. Available: https://www.sciencedirect.com/science/article/pii/S0378779621004259

[6] ‘What caused Iberia’s blackout? Renewable energy’s opponents were quick to blame solar and wind, but multiple factors appear to be at play’, https://science.feedback.org/. Accessed: Feb. 01, 2026. [Online]. Available: https://science.feedback.org/what-caused-iberias-blackout/

[7] J. Usaola, ‘Probabilistic load flow with wind production uncertainty using cumulants and Cornish–Fisher expansion’, *Int. J. Electr. Power Energy Syst.*, vol. 31, no. 9, pp. 474–481, Oct. 2009, doi: 10.1016/j.ijepes.2009.02.003.

[8] G. K. Singh, ‘Power system harmonics research: a survey’, *Eur. Trans. Electr. Power*, vol. 19, no. 2, pp. 151–172, 2009, doi: 10.1002/etep.201.

[9] J. Lu, ‘A new method for harmonic penetration study in power networks with renewable generation’.

[10] G. Desrochers, M. Blanchard, and S. Sud, ‘A Monte-Carlo Simulation Method for

the Economic Assessment of the Contribution of Wind Energy to Power Systems', *IEEE Trans. Energy Convers.*, vol. EC-1, no. 4, pp. 50–56, Dec. 1986, doi: 10.1109/TEC.1986.4765774.

[11] R. Billinton and L. Gan, 'Wind power modeling and application in generating adequacy assessment', in *IEEE WESCANEX 93 Communications, Computers and Power in the Modern Environment - Conference Proceedings*, May 1993, pp. 100–106. doi: 10.1109/WESCAN.1993.270560.

[12] K. Srilakshmi, P. R. Babu, Y. Venkatesan, and A. Palanivelu, 'Soccer league optimization for load flow analysis of power systems', *Int. J. Numer. Model. Electron. Netw. Devices Fields*, vol. 35, no. 2, p. e2965, Mar. 2022, doi: 10.1002/jnm.2965.

[13] J. G. Mayordomo, M. Lopez, R. Asensi, L. F. Beites, J. Bueno, and J. M. Rodriguez, 'A general treatment of traction PWM converters for load flow and harmonic penetration studies', in *8th International Conference on Harmonics and Quality of Power. Proceedings (Cat. No.98EX227)*, Oct. 1998, pp. 685–692 vol.2. doi: 10.1109/ICHQP.1998.760128.

[14] X. Lin, Y. Jiang, S. Peng, H. Chen, J. Tang, and W. Li, 'An efficient Nataf transformation based probabilistic power flow for high- dimensional correlated uncertainty sources in operation', *Int. J. Electr. Power Energy Syst.*, vol. 116, Oct. 2019, doi: 10.1016/j.ijepes.2019.105543.

[15] K. Murari and N. P. Padhy, 'Graph-theoretic-based approach for solving load flow problem of AC–DC radial distribution network with distributed generations', *IET Gener. Transm. Distrib.*, vol. 14, no. 22, pp. 5327–5346, 2020, doi: 10.1049/iet-gtd.2019.1416.

[16] 'Stochastic optimal power flow in islanded DC microgrids with correlated load and solar PV uncertainties - ScienceDirect'. Accessed: Feb. 25, 2025. [Online]. Available: https://www.sciencedirect.com/science/article/pii/S0306261921013726

[17] X. Lin, Y. Jiang, S. Peng, H. Chen, J. Tang, and W. Li, 'An efficient Nataf transformation based probabilistic power flow for high-dimensional correlated uncertainty sources in operation', *Int. J. Electr. Power Energy Syst.*, vol. 116, p. 105543, Mar. 2020, doi: 10.1016/j.ijepes.2019.105543.

[18] ‘Harmonic power flow in electric power systems using modified Newton Raphson method | Request PDF’, *ResearchGate*, Aug. 2025, Accessed: Sep. 28, 2025. [Online]. Available: https://www.researchgate.net/publication/286909060_Harmonic_power_flow_in_electric_power_systems_using_modified_Newton_Raphson_method

[19] A. Rashid, J. J. Mesas, and L. Sainz, ‘An Improved Harmonic Load Flow Formulation’, *Electr. Power Compon. Syst.*, vol. 47, no. 16–17, pp. 1562–1573, Oct. 2019, doi: 10.1080/15325008.2019.1689450.

[20] E. F. El-Saadany, ‘Parameters affecting harmonic propagation and distortion levels in nonlinear distribution systems’, in *IEEE Power Engineering Society Summer Meeting,* Jul. 2002, pp. 1010–1016 vol.2. doi: 10.1109/PESS.2002.1043552.

[21] F. Nasrfard-Jahromi and M. Mohammadi, ‘Probabilistic harmonic load flow using an improved kernel density estimator’, *Int. J. Electr. Power Energy Syst.*, vol. 78, pp. 292–298, Jun. 2016, doi: 10.1016/j.ijepes.2015.11.076.

[22] J. K. M. Becker, A. M. Kettner, L. Reyes-Chamorro, Z. Zou, M. Liserre, and M. Paolone, ‘Harmonic Power-Flow Study of Polyphase Grids With Converter-Interfaced Distributed Energy Resources—Part II: Model Library and Validation’, *IEEE Trans. Smart Grid*, vol. 13, no. 1, pp. 470–481, Jan. 2022, doi: 10.1109/TSG.2021.3120081.

[23] C. Cadena-Zarate, J. Caballero-Peña, and G. Osma-Pinto, ‘Simulation-based probabilistic-harmonic load flow for the study of DERs integration in a low-voltage distribution network’, *AIMS Electron. Electr. Eng.*, vol. 8, no. 1, pp. 53–70, Mar. 2024, doi: 10.3934/electreng.2024003.

[24] ‘Online Static Security Assessment Module Using Artificial Neural Networks | IEEE Journals & Magazine | IEEE Xplore’. Accessed: Feb. 26, 2025. [Online]. Available: https://ieeexplore-ieee-org.proxy.lib.strath.ac.uk/document/6547732

[25] ‘Groundwater Quality Evaluation of the Dawu Water Source Area Based on Water Quality Index (WQI): Comparison between Delphi Method and Multivariate Statistical Analysis Method’. Accessed: Feb. 26, 2025. [Online]. Available: https://www.mdpi.com/2073-4441/13/8/1127

[26] ‘Reliability evaluation method of distribution network considering new energy access’. Accessed: Feb. 26, 2025. [Online]. Available: https://www.spiedigitallibrary.org/conference-proceedings-of-spie/12302/2645799/Reliability-evaluation-method-of-distribution-network-considering-new-energy-access/10.1117/12.2645799.full

[27] C. Wu, ‘Research on the teaching quality evaluation of neural network machine learning algorithm’, vol. 12625, p. 126251Z, Jun. 2023, doi: 10.1117/12.2670410.

[28] N. He, D. Xu, and L. Huang, ‘The Application of Particle Swarm Optimization to Passive and Hybrid Active Power Filter Design’, *IEEE Trans. Ind. Electron.*, vol. 56, no. 8, pp. 2841–2851, Aug. 2009, doi: 10.1109/TIE.2009.2020739.

[29] R. W. Grubbström and O. Tang, ‘The moments and central moments of a compound distribution’, *Eur. J. Oper. Res.*, vol. 170, no. 1, pp. 106–119, Apr. 2006, doi: 10.1016/j.ejor.2004.06.012.

[30] L. Menini and A. Tornambè, *Symmetries and Semi-invariants in the Analysis of Nonlinear Systems*. Springer Science & Business Media, 2011.

[31] B. Pirouz and F. Guerriero, ‘Multi-objective stochastic optimization problem: a systematic literature review’, *Appl. Energy*, vol. 405, p. 127237, Feb. 2026, doi: 10.1016/j.apenergy.2025.127237.

[32] A. Alanazi, M. Alanazi, Z. A. Memon, A. B. Awan, and M. Deriche, ‘Availability and uncertainty-aware optimal placement of capacitors and DSTATCOM in distribution network using improved exponential distribution optimizer’, *Sci. Rep.*, vol. 15, no. 1, p. 13204, Apr. 2025, doi: 10.1038/s41598-025-87139-9.

[33] H. Liu, L. Feng, Y. Wu, J. Teng, and D. Xiao, ‘Distribution network power flow calculation based on the BPNN optimized by GA-ADAM’, *J. Eng.*, vol. 2023, no. 12, p. e12330, 2023, doi: 10.1049/tje2.12330.

[34] O. D. Montoya, A. Molina-Cabrera, and J. C. Hernández, ‘A Comparative Study on Power Flow Methods Applied to AC Distribution Networks with Single-Phase Representation’, *Electronics*, vol. 10, no. 21, Art. no. 21, Jan. 2021, doi: 10.3390/electronics10212573.

[35] S. S. Shawlin, ‘Sparse Matrix Based Power Flow Solver For Real-Time Simulation of Power System’.
[36] S. Mishra and D. Das, ‘Distribution System Load Flow Methods: A Review’, no. 2, 2008.
[37] N. Lad and A. Pachori, ‘Forward and Backward Sweep Algorithm for Distribution Power Flow Analysis and Comparison of Different Load Flow Methods’, vol. 4, 2016.
[38] M. Heidarifar, ‘LOAD FLOW AND OPTIMAL POWER FLOW IN POWER DISTRIBUTION SYSTEMS - APPLICATION OF RIEMANNIAN OPTIMIZATION AND HOLOMORPHIC EMBEDDING’.
[39] H. Tian, H. Zhao, C. Liu, J. Chen, Q. Wu, and V. Terzija, ‘A dual-driven linear modeling approach for multiple energy flow calculation in electricity–heat system’, *Appl. Energy*, vol. 314, p. 118872, May 2022, doi: 10.1016/j.apenergy.2022.118872.
[40] ‘A Comparative Study on Power Flow Methods Applied to AC Distribution Networks with Single-Phase Representation’. Accessed: Feb. 24, 2025. [Online]. Available: https://www.mdpi.com/2079-9292/10/21/2573
[41] E. N. M. Silva, A. B. Rodrigues, and M. da Guia da Silva, ‘Approximated and Iterative Power Flow Algorithms for Islanded DC Microgrids’, *Electr. Power Syst. Res.*, vol. 215, p. 108972, Feb. 2023, doi: 10.1016/j.epsr.2022.108972.
[42] ‘Electrical Power Systems Quality, Second Edition’, 2004.
[43] N. R. Watson, T. L. Scott, and S. J. J. Hirsch, ‘Implications for Distribution Networks of High Penetration of Compact Fluorescent Lamps’, *IEEE Trans. Power Deliv.*, vol. 24, no. 3, pp. 1521–1528, Jul. 2009, doi: 10.1109/TPWRD.2009.2014036.
[44] M. C. Benhabib, J. M. A. Myrzik, and J. L. Duarte, ‘Harmonic effects caused by large scale PV installations in LV network’, in *2007 9th International Conference on Electrical Power Quality and Utilisation*, Oct. 2007, pp. 1–6. doi: 10.1109/EPQU.2007.4424134.
[45] J. C. Hernández, M. J. Ortega, J. De La Cruz, and D. Vera, ‘Guidelines for the technical assessment of harmonic, flicker and unbalance emission limits for PV-distributed generation’, *Electr. Power Syst. Res.*, vol. 81, no. 7, pp. 1247–1257, Jul.

2011, doi: 10.1016/j.epsr.2011.03.012.

[46] D. Patel, R. K. Varma, R. Seethapathy, and M. Dang, ‘Impact of wind turbine generators on network resonance and harmonic distortion’, in *CCECE 2010*, May 2010, pp. 1–6. doi: 10.1109/CCECE.2010.5575109.

[47] P. Mitra, A. Ghosh, S. Ghosh, A. De, and A. Chakrabarti, ‘Analysis of harmonics in switching transients of an integrated steel plant — A case study’, in *2012 Annual IEEE India Conference (INDICON)*, Dec. 2012, pp. 643–648. doi: 10.1109/INDCON.2012.6420697.

[48] M. Ahmed and S. Mekhilef, ‘A three-phase three-level voltage source inverter with a three-phase two-level inverter as a main circuit’, in *2008 4th IET Conference on Power Electronics, Machines and Drives*, Apr. 2008, pp. 640–644. doi: 10.1049/cp:20080600.

[49] Y. Ounejjar and K. Al-Haddad, ‘Multilevel hysteresis controller of the novel seven-level packed U cells converter’, in *SPEEDAM 2010*, Jun. 2010, pp. 186–191. doi: 10.1109/SPEEDAM.2010.5542178.

[50] K.N Md Hasan, Kalle Rauma, Alvaro Luna, J. Ignacio Candela, and P.Rodriguez, ‘Harmonic Resonance Study for Wind Power Plant’, *RE&PQJ*, vol. 10, no. 11, Jan. 2024, doi: 10.24084/repqj10.746.

[51] R. Arghandeh, A. Onen, J. Jung, and R. P. Broadwater, ‘Harmonic interactions of multiple distributed energy resources in power distribution networks’, *Electr. Power Syst. Res.*, vol. 105, pp. 124–133, Dec. 2013, doi: 10.1016/j.epsr.2013.07.018.

[52] ‘A Controllably Inductive Filtering Method With Transformer-Integrated Linear Reactor for Power Quality Improvement of Shipboard Power System | IEEE Journals & Magazine | IEEE Xplore’. Accessed: Feb. 24, 2025. [Online]. Available: https://ieeexplore-ieee-org.proxy.lib.strath.ac.uk/document/7487006

[53] ‘Harmonic modelling and prediction of high speed electric train based on non-parametric confidence interval estimation method - ScienceDirect’. Accessed: Feb. 24, 2025. [Online]. Available: https://www.sciencedirect.com/science/article/pii/S0142061516303210

[54]‘A Near Field Analytical Model for EMI Reduction and Efficiency Enhancement Using an nth Harmonic Frequency Shielding Coil in a Loosely Coupled Automotive WPT System | IEEE Journals & Magazine | IEEE Xplore’. Accessed: Feb. 24, 2025. [Online]. Available: https://ieeexplore-ieee-org.proxy.lib.strath.ac.uk/document/9288921

[55]X. Ma, W. Quan, C. Si, Z. Dong, and Y. Dong, ‘Analytical solution for the mechanical responses of transversely isotropic viscoelastic multi-layered asphalt pavement subjected to moving harmonic load’, *Soil Dyn. Earthq. Eng.*, vol. 147, p. 106822, Aug. 2021, doi: 10.1016/j.soildyn.2021.106822.

[56]S. Liu, Y. Cui, Y. Wang, Y. Fu, B. Lv, and Y. Qian, ‘The effect of lubricant film on the dynamic response and signal transmission of moving load dynamic problems’, *Mech. Syst. Signal Process.*, vol. 151, p. 107435, Apr. 2021, doi: 10.1016/j.ymssp.2020.107435.

[57]R. Lu and Y. Shen, ‘Distinctive trembling features following resonance peaks at zero group velocity frequencies in harmonic analysis’, vol. 12951, p. 129510G, May 2024, doi: 10.1117/12.3010690.

[58]‘Harmonic mitigation throughout a distribution system: a distributed-generator-based solution’. Accessed: Apr. 16, 2026. [Online]. Available: https://digital-library.theiet.org/doi/epdf/10.1049/ip-gtd%3A20050086

[59]H. A. Kazem, ‘Harmonic Mitigation Techniques Applied to Power Distribution Networks’, *Adv. Power Electron.*, vol. 2013, no. 1, p. 591680, 2013, doi: 10.1155/2013/591680.

[60]H. Attia, M. El-Metwally, and O. Fahmy, ‘Harmonic Distortion Effects and Mitigation in Distribution Systems’, *J. Am. Sci.*, vol. 6.

[61]A. Abdelaziz, ‘Sources and Mitigation of Harmonics in Industrial Electrical Power Systems: State of the Art’, Jan. 2012, Accessed: Apr. 16, 2026. [Online]. Available: https://www.academia.edu/55653802/Sources_and_Mitigation_of_Harmonics_in_Industrial_Electrical_Power_Systems_State_of_the_Art

[62]F. M. Camilo, V. F. Pires, R. Castro, and M. E. Almeida, ‘The impact of harmonics

compensation ancillary services of photovoltaic microgeneration in low voltage distribution networks’, *Sustain. Cities Soc.*, vol. 39, pp. 449–458, May 2018, doi: 10.1016/j.scs.2018.03.016.

[63] K.-N. D. Malamaki, D.-A. Christofis, G. C. Kryonidis, and C. S. Demoulias, ‘Voltage Harmonic Mitigation by Distributed Renewable Energy Sources in Low-Voltage Distribution Networks: Sensitivity Analysis’, *IEEE Trans. Ind. Appl.*, vol. 60, no. 5, pp. 7656–7671, Sep. 2024, doi: 10.1109/TIA.2024.3420826.

[64] M. N. D. Dang, N. Al-Mutawaly, and J. Lepoutre, ‘From transmission to distribution networks-harmonic impacts on modern grid’, in *2015 IEEE 28th Canadian Conference on Electrical and Computer Engineering (CCECE)*, May 2015, pp. 452–459. doi: 10.1109/CCECE.2015.7129319.

[65] I. O. Adeniji, H. Shittu, K. O. Liadi, M. A. Shittu, R. Adesola, and O. Oteri, ‘Mitigating Harmonic Distortion in Urban Distribution Networks Using Hybrid AI-Based Control Models’.

[66] C. M. Ndung’u, ‘Analysis and Mitigation of Harmonics in Power Distribution Network’.

[67] D. K. Mander, S. K. Saini, and P. Student, ‘Load Flow Analysis: A Review’, vol. 5, no. 3.

[68] ‘Backward/Forward Sweep-Based Harmonic Analysis Method for Distribution Systems’, *ResearchGate*, Oct. 2024, doi: 10.1109/TPWRD.2007.899523.

[69] R. L. J. Sprangers, B. L. J. Gysen, J. J. H. Paulides, J. Waarma, and E. A. Lomonova, ‘Calculation of induced rotor current in induction motors using a slotted semi-analytical harmonic model’, in *2014 International Conference on Electrical Machines (ICEM)*, Sep. 2014, pp. 2709–2714. doi: 10.1109/ICELMACH.2014.6960571.

[70] ‘Compensated carrier PWM synchronization: a novel method to achieve self-regulation and AC unbalance compensation in AC fed converters | IEEE Journals & Magazine | IEEE Xplore’. Accessed: Feb. 24, 2025. [Online]. Available: https://ieeexplore-ieee-org.proxy.lib.strath.ac.uk/document/136252

[71] A. M. Kettner, L. Reyes-Chamorro, J. K. Maria Becker, Z. Zou, M. Liserre, and M.

Paolone, ‘Harmonic Power-Flow Study of Polyphase Grids With Converter-Interfaced Distributed Energy Resources—Part I: Modeling Framework and Algorithm’, *IEEE Trans. Smart Grid*, vol. 13, no. 1, pp. 458–469, Jan. 2022, doi: 10.1109/TSG.2021.3120108.

[72] P. C. Gupta and K. Yamada, ‘Adaptive Short-Term Forecasting of Hourly Loads Using Weather Information’, *IEEE Trans. Power Appar. Syst.*, vol. PAS-91, no. 5, pp. 2085–2094, Sep. 1972, doi: 10.1109/TPAS.1972.293541.

[73] H. Modir and R. A. Schlueter, ‘A dynamic state estimator for power system dynamic security assessment’, *Automatica*, vol. 20, no. 2, pp. 189–199, Mar. 1984, doi: 10.1016/0005-1098(84)90024-4.

[74] D. Zhai, A. M. Breipohl, F. N. Lee, and R. Adapa, ‘The effect of load uncertainty on unit commitment risk’, *IEEE Trans. Power Syst.*, vol. 9, no. 1, pp. 510–517, Feb. 1994, doi: 10.1109/59.317572.

[75] ‘Cost of Reliability Analysis Based on Stochastic Unit Commitment | IEEE Journals & Magazine | IEEE Xplore’. Accessed: Feb. 25, 2025. [Online]. Available: https://ieeexplore-ieee-org.proxy.lib.strath.ac.uk/document/4511485/

[76] ‘Integration of Plug-in Hybrid Electric Vehicles into Residential Distribution Grid Based on Two-Layer Intelligent Optimization | IEEE Journals & Magazine | IEEE Xplore’. Accessed: Feb. 25, 2025. [Online]. Available: https://ieeexplore-ieee-org.proxy.lib.strath.ac.uk/document/6839090

[77] S. Zhong, R. Broadwater, and S. Steffel, ‘Medium term stochastic load model for transformer and feeder from AMI load data spectral analysis’, *Int. J. Electr. Power Energy Syst.*, vol. 91, pp. 1–9, Oct. 2017, doi: 10.1016/j.ijepes.2017.02.010.

[78] ‘Stochastic modeling of traction load of electrified railway’. Accessed: Feb. 25, 2025. [Online]. Available: https://www.spiedigitallibrary.org/conference-proceedings-of-spie/12249/122492W/Stochastic-modeling-of-traction-load-of-electrified-railway/10.1117/12.2637040.full

[79] K. Liu, Q. Kong, B. Sun, Y. Xue, X. Chen, and B. Zhang, ‘A novel power balance model for power systems considering two-sided stochastic source-load’, in *2nd*

International Conference on Applied Mathematics, Modelling, and Intelligent Computing (CAMMIC 2022), SPIE, May 2022, pp. 940–945. doi: 10.1117/12.2640020.
[80] 'Optimal power system dispatch model considering carbon emission accounting and source-load uncertainty', in *ResearchGate*, Oct. 2024. doi: 10.1117/12.2689696.
[81] X. He, D. H. K. Tsang, and Y. Chen, 'Long-Term Carbon-Efficient Planning for Geographically Shiftable Resources: A Monte Carlo Tree Search Approach', Aug. 09, 2024, *arXiv*: arXiv:2312.06144. doi: 10.48550/arXiv.2312.06144.
[82] E. Kipchirchir, J. Liebeton, and D. Söffker, 'A hybrid prognosis approach for robust lifetime control of commercial wind turbines', Apr. 29, 2024, *arXiv*: arXiv:2404.18593. doi: 10.48550/arXiv.2404.18593.
[83] '[2411.02159] Distributed Stochastic ACOPF Based on Consensus ADMM and Scenario Reduction'. Accessed: Feb. 25, 2025. [Online]. Available: https://arxiv.org/abs/2411.02159
[84] V. S. Pappala, I. Erlich, K. Rohrig, and J. Dobschinski, 'A Stochastic Model for the Optimal Operation of a Wind-Thermal Power System', *IEEE Trans. Power Syst.*, vol. 24, no. 2, pp. 940–950, May 2009, doi: 10.1109/TPWRS.2009.2016504.
[85] Q. Wang, Y. Guan, and J. Wang, 'A Chance-Constrained Two-Stage Stochastic Program for Unit Commitment With Uncertain Wind Power Output', *IEEE Trans. Power Syst.*, vol. 27, no. 1, pp. 206–215, Feb. 2012, doi: 10.1109/TPWRS.2011.2159522.
[86] 'Combined heat and power dispatch with wind power: A stochastic model and solutions | IEEE Conference Publication | IEEE Xplore'. Accessed: Feb. 25, 2025. [Online]. Available: https://ieeexplore-ieee-org.proxy.lib.strath.ac.uk/document/5589287
[87] 'ARIMA-Based Time Series Model of Stochastic Wind Power Generation | IEEE Journals & Magazine | IEEE Xplore'. Accessed: Feb. 25, 2025. [Online]. Available: https://ieeexplore-ieee-org.proxy.lib.strath.ac.uk/abstract/document/5340622
[88] 'Assessment of Impacts of PHEV Charging Patterns on Wind-Thermal Scheduling by Stochastic Unit Commitment | IEEE Journals & Magazine | IEEE Xplore'. Accessed:

Feb. 25, 2025. [Online]. Available: https://ieeexplore-ieee-org.proxy.lib.strath.ac.uk/document/6182731
[89] 'Stochastic predictive control of battery energy storage for wind farm dispatching: Using probabilistic wind power forecasts - ScienceDirect'. Accessed: Feb. 25, 2025. [Online]. Available: https://www.sciencedirect.com/science/article/pii/S0960148115000919
[90] 'Optimal reactive power dispatch: a review, and a new stochastic voltage stability constrained multi-objective model at the presence of uncertain wind power generation | IET Generation, Transmission & Distribution'. Accessed: Feb. 25, 2025. [Online]. Available: https://digital-library.theiet.org/doi/10.1049/iet-gtd.2016.1545
[91] 'Fuzzy Stochastic Unit Commitment Model with Wind Power and Demand Response under Conditional Value-At-Risk Assessment'. Accessed: Feb. 25, 2025. [Online]. Available: https://www.mdpi.com/1996-1073/11/2/341
[92] L. Yao, L. He, X. Chen, A. Xiao, and H. Wang, 'Optimal day-ahead coordination on wind-pumped-hydro system by using multiobjective multistage model', *Int. J. Energy Res.*, vol. 44, no. 8, pp. 6843–6859, 2020, doi: 10.1002/er.5432.
[93] 'Long-term offshore wind power prediction using spatiotemporal kriging: A case study in China's Guangdong Province - Hongda Hu, Zhiyong Hu, Kaiwen Zhong, Jianhui Xu, Pinghao Wu, Yi Zhao, Feifei Zhang, 2020'. Accessed: Feb. 25, 2025. [Online]. Available: https://journals.sagepub.com/doi/full/10.1177/0144598719889368
[94] H. Li, Y. Qiao, Z. Lu, B. Zhang, and F. Teng, 'Frequency-Constrained Stochastic Planning Towards a High Renewable Target Considering Frequency Response Support From Wind Power', *IEEE Trans. Power Syst.*, vol. 36, no. 5, pp. 4632–4644, Sep. 2021, doi: 10.1109/TPWRS.2021.3066991.
[95] '(PDF) Estimating Wind Farm Transformers Rating through Lifetime Characterization Based on Stochastic Modeling of Wind Power'. Accessed: Feb. 25, 2025. [Online]. Available: https://www.researchgate.net/publication/349942323_Estimating_Wind_Farm_Transformers_Rating_through_Lifetime_Characterization_Based_on_Stochastic_Modeling_

of_Wind_Power
[96]‘Estimating energy storage size for Nuclear-Renewable hybrid energy systems using data-driven stochastic emulators - ScienceDirect’. Accessed: Feb. 25, 2025. [Online]. Available: https://www.sciencedirect.com/science/article/pii/S2352152X21005144
[97]‘Distributed Optimal Load Frequency Control with Stochastic Wind Power Generation | IEEE Conference Publication | IEEE Xplore’. Accessed: Feb. 25, 2025. [Online]. Available: https://ieeexplore-ieee-org.proxy.lib.strath.ac.uk/document/9655085
[98]‘Stochastic modeling of rechargeable battery life in a photovoltaic power system | IEEE Conference Publication | IEEE Xplore’. Accessed: Feb. 25, 2025. [Online]. Available: https://ieeexplore-ieee-org.proxy.lib.strath.ac.uk/document/870901
[99]‘Quantifying self-consumption of on-site photovoltaic power generation in households with electric vehicle home charging - ScienceDirect’. Accessed: Feb. 25, 2025. [Online]. Available: https://www.sciencedirect.com/science/article/pii/S0038092X13003253
[100] ‘A stochastic approach to optimum placement of photovoltaic generation in distribution feeder | IEEE Conference Publication | IEEE Xplore’. Accessed: Feb. 25, 2025. [Online]. Available: https://ieeexplore-ieee-org.proxy.lib.strath.ac.uk/document/7462847
[101] R. Hemmati and H. Saboori, ‘Stochastic optimal battery storage sizing and scheduling in home energy management systems equipped with solar photovoltaic panels’, *Energy Build.*, vol. 152, pp. 290–300, Oct. 2017, doi: 10.1016/j.enbuild.2017.07.043.
[102] ‘Multi-objective stochastic scheduling optimization model for connecting a virtual power plant to wind-photovoltaic-electric vehicles considering uncertainties and demand response - ScienceDirect’. Accessed: Feb. 25, 2025. [Online]. Available: https://www.sciencedirect.com/science/article/pii/S0196890416308718
[103] ‘Optimal stochastic management of renewable MG (micro-grids) considering

electro-thermal model of PV (photovoltaic) - ScienceDirect'. Accessed: Feb. 25, 2025. [Online]. Available: https://www.sciencedirect.com/science/article/pii/S0360544215017673

[104] 'Novel stochastic methods to predict short-term solar radiation and photovoltaic power - ScienceDirect'. Accessed: Feb. 25, 2025. [Online]. Available: https://www.sciencedirect.com/science/article/pii/S0960148119307463

[105] 'Very Short-Term Photovoltaic Power Forecasting Considering the Stochastic Factors | IEEE Conference Publication | IEEE Xplore'. Accessed: Feb. 25, 2025. [Online]. Available: https://ieeexplore-ieee-org.proxy.lib.strath.ac.uk/document/8692258

[106] 'Incorporating Concentrating Solar Power into High Renewables Penetrated Power System: A Chance-Constrained Stochastic Unit Commitment Analysis'. Accessed: Feb. 25, 2025. [Online]. Available: https://www.mdpi.com/2076-3417/9/11/2340

[107] 'Optimal stochastic scheduling of hydropower-based compensation for combined wind and photovoltaic power outputs - ScienceDirect'. Accessed: Feb. 25, 2025. [Online]. Available: https://www.sciencedirect.com/science/article/pii/S0306261920310138

[108] D. Dwivedi, P. K. Yemula, and M. Pal, 'Detection of Malfunctioning Modules in Photovoltaic Power Plants using Unsupervised Feature Clustering Segmentation Algorithm', Dec. 30, 2022, *arXiv*: arXiv:2212.14653. doi: 10.48550/arXiv.2212.14653.

[109] L. Ceferino, N. Lin, and D. Xi, 'Stochastic modeling of solar irradiance during hurricanes', *Stoch. Environ. Res. Risk Assess.*, vol. 36, no. 9, pp. 2681–2693, Sep. 2022, doi: 10.1007/s00477-021-02154-2.

[110] 'An alternative optimal strategy for stochastic model predictive control of a residential battery energy management system with solar photovoltaic - ScienceDirect'. Accessed: Feb. 25, 2025. [Online]. Available: https://www.sciencedirect.com/science/article/pii/S0306261920316767

[111] 'Economic Control for a Residential Photovoltaic-Battery System by

Combining Stochastic Model Predictive Control and Improved Correction Strategy | J. Energy Resour. Technol. | ASME Digital Collection’. Accessed: Feb. 25, 2025. [Online]. Available:
https://asmedigitalcollection.asme.org/energyresources/article/144/5/054501/1114463/Economic-Control-for-a-Residential-Photovoltaic

[112] A. Cheema, M. F. Shaaban, and M. H. Ismail, ‘A novel stochastic dynamic modeling for photovoltaic systems considering dust and cleaning’, *Appl. Energy*, vol. 300, p. 117399, Oct. 2021, doi: 10.1016/j.apenergy.2021.117399.

[113] N. Liao, Z. Hu, V. Mrzljak, and S. Arabi Nowdeh, ‘Stochastic Techno-Economic Optimization of Hybrid Energy System with Photovoltaic, Wind, and Hydrokinetic Resources Integrated with Electric and Thermal Storage Using Improved Fire Hawk Optimization’, *Sustainability*, vol. 16, no. 16, Art. no. 16, Jan. 2024, doi: 10.3390/su16166723.

[114] V. Kumar, S. Sharma, V. Kumar, S. Sharma, and A. Dev, ‘Optimal voltage and frequency control strategy for renewable-dominated deregulated power network’, *Sci. Rep.*, vol. 15, no. 1, p. 398, Jan. 2025, doi: 10.1038/s41598-024-84549-z.

[115] A. E. Feijoo, J. Cidras, and J. L. G. Dornelas, ‘Wind speed simulation in wind farms for steady-state security assessment of electrical power systems’, *IEEE Trans. Energy Convers.*, vol. 14, no. 4, pp. 1582–1588, Dec. 1999, doi: 10.1109/60.815109.

[116] ‘Expected power loss calculation including protection failures using importance sampling and SOM | IEEE Conference Publication | IEEE Xplore’. Accessed: Feb. 25, 2025. [Online]. Available: https://ieeexplore-ieee-org.proxy.lib.strath.ac.uk/document/1372787

[117] ‘Modeling the repair process of a power distribution system | IEEE Conference Publication | IEEE Xplore’. Accessed: Feb. 25, 2025. [Online]. Available: https://ieeexplore-ieee-org.proxy.lib.strath.ac.uk/document/4641852

[118] ‘A Chance Constrained Transmission Network Expansion Planning Method With Consideration of Load and Wind Farm Uncertainties | IEEE Journals & Magazine | IEEE Xplore’. Accessed: Feb. 25, 2025. [Online]. Available: https://ieeexplore-ieee-

org.proxy.lib.strath.ac.uk/document/4909013
[119] N. Zhou, Z. Huang, L. Dosiek, D. Trudnowski, and J. W. Pierre, ‘Electromechanical mode shape estimation based on transfer function identification using PMU measurements’, in *2009 IEEE Power & Energy Society General Meeting*, Jul. 2009, pp. 1–7. doi: 10.1109/PES.2009.5275924.
[120] ‘Probabilistic Analysis of Small-Signal Stability of Large-Scale Power Systems as Affected by Penetration of Wind Generation | IEEE Journals & Magazine | IEEE Xplore’. Accessed: Feb. 25, 2025. [Online]. Available: https://ieeexplore-ieee-org.proxy.lib.strath.ac.uk/document/6084851
[121] ‘An Affine Arithmetic-Based Method for Voltage Stability Assessment of Power Systems With Intermittent Generation Sources | IEEE Journals & Magazine | IEEE Xplore’. Accessed: Feb. 25, 2025. [Online]. Available: https://ieeexplore-ieee-org.proxy.lib.strath.ac.uk/document/6583295
[122] ‘Reliability Modeling for Metallized Film Capacitors Based on Time-Varying Stress Mission Profile and Aging of ESR | IEEE Journals & Magazine | IEEE Xplore’. Accessed: Feb. 25, 2025. [Online]. Available: https://ieeexplore-ieee-org.proxy.lib.strath.ac.uk/abstract/document/9115000
[123] ‘Monte-Carlo optical model coupled with Inverse Adding-Doubling for Building Integrated Photovoltaic smart window design and characterisation - ScienceDirect’. Accessed: Feb. 25, 2025. [Online]. Available: https://www.sciencedirect.com/science/article/pii/S0927024821000167
[124] ‘Gaussian Process Learning-Based Probabilistic Optimal Power Flow | IEEE Journals & Magazine | IEEE Xplore’. Accessed: Feb. 25, 2025. [Online]. Available: https://ieeexplore-ieee-org.proxy.lib.strath.ac.uk/document/9226481
[125] ‘Reliability of power systems with climate change impacts on hierarchical levels of PV systems - ScienceDirect’. Accessed: Feb. 25, 2025. [Online]. Available: https://www.sciencedirect.com/science/article/pii/S0378779620306301
[126] ‘An Application of State Estimation to Short-Term Load Forecasting, Part I: Forecasting Modeling | IEEE Journals & Magazine | IEEE Xplore’. Accessed: Feb. 25,

2025. [Online]. Available: https://ieeexplore-ieee-org.proxy.lib.strath.ac.uk/document/4074247

[127] T. Hiyama and K. Kitabayashi, 'Neural network based estimation of maximum power generation from PV module using environmental information', *IEEE Trans. Energy Convers.*, vol. 12, no. 3, pp. 241–247, Sep. 1997, doi: 10.1109/60.629709.

[128] 'Prony analysis and power system stability-some recent theoretical and applications research | IEEE Conference Publication | IEEE Xplore'. Accessed: Feb. 25, 2025. [Online]. Available: https://ieeexplore-ieee-org.proxy.lib.strath.ac.uk/document/868827

[129] 'An Advanced Statistical Method for Wind Power Forecasting | IEEE Journals & Magazine | IEEE Xplore'. Accessed: Feb. 25, 2025. [Online]. Available: https://ieeexplore-ieee-org.proxy.lib.strath.ac.uk/document/4077140

[130] 'A Proposal for On-Line Detection and Classification of Voltage Events in Power Systems | IEEE Journals & Magazine | IEEE Xplore'. Accessed: Feb. 25, 2025. [Online]. Available: https://ieeexplore-ieee-org.proxy.lib.strath.ac.uk/document/4483702

[131] 'Electromechanical mode shape estimation based on transfer function identification using PMU measurements | IEEE Conference Publication | IEEE Xplore'. Accessed: Feb. 25, 2025. [Online]. Available: https://ieeexplore-ieee-org.proxy.lib.strath.ac.uk/document/5275924

[132] G. Valverde and V. Terzija, 'Unscented Kalman filter for power system dynamic state estimation', *IET Gener. Transm. Distrib.*, vol. 5, no. 1, pp. 29–37, Jan. 2011, doi: 10.1049/iet-gtd.2010.0210.

[133] 'An optimized mean variance estimation method for uncertainty quantification of wind power forecasts - ScienceDirect'. Accessed: Feb. 25, 2025. [Online]. Available: https://www.sciencedirect.com/science/article/pii/S0142061514001719

[134] 'SVM-based Channel Estimation and Data Detection for Massive MIMO Systems with One-Bit ADCs | IEEE Conference Publication | IEEE Xplore'. Accessed: Feb. 25, 2025. [Online]. Available: https://ieeexplore-ieee-

org.proxy.lib.strath.ac.uk/document/9148630

[135] R. L. G. Cavalcante and S. Stańczak, ‘Hybrid data and model driven algorithms for angular power spectrum estimation’, in *GLOBECOM 2020 - 2020 IEEE Global Communications Conference*, Dec. 2020, pp. 1–6. doi: 10.1109/GLOBECOM42002.2020.9348163.

[136] B. R. Prusty and D. Jena, ‘A critical review on probabilistic load flow studies in uncertainty constrained power systems with photovoltaic generation and a new approach’, *Renew. Sustain. Energy Rev.*, vol. 69, pp. 1286–1302, Mar. 2017, doi: 10.1016/j.rser.2016.12.044.

[137] ‘Assessing Voltage Stability in Distribution Networks: A Methodology Considering Correlation among Stochastic Variables’. Accessed: Feb. 25, 2025. [Online]. Available: https://www.mdpi.com/2076-3417/14/15/6455

[138] J. Xiao, Y. Li, X. Qiao, Y. Tan, Y. Cao, and L. Jiang, ‘Enhancing Hosting Capacity of Uncertain and Correlated Wind Power in Distribution Network With ANM Strategies’, *IEEE Access*, vol. 8, pp. 189115–189128, 2020, doi: 10.1109/ACCESS.2020.3030705.

[139] ‘Distributed generation hosting capacity in electric distribution network in the presence of correlated uncertainties - Solat - 2021 - IET Generation, Transmission & Distribution - Wiley Online Library’. Accessed: Feb. 25, 2025. [Online]. Available: https://ietresearch.onlinelibrary.wiley.com/doi/full/10.1049/gtd2.12062

[140] S. Solat, F. Aminifar, and H. Shayanfar, ‘Distributed generation hosting capacity in electric distribution network in the presence of correlated uncertainties’, *IET Gener. Transm. Distrib.*, vol. 15, no. 5, pp. 836–848, 2021, doi: 10.1049/gtd2.12062.

[141] M. Shaik, D. N. Gaonkar, R. S. S. Nuvvula, S. M. Muyeen, Sk. A. Shezan, and G. M. Shafiullah, ‘Nataf-KernelDensity-Spline-based point estimate method for handling wind power correlation in probabilistic load flow’, *Expert Syst. Appl.*, vol. 245, p. 123059, Jul. 2024, doi: 10.1016/j.eswa.2023.123059.

[142] P. F. Austnes, C. García-Pareja, F. Nobile, and M. Paolone, ‘Probabilistic Load Forecasting of distribution power systems based on empirical copulas’, *Sustain. Energy*

Grids Netw., vol. 42, p. 101708, Jun. 2025, doi: 10.1016/j.segan.2025.101708.

[143] 'New risk analysis considering spatial correlations among connected PVs for bidirectional distribution feeders - Al-Saadi - 2020 - International Transactions on Electrical Energy Systems - Wiley Online Library'. Accessed: Feb. 25, 2025. [Online]. Available: https://onlinelibrary.wiley.com/doi/full/10.1002/2050-7038.12319

[144] 'Stochastic multi-stage joint expansion planning of transmission system and energy hubs in the presence of correlated uncertainties - Allahvirdizadeh - 2023 - IET Renewable Power Generation - Wiley Online Library'. Accessed: Feb. 25, 2025. [Online]. Available: https://ietresearch.onlinelibrary.wiley.com/doi/full/10.1049/rpg2.12762

[145] 'WES - Correlations of power output fluctuations in an offshore wind farm using high-resolution SCADA data'. Accessed: Feb. 25, 2025. [Online]. Available: https://wes.copernicus.org/articles/6/997/2021/

[146] N. H. Afgan, M. G. Carvalho, and M. Jovanovic, 'Biomass-fired power plant: the sustainability option', *Int. J. Sustain. Energy*, vol. 26, no. 4, pp. 179–193, Dec. 2007, doi: 10.1080/14786450701550434.

[147] '(PDF) The Extension Evaluation Theory Based on Wind Power Project Quality', in *ResearchGate*, Nov. 2024. doi: 10.2991/mce-14.2014.127.

[148] Y. Song and Y. Jiao, 'Fuzzy comprehensive evaluation of the factors affecting the data quality of power system', presented at the 2016 4th International Conference on Mechanical Materials and Manufacturing Engineering, Atlantis Press, Oct. 2016, pp. 359–362. doi: 10.2991/mmme-16.2016.81.

[149] 'Notice of Retraction: Application of weighted Principal Component Analysis in comprehensive evaluation for power quality | IEEE Conference Publication | IEEE Xplore'. Accessed: Feb. 26, 2025. [Online]. Available: https://ieeexplore-ieee-org.proxy.lib.strath.ac.uk/document/6135114

[150] 'Evaluation method of economic benefit of power grid construction based on ambiguity entropy', in *ResearchGate*, doi: 10.1117/12.2659670.

[151] M. Huang, S. Guo, W. Song, and Z. Liao, 'An intelligent assessment method

of power information intrusion tolerance based on machine learning', in *Third International Conference on Computer Communication and Network Security (CCNS 2022)*, C. Zhao and H. Imane, Eds, Hohhot, China: SPIE, Oct. 2022, p. 41. doi: 10.1117/12.2659586.

[152] 'Status comprehensive evaluation of power grid low voltage distribution district'. Accessed: Feb. 26, 2025. [Online]. Available: https://www.spiedigitallibrary.org/conference-proceedings-of-spie/12302/123020U/Status-comprehensive-evaluation-of-power-grid-low-voltage-distribution-district/10.1117/12.2645563.full

[153] 'Construction of power system evaluation system oriented to common prosperity based on entropy weight method'. Accessed: Feb. 26, 2025. [Online]. Available: https://www.spiedigitallibrary.org/conference-proceedings-of-spie/12979/1297962/Construction-of-power-system-evaluation-system-oriented-to-common-prosperity/10.1117/12.3015519.full

[154] C. F. M. Almeida and N. Kagan, 'Harmonic coupled norton equivalent model for modeling harmonic-producing loads', in *Proceedings of 14th International Conference on Harmonics and Quality of Power - ICHQP 2010*, Sep. 2010, pp. 1–9. doi: 10.1109/ICHQP.2010.5625491.

[155] H. Akagi, 'Active harmonic filters', *Proc. IEEE*, vol. 93, no. 12, pp. 2128–2141, 2005, doi: 10.1109/JPROC.2005.859603.

[156] J. Miret Tomàs, M. Castilla Fernández, J. Matas Alcalá, J. M. Guerrero Zapata, and J. C. Vásquez Quintero, 'Selective harmonic-compensation control for single-phase active power filter with high harmonic rejection', *IEEE Trans. Ind. Electron.*, vol. 56, no. 8, pp. 3117–3127, Aug. 2009.

[157] P. Salmerón Revuelta, S. Pérez Litrán, and J. Prieto Thomas, 'Introduction to Power Quality from Power Conditioning', in *Active Power Line Conditioners*, Elsevier, 2016, pp. 1–21. doi: 10.1016/B978-0-12-803216-9.00001-8.

[158] 'Series LC filter for harmonic compensation of AC drives - Oak Ridge National Laboratory'. Accessed: Apr. 02, 2025. [Online]. Available:

https://impact.ornl.gov/en/publications/series-lc-filter-for-harmonic-compensation-of-ac-drives
[159] 'Experience with an inverter-based dynamic voltage restorer'. Accessed: Apr. 02, 2025. [Online]. Available: https://ieeexplore.ieee.org/abstract/document/772390
[160] F. Z. Peng, H. Akagi, and A. Nabae, 'Compensation characteristics of the combined system of shunt passive and series active filters', *IEEE Trans. Ind. Appl.*, vol. 29, no. 1, pp. 144–152, Jan. 1993, doi: 10.1109/28.195900.
[161] 'Improvement of The Power Quality With Series Active Filter According To The IEC 61000-2006 | PDF | Power Inverter | Telecommunications Engineering'. Accessed: Apr. 02, 2025. [Online]. Available: https://www.scribd.com/document/316987852/Improvement-of-the-Power-Quality-With-Series-Active-Filter-According-to-the-IEC-61000-2006
[162] 'A practical approach to harmonic compensation in power systems-series connection of passive and active filters', in *SciSpace - Paper*, IEEE, Oct. 1990, pp. 1020–1025. doi: 10.1109/28.108451.
[163] L. F. C. Monteiro, M. Aredes, and J. A. Moor Neto, 'A control strategy for unified power quality conditioner', *2003 IEEE Int. Symp. Ind. Electron. Cat No03TH8692*, vol. 1, pp. 391–396, 2003, doi: 10.1109/ISIE.2003.1267280.
[164] 'A new optimized SVPWM technique control for autonomous parallel active filter | IEEE Conference Publication | IEEE Xplore'. Accessed: Feb. 28, 2025. [Online]. Available: https://ieeexplore-ieee-org.proxy.lib.strath.ac.uk/abstract/document/1409338
[165] A. V. Vyngra, S. G. Chernyi, and S. S. Sokolov, 'Development an Active Filter Control Software with the Addition of Algorithms for Working at Perturbations', in *2022 Conference of Russian Young Researchers in Electrical and Electronic Engineering (ElConRus)*, Jan. 2022, pp. 497–499. doi: 10.1109/ElConRus54750.2022.9755540.
[166] S. Rahmani, K. Al-Haddad, and H. Y. Kanaan, 'Average Modeling and Hybrid Control of a Three-Phase Series Hybrid Power Filter', in *2006 IEEE International*

Symposium on Industrial Electronics, Jul. 2006, pp. 919–924. doi: 10.1109/ISIE.2006.295758.

[167] 'Full article: A novel shunt hybrid active power filter based on magnetic flux compensation'. Accessed: Feb. 28, 2025. [Online]. Available: https://www.tandfonline.com/doi/full/10.1080/00207210902977814

[168] Z. Chen, Y. Luo, and M. Chen, 'Control and Performance of a Cascaded Shunt Active Power Filter for Aircraft Electric Power System', *IEEE Trans. Ind. Electron.*, vol. 59, no. 9, pp. 3614–3623, Sep. 2012, doi: 10.1109/TIE.2011.2166231.

[169] B. Ge *et al.*, 'An Active Filter Method to Eliminate DC-Side Low-Frequency Power for a Single-Phase Quasi-Z-Source Inverter', *IEEE Trans. Ind. Electron.*, vol. 63, no. 8, pp. 4838–4848, Aug. 2016, doi: 10.1109/TIE.2016.2551680.

[170] 'Full article: Type-2 Fuzzy Logic Controlled Three-level Shunt Active Power Filter for Power Quality Improvement'. Accessed: Feb. 28, 2025. [Online]. Available: https://www.tandfonline.com/doi/full/10.1080/15325008.2016.1138158

[171] 'Improvement of Power Quality Using a Robust Hybrid Series Active Power Filter | Request PDF'. Accessed: Feb. 28, 2025. [Online]. Available: https://www.researchgate.net/publication/304663025_Improvement_of_Power_Quality_Using_a_Robust_Hybrid_Series_Active_Power_Filter

[172] '(PDF) A Decoupling Control Method for Shunt Hybrid Active Power Filter Based on Generalized Inverse System', *ResearchGate*, Dec. 2024, doi: 10.1155/2017/5232507.

[173] Y. Chu, X. Luo, S. Hou, and J. Fei, 'Robust hybrid intelligent control using probabilistic feature for active power filter', *Control Eng. Pract.*, vol. 141, p. 105712, Dec. 2023, doi: 10.1016/j.conengprac.2023.105712.

[174] L. Wang, C.-S. Lam, and M.-C. Wong, 'Modeling and Parameter Design of Thyristor-Controlled LC-Coupled Hybrid Active Power Filter (TCLC-HAPF) for Unbalanced Compensation', *IEEE Trans. Ind. Electron.*, vol. 64, no. 3, pp. 1827–1840, Mar. 2017, doi: 10.1109/TIE.2016.2625239.

[175] A. Mallik, W. Ding, and A. Khaligh, 'A Comprehensive Design Approach to

an EMI Filter for a 6-kW Three-Phase Boost Power Factor Correction Rectifier in Avionics Vehicular Systems', *IEEE Trans. Veh. Technol.*, vol. 66, no. 4, pp. 2942–2951, Apr. 2017, doi: 10.1109/TVT.2016.2590462.

[176] K. Mahesh, P. Nallagownden, and I. Elamvazuthi, 'Advanced Pareto Front Non-Dominated Sorting Multi-Objective Particle Swarm Optimization for Optimal Placement and Sizing of Distributed Generation', *Energies*, vol. 9, no. 12, Art. no. 12, Dec. 2016, doi: 10.3390/en9120982.

[177] J. Silva Lomba and M. I. Fraga Alves, 'Moments', in *Encyclopedia of Mathematical Geosciences*, B. S. Daya Sagar, Q. Cheng, J. McKinley, and F. Agterberg, Eds, in Encyclopedia of Earth Sciences Series. , Cham: Springer International Publishing, 2021, pp. 1–8. doi: 10.1007/978-3-030-26050-7_454-1.

[178] R. Cleroux and D. J. McConalogue, 'A Numerical Algorithm for Recursively-Defined Convolution Integrals Involving Distribution Functions', *Manag. Sci.*, vol. 22, no. 10, pp. 1138–1146, Jun. 1976, doi: 10.1287/mnsc.22.10.1138.

[179] V. P. Leonov and A. N. Shiryaev, 'On a Method of Calculation of Semi-Invariants', *Theory Probab. Its Appl.*, vol. 4, no. 3, pp. 319–329, Jan. 1959, doi: 10.1137/1104031.

[180] C.-L. Su, 'Probabilistic load-flow computation using point estimate method', *IEEE Trans. Power Syst.*, vol. 20, no. 4, pp. 1843–1851, Nov. 2005, doi: 10.1109/TPWRS.2005.857921.

[181] J. Usaola, 'Probabilistic load flow with wind production uncertainty using cumulants and Cornish–Fisher expansion', *Int. J. Electr. Power Energy Syst.*, vol. 31, no. 9, pp. 474–481, Oct. 2009, doi: 10.1016/j.ijepes.2009.02.003.

[182] E. A. Cornish and R. A. Fisher, 'Moments and Cumulants in the Specification of Distributions', *Rev. Inst. Int. Stat. Rev. Int. Stat. Inst.*, vol. 5, no. 4, p. 307, Jan. 1938, doi: 10.2307/1400905.

[183] N. L. Johnson, S. Kotz, and N. Balakrishnan, 'Continuous univariate distributions. 2', 2. ed., New York: Wiley, 1995.

[184] Alexander, 'Weibull Distribution and Weibull Analysis', Statistics How To.

Accessed: Mar. 29, 2025. [Online]. Available: https://www.statisticshowto.com/weibull-distribution/

[185] C. G. Justus and A. Mikhail, 'Height variation of wind speed and wind distributions statistics', *Geophys. Res. Lett.*, vol. 3, no. 5, pp. 261–264, 1976, doi: 10.1029/GL003i005p00261.

[186] H. P. Hong, 'An efficient point estimate method for probabilistic analysis', *Reliab. Eng. Syst. Saf.*, vol. 59, no. 3, pp. 261–267, Mar. 1998, doi: 10.1016/S0951-8320(97)00071-9.

[187] Juan. M. Morales and Juan. Perez-Ruiz, 'Point Estimate Schemes to Solve the Probabilistic Power Flow', *IEEE Trans. Power Syst.*, vol. 22, no. 4, pp. 1594–1601, Nov. 2007, doi: 10.1109/TPWRS.2007.907515.

[188] 'Point estimates for probability moments | PNAS'. Accessed: Mar. 29, 2025. [Online]. Available: https://www.pnas.org/doi/10.1073/pnas.72.10.3812

[189] S. Song, C. Han, S. Jung, M. Yoon, and G. Jang, 'Probabilistic Power Flow Analysis of Bulk Power System for Practical Grid Planning Application', *IEEE Access*, vol. 7, pp. 45494–45503, 2019, doi: 10.1109/ACCESS.2019.2909537.

[190] M. Aien, M. Rashidinejad, and M. F. Firuz-Abad, 'Probabilistic optimal power flow in correlated hybrid wind-PV power systems: A review and a new approach', *Renew. Sustain. Energy Rev.*, vol. 41, pp. 1437–1446, Jan. 2015, doi: 10.1016/j.rser.2014.09.012.

[191] 'Probabilistic load flow computation of a power system containing wind farms using the method of combined cumulants and Gram–Charlier expansion'. Accessed: Mar. 29, 2025. [Online]. Available: https://digital-library.theiet.org/doi/epdf/10.1049/iet-rpg.2010.0218

[192] Juan. M. Morales and Juan. Perez-Ruiz, 'Point Estimate Schemes to Solve the Probabilistic Power Flow', *IEEE Trans. Power Syst.*, vol. 22, no. 4, pp. 1594–1601, Nov. 2007, doi: 10.1109/TPWRS.2007.907515.

[193] C.-L. Su, 'Probabilistic load-flow computation using point estimate method', *IEEE Trans. Power Syst.*, vol. 20, no. 4, pp. 1843–1851, Nov. 2005, doi:

10.1109/TPWRS.2005.857921.

[194] ‘Markov Chain Monte Carlo’, in *Simulation and the Monte Carlo Method*, John Wiley & Sons, Ltd, 2016, pp. 187–220. doi: 10.1002/9781118631980.ch6.

[195] R. E. Caflisch, ‘Monte Carlo and quasi-Monte Carlo methods’, *Acta Numer.*, vol. 7, pp. 1–49, Jan. 1998, doi: 10.1017/S0962492900002804.

[196] A. m. L. Da Silva, V. L. Arienti, and R. N. Allan, ‘Probabilistic Load Flow Considering Dependence Between Input Nodal Powers’, *IEEE Trans. Power Appar. Syst.*, vol. PAS-103, no. 6, pp. 1524–1530, Jun. 1984, doi: 10.1109/TPAS.1984.318493.

[197] P. Zhang and S. T. Lee, ‘Probabilistic load flow computation using the method of combined cumulants and Gram-Charlier expansion’, *IEEE Trans. Power Syst.*, vol. 19, no. 1, pp. 676–682, Feb. 2004, doi: 10.1109/TPWRS.2003.818743.

[198] Department of Electrical Engineering, Kermanshah Branch, Islamic Azad University, Kermanshah, Iran *et al.*, ‘Comparison of solving probabilistic optimal power flow methods in the presence of wind and solar sources’, *Mehran Univ. Res. J. Eng. Technol.*, vol. 41, no. 3, pp. 54–71, Jul. 2022, doi: 10.22581/muet1982.2203.06.

[199] B. Borkowska, ‘Probabilistic Load Flow’, *IEEE Trans. Power Appar. Syst.*, vol. PAS-93, no. 3, pp. 752–759, May 1974, doi: 10.1109/TPAS.1974.293973.

[200] B. Stott, ‘Review of load-flow calculation methods’, *Proc. IEEE*, vol. 62, no. 7, pp. 916–929, Jul. 1974, doi: 10.1109/PROC.1974.9544.

[201] William. F. Tinney and C. E. Hart, ‘Power Flow Solution by Newton’s Method’, *IEEE Trans. Power Appar. Syst.*, vol. PAS-86, no. 11, pp. 1449–1460, Nov. 1967, doi: 10.1109/TPAS.1967.291823.

[202] O. A. Afolabi, W. H. Ali, P. Cofie, J. Fuller, P. Obiomon, and E. S. Kolawole, ‘Analysis of the Load Flow Problem in Power System Planning Studies’, *Energy Power Eng.*, vol. 7, no. 10, Art. no. 10, Sep. 2015, doi: 10.4236/epe.2015.710048.

[203] V. Ajjarapu, Ed., ‘Continuation Power Flow’, in *Computational Techniques for Voltage Stability Assessment and Control*, Boston, MA: Springer US, 2007, pp. 49–116. doi: 10.1007/978-0-387-32935-2_3.

[204] P. W. Sauer and M. A. Pai, ‘POWER SYSTEM DYNAMICS AND

STABILITY'.

[205] Allan, *Reliability Evaluation of Power Systems*. New York, NY: Springer, 1996.

[206] R. Billinton and R. N. Allan, 'Probability distributions in reliability evaluation', in *Reliability Evaluation of Engineering Systems: Concepts and Techniques*, R. Billinton and R. N. Allan, Eds, Boston, MA: Springer US, 1983, pp. 124–169. doi: 10.1007/978-1-4615-7728-7_6.

[207] Y. M. Atwa, E. F. El-Saadany, M. M. A. Salama, and R. Seethapathy, 'Optimal Renewable Resources Mix for Distribution System Energy Loss Minimization', *IEEE Trans. Power Syst.*, vol. 25, no. 1, pp. 360–370, Feb. 2010, doi: 10.1109/TPWRS.2009.2030276.

[208] J. A. Carta, P. Ramírez, and S. Velázquez, 'A review of wind speed probability distributions used in wind energy analysis: Case studies in the Canary Islands', *Renew. Sustain. Energy Rev.*, vol. 13, no. 5, pp. 933–955, Jun. 2009, doi: 10.1016/j.rser.2008.05.005.

[209] C. Genest and A.-C. Favre, 'Everything You Always Wanted to Know about Copula Modeling but Were Afraid to Ask', *J. Hydrol. Eng.*, vol. 12, no. 4, pp. 347–368, Jul. 2007, doi: 10.1061/(ASCE)1084-0699(2007)12:4(347).

[210] P.-L. Liu and A. Der Kiureghian, 'Multivariate distribution models with prescribed marginals and covariances', *Probabilistic Eng. Mech.*, vol. 1, no. 2, pp. 105–112, Jun. 1986, doi: 10.1016/0266-8920(86)90033-0.

[211] Y. Zhang and S. Wang, 'Harmonic power flow analysis for distribution system with distributed generations', in *2014 China International Conference on Electricity Distribution (CICED)*, Sep. 2014, pp. 1565–1569. doi: 10.1109/CICED.2014.6991969.

[212] Z. Hu, Y. Han, A. S. Zalhaf, S. Zhou, E. Zhao, and P. Yang, 'Harmonic Sources Modeling and Characterization in Modern Power Systems: A Comprehensive Overview', *Electr. Power Syst. Res.*, vol. 218, p. 109234, May 2023, doi: 10.1016/j.epsr.2023.109234.

[213] E. Thunberg and L. Soder, 'A Norton approach to distribution network modeling for harmonic studies', *IEEE Trans. Power Deliv.*, vol. 14, no. 1, pp. 272–277,

Jan. 1999, doi: 10.1109/61.736738.

[214] A. Testa *et al.*, 'Interharmonics: Theory and Modeling', *IEEE Trans. Power Deliv.*, vol. 22, no. 4, pp. 2335–2348, Oct. 2007, doi: 10.1109/TPWRD.2007.905505.

[215] J.-H. Han, K.-B. Lee, C.-H. Park, and G.-S. Jang, 'Estimation of Harmonic Sources in a Power System using Recursive Least-Squares Technique', *Trans. Korean Inst. Electr. Eng.*, vol. 60, no. 9, pp. 1639–1645, 2011, doi: 10.5370/KIEE.2011.60.9.1639.

[216] 'Power System Harmonics | Wiley Online Books'. Accessed: Apr. 02, 2025. [Online]. Available: https://onlinelibrary.wiley.com/doi/book/10.1002/0470871229

[217] D. Xia and G. T. Heydt, 'Harmonic Power Flow Studies Part I - Formulation and Solution', *IEEE Trans. Power Appar. Syst.*, vol. PAS-101, no. 6, pp. 1257–1265, Jun. 1982, doi: 10.1109/TPAS.1982.317171.

[218] Z. A. Memon, R. Trinchero, Y. Xie, F. G. Canavero, and I. S. Stievano, 'An Iterative Scheme for the Power-Flow Analysis of Distribution Networks based on Decoupled Circuit Equivalents in the Phasor Domain', *Energies*, vol. 13, no. 2, Art. no. 2, Jan. 2020, doi: 10.3390/en13020386.

[219] S. M. Mohd Shokri, M. M. Othman, M. A. Abdul Razak, I. Musirin, Z. Zakaria, and M. N. Kari, 'A direct approach used for solving the distribution system and harmonic load flow solutions', in *2013 IEEE 7th International Power Engineering and Optimization Conference (PEOCO)*, Jun. 2013, pp. 708–713. doi: 10.1109/PEOCO.2013.6564638.

[220] Y. Shiwen, H. Hui, W. Chengzhi, G. Hao, and F. Hao, 'Review on Risk Assessment of Power System', *Procedia Comput. Sci.*, vol. 109, pp. 1200–1205, Jan. 2017, doi: 10.1016/j.procs.2017.05.399.

[221] S. Nikolovski, D. Sljivac, and B. Stefic, 'State enumeration approach in reliability assessment of the Eastern Croatia bulk power system', in *PowerTech Budapest 99. Abstract Records. (Cat. No.99EX376)*, Aug. 1999, pp. 138-. doi: 10.1109/PTC.1999.826569.

[222] 'Simulation of Discrete-Event Systems', in *Simulation and the Monte Carlo*

Method, John Wiley & Sons, Ltd, 2016, pp. 91–106. doi: 10.1002/9781118631980.ch3.

[223] S. Liu, Y. Yin, J. Yan, and Z. Yu, 'Review and prospects of research on risk assessment of power system', in *2014 China International Conference on Electricity Distribution (CICED)*, Sep. 2014, pp. 537–542. doi: 10.1109/CICED.2014.6991767.

[224] J. Arrillaga, 'Power system quality assessment'.

[225] F. Li, J. Yang, S. Shen, K. Zhu, J. Qian, and C. Yan, 'Adaptability Evaluation of Power Grid Planning Scheme Based on Improved AHP-CRITIC-TOPSIS with High Proportion of Renewable Energy', in *2023 IEEE International Conference on Power Science and Technology (ICPST)*, May 2023, pp. 623–630. doi: 10.1109/ICPST56889.2023.10165456.

[226] Y. Chen *et al.*, 'A Novel Approach for Evaluating Power Quality in Distributed Power Distribution Networks Using AHP and S-Transform', *Energies*, vol. 17, no. 2, p. 411, Jan. 2024, doi: 10.3390/en17020411.

[227] A. R. Krishnan, M. M. Kasim, R. Hamid, and M. F. Ghazali, 'A Modified CRITIC Method to Estimate the Objective Weights of Decision Criteria', *Symmetry*, vol. 13, no. 6, p. 973, Jun. 2021, doi: 10.3390/sym13060973.

[228] D. Buła, D. Grabowski, and M. Maciążek, 'A Review on Optimization of Active Power Filter Placement and Sizing Methods', *Energies*, vol. 15, no. 3, p. 1175, Jan. 2022, doi: 10.3390/en15031175.

[229] 'Research on Distribution Network Harmonic Mitigation and Optimization Control Strategy Oriented by Source Tracing'. Accessed: Apr. 19, 2026. [Online]. Available: https://www.mdpi.com/2227-9717/13/10/3268

[230] 'Harmonic Mitigation Using Phase-shifting Transformers and Harmonic Filters - Technical Articles'. Accessed: Sep. 29, 2025. [Online]. Available: https://eepower.com/technical-articles/harmonic-mitigation-using-phase-shifting-transformers-and-harmonic-filters/

[231] Sindhu S., M. R. Sindhu, and T. N. P. Nambiar, 'An Exponential Composition Algorithm Based UPQC for Power Quality Enhancement', *Procedia Technol.*, vol. 21, pp. 415–422, 2015, doi: 10.1016/j.protcy.2015.10.062.

[232] W. Guo and W. Xu, ‘Research on optimization strategy of harmonic suppression and reactive power compensation of photovoltaic multifunctional grid connected inverter’, *Int. J. Electr. Power Energy Syst.*, vol. 145, p. 108649, Feb. 2023, doi: 10.1016/j.ijepes.2022.108649.

[233] N. Kashyap and A. Mishra, ‘A discourse on metaheuristics techniques for solving clustering and semisupervised learning models’, in *Cognitive Big Data Intelligence with a Metaheuristic Approach*, Elsevier, 2022, pp. 1–19. doi: 10.1016/B978-0-323-85117-6.00012-1.

[234] J. Kennedy and R. Eberhart, ‘Particle swarm optimization’, in *Proceedings of ICNN’95 - International Conference on Neural Networks*, Nov. 1995, pp. 1942–1948 vol.4. doi: 10.1109/ICNN.1995.488968.

[235] ‘NETWORK RECONFIGURATIONIN DISTRIBUTIONSYSTEMS FOR LOSS REDUCTIONAND LOAD BALANCING’.

[236] X. Xie and Y. Sun, ‘A piecewise probabilistic harmonic power flow approach in unbalanced residential distribution systems’, *Int. J. Electr. Power Energy Syst.*, vol. 141, p. 108114, Oct. 2022, doi: 10.1016/j.ijepes.2022.108114.

[237] D. Šošić, M. Žarković, and G. Dobrić, ‘Fuzzy-based Monte Carlo simulation for harmonic load flow in distribution networks’, *IET Gener. Transm. Distrib.*, vol. 9, no. 3, pp. 267–275, 2015, doi: 10.1049/iet-gtd.2014.0138.

[238] M. E. Baran and F. F. Wu, ‘Network reconfiguration in distribution systems for loss reduction and load balancing’, *IEEE Trans. Power Deliv.*, vol. 4, no. 2, pp. 1401–1407, Apr. 1989, doi: 10.1109/61.25627.

[239] J. Kennedy and R. Eberhart, ‘Particle swarm optimization’, in *Proceedings of ICNN’95 - International Conference on Neural Networks*, Nov. 1995, pp. 1942–1948 vol.4. doi: 10.1109/ICNN.1995.488968.

[240] X. Lv, Y. Wang, J. Deng, G. Zhang, and L. Zhang, ‘Improved Particle Swarm Optimization Algorithm Based on Last-Eliminated Principle and Enhanced Information Sharing’, *Comput. Intell. Neurosci.*, vol. 2018, no. 1, p. 5025672, 2018, doi: 10.1155/2018/5025672.

[241] Z. Xie, X. Huang, and W. Liu, ‘Subpopulation Particle Swarm Optimization with a Hybrid Mutation Strategy’, *Comput. Intell. Neurosci.*, vol. 2022, no. 1, p. 9599417, 2022, doi: 10.1155/2022/9599417.

[242] M. Primorac, Z. Klaić, M. Žnidarec, and H. Adrić, ‘Optimal allocation and sizing of shunt active power filter in radial distribution systems using particle swarm optimization’, in *IEEE EUROCON 2023 - 20th International Conference on Smart Technologies*, Jul. 2023, pp. 239–244. doi: 10.1109/EUROCON56442.2023.10199030.